Superconducting Proximity Effect in Nanowire Josephson Junctions

by

Kaveh Gharavi

A thesis
presented to the University of Waterloo
in fulfillment of the
thesis requirement for the degree of
Doctor of Philosophy
in
Physics (Quantum Information)

Waterloo, Ontario, Canada, 2023

List of Examining Committee Members

The following served on the Examining Committee for this thesis. The decision of the Examining Committee is by majority vote.

External Examiner
Dr. Michael HILKE
McGill University

Supervisor
Dr. Jonathan BAUGH
University of Waterloo

Internal Member
Dr. Adrian LUPASCU
University of Waterloo

Internal Member
Dr. Roger MELKO
University of Waterloo

Internal-external Member
Dr. Chris WILSON
University of Waterloo

Author's Declaration

This thesis consists of material all of which I authored or co-authored: see Statement of Contributions included in the thesis. This is a true copy of the thesis, including any required final revisions, as accepted by my examiners.

I understand that my thesis may be made electronically available to the public.

Statement of Contributions

Chapter 1

Kaveh Gharavi is the sole author of this chapter.

K.G. thanks Sean Walker for helpful discussions and general awesomeness.

Chapter 2

Kaveh Gharavi, Gregory W. Holloway, Chris M. Haapamaki, Mohammad H. Ansari, Mustafa Muhammad, Ray R. LaPierre, and Jonathan Baugh contributed to this chapter.

K.G. and J.B. designed the experiment. C.M.H. and R.R.L. performed nanowire growth. G.W.H., M.M. and K.G. fabricated the junction devices. J.B. and K.G. acquired the experimental data. K.G. performed data analysis and fitting. K.G. and M.H.A. developed the semiclassical model in consultation with J.B. K.G. wrote this chapter. The project was supervised by J.B.

We gratefully acknowledge discussions with A. J. Leggett, B. Spivak, A. Burkov, R. Aguado, and E. Prada, and the technical support provided by the Quantum NanoFab facility. R. Romero provided technical assistance. We are grateful to B. Plourde and M. Ware (Syracuse University) for assistance with Nb deposition.

Chapter 3

Kaveh Gharavi and Jonathan Baugh contributed to this chapter.

K.G. developed the model in consultation with J.B. K.G. performed numerical calculations and analysis. K.G. wrote this chapter. The project was supervised by J.B.

We thank A. J. Leggett and S. Frolov for helpful discussions.

Chapter 4

Kaveh Gharavi, Gregory W. Holloway, Ray R. LaPierre, and Jonathan Baugh contributed to this chapter.

K.G. designed the experiment in consultation with J.B. Nanowire growth was performed in the group of R.R.L. K.G. performed device fabrication with help from G.W.H. K.G. and J.B.

acquired experimental data. K.G. performed data analysis and developed numerical models for data. K.G. wrote this chapter. The project was supervised by J.B.

We thank Karsten Flensbserg and Francois Sfigakis for helpful discussions. K.G. thanks Eduardo Barrera for technical assistance. Nanowire growth was performed at The Centre for Emerging Device Technologies at McMaster University. The University of Waterloo's Quantum NanoFab was used for device fabrication.

Chapter 5

Kaveh Gharavi, Gregory W. Holloway, Ray R. LaPierre, and Jonathan Baugh contributed to this chapter.

K.G. designed the experiment in consultation with J.B. Nanowire growth was performed in the group of R.R.L. K.G. performed device fabrication with help from G.W.H. K.G. acquired experimental data. K.G. performed data analysis. K.G. wrote this chapter. The project was supervised by J.B.

K.G. thanks Kyle Willick for helpful discussions and Francois Sfigakis for technical assistance.

Chapter 6

Kaveh Gharavi, Darryl Hoving, and Jonathan Baugh contributed to this chapter.

J.B. proposed the idea. K.G. and D.H. developed the model in consultation with J.B. K.G. developed software for numerical calculations. D.H. and K.G. performed numerical calculations. K.G. wrote this chapter. The project was supervised by J.B.

We thank K. Flensberg for helpful discussions. D.H. thanks M. Mosca for guidance and discussions.

Chapter 7

Kaveh Gharavi is the sole author of this chapter.

K.G. thanks Bhaskaran Muralidharan and Praveen Sriram for helpful discussions.

Abstract

Semiconducting nanowires contacted with superconductors are an interesting class of hybrid mesoscopic devices, in which charge transport is quantum mechanical due to the confinement potential of the nanowire, as well as the quantum mechanical nature of superconductivity. Especially interesting is the case where transport is phase coherent, resulting in the semiconductor inheriting certain properties of the superconductor (e.g. sustaining a dissipation-less current), a phenomenon called proximity superconductivity. Proximity effects allow for rich and interesting physics to occur at the intersection of superconductivity and mesoscopic transport, which are the subject of study in this thesis. Furthermore, proximitized nanowire devices with a strong spin-orbit coupling are promising candidates for the realization of Majorana bound states — quasiparticle states that are topological in nature and have enjoyed much recent attention due to their applications to topological quantum computing. As well as fundamental curiosity about proximity phenomena, it is imperative to fully understand them in order to utilize hybrid nanowire devices as the building blocks of a topological quantum computer.

In this thesis we present experimental studies of three generations of Nb/InAs nanowire/Nb Josephson junctions in which proximity superconductivity is observed. Cryogenic transport measurements allow us to identify Andreev reflection as the mechanism behind the proximity effects — a mechanism wherein an electron incident on the superconductor/semiconductor interface is retro-reflected as a (conduction band) hole, carrying a charge equal to twice the electronic charge from the semiconductor into the superconductor, where it is carried as a Cooper pair. This mechanism is critically dependent on the transparency of the superconductor/semiconductor interface, whose qualities are successively improved over the three generations of devices. Further interesting and rich phenomena are also observed in the nanowire junctions, including Multiple Andreev reflections, Andreev bound states, and the likelihood of a novel form of Josephson interference called Orbital Josephson interference. We present theoretical and numerical studies that model these observed phenomena. Finally, we explore the relevance of this work to the topological quantum computing community by describing future challenges and experiments which can reveal the physics of Majorana bound states in similar systems. We give an in-depth proposal involving a proximitized nanowire and a quantum dot which can be used to verify the topological nature of the system, as well as read out the parity state of the Majorana bound states within the system.

Acknowledgements

First and foremost I owe an immense debt of gratitude to my family for their unrelenting love. My parents, who withheld nothing and always invested in me, my brother Dara whom I miss dearly, and my lovely wife Jessica — who has stuck with me through thick and thin (mostly "thin", honestly) with amazing strength. I don't know if I'll ever be able to repay you.

Great thanks are owed to my PhD advisor Dr. Jonathan Baugh for the many lessons I have learned from him, not the least of which is clear and precise scientific thought, and for his formidable and admirable work ethic. Many thanks to all the members of the Coherent Spintronics Group for their collaborations, support, and friendship: Greg Holloway, Chris Haapamaki, Kyle Willick, Annelise Bergeron, Eduardo Barrera, Francois Sfigakis, and many others. Sean Walker deserves and gets special mention for special awesomeness.

I'm deeply grateful to friends and family without whose emotional and material support I would not have survived — which, unfortunately, is not a hyperbolic statement. Krista, Hilary, Razieh, Katja, Marcus, Emily, John, Chris P, Cassandra, Niloufar, Farid, Javad, Ameneh, and Reza Joon — thank you!

Unique thanks are owed to Ghazaleh, Touba, and Souzan for their love. Touran was also present.

Lastly, praise be to the great poet Ferdowsi, whose genius epic *Shahnameh* has been a reliable source of calm and joy in a chaotic world.

چنین است رسم جهان جهان　　همی راز خویش از تو دارد نهان
نسازد تو ناچار با او بساز　　که روزی نشیب است و روزی فراز

Dedication

To the loving memory of my grandfather
Morteza Gharavi
(1919 — 2017)
this thesis is humbly dedicated.

آن میر غوغا را بگو وان شور و سودا را بگو وان سرو خضرا را بگو مستان سلامت می‌کنند

Table of Contents

List of Tables

List of Figures

Chapter 1

Introduction

In 1937, Ettore Majorana proposed [1] a real version of Dirac's equation for the electron. The hypothetical solutions to this equation bear the name Majorana fermions (MFs). These particles, due to the realness of the Majorana equation, are spinless and chargeless. There is an open question in high-energy physics as to whether free-standing MFs exist and whether (some) neutrinos have Majorana mass versus Dirac mass, which is beyond the scope of this thesis (see, e.g., Ref. [2] for a review).

The name 'Majorana' is also used to refer to an entirely different class of objects: quasiparticle excitations of certain two (or one) dimensional condensed matter systems at low temperature. These quasiparticles are also charge- and spinless (a fact first discovered by Fu and Kane [3] in 2008), and called Majorana Zero Modes (MZMs) or Majorana Bound States (MBS) [4, 5, 6, 7, 8]. MBS enjoy non-Abelian exchange statistics (Section 1.1), a fact that makes them useful as qubit candidates in quantum computing (Section 1.3), and has garnered enormous theoretical and experimental interest in the past decade (Section 1.4). In this thesis we are interested in the experimental development and study of topological superconductors (Section 1.2) as a platform for hosting MBS, specifically hybrid superconducting-semiconducting nanowire Josephson junctions. We find these devices to be promising, showcasing rich and complex phenomena involving the interplay of superconductivity, Coulomb interactions, and the Zeeman effect.

Before describing our experiments on these devices, we provide a quick exploration of the theoretical background to the key concepts related to MBS, starting with non-Abelian exchange statistics and continuing to topological superconductivity and quantum computing using MBS. Our aim is to provide a theoretical foundation for the reader interested in this topic, at a level of detail that addresses or at least alludes to all important concepts while still being relevant to an experimentalist — a resource we found hard to come by at the time of writing.

1.1 Exchange Statistics and Non-Abelian Anyons

Because Majorana Zero Modes are two-dimensional objects, in order to describe their relevance to quantum computing we must first discuss the fundamentals of particle exchange statistics in two dimensions.

It is a well known fact that, in a universe with three spatial and one temporal dimensions (3+1d), elementary particles are observed to be bosons if and only if they have integer spin, or fermions if and only if they have half-integer spin [9]. This observation is theoretically supported by the spin-statistics theorem [10, 11, 12]. While a detailed discussion of the spin-statistics theorem is left to textbooks on quantum field theory (QFT), we briefly mention that the theorem states the following: any reasonable QFT — namely, any QFT who is Lorentz-invariant, and describes real excitations (of a quantum field) that have finite mass (i.e., "particles") — will necessarily describe particles with either integer or half-integer spin. The former of these are called bosons, and the wavefunction describing two or more identical bosons retains the same value when the positions of any two of the identical boson are swapped; and the latter are called fermions. The value of the wavefunction describing two or more identical fermions changes sign when any two of the identical fermions are swapped. This behaviour with respect to swapping the positions of identical particles is called exchange statistics, and is the ultimate reason behind the different behaviour of the (macroscopic) quantum state of a collection of bosons (e.g. the coherent state of light in a laser) versus fermions (e.g. the Fermi sea in a metal or semiconductor) as described in quantum statistical physics.

Exchange statistics is fundamentally different in a universe with two spatial and one temporal dimensions (2+1d) [4]. Specifically, in 2+1d, describing the operation of swapping the positions of two identical particles (e.g. (r_1, r_2) at some initial time $\rightarrow$ (r_2, r_1) at final time) is ambiguous without also specifying a chirality (handedness). Figure 1.1 panels (a) and (b) showcase this point, with the former displaying a representation of the worldlines of two identical particles swapped counter-clockwise, and the latter clockwise, in 2+1d. The trajectories do not cross, but rather show one particle going behind the other in the x-y plane in order to perform the swap; time displayed in the vertical direction. We say that the two swaps are not *topologically equivalent*, meaning that there exists no smooth, continuous transformation that converts one to the other. That is at least, not without committing disallowed actions, such as (1) "doubling back" at some point in the transformation — which implies moving back in time and/or the creation/annihilation of a corresponding anti-particle (which does not conserve particle number and is not a swap operation); or (2) moving the particles "through" each other by crossing the trajectories (which may or may not be possible depending on if there is a hard-core repulsion between the particles, but regardless also does not describe a swap operation). By contrast, in 3+1d, the third spatial dimension can be used to "disentangle" the two

trajectories in a smooth manner, and so swaps have no chirality in 3+1d. This fundamental difference between systems with different dimensions was realized by Leinaas and Myrheim [13] and Wilczek [14], and allows for different possibilities for quantum mechanical properties to emerge in 2+1d, as first described in the early 1980s [15].

The mathematical object describing chiral exchange in 2+1d is the braid group [4], originally so named because it abstractifies the braiding of strands in three dimensions — in our case, equivalently, the braiding of worldline trajectories in 2+1d. The n-dimensional braid group Br_n describes the braiding of n strands. Figure 1.1 shows several members of the group Br_3. Algebraically speaking, Br_n is described by generators $\left\{e, \sigma_1, \ldots \sigma_{n-1}, \sigma_1^{-1}, \ldots, \sigma_{n-1}^{-1}\right\}$, where e is the identity element (i.e. describes the "no braiding" operation), and σ_i describes the counterclockwise braiding of the $i, i+1$ strands; the inverse element σ_i^{-1} therefore describes the clockwise braiding of the same strands (see fig. 1.1, panels (a), (b), (c)). The multiplication of two (or more) σs is therefore another element of the group, describing two (or more) successive braids. The generators obey the following relations: $\sigma_i\sigma_j = \sigma_j\sigma_i$ iff $|i-j| \geq 2$ (i.e., the group is generally non-Abelian, see panel (d)), and $\sigma_i\sigma_{i+1}\sigma_i = \sigma_{i+1}\sigma_i\sigma_{i+1}$ for $1 \leq i \leq n-1$ (see panel (e)).

The only algebraic difference between this group and the permutation group (which abstractifies exchange in 3+1d) is $\sigma_i^2 \neq e$. This has a significant effect. For one, the braid group is infinite, even for just two particles (e.g. $\sigma_1^k \in \mathrm{Br}_2$ is a unique element of the group for any integer k). By contrast, the n-dimensional permutation group S_n has cardinality $|S_n| = n!$. Furthermore, the braid group allows non-Abelian representations in the Hilbert spaces of particle wavefunctions. We shall describe what this means now.

Members of the braid group are abstract objects; in order to describe how braiding would affect physical objects of interest, we need to give a *representation* of the braid group in the Hilbert space $\mathcal{H}$ in which the wavefunction or state-vector of objects live. Specifically for our case, a representation of the braid group is a function $\Phi : \mathrm{Br}_n \times \mathcal{H} \to \mathcal{H}$ who follows these requirements: firstly, Φ is linear over $\mathcal{H}$, secondly, $\Phi(e, \psi)$ is $\mathcal{H}$'s identity operator $\mathbf{I}$ for any $\psi \in \mathcal{H}$, and thirdly, for any two braids b_1, b_2 in Br_n and any $\psi \in \mathcal{H}$:

$$\Phi(b_1 b_2, \psi) = \Phi(b_1, \Phi(b_2, \psi)). \tag{1.1}$$

Eq. 1.1 is saying that Φ chains in the same manner that the members of the braid group multiply, and so carries forward the properties of the braid group. Given the linearity of Φ over $\mathcal{H}$, it may be intuitively instructive to think of $\Phi(b) : \mathcal{H} \to \mathcal{H}$ as being a map which takes the state-vector ψ to some other value ψ', and depends (only) on the performed braid $b \in \mathrm{Br}_n$. The above equation strictly restricts what those maps may be.

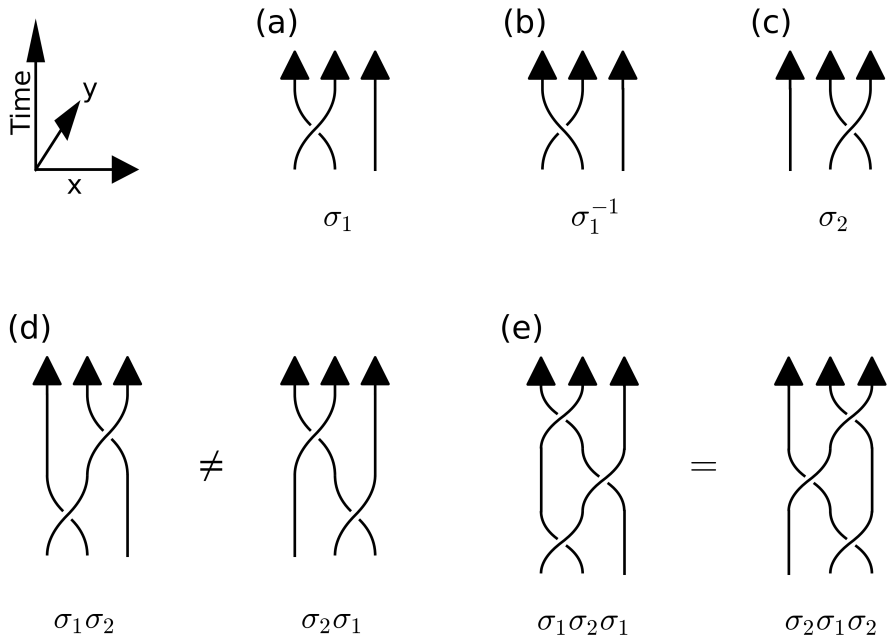

Figure 1.1: Worldline trajectories of three identical particles, showing the action of swapping positions in 2+1d, abstractified as members of the braid group Br_3. (a)- (b) Swapping the positions of the first two particles has chirality, with a counter-clockwise swap in panel (a) and clockwise swap in panel (b), identified as two of the generators of the Br_3 group σ_1, σ_1^{-1}. These two operations are not equivalent to each other, unlike in 3+1d. Another generator σ_2 is shown in panel (c); not shown are the remaining two generators e (identity) and σ_2^{-1}. Panel (d) demonstrates that the braid group is generally non-Abelian. In fact, the generators commute only if they act on non-adjacent strands. (e) An example of the defining relations of the braid group, $\sigma_i\sigma_{i+1}\sigma_i = \sigma_{i+1}\sigma_i\sigma_{i+1}$ for $1 \leq i \leq n-1$.

By contrast, for the case of 3+1d, the Φs are representations of the permutation group, and as permutations square to identity, eq. 1.1 implies that so do the Φs. Hence, the Φs reduce to factors of ± 1 for bosons/fermions respectively. However, in 2+1d, braids don't square to iden-

tity as mentioned above. For the simplest case of n identical particles in positions $r_1, r_2, \ldots, r_n$ described by a single valued wavefunction ψ, doing a counter-clockwise swap of the first two particles results in

$$\psi(r_2, r_1, \ldots, r_n) = \Phi(\sigma_1)\psi(r_1, r_2, \ldots, r_n) = \exp(i\theta)\psi(r_1, r_2, \ldots, r_n).$$

Here, θ (the so-called braiding phase) can take any value, modulo π (see, e.g. Ref. [16] as to why an arbitrary phase factor θ is the most general form acceptable for Φ). $\theta = 0, \pi$ are special cases corresponding to bosons and fermions. For other values of θ, the particles in question are called (Abelian) anyons. As the particles are all identical, we can derive that for any of the counter-clockwise braid generators σ_i, $\Phi(\sigma_i) = \exp(i\theta)$. Notice that even though the braid group itself is non-Abelian (e.g. $\sigma_1\sigma_2 \neq \sigma_2\sigma_1$), there is no requirement on Φ to be injective from the braid group; hence the Abelian nature of this representation. For example here we have $\Phi(\sigma_1\sigma_2) = \Phi(\sigma_2\sigma_1) = \exp(2i\theta)$.

Non-Abelian anyons arise when the state-vector is multivalued (e.g., a spinor). For n identical particles described by an m-valued state-vector $\Psi = [\psi_1(r_1, \ldots, r_n), \ldots, \psi_m(r_1, \ldots, r_n)]^T$, the most general form of $\Phi(\sigma_i)$ is an $m \times m$ matrix. As matrices are generally not Abelian under multiplication ($AB \neq BA$ in general for matrices A, B), it follows that the effect of braiding two or more of the identical particles can also be non-Abelian. For example, braiding the first two particles results in

$$\begin{bmatrix} \psi_1(r_2, r_1, \ldots, r_n) \\ \psi_2(r_2, r_1, \ldots, r_n) \\ \cdot \\ \cdot \\ \cdot \\ \psi_m(r_2, r_1, \ldots, r_n) \end{bmatrix} = \Phi(\sigma_1) \begin{bmatrix} \psi_1(r_1, r_2, \ldots, r_n) \\ \psi_2(r_1, r_2, \ldots, r_n) \\ \cdot \\ \cdot \\ \cdot \\ \psi_m(r_1, r_2, \ldots, r_n) \end{bmatrix} = \rho(\sigma_1)_{m\times m} \begin{bmatrix} \psi_1(r_1, r_2, \ldots, r_n) \\ \psi_2(r_1, r_2, \ldots, r_n) \\ \cdot \\ \cdot \\ \cdot \\ \psi_m(r_1, r_2, \ldots, r_n) \end{bmatrix}$$

for some $m \times m$ matrix $\rho(\sigma_1)$, and if this matrix does not commute with some other ρ, e.g. $\rho(\sigma_2)$, then the constituting identical particles are said to be non-Abelian anyons.

Since the action of braiding particles in a closed quantum system is expected to be reversible (following e.g. $\sigma_1\sigma_1^{-1} = e$), the ρs are unitary matrices evolving the state-vector of the system in question in a manner similar to the time evolution operator (see Ref. [4] for a rigorous argument for unitarity). However, in the case of braiding, the unitary operation effected on the state-vector depends only on the braid performed — modulo a "dynamical phase" which is expected to be negligible when the operation is done adiabatically (Refs [17, 18]). Since unique elements of the braid group refer to unique topologies of knots or braids, these operations are called topological operations. Section 1.3 describes how these topological operations can be utilized

for the purposes of quantum computation, and the "topological error protection" afforded by them.

Also due to the relation between braiding topologies and anyonic exchange statistics, a quantum field theory whose excitations are anyons is called a topological quantum field theory (TQFT). TQFTs are necessarily 2+1d, and fall under the broader category of Chern-Simons theories [19]; broadly speaking they describe particles (i.e. anyons) with exotic spin (values other than integer or half integer) in two spatial dimensions. Since the physical universe is 3+1d, physical realizations of TQFTs are restricted to descriptions of effective and/or emergent quasiparticles in 2+1d condensed matter systems. An example of this emergent anyonic behaviour is the $\nu = 1/3$ Laughlin state in the fractional Quantum Hall Effect [20], which is hypothesized to be an abelian anyon with charge $e/3$ and braiding phase $\theta = \pi/3$.

Whereas the braiding phase θ is sufficient to describe the exchange statistics of an Abelian anyon, non-Abelian anyons are categorized according to their fusion rules. Fusion rules are the set of rules that describe the exchange statistics of bound states of (Abelian or non-Abelian) anyons, and are analogous to spin addition rules in 3+1d, which for example describe how the bound state of two spin $1/2$ elections is a boson with integer spin (either a spin singlet or a triplet). The bound state of two or more anyons is itself generally an anyon, and so systems hosting anyons usually host multiple types of anyons.

An important category of non-Abelian anyons are the so called Ising anyons [4, 21], whose fusion rule can be written symbolically as follows:

$$\mathbf{1/2} \times \mathbf{1/2} = \mathbf{0} + \mathbf{1}. \tag{1.2}$$

Here, the $\mathbf{1/2}$ particle is a non-Abelian particle whose bound state with itself is either the vacuum particle $\mathbf{0}$, or a standard fermion $\mathbf{1}$ (cf. the similarity to the bound state of to spin 1/2 particles, which is either a spin singlet or a triplet). Topological superconductors [22] (including MZMs and Majorana Bound States), topological insulators [23], and the $\nu = 5/2$ fractional Quantum Hall Effect state [24, 25, 26] are considered to be examples of Ising anyons. Ising anyons are the simplest possible non-Abelian particles, and as such do not afford universal topologically protected operations [27] for the purposes of quantum computing (more on this in Section 1.3). Another theorized class non-Abelian anyons named Fibonacci anyons [28] possess complex enough fusion rules which would allow universal quantum computing in a topologically protected manner, although as of this writing we know of no TQFTs describing a physical system whose excitation quasiparticles behave as Fibonacci anyons, nor of any other TQFT whose excitations would allow universal + topologically protected quantum computing.

1.2 Theory of Majorana Zero Modes in Topological Superconductors

Our interest in this thesis lies primarily in developing and understanding topological superconducting materials. In their seminal work, Fu and Kane discovered [3] that the excitations states inside the vortex core of a so-called p+ip chiral superconductor[29, 30, 31] are non-Ableian anyons. Later, Kitaev proposed [32] a significantly simpler toy model for a topological superconductor, in the form of a one dimensional superconducting chain. Non-Ableian particles could arise at the ends of this chain following the Ising fusion rules. Furthermore, the particles are chargeless and at zero energy, and due to their fusion rules can combine to form the vacuum particle. Therefore, they can be thought of as their own anti-particle. It is by this analogy to Majorana's proposed chargeless elementary particle (who is equal to its own anti-particle), that these emergent anyons are called Majorana Zero Modes. Alternatively, two MZMs could combine to form a (non-local) electron, further motivating the notation in eq. 1.2 which denotes the non-Abelian particles as $\mathbf{1/2}$ — in a certain way, MZMs behave like "half of an electron."

Whereas Kitaev's model is simple and elucidating, it is also unrealistic in that it requires a spinless p-wave superconductor. While some organic superconductors [33] are considered intrinsically p-wave, these are exotic (and spinful) materials. In the next section, we focus on realistic physical implementations of this model using standard s-wave superconductors and describe how these implementations result in emergent p-wave and non-Abelian behaviour.

In early 2010's several papers [6, 8, 34, 35, 5, 7] suggested a "recipe" for creating Majorana Zero Modes (i.e. the quasiparticles hypothesized by Kitaev in his toy model [32]) in a realistic semiconductor system. The recipe includes the following elements:

- 1-Dimensional (1d) semiconducting nanowire
- Strong Rashba-type spin-orbit coupling (SOI), which occurs in materials such as InAs [36, 37] and InSb [38, 39]
- Magnetic field perpendicular to the spin-orbit coupling
- Proximitized superconductivity in the semiconductor [40]

We show below how this recipe creates a system which hosts Majorana Zero Modes.

The starting point is the single particle Hamiltonian for an electron in the 1d nanowire along the x direction, with SOI and B-field:

$$\hat{H}(x) = -\hbar^2 \frac{\partial_x^2}{2m} - \mu(x) - i\alpha\partial_x\sigma_y + g\mu_B B_x(x)\sigma_x/2, \tag{1.3}$$

which can be written in second-quantized form as an integral over a Hamiltonian density $\hat{h}$ as

$$\hat{H}_0 = \sum_{\sigma,\sigma' \in \{\uparrow,\downarrow\}} \int_{-\infty}^{+\infty} \mathrm{d}x \hat{\psi}^\dagger_{x,\sigma} \langle \sigma | \hat{h} | \sigma' \rangle \hat{\psi}_{x,\sigma'}. \tag{1.4}$$

Here, $\uparrow, \downarrow$ refer to σ_z eigenstates, $\hat{\psi}_{x,\sigma} = \sum_i \langle x | \psi_{i,\sigma} \rangle \hat{a}_{i,\sigma}$ is the quantum field operator which annihilates an electron with spin σ at position x, and $\hat{\psi}^\dagger_{x,\sigma}$ is the corresponding creation operator. The $\hat{a}_i (\hat{a}^\dagger_i)$ are annihilation (creation) operators acting on the electron occupation Fock space, and ψ_i are the (single electron) eigenfunctions of Eq. 1.3. We use the hatted symbol $\hat{\psi}$ so as to not confuse these operators with the wavefunctions ψ. Notice that $\hat{\psi}$ and $\hat{h}$ do not commute, due to the former's dependence on x via ψ_i. Let us declutter by defining the notation $\hat{h}^{\sigma,\sigma'} := \langle \sigma | \hat{h} | \sigma' \rangle$, and

$$\hat{H}_0 = \sum_{\sigma,\sigma' \in \{\uparrow,\downarrow\}} \int_{-\infty}^{+\infty} \mathrm{d}x \hat{\psi}^\dagger_{x,\sigma} \hat{h}^{\sigma,\sigma'} \hat{\psi}_{x,\sigma'} := \int_{-\infty}^{+\infty} \mathrm{d}x \hat{\psi}^\dagger_{x,\sigma} \hat{h}^{\sigma,\sigma'} \hat{\psi}_{x,\sigma'}, \tag{1.5}$$

i.e., similarly to Einstein's notation, summation over cross-diagonal σ indices is implied. If a realistic device simulation is desired, Eq. 1.5 has to be discretized and diagonalized numerically; we do that in the next section. It is also instructive to look at the behaviour of an infinite, uniform nanowire, which can be solved analytically. For that, it is useful to rewrite Eq. 1.5 in reciprocal space via the Fourier transforms

$$\begin{aligned} \hat{\psi}_{x,\sigma} &\longrightarrow \frac{1}{\sqrt{2\pi}} \int_{-\infty}^{+\infty} \mathrm{d}k e^{ikx} \hat{c}_{k,\sigma}, \\ \hat{\psi}^\dagger_{x,\sigma} &\longrightarrow \frac{1}{\sqrt{2\pi}} \int_{-\infty}^{+\infty} \mathrm{d}k' e^{-ik'x} \hat{c}^\dagger_{k',\sigma}, \end{aligned}$$

where k is the wave-number (shorthand for k_x) and $\hat{c}_{k,\sigma}$ are momentum-space analogues of the $\hat{\psi}$ operators. Eq. 1.5 becomes

$$\begin{aligned} \hat{H}_0 &= \frac{1}{2\pi} \int_{-\infty}^{+\infty} \mathrm{d}k \int_{-\infty}^{+\infty} \mathrm{d}k' \hat{c}^\dagger_{k,\sigma} \hat{h}^{\sigma,\sigma'} \hat{c}_{k',\sigma'} \int_{-\infty}^{+\infty} \mathrm{d}x e^{i(k-k')x} \\ &= \int_{-\infty}^{+\infty} \mathrm{d}k \hat{c}^\dagger_{k,\sigma} \hat{h}^{\sigma,\sigma'} \hat{c}_{k,\sigma'}. \end{aligned} \tag{1.6}$$

Here, we used the definition of the Dirac delta function to identify the third integral as $2\pi\delta(k - k')$, which in turn reduces the second integral. Now, the first and third terms of $\hat{h}$ (kinetic energy term and spin-orbit coupling term) are diagonal in the momentum basis, and so commute

with the $\hat{c}$ operators. To further simplify, let us assume the nanowire is uniform, in a uniform magnetic field, and infinitely long (which justifies integrating from $-\infty$ to ∞), and so μ and B_x lose their x dependence, and they too commute with the $\hat{c}$ operators. The Hamiltonian simplifies to

$$\hat{H}_0 = \int_{-\infty}^{+\infty} \mathrm{d}k \hat{h}_0^{\sigma,\sigma'}(k) \hat{c}_{k,\sigma}^\dagger \hat{c}_{k,\sigma'}, \quad \text{with} \tag{1.7}$$

$$\hat{h}_0(k) = \frac{\hbar^2 k^2}{2m} - \mu + \alpha k \sigma_y + g\mu_B B_x \sigma_x/2. \tag{1.8}$$

We write out all terms of $\hat{H}_0$ explicitly for completeness:

$$\begin{aligned}\hat{H}_0 = \int_{-\infty}^{+\infty} \mathrm{d}k \Big[&(\frac{\hbar^2 k^2}{2m} - \mu)(\hat{c}_{k,\uparrow}^\dagger \hat{c}_{k,\uparrow} + \hat{c}_{k,\downarrow}^\dagger \hat{c}_{k,\downarrow}) + \\ &(g\mu_B B_x/2 + i\alpha k)(\hat{c}_{k,\uparrow}^\dagger \hat{c}_{k,\downarrow}) + (g\mu_B B_x/2 - i\alpha k)(\hat{c}_{k,\downarrow}^\dagger \hat{c}_{k,\uparrow}) \Big].\end{aligned} \tag{1.9}$$

The eigenenergies of $\hat{H}_0$ describe the basic electronic band structure of the nanowire in the absence of superconductivity.

We include proximity superconductivity by adding a mean-field BCS pairing potential

$$\hat{H}_i(x) = \Delta(x) \hat{\psi}_{x,\uparrow}^\dagger \hat{\psi}_{x,\downarrow}^\dagger + \text{h.c.}$$

Again, let us assume Δ has no x dependence (i.e., an infinitely long, uniform, proximitezed nanowire), so it can be easily written in k-space. Using the Fourier transform described above, we find

$$\hat{H}_i = \Delta \hat{c}_{k,\uparrow}^\dagger \hat{c}_{-k,\downarrow}^\dagger + \text{h.c.} \tag{1.10}$$

The total Hamiltonian is

$$\hat{H} = \hat{H}_0 + \hat{H}_i, \tag{1.11}$$

but we find $\hat{H}$ as is written here difficult to diagonalize due to the $\hat{c}^\dagger \hat{c}^\dagger$ terms in $\hat{H}_i$. This problem is solved by defining a so-called Nambu vector (see texts regrading solutions to superconducting quasiparticle energies for an introduction to Nambu vectors; e.g. [41]) $\Psi = [\hat{c}_{k,\uparrow}, \hat{c}_{k,\downarrow}, -\hat{c}_{-k,\downarrow}^\dagger, \hat{c}_{-k,\uparrow}^\dagger]^\mathrm{T}$ in electron-hole space, where the first (last) two elements correspond to the electron (hole) block. The total Hamiltonian can be rewritten as

$$\hat{H} = \frac{1}{2} \int \mathrm{d}k \Psi^\dagger(k) \hat{h}_{BdG}(k) \Psi(k), \tag{1.12}$$

where $\hat{h}_{BdG}$ is Bogoliubov-de Gennes Hamiltonian density:

$$\hat{h}_{BdG}(k) = \begin{pmatrix} \hat{h}_0(k) & \Delta \\ \Delta^* & -\sigma_y \hat{h}_0(k) \sigma_y \end{pmatrix}. \tag{1.13}$$

Several notes are to be made here: first, the term $-\sigma_y \hat{h}_0(k)\sigma_y$ is recognized as the spin and time-reversed version of $\hat{h}_0$, i.e. the "holes" in question here are not valence band holes, but rather time-reversed electrons in the conduction band. Second, by considering these "holes" as independent particles we have artificially doubled the dimensions of the problem (i.e., by adding the electron-hole component of the Nambu vector). This is justified by realizing an inherent symmetry of the BdG Hamiltonian: particle-hole symmetry. Namely if $\hat{h}_{BdG}$ admits an eigenenergy E, then it also admits -E as an eigenenergy, thus reducing the effective degrees of freedom by a factor of two. Mathematically speaking, the operator $P = \tau^y \otimes \sigma^y K$ commutes with the Hamiltonian; where τ are Pauli-matrices operating on the particle-hole subspace, and K is the complex-conjugation operator. We have

$$\left\{\hat{H}, P\right\} = \left\{\hat{h}_{BdG}, P\right\} = 0. \tag{1.14}$$

The reader who attempted to derive Eq. 1.9 from Eq. 1.7 by multiplying out the Nambu vector terms will have noticed that the derivation requires use of identities such as

$$\hat{c}^\dagger_{k,\uparrow} = \hat{c}_{-k,\downarrow}, \tag{1.15}$$

and similar for $\hat{c}$, for $\uparrow, \downarrow; \pm k$. These relations follow from the particle-hole symmetry of the problem. For example, Eq. 1.15 is saying that the effect of creating an electron with momentum k and spin up is the same as removing an electron (creating a hole) with momentum $-k$ and spin down.

Third, the choice of the Nambu vector Ψ is not unique. The one used here will be recognized by those familiar with the solution to the original, spinless Bogoliubov-de Gennes equations via canonical transformation [41]. However, any linearly independent combination of four $\hat{c}, \hat{c}^\dagger$ operators from the two different spin channels can be used in principle. Sometimes it is helpful to use $\Psi = [\hat{c}_{k,\uparrow}, \hat{c}_{k,\downarrow}, \hat{c}^\dagger_{-k,\uparrow}, \hat{c}^\dagger_{-k,\downarrow}]^{\mathrm{T}}$. This results in a slightly different form for the BdG Hamiltonian:

$$\hat{h}_{BdG}(k) = \begin{pmatrix} \hat{h}_0(k) & -i\sigma_y \Delta \\ i\sigma_y \Delta^* & -\hat{h}_0(k) \end{pmatrix}, \tag{1.16}$$

which is a helpful form in that it can be written out using tensor products of two sets of Pauli matrices, σ, τ, pertaining to spin and electron-hole spaces respectively:

$$\begin{aligned}\hat{h}_{BdG}(k) = \quad & (\hbar^2 k^2/(2m^*) - \mu)\sigma_0\tau_z \\ & + (\alpha k)\sigma_y\tau_z \\ & + (g\mu_B B_x/2)\sigma_x\tau_z \\ & + \Delta\sigma_y\tau_y. \end{aligned} \tag{1.17}$$

Here, we have dropped the tensor product symbol "$\otimes$" between the σs and τs for brevity of notation, and assumed a real, constant Δ. The form for P also changes to $P = \tau^x K$. While mathematically useful (e.g. for numerical simulations), this picture is not as easy to physically interpret as the previous one.

Forth, this freedom in the choice of Ψ is sometimes called the "Majorana gauge" choice. Furthermore, notice that the total Hamiltonian is not (global) gauge-invariant due to the presence of the BCS term (as is well known that BCS violates gauge invariance). This is not in violation of Elitzur's theorem [11], which only requires local gauge-invariance for physically meaningful Hamiltonians. Lack of gauge invariance is ultimately why the Majorana solution to $\hat{H}$ cannot couple to electromagnetic fields and is charge neutral.

Now, finally, we are in a position to diagonalize $\hat{H}$. We do so by first diagonalizing $\hat{h}_{BdG}$ (which is possible to do analytically for an infinite, uniform nanowire). Assuming we have eigensolutions ϕ such that $\hat{h}_{BdG}\phi_i = E_i\phi_i$, then

$$\hat{H} = \frac{1}{2}\sum_i E_i a_i^\dagger a_i, \tag{1.18}$$

where

$$a_i = \int \mathrm{d}k \phi_i^*(k)\Psi(k). \tag{1.19}$$

We are now equipped to study the infinite, uniform nanowire, for which $\hat{h}_{BdG}$ becomes a simple 4×4 Hamiltonian, dependent on a single parameter k. The results of this calculation are presented in Section 1.2.2.

1.2.1 Discretization of Nanowire Hamiltonian

As mentioned above, the simulation of a nanowire with position-dependent parameters requires a real-space description such that can be numerically solved. Our starting point is the real-space version of Eq. 1.17, the BdG Hamiltonian:

$$\begin{aligned}\hat{h}_{BdG}(x) = \quad & (-\hbar^2\partial_x^2/(2m^*) - \mu(x))\sigma_0\tau_z \\ & + (-i\alpha\partial_x)\sigma_y\tau_z \\ & + (g\mu_B B_x(x)/2)\sigma_x\tau_z \\ & + \Delta(x)\sigma_y\tau_y, \end{aligned} \tag{1.20}$$

where we have assumed a space-dependent chemical potential, magnetic field, and superconducting order parameter. Δ is taken to be real which is possible for when there is no time-dependence (ac Josephson effect). We then define

$$\hat{H} = \frac{1}{2}\int \mathrm{d}x \Psi^\dagger(x)\hat{h}_{BdG}(x)\Psi(x), \tag{1.21}$$

where the Nambu vector $\Psi(x)$ is defined similarly to above, but in real space. The Hamiltonian is then discretized using a standard nearest-neighbour tight-binding chain model, by converting the integral to a sum, and using the standard discretization formulas

$$\partial_x \to \frac{1}{2a}\left(|i+1\rangle\langle i| - |i-1\rangle\langle i|\right), \tag{1.22}$$

and

$$\partial_x^2 \to \frac{1}{a^2}\left(|i\rangle\langle i+1| + |i+1\rangle\langle i| - 2|i\rangle\langle i|\right), \tag{1.23}$$

where discretization is occurring on a uniform chain with site indices $|i\rangle$. Real-space position x is approximated to the closest $i \times a$, where a is the discretization length. The result is

$$\begin{aligned}\hat{H} = & \sum_i |i\rangle\langle i| \left\{(2t-\mu)\sigma_0\tau_z + (g\mu_B B_x/2)\sigma_x\tau_z + \Delta\sigma_y\tau_y\right\} \\ & + \sum_i (|i\rangle\langle i+1| + |i+1\rangle\langle i|)\left\{(-t)\sigma_0\tau_z + (-i\alpha/2a)\sigma_y\tau_y\right\}. \end{aligned} \tag{1.24}$$

Here, the terms on the first line are the so-called on-site terms, and the terms on the second line are the hopping terms. The parameter $t = \hbar^2/2m^*a^2$ is the hopping energy. For the tight-binding approximation to be valid, a necessary condition is that the hopping energy must be the largest energy in the system by some margin.

1.2.2 Results

Below we show the results of computing the dispersion relation of an infinite, uniform InAs nanowire (calculated from Eq. 1.24) and compare with the case of a finite InAs nanowire, as a function of axial magnetic field. The finite nanowire is in contact with a Nb superconductor from one end. The Nb contact is assumed to have a BCS superconducting gap of 1.4 meV, and a BCS-like decay [42] $\propto \sqrt{1 - B_x^2/H_c^2}$ of the superconducting gap versus the applied magnetic field, appropriate for a type II superconductor. We use the value $H_c = 3.1$ T for the Nb thin film. The other end of the nanowire is contacted with a normal metal. The local density of states (LDOS (x) = $\Sigma|\psi(x)|^2$, summed on all eigensolutions ψ) of the finite nanowire is calculated with use of the Kwant software package [43]. Kwant is an open source tool written in the Python programming language that can numerically solve (elastic) scattering and transmission problems in many different systems and situations. Here we use it to find reflected and transmitted wavefunctions, given incident wavefunctions on our nanowire (Figure 1.2 panel a) from positive or negative infinity, at different energies, at temperature $T = 0$. Standing-wave solutions (bound states) and local density of states (LDOS) can thence be calculated.

Figure 1.2 panels (d) and (e) pertain to zero magnetic field. We see in (d) that the infinite nanowire's dispersion relation shows four bands, corresponding to the two spin-channels and the electron-hole channel of the Nambu vector, which cross at $k = 0$. We also see a symmetric band gap around zero energy within which no state is possible. The value of the band gap equals 1.4 meV, the superconducting gap of the Nb contact. The same band gap is seen in the LDOS of the finite nanowire in (e). The 'skewness' of the states above the gap in the finite nanowire relate to the difference in the coupling strength to the two different contacts: a roughly 10 times stronger coupling to the Nb superconducting contact ensures proximity superconductivity in the nanowire, the weaker tunnel-like coupling to the normal contact limits the broadening of the states.

The bandgap is bottlenecked at two points: the interior gap at $k = 0$, sometimes called the "topological" gap Δ_1, and the exterior gap Δ_2 at high k. With the application of a magnetic field, the four bands of the dispersion relation split, two moving closer together and two further apart. Panel (b) shows that as the inner two bands move closer together with B_x, the interior gap shrinks, until it closes at some critical value $B_c = 2.42$ T. Panels (f, g) show the dispersion relation and the LDOS of the nanowire at this critical field, respectively. The critical magnetic field generally follows the formula $B_c^2 = \Delta_{sc}^2 + \mu^2$ and refers to the point where a *topological phase transition* occurs. The word topological is used here in a different sense than in Section 1.1, and refers to the nature of the ground state of the system as a component variable (in our case the axial magnetic field) is being continuously varied. The ground state of the system must smoothly and continuously vary so long as the gap doesn't close, but may have a discontinuity

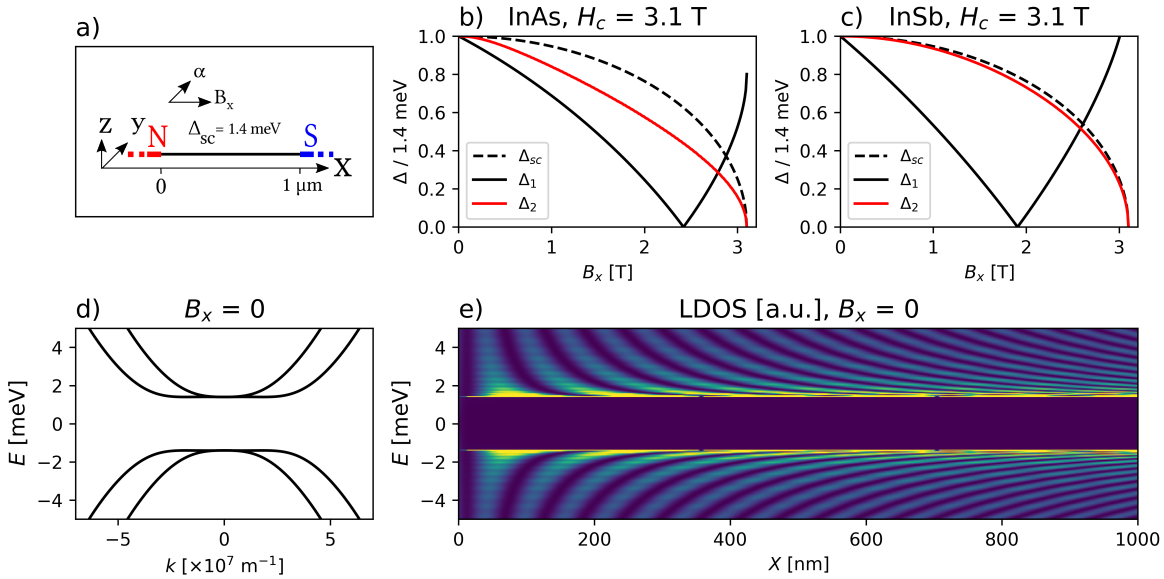

Figure 1.2: *(N.b. two-page figure & caption.)* (a) Schematic of a nanowire (black) of length 1 μm which can host MZM. Transparent contact to a superconductor S from the right induces a proximity superconducting gap of 1.4 meV. Tunnel coupling to normal metal contact N from the left defines the edge of the topological regime. The nanowire satisfies the recipe for hosting MZM, namely a strong Rashba spin-orbit coupling along y and a magnetic field B_x along the axis of the nanowire. A large g factor $g = 12.5$ relevant to InAs is assumed. Other parameters in this panel and other panels are also relevant to InAs—except in panel c where InSb is used. Specifically, $m^* = 0.023\ m_e$, $\alpha = 0.3$ eVÅ. (b) "Topological" gap Δ_1 (i.e. gap at $k = 0$, see panel d) as well as exterior gap Δ_2 and magnetic field-dependent proximity superconducting gap Δ_{sc} vs axial magnetic field B_x for an InAs proximitized device. Parameters pertaining to Nb are used, namely Δ_{sc} (0) = 1.4 meV and critical magnetic field $H_c = 3.1$ T (relevant to Nb thin films). With Δ_1 closing at $B_x = 2.42$ T the system enters the topological regime. Maximal topological protection occurs at $B_x = 2.79$ T when $\Delta_1 = \Delta_2$ for a value of ~ 490 μeV. (c) Same as panel b, but for InSb parameters, namely $m^* = 0.014 m_e$, $g = 21$, $\alpha = 1.0$ eVÅ. Transition to the topological regime occurs at $B_x = 1.81$ T, and topological protection is maximal at $B_x = 2.56$ T, with a value of ~ 770 μeV. (d, f, h) Dispersion relation (i.e. energy vs wavevector k) for an infinite nanowire ("Bulk Spectrum") calculated from diagonalizing Eq. 1.24. (d) At B_x = 0, the superconducting gap can be seen separating the positive "electron" solutions from the negative "hole" solutions. (e, g, i) Local density of states (LDOS), i.e., the sum of the densities $\sum |\psi(x, E)|^2$ of the eigensolutions of the discretized Hamiltonian (Eq.1.24), in arbitrary normalized units (lighter = more density), vs position x and energy E, as a function of axial magnetic field.

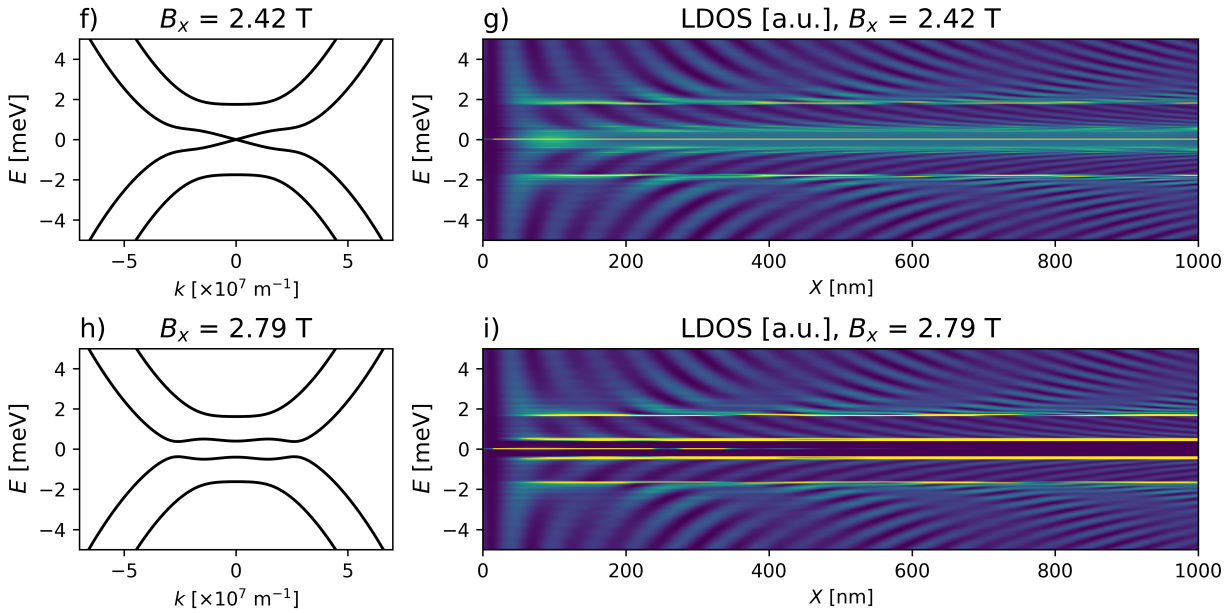

Figure 1.2: *(Cont. from prev. page.)* (f) At $B_x = B_c = 2.42$ T, the gap closes, signifying the transition to the topological regime. (h) The "deepest" part of the topological regime, with a topological gap $\simeq 470$ μ eV. The MZM cannot be seen in the bulk spectrum, as an infinite nanowire has no edge at which the MZM could localize. (g, i) LDOS calculated using Kwant for a 1 μm long nanowire with the same parameters as those in panel a. Bulk-Edge correspondence can be seen by comparing the LDOS graph with the bulk spectrum graph to its left: in panel e (prev. page), a dark superconducting gap region with no states is seen, which closes as the topological gap closes at $B_x = B_c$ in panel g. In panel i, an MZM can be seen pinned at zero energy and localized near the edge of topological region at $x = 0$.

at the topological transition point [44]. This is indeed what happens at $B_x = B_c$: a pair of eigensolutions appear (discontinuously), pinned to zero energy (i.e., are chargeless) which are an instance of Majorana zero modes. The number of MZM is the topological invariant [4, 44], a quantity that is conserved versus the magnetic field, other than at the topological transition point, where it is discontinuous and changes by two. MZM, as solutions to the BdG equation, always come in pairs and are localized near the edges of the proximitized region.

Panels (h, i) show the dispersion relation and the LDOS of the nanowire above the topological transition point, at $B_x = 2.79$ T. A zero energy state is seen in the LDOS of the finite nanowire near the N-contact, the edge of the proximitized region. Another MZM is expected at the other edge of the proximitized region, at position $x = +\infty$; so it is not shown. The dispersion relation of the infinite nanowire, whose "edge of the proximitezed region" is undefined, does not show any signatures of MZMs.

Focusing again on panel (b) we see that the interior gap opens with increasing magnetic field above the topological transition filed B_c. Nothing in particular happens to the exterior gap Δ_2 at this critical field value. However, Δ_2 depends on SOI coupling strength α and disappears for $\alpha = 0$. (The exact dependence is complicated [44], but for low B_x, μ is proportional to $\sqrt{\alpha}$.) So, a large SOI coupling is required for the MZM to be well-separated from other states at $B_x > B_c$. Δ_2 also scales with the BCS gap of the Nb contact. Given that the minimum of Δ_1, Δ_2 decides the maximum gap (separation of MZM from other states), the optimal point occurs at $\Delta_1 = \Delta_2$. Using our parameters for InAs, this occurs at $B_x = 2.79$ T (as plotted in panels (h, i)), for a maximal gap value of $\sim 490\mu$eV. For InSb (panel c), the gap is maximal at $B_x = 2.56$ T, with a value of $\sim 770\mu$eV. This separation of the MZM from other states is sometimes called the topological gap or the topological protection, and is the subject of Section 1.3.

At this point we turn our attention to the simulated MZM wavefunction. Ref. [45] calculates the wavefunction as an oscillatory function with an exponential envelope, following a generic formula

$$\psi(x) = \psi_0 \mathrm{e}^{ik_f x} \mathrm{e}^{-x/\xi}. \tag{1.25}$$

We can extract the wavelength $\lambda = \hbar/k_f$ for the oscillation and the length-scale for the exponential envelope ξ from our numerical simulations, and compare with the analytical results provided in Ref. [45]. In deriving the analytical result the two following limiting cases are used: The weak SOI regime, in which Δ is the largest energy scale, and the strong SOI regime, in which $E_{so} = \hbar^2 k_{so}^2/2m^*; k_{so} = m^*\alpha/\hbar^2$ is the largest energy scale. Here, α is the Rashba SOI strength parameter. Figure 1.3 shows λ, ξ vs axial magnetic field for the weak SOI regime. We compare the analytical results of Ref. [45] with the parameters extracted from our numerical simulation, and observe that meaningful convergence between the two can only be achieved for extremely large B-fields.

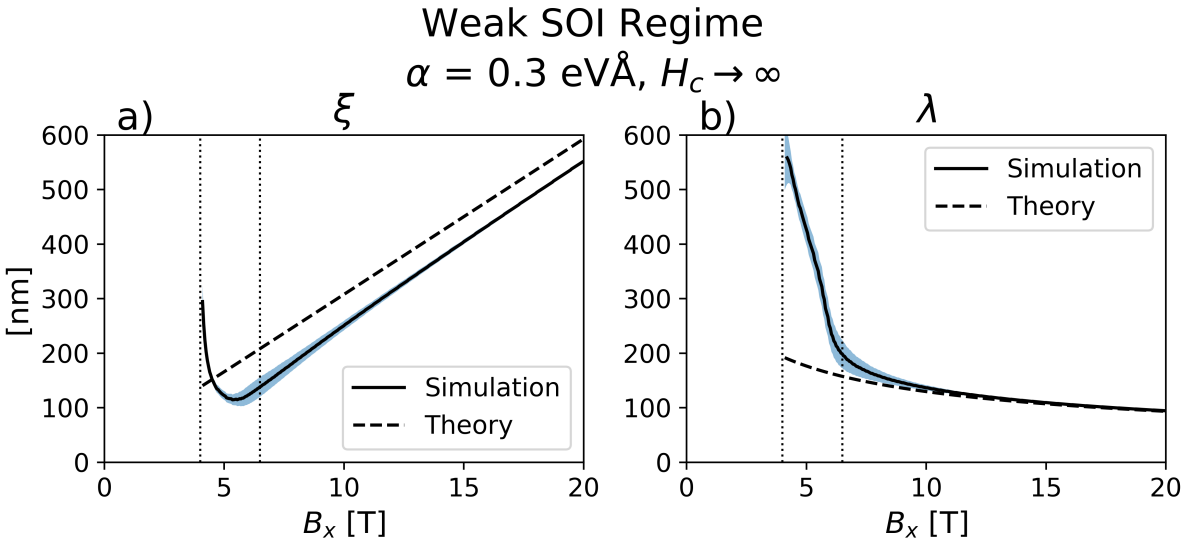

Figure 1.3: (a) MZM decay length ξ and (b) MZM oscillation period λ in the weak SOI regime, vs axial magnetic field B_x. Here we have assumed that the superconducting critical field H_c is infinite, but otherwise realistic parameters relevant to Nb and InAs are used. The solid lines are parameters extracted from the numerical LDOS, while the dotted lines are λ, ξ reported in Ref. [45] following Eq. 1.25. The shaded region depicts 10 times the one-standard-deviation numerical confidence in the extracted parameters (calculated from the covariance matrix of the least-squares fit). The discrepancy between the numerical and the theoretical curves (especially in ξ) shows that with realistic Nb+InAs parameters, we are not in the limiting case regime where $\Delta_z \gg \Delta_{sc}$, so a numerical calculation is required for a correct answer. The first dotted vertical line at ($B = 4$ T) is the edge of the topological regime (ξ is divergent as we approach the transition, and the wavefunction spans the entire nanowire). The second vertical line at $B = 6.5$ T signifies $k_z/k_f = 95\%$, i.e. $k_z \gg k_{so}$, above which the parameters start converging to their limit case values, although very slowly. Extremely large magnetic fields ($B_x > 10^4$ T) are required for numerical agreement within 1%.

Similarly, figure 1.4 shows λ, ξ for the strong SOI regime, defined as $E_{so} > \Delta_{sc}, \Delta_z = g\mu_b B_x/2$; comparing our numerically extracted parameters with the analytically derived ones. Again, we see that meaningful convergence is only achieved for extremely large values of α. These results convey the idea that for realistic devices, in order to be able to accurately estimate the behaviour of the MZM, a numerical simulation using realistic device-specific parameters are required.

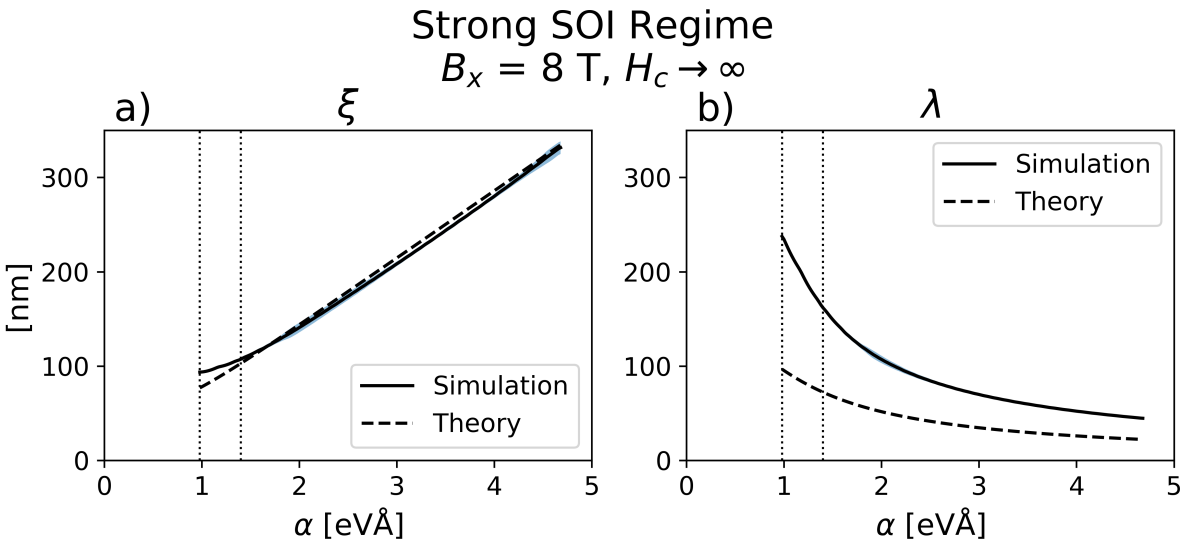

Figure 1.4: (a) MZM decay length ξ and (b) MZM oscillation period λ in the strong SOI regime, vs spin-orbit strength. $B_x = 8$ T and infinite H_c is assumed. Parameters for Nb+InAs are used (other than α which is swept). Similarly to Fig. 1.3, the shaded region depicts 10 times the one-standard-deviation numerical confidence in the extracted parameters. As with the weak SOI regime, the theoretical curves (but this time λ, see Eq. 1.25) do not agree with numerical values in realistic regimes, and a numerical calculation is required for the correct answer. The first vertical line at $\alpha = 0.98$ eVÅ signifies $E_{so} > \Delta_{sc}$, above which the strong SOI regime can be used. The parameters start slowly converging to their theoretical values above $\alpha = 1.4$ eVÅ (second vertical line), i.e. $E_{so} > \Delta_z$.

1.2.3 Discussion

We have simulated MZM in a semi-infinite nanowire contacted with Nb, using realistic parameters relevant to InAs and InSb. We observe that the topological transition is expected to occur at around 2 T for InAs devices, and 1.5 T for InSb devices. This is a relatively high value of the axial magnetic field, which will contend with the superconductivity in the Nb or Al contacts. A next step in simulating the contacts will take into account the effects of field focusing onto the region of interest of the nanowire, as the superconducting thin film excludes the magnetic field from its interior. Al, a type I SC may be more effective at excluding the field, and may show a certain advantage in this regard. However, the lower critical field of the Al thin films will favour InSb nanowires, due the larger g-value of InSb.

As we see in Fig. 1.2, when $B_x > B_c = \sqrt{\mu^2 + \Delta_{sc}^2}$, the gap reopens; however, since the Nb

thin film's superconducting gap closes with the axial magnetic field, for larger magnetic fields it closes again. Therefore, there is a maximal value for the topological gap that can be expected, around 500 μ eV. For our parameters, this occurs at 2.79 T. Ref. [46] and the references therein discuss the required extensions to the simple models (such as the one used here) pertinent to the formation of subgap states (including MBS) in a realistic nanowire device. Myriad effects relevant to the mechanisms and phenomenology of subgap states are explored, such as multimode effects, the surrounding electrostatic environment, g-factor and SOI renormalization, field focusing, inhomogeneity of pairing to the external leads, and effects of strong proximity effect to the metallic superconductor.

As mentioned above, the MZM wavefunctions have a long exponential tail, with a envelope lengthscale $\xi \sim 500$ nm for our parameters. In a finite device, MZMs at the two ends of a nanowire would hybridize [47, 48] and lift above zero energy (i.e., no longer strictly Majorana-like), in a manner proportional to the overlap of the wavefunctions. A realistic simulation of the wavefunction is required to yield its relevant lengthscales, and allow realistic device designs. Specifically, ξ can be in the range of a few hundred nanometers, providing a challenge and requiring a long device $\sim> 1\mu$m in length in order to avoid this overlap.

1.3 Quantum Computing with Majorana Bound States

The central idea behind quantum computing with Majorana Bound States is the concept of topological protection from error, which refers to the topological energy gap, i.e., the energy gap that opens and separates the MZM from other states at magnetic fields above the topological transition. As mentioned in the previous section, the value of this gap could be a few hundred μ eV in realistic conditions. If a qubit is so defined that quantum information is encoded in the shared non-local wavefunction of the two MZM (one at each end of the nanowire), then it shall be isolated and protected from all other states (and noise) by the value of this gap, possibly providing long-term coherent storage of information in time. Furthermore, as MZM are Ising anyons, if the two MZM are braided, then a certain operation (whose detail depends on how exactly the qubit is defined) occurs in the Hilbert space of the shared MZM wavefunction [27], in an exact and fault-tolerant manner [4, 49, 50]. Therefore, the MZM can be thought of as a potential platform for fault-tolerant computing — provided that several obstacles are overcome. Firstly, care should be taken in describing MZM in nanowire devices as truly isolated from other states. The nanowire is connected to external leads, whence electrons and Cooper pairs can tunnel into the device. In other words, these systems are subject to quasiparticle poisoning [51] from the leads as well as the continuum of states above the gap. The total number of electrons in a (proximitized) superconductor is not a good quantum number [52], but the even-or-oddness

of this number (electron parity) is. It is more accurate to say that so long as the parity of the electrons in the system are conserved, then the system enjoys topological protection from error, or in other words, the system enjoys "parity protection" [47]. In order to increase the effectiveness of such protection, designs involving Majorana islands have been proposed, where the idea is to use a non-negligible charging energy in order to protect the quantum state of the "island" from electrons in the external leads [53, 54, 55, 56]. Secondly, while braiding the MZM will result in some entangling two-qubit gate (again, the details depend on how the qubits are defined), it is by itself not sufficient for universal quantum computing [4, 50]. Arbitrary single qubit phase gates must be performed in some topologically non-protected manner in order to achieve universal quantum computing. Measurement of the quantum state at the end of the computation also requires breaking topological protection. So long as the information resides in the shared degenerate ground state of the MZM — or in other words it is truly isolated from the rest of the universe — then readout is not possible. This topologically protected state needs to be converted into some other form of accessible quantum information such as charge or flux, before readout can occur. In Ch. 6, we propose an experiment in which the charge state of a quantum dot is used to read out the state of an MZM qubit. The paper by Karzig et al. [27] as well as several others [57, 58, 59, 60, 61, 62, 63] have proposed scalable designs for universal quantum computing based on MZM, where in single qubit operations can be performed via controlled overlap of the MZM [63], an external flux [64, 65, 66], or coupling with a spin [67] or charge qubit [68]. In a similar manner, read out is performed [69] via the charge state of quantum dots, the current-phase relation of a SQUID, or via a large overlap of the MZM so that an anyonic fusion operation is performed [70, 63]. We point the reader interested in further details to Refs. [71, 50].

1.4 Review of Experimental Aspects of Majorana Bound States in Condensed Matter

Due to the possibility of using MBS as a building block of a qubit, there has been enormous interest in Majorana physics in condensed matter in the past decade or so. The sheer volume of literature surrounding the topic means that a comprehensive literature review would take on the scope of a long review article by itself; we point the interested reader to Refs. [72, 73, 74, 75]. Here we outline the most relevant developments in the field regarding experimental realization of MZM in nanowires, as well as two dimensional heterostructures. Following the breakthrough realization of Fu and Kane [3] that effective p-wave pairing can be induced in a proximitized semiconductor via a magnetic field, several "signatures" of the presence of MZM in realistic devices were theorized in "recipe" papers mentioned above. These signatures include a zero bias

conductance peak (ZPB) when tunneling into the MZM from a normal contact [8, 34, 5, 7], quantized at $2e^2/h$ (as opposed to e^2/h for a trivial device); a 4π periodic current phase realization of a SQUID hosting MZM [6, 35], and the skipping of the odd Shapiro steps in a Josephson junction hosting MZM when excited with microwave radiation [35]. The latter two are ultimately related to MZM behaving like "half of an electron", while the doubling of the expected conductance peak is due to the double degeneracy of the MZM wavefunction. The first report of an experimental observation of a ZBP came in 2012 by Mourik [76], followed by several other papers [77, 78, 79, 80] claiming to have observed ZBP as well as missing Shapiro steps [81]. There has been significant debate (summarized in Ref. [46]) regarding the interpretation of ZBP as the signature of MZM. Firstly it was pointed out [82, 83] that the observed peak is not exactly quantized at the expected value ($2e^2/h$). Primary culprits were identified as the background electrostatic landscape of the nanowire, disorder in the nanowire, and perhaps most importantly, a lack of optimal contact transparency between the nanowire and the superconducting leads, resulting in a "soft" proximity superconductivity. The efforts to alleviate these concerns has lead to significant development in the material science and technical expertise of fabricating hybrid junctions in nanowires and heterostructures — including but not limited to epitaxially grown Al on InAs and InSb nanowires in full-shell [84] and half-shell [74] configurations displaying near-perfect transparency and a "hard" superconducting gap [85, 86], clean heterostructures and nanowires that show ballistic transport and little disorder [87], epitaxially contacted junctions on high mobility InAs and InSb heterostructures [88, 89], and highly transparent contacts made between semiconductors and ex situ deposited superconducting leads [90]. Since then, observations on ZBPs quantized to the expected value $2e^2/h$ have been reported [91, 92, 84, 93], with considerable robustness of the ZBP as compared to the earlier experiments. However, as the theoretical and numerical understanding of realistic heterojunctions has grown [54], the idea of using ZBPs as a signature for MZM has been fundamentally challenged [94]; with simulations revealing myriad phenomena including inhomogeneity of contacts, non-negligible Coulomb interactions, multi-band effects, and other local effects potentially causing ZBPs in topologically trivial conditions [46, 95]. Reference has been made to (topologically trivial) Andreev Bound States (ABS) that mimic MBS behaviour, sometimes called quasi-Majorana or pseudo-Majorana states [53, 96, 97]. Refs. [98, 99] claims to have observed quantized ZBPs in topologically trivial nanowire junctions, due to correlated subgap states. Concerns regarding the non-reproducibility of non-zero peak experiments have been raised, [74], and a prominent 2018 paper [100] claiming unequivocal MZM observations was retracted and corrected with broader interpretations admitting the possibility of topologically trivial ZBPs [101]. Similarly, Ref. [102] sees the reappearance of the missing Shapiro steps under topologically trivial conditions. Thus, the robustness of the ZBP and Shapiro step signatures [103] may be insufficient as unequivocal evidence for MZM. The more promising avenue appears to be the signatures that rely on the non-local nature of the MZM wavefunction. The observed exponential overlap of MZM

versus junction length [47], as well as proposed and realized [48] experiments based on non-local and Crossed Andreev Reflection [104], and larger SQUIDs whose current-phase relation is a function of the coherence of the shared MZM wavefunction over a large distance [48, 105] are interesting avenues currently under perusal. Ultimately, the only irrefutable signature of MZM and its topological nature would be an observation of its braiding statistics. Multiple proposals for realistic and scalable platforms for experiments have been put forth [57, 58], as well as proposals for using such devices for quantum computing as mentioned in the previous section. However, as of this writing, we are unaware of any experiments reporting successful observation of non-trivial braiding statistics; the completion of such an experiment remains the holy grail of this field. Additionally, while not directly related to the topic of this thesis, we point to experiments pertaining to MZM conducted in atomic chains [106, 107], monolayer islands [108, 109, 110], and topological insulators [111, 112].

1.5 Structure of this Thesis

This thesis is structured around three generations of InAs nanowire Josephson Junction devices, fabricated with the aim of studying proximity superconductivity and the possibility of the realization of MZMs. Ch. 2 details the first generation devices, our first attempt. Analysis of those devices revealed a novel Orbital Josephson effect, a simplified theory for which is described in Ch. 3. The second generation devices, which show signs of Andreev bound states, are described in Ch. 4. Ch. 5 details our third generation devices, which, while successful in showing signatures of ABS and proximity superconductivity, reveal the difficulties in realizing MZM using InAs nanowire devices. This is discussed in Ch. 7, as well as the outlook for future devices and experiments. Ch. 6 details a proposal to use devices similar to ours in order to make a charge-readout of the parity of an MZM pair, a necessary step for the realization of topological quantum computation.

Chapter 2

Josephson Interference due to Orbital States in a Nanowire Proximity Effect Junction

2.1 Introduction

In this chapter we describe the first generation of hybrid nanowire devices studied experimentally [113]. We focus on one Josephson junction made with InAs nanowire and contacted with Nb. Proximity superconductivity is observed in the form of a supercurrent across the Josephson junction. The nanowires rest on top of five local bottom gates. The original idea was to use the bottom gates to tune the nanowire into a quantum dot regime, and study the proximity effect in the presence of a quantum dot. This proved to be difficult to achieve, as when the device was tuned into the quantum dot regime it showed very little superconductivity. This may be due to the quality of Nb/InAs interfaces in this device, which, as described in Chapter 1, is a crucial quantity describing the proximity superconductivity. We find the contact transparency t to be dependent on the gate voltages through the density of electrons in the nanowire. For this device we achieve $t = 0.4$ to $t = 0.65$. These values are improved in the later generation devices (chapters 4 and 5), where the devices can be tuned to the quantum dot regime as well as the Josephson regime.

One observation made during this experiment was that of the modulation of the critical current of the Josephson junction in the presence of an axial magnetic field. This is a phenomenon that was observed in the other generation devices as well. We develop in this chapter a model called Orbital Josephson interference that may describe this interesting observation. Understanding this phenomenon is particularly important as it occurs in the exact configuration in

which the device is predicted to go into the topological regime — so any signatures of Majorana bound states in the critical current need to be deconvolved from the Orbital Josephson effect.

The model presented in this chapter for the Orbital Josephson effect is rather simple and highly idealized. This is greatly improved in Chapter 3 where a more realistic version of the model is presented; however, the essence of the model remains the same: imagine the InAs nanowire as a tube. Due to Fermi level pinning on the surface of InAs nanowires, most of the transport is, semiclassically speaking, occurring on the surface of this tube. Electrons can occupy different orbital angular momentum states in the nanowire, and non-zero angular momentum states can be imagined as spiral (helical) paths on the surface of this tube. These spiral paths have a component of their momentum perpendicular to the axially applied magnetic field; this allows for some phase to be picked up by the electrons. The same goes for the conduction band holes that make the other half of an Andreev pair. Orbital Josephson interference occurs as an interference effect due to these different spiral paths.

The Josephson supercurrent in a Nb-InAs nanowire-Nb junction was studied experimentally. The nanowire goes superconducting due to the proximity effect, and can sustain a phase coherent supercurrent. An unexpected modulation of the junction critical current in an axial magnetic field is observed, which we attribute to a novel form of Josephson interference, due to the multi-band nature of the nanowire. Andreev pairs occupying states of different orbital angular momentum acquire different superconducting phases, producing oscillations of the critical current versus magnetic flux. We develop a semi-classical multi-band model that reproduces the experimental data well. While spin-orbit and Zeeman effects are predicted to produce similar behaviour, the orbital effects are dominant in the device studied here. This interplay between orbital states and magnetic field should be accounted for in the study of multi-band nanowire Josephson junctions, in particular, regarding the search for signatures of topological superconductivity in such devices.

2.2 Motivation

There has been much recent focus on topological superconductors because of the anyonic character of the states they support [4], and their possible applications to quantum information processing [4, 25]. A promising avenue for the realization of topological superconductors is via the superconducting proximity effect. Majorana fermions (MFs) [1] are predicted to be observed with a combination of conventional s-wave superconductivity, a proximate semiconductor with strong spin-orbit coupling and a suitable Zeeman splitting [6, 8, 34, 35, 5, 7]. Low bandgap semiconductor (InAs, InSb) nanowires have attracted attention as candidates for the realization of such hybrid devices. They form transparent, Schottky barrier-free contacts with

superconductors such as Nb and Al [40], have a strong Rashba spin-orbit coupling, and their high Landé g-factor allows them to be driven into the topological phase in the presence of a magnetic field applied perpendicular to the spin-orbit vector. Several proposals for observing MFs in such devices have been put forward [6, 114, 115, 116, 117, 118, 119, 82], and several reports of zero-bias anomalies (ZBAs) in differential tunnelling conductance [76, 78, 77] consistent with MFs [120] have been made. However, similar ZBAs may arise from a non-topological origin such as strong disorder [121, 122, 123, 124], Kondo resonances [125], or smooth confinement potentials in the nanowire [120, 121, 126, 127, 128]. Indeed, there have been observations of ZBAs from apparently non-Majorana origins [79, 80, 129].

The topological phase is theoretically predicted to arise in multiband nanowires, even in the presence of moderate disorder [130]. The structure of transverse subbands due to radial confinement in semiconductor nanowires has been the subject of several recent studies [36, 131]. Since proximity superconductivity is mediated by the Andreev reflection of electron-hole pairs [132], and the constituent carriers occupy certain transverse subbands in the nanowire, one might expect an interplay between the proximity effect and the nanowire subband structure. In this chapter, we ask how this interplay affects the critical current of a semiconductor nanowire Josephson junction in the presence of a magnetic field. The result is crucial for properly interpreting experiments on nanowire Josephson junctions, particularly with respect to recently proposed MF detection protocols which rely on the measurement of the critical current rather than ZBAs [133]. Motivated by experimental observations, we develop a model describing a novel form of Josephson interference arising in a nanowire junction under an applied axial magnetic field. The axial field orientation is needed to reach the topological phase in InAs and InSb junctions. It is shown that the interference model can explain our experimental observations on a Nb-InAs nanowire-Nb junction.

2.3 Results

2.3.1 Nanowire-based Josephson Junction

A Superconductor/Normal conductor/Superconductor (SNS) Josephson junction was fabricated, wherein an InAs nanowire is used as the N weak link, and is contacted by Nb leads as shown schematically in Figure 2.1a. Extensive dc electrical measurements of the junction were made in a dilution refrigerator with a base lattice temperature of 25 mK. A superconducting proximity effect is observed in the junction in the form of a dissipationless current. When the current bias exceeds a switching current value I_{sw}, the junction switches to the normal state. The value for the switching current depends on the voltages applied to the local gates, and can

be as high as 55 nA. The phase dynamics of the junction are overdamped, so I_{sw} approximates the thermodynamic critical current I_c (see Section 2.6.1 for further details.) Conductance modulations at voltages $V_n = 2\Delta_{\text{Nb}}/(en)$, for integer n, signify multiple Andreev reflections and indicate phase coherence across the junction. Here, $\Delta_{\text{Nb}} = 1.2$ meV is the superconducting energy gap in the Nb leads, and e is the electronic charge. An excess current [134] of about 42 nA indicates a Nb-InAs contact transparency $t \sim 0.65$ – see Section 2.6.1. The figure of merit product $I_c R_N$ of the junction is ~ 0.4 mV, where R_N is the normal state resistance of the junction. This is considerably smaller than the $\Delta_{\text{Nb}}/e = 1.2$ mV expected for a ballistic junction, but not by multiple orders of magnitude as in a tunnel junction, putting us in the mesoscopic scattering regime. The normal section of the junction is semiconducting, and tuning the local potential with voltages on the bottom gates, especially V_3 (see Figure 2.1a) modulates the critical current. Variations of I_c and the normal state conductance $G_N = 1/R_N$ with gate voltage are correlated, as seen previously by others [135]. The junction is long compared to the superconducting coherence length in Nb, $\xi_{\text{Nb}} \ll L \sim 200$ nm. We estimate an electronic mean free path l_e on the order of 100 nm, resulting in an intermediate regime between ballistic and diffusive transport. The mini-gap in the nanowire is determined [136, 137] by the Thouless energy $E_{\text{Th}} = \hbar D/L^2$. Here, $D = l_e v_F/3$ is the electron diffusion constant in the nanowire, and v_F is the Fermi velocity. Using an estimated value for the Fermi energy $E_F \sim 150$ meV, we obtain $E_{\text{Th}} \sim 0.5\Delta_{\text{Nb}}$. As discussed in Section 2.6.1, the superconducting coherence length in InAs, ξ_{InAs}, is limited by dephasing to the inelastic scattering lengthscale, l_{in}. Using values for l_{in} from magnetotransport studies on similar nanowires [138], we estimate $\xi_{\text{InAs}} \sim 250 - 500$ nm.

The junction critical current I_c was measured in perpendicular and axial magnetic fields, $B_\perp$ and $B_\parallel$ respectively. Below we discuss the behaviour of I_c in each field direction.

2.3.2 Perpendicular Magnetic Field

The perpendicular field $B_\perp$ was applied in the plane of the substrate and at an angle $2° \pm 3°$ with respect to $\hat{\boldsymbol{y}}$, the perpendicular direction to the nanowire axis. A complete penetration of the magnetic field into the normal section of the junction is assumed, and the screening of the field by Josephson supercurrents neglected. I_c is found to have a monotonic, quasi-Gaussian decay with $B_\perp$ (Figure 2.1b). The field was not increased beyond $B_\perp = 0.55$ T, where the switching transition becomes too weak for I_c to be determined.

A similar, monotonic behaviour of I_c in a perpendicular field was observed previously for InAs and InN nanowire junctions [139, 140]. In the narrow planar junction limit with perfect interfaces, I_c is expected to exhibit a Gaussian decay [141, 142], $I_c(B) = I_c(0)e^{-0.238(\Phi/\Phi_0)^2}$, due to depairing. Here, Φ is the magnetic flux through the junction, $\Phi = B_\perp L d$, d the nanowire

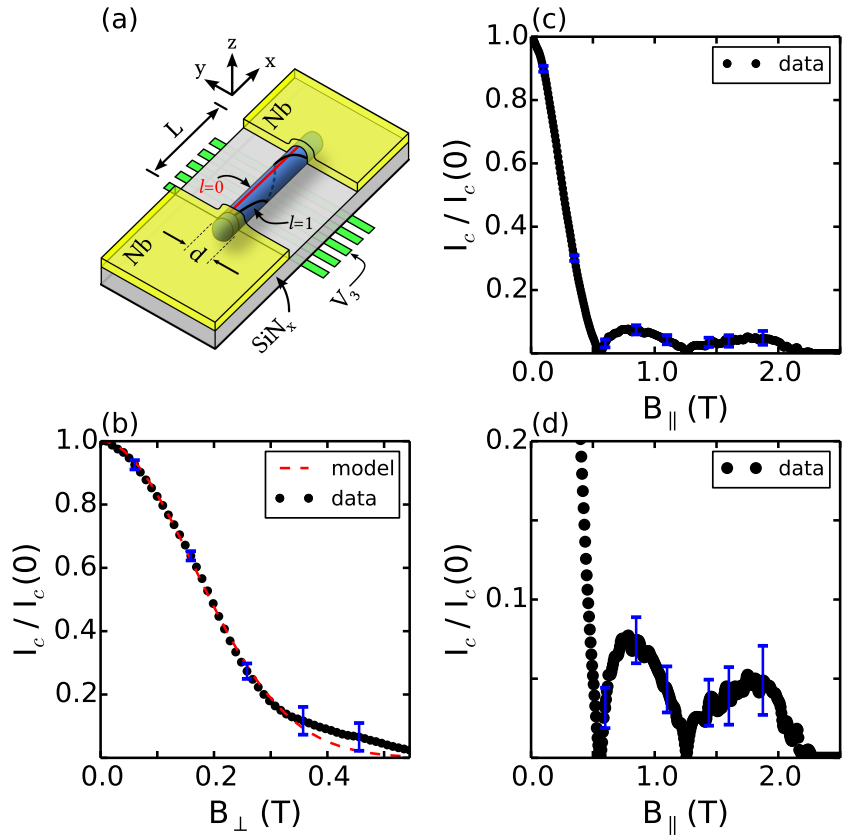

Figure 2.1: (a) Schematic of the nanowire SNS junction. The set of bottom gates, especially V_3, are used to modulate the local potential. Our model treats the nanowire section as a cylindrical shell conductor of diameter d, contacted by Nb leads. We use $d = 63$ nm, from a scanning electron micrograph of the device studied experimentally. (b) Monotonic, quasi-Guassian decay of the junction critical current I_c in a perpendicular magnetic field. The data (solid circles) can be fit to a Gaussian function (dashed line), $\exp\left(-0.499(\Phi/\Phi_0)^2\right)$. Here Φ is the flux corresponding to the perpendicular field and Φ_0 is the flux quantum. (c) Oscillatory behaviour of I_c in an axial magnetic field. (d) The same data as (c), enlarged to show nodes. We explain these oscillations as Josephson interference due to classical spiral trajectories of Andreev pairs on the cylindrical shell. Different paths correspond to nanowire subbands of different orbital angular momentum. Example trajectories corresponding to $l = 0, 1$ are shown in (a). Representative error bars are shown for selected data points in (b,c,d) in blue colour.

diameter, and Φ_0 the (superconducting) flux quantum, $\Phi_0 = h/(2e)$. The experimental data, however, is best fit to a curve $I_c(B) = I_c(0)e^{-0.499(\Phi/\Phi_0)^2}$. This discrepancy between the numer-

ical factors can be explained in terms of non-ideal interfaces [143], i.e. a contact transparency less than 1 — see Section 2.6.2.

2.3.3 Axial Magnetic Field

An axial magnetic field is perpendicular to the Rashba spin-orbit direction, and the junction is predicted to enter the topological phase for a certain range of $B_\parallel$ values. Here, we study the dependence of I_c on $B_\parallel$. The axial field was applied at an angle $\sim 8^\circ \pm 4^\circ$ with respect to the nanowire axis. The misalignment in $B_\parallel$ is shown in Section 2.6.5 to have little effect on fitting the experimental data to the model, so for simplicity in what follows we assume $B_\parallel$ to be aligned. As with the perpendicular field, a complete penetration of $B_\parallel$ into the normal section of the junction is assumed, and the screening of the field by Josephson supercurrents neglected.

Since the Josephson current is aligned with the field direction, naively one would expect no interference effects, and simply a slow decrease in I_c with magnetic field due to depairing in the Nb leads. However, an oscillating behaviour in I_c vs. $B_\parallel$ is observed, as shown in Figure 2.1c. In terms of the flux through the axial cross-section of the nanowire $\Phi_{\text{nw}} = B_\parallel \pi d^2/4$, the oscillations do not exhibit Φ_0-periodicity. Moreover, the shape and periodicity of the oscillations can be modified by changing the gate voltages.

What is the underlying physics of the observed oscillations? Recent observations of an oscillatory critical current in InSb junctions are consistent with 0-π transitions of the junction phase in the presence of spin-orbit and Zeeman effects [144]. However, we estimate for the InAs junction studied here, the magnetic field at which I_c is predicted to have a minimum due to a 0-π transition is ~ 7 T, an order of magnitude larger than the values observed ~ 0.6 T (see Section 2.6.3). Instead, we explain the effect as a form of Josephson interference that is analogous to the well-known effect for wide planar junctions in a perpendicular field that produces a Fraunhofer pattern, but here the azimuthal velocity component of carriers occupying subbands of finite orbital angular momentum yields a phase of magnetic origin, in addition to the zero-field superconducting phase difference across the junction. For simplicity we consider conduction on a shell, motivated by the tendency in InAs nanowires to form a surface accumulation layer of electrons due to the presence of surface states. Furthermore we use classical paths on the shell to calculate the additional phase for a given angular momentum state. While this model is semi-classical and based on simplifying assumptions, it illustrates that orbital subband effects can dominate the behaviour of I_c in an axial field for multi-band nanowire SNS junctions. Good agreement is found between the model and experimental results using a physically reasonable set of fitting parameters.

2.3.4 Junction Critical Current in a Shell Conduction Model

Intrinsic InAs nanowires typically have surface band bending $\sim 100-200$ meV [145] due to the pinning of the Fermi energy above the conduction band at the nanowire surface [146, 147, 148], and a corresponding surface accumulation of carriers. We model the InAs nanowire junction as a cylindrical shell 2-dimensional electron gas (2DEG) contacted by Nb leads in the geometry of Figure 2.1a. The 2DEG is assumed to be at a radius $d/2$ from the nanowire center. We consider relaxing this assumption and allowing more realistic transverse wavefunctions later. For numerical calculations, we choose the gauge $\mathbf{A} = (d/4)B_{\parallel}\hat{\boldsymbol{\theta}}$ for the vector potential ($\hat{\boldsymbol{\theta}}$ is the azimuthal direction in the yz plane).

The motion of an electron in the 2DEG can be decomposed into an axial degree of freedom along $\hat{\boldsymbol{x}}$ and an azimuthal degree of freedom along $\hat{\boldsymbol{\theta}}$. The allowed quantum states are characterized by an angular momentum quantum number $l = 0, \pm 1, \pm 2,$ etc; i.e. we have assumed cylindrical symmetry. In Chapter 7 we discuss calculations and realistic device simulations in which this condition is relaxed, yet the picture remains qualitatively unchanged. In the ballistic limit, classical trajectories of electrons in subband l going from source to drain are spiral paths on the cylindrical shell with a winding angle θ_l equal to the azimuthal arc length divided by the radius. So, $\theta_l = (v_\theta(l)) \times (L/v_x) \times (2/d)$, where v_x, v_θ are the axial and azimuthal velocities, respectively, and v_θ is explicitly a function of the quantum number l. Below we also consider trajectories in the presence of back-scattering. The Andreev process involves an electron and a retroreflected hole, both located in the conduction band of the normal section of the junction [149]. Therefore, the hole is considered to be a time and charge-reversed electron, with the same effective mass m^*, mean free path l_e and radial position. The relative motion of the electron and hole can be neglected [150], and the charge transport described in terms of an 'Andreev pair' [151] with charge $-2e$, which follows the same trajectory as the electron. As long as the center of mass of the Andreev pair follows a spiral trajectory, the interference effect should appear, even if the holes do not have the same wavefunctions as electrons. Schematic examples of classical trajectories are shown in Figure 2.1a for $l = 0$ and $l = 1$ states.

An Andreev pair traversing the junction acquires a gauge-independent phase $\phi = (2e/\hbar) \times \int \mathbf{A} \cdot \mathrm{dl}$, due to the $\hat{\boldsymbol{\theta}}$ component of its momentum perpendicular to the field. This follows from the Ginzburg-Landau formula for the gauge-invariant phase [152]. The line integral, taken from one Nb electrode to the other, depends only on the azimuthal angle θ between the start and finish points, and not on the details of the path. For a spiral trajectory with winding angle θ_l, one obtains $\phi = \frac{\Phi_{\mathrm{nw}}}{\Phi_0}\theta_l$. To our knowledge, the current-phase relationship (CPR) of a semiconducting nanowire SNS junction has not been experimentally determined. Since we have $L \lesssim \xi_{\mathrm{InAs}}$, a sinusoidal CPR is assumed. The phase difference γ between the Nb leads is assumed to be independent of the position along $\hat{\boldsymbol{y}}$, since the junction width is similar in order to the Nb

coherence length, $d \sim \xi_{Nb}$, corresponding to the narrow junction limit for a planar junction.

Similar to the case of a wide planar junction in a perpendicular field [153] where the superconducting phase depends linearly on the position along the junction width, here the phase due to an axial field is linear in the winding angle θ. Using the sinusoidal CPR, we define an angular supercurrent density $J(\theta) = J_c(\theta) \sin\left(\frac{\Phi_{\rm nw}}{\Phi_0}\theta + \gamma\right)$, where $J_c(\theta)$ is the critical current density. The supercurrent is obtained [153] by integrating the supercurrent density over θ:

$$I(\Phi_{\rm nw}) = \int_{-\infty}^{\infty} J(\theta) \mathrm{d}\theta, \tag{2.1}$$

and the critical current is the maximum supercurrent over the junction phase γ:

$$I_c(\Phi_{\rm nw}) = \max_{\gamma \in [0, 2\pi)} (I) = \left| \int_{-\infty}^{\infty} J_c(\theta) \mathrm{e}^{\left(i \frac{\Phi_{\rm nw}}{\Phi_0} \theta\right)} \mathrm{d}\,\theta \right|. \tag{2.2}$$

Since I_c and J_c are related as a Fourier pair, $J_c(\theta)$ can be thought of as a spectral density that is a function of winding angle.

2.3.5 Spectral Density of Critical Current Oscillations

We model the spectral density $J_c(\theta)$ (see Eq. 2.2) as a weighted sum of Gaussian functions in order to satisfy the following properties: (i) The subband l contributes a peak to J_c at its winding angle θ_l, (ii) J_c is proportional to the normal state conductance G_N, as required for an SNS junction, (iii) J_c goes to zero for large $|\theta|$, where the trajectory length is much longer than the phase coherence length $\xi_{\rm InAs}$. We write

$$J_c(\theta) = J_{\rm max}(\theta) \sum_l \frac{n_l}{\sigma\sqrt{2\pi}} \exp\left(-\frac{(\theta - \theta_l)^2}{2\sigma^2}\right), \tag{2.3}$$

where n_l is the number of radial subbands occupied with angular momentum l. Here we allow $n_l > 1$ in the spirit of later relaxing the assumption of strictly two-dimensional shell conduction so that higher radial excitations are possible. $J_{\rm max}$ takes into account the suppression of critical current density for large $|\theta|$, and is calculated from the Usadel equations in Section 2.6.8. The Gaussian peak width is determined by the parameter σ.

Let us consider first the ballistic limit $L \ll l_e$. One would expect sharp peaks (i.e. $\sigma \to 0$) in $J_c(\theta)$ at $\theta = \theta_l$ for any subband l that is occupied. In this limit, v_x approximately equals the

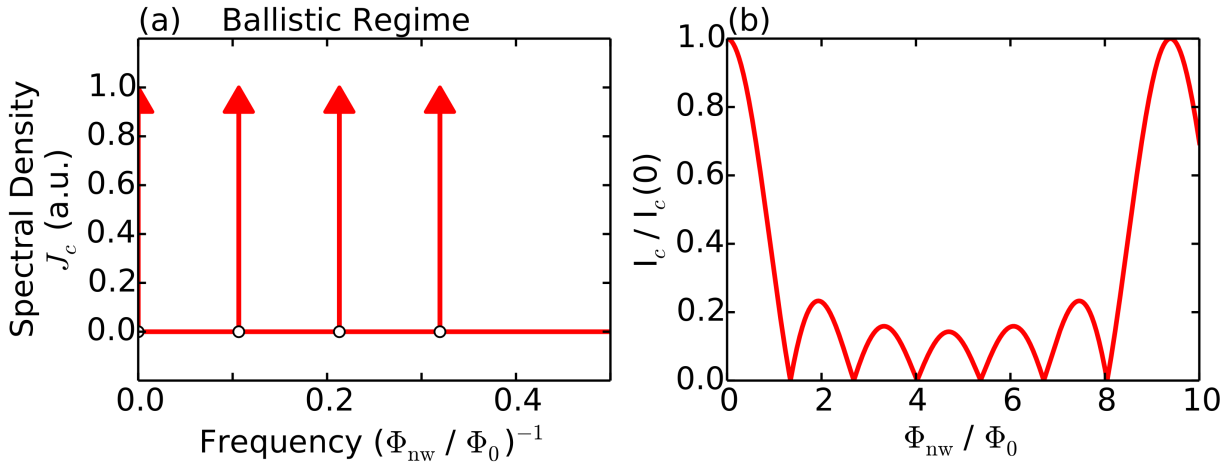

Figure 2.2: *(N.b. two-page figure & caption.)* Spectral densities (left) and critical currents (right) for the examples given in the text, for (a,b) the ballistic regime, and (c,d) the quasiballistic regime (next page). Although the spectral density is explicitly a function of the winding angle θ, here it is plotted versus the magnetic frequency Φ_0/Φ_{nw}, since the inverse quantity Φ_{nw}/Φ_0 is the conjugate variable to θ in Eq. 2.2. (a,b) A uniform $J_{max}(\theta) = J_0$ is used in this example. The resulting I_c is the absolute value of the sum of cosines in Eq. 2.4b.

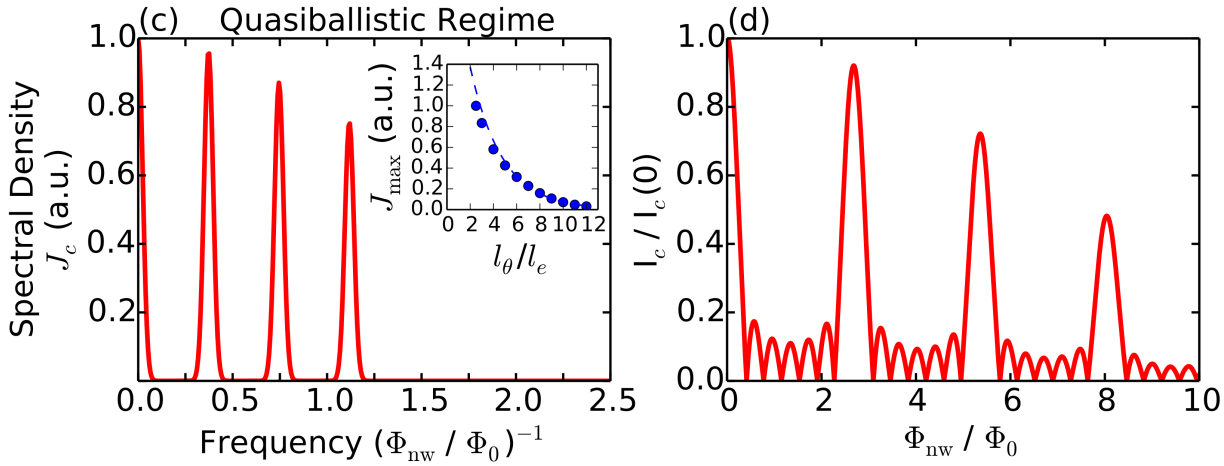

Figure 2.2: *(Cont. from prev. page.)* (c,d) In the presence of back-scattering, the peaks in J_c move to higher frequencies (Eq. 2.5) as the carriers spend more time in the junction and accumulate more phase. Note that the frequency scales in (a) and (c) are not the same. The higher frequency peaks in J_c are suppressed by $J_{\max}(\theta)$, which falls off with increasing winding angle, or equivalently, frequency. The oscillations in I_c are qualitatively similar to the ballistic case, but have a shorter period, and attenuate with magnetic flux due to the broadening σ of the J_c peaks. (c, inset) $J_{\max}$, as calculated from the Usadel equations, vs. l_θ/l_e. Here, l_θ is the length of a spiral path with winding angle θ, and an inelastic scattering length $l_{in} = 5l_e$ is chosen arbitrarily. The dashed line is an exponential fit to the $l_\theta > l_{in}$ region. Longer paths contribute less to J_c because of dephasing, resulting in the suppression of the peak amplitudes with increasing magnetic frequency seen in panel (c). The following parameters (defined in the text) were used in these simulations: $d = 63$ nm, $L = 200$ nm, $l_e = 80$ nm, $l_{in} = 400$ nm, $E_F = 150$ meV, $n_l = 1$ for $|l| \leq 3$, and $n_l = 0$ otherwise.

Fermi velocity of the electron, $v_x \simeq v_F = \sqrt{2E_F/m^*}$, and $v_\theta(l) = 2\hbar l/(m^* d) \ll v_x$. We use $m^* = 0.023 m_e$ as the effective mass in InAs. As an illustrative example, let $J_{\text{max}}(\theta) = J_0$ for all θ, and let n_l = 1 for $|l| \leq 3$, and zero otherwise. Then, the critical current density is a sum of Dirac delta functions, and we have

$$J_c(\theta) = J_0 \sum_{l=-3}^{3} \delta(\theta - \theta_l), \tag{2.4a}$$

$$\begin{aligned} I_c(B_\parallel) &= J_0 \left| \sum_{l=-3}^{3} \exp\left(i \frac{\Phi_{\text{nw}}}{\Phi_0} \theta_l \right) \right| \\ &= J_0 \left| 1 + 2 \sum_{l=1}^{3} \cos\left(\left(\frac{eLl}{m^* v_F} \right) B_\parallel \right) \right|. \end{aligned} \tag{2.4b}$$

Even though $\Phi_{\text{nw}} \propto d^2$, $I_c(B)$ does not depend on d because for a fixed angular momentum, $v_\theta \propto 1/d$ so $\theta_l \propto 1/d^2$ which cancels with the d^2 dependence of flux. This shows the interference effect is not sensitive to the radial position of carriers in the ballistic regime. In the limit $d \to 0$, states with finite angular momentum become very high in energy and will not be populated.

In Figure 2.2a is plotted $J_c(\theta)$ and $I_c(B_\parallel)$ for the example above (Eq. 2.4). Note that the θ_l which determine the peak positions in $J_c(\theta)$ depend on device-specific parameters L, v_F, and d, and can take on any value. Thus, the periodicity seen in I_c versus Φ_{nw} generally does not correspond to an integer multiple of Φ_0.

We extend the model for J_c to the quasiballistic regime $l_e \lesssim L$ by invoking the following assumption: the electron undergoes back-scattering events along $\hat{\boldsymbol{x}}$ only. This is justified as long as the scattering does not substantially mix the orbital angular momentum states, such as when the scattering potential does not explicitly depend on the azimuthal position [154]. Therefore, in a scattering event $v_x \to -v_x$, but v_θ is unchanged, so on average the particle spends more time in the junction, accumulating more phase. Noting that in the ballistic limit we have $v_x \simeq v_F$, the drift velocity along the nanowire axis now becomes $v_x \simeq v_F \times l_e/(l_e + L)$. This follows from the scaling of the conductance G from the Landauer-Büttiker quantum conductance value by the factor $l_e/(l_e + L)$, as discussed in Refs. [37, 155]. Therefore, for quasiballistic transport due to back-scattering, the winding angle θ_l is taken as

$$\theta_l = \left(\frac{L + l_e}{l_e}\right)\left(\frac{L}{v_F}\right)\left(\frac{2}{d}\right) v_\theta(l). \tag{2.5}$$

V_3 (V)	l_e (nm)	σ	n_0	$n_{\pm1}$	$n_{\pm2}$	$n_{\pm3}$
1.4	83.1	0.9	2.0	2.1	0.7	0.2
0.7	94.9	0.9	2.0	1.3	1.0	0.0
-1.4	168.0	0.8	1.0	1.1	0.3	0.2

Table 2.1: The parameters used in the fits of Figure 2.3; l_e is the mean free path, n_l are the subband occupation numbers, and σ describes the broadening of the angular spectral density function. Since the model only constrains the ratios n_l/n_{l+1}, the n_l here are adjusted to be consistent with the experimental normal state conductance, G_N, at each gate voltage. The following parameters (defined in the text) are used but not varied between the three data sets: $d = 63$ nm, $L = 200$ nm, $E_F = 150$ meV, $l_{in} = 400$ nm.

In Figure 2.2b we plot $J_c(\theta)$ in the quasiballistic regime, corresponding to the example where n_l = 1 for $|l| \leq 3$ and is zero otherwise. Using l_e values typical for these nanowires [37], we obtain $(L + l_e)/l_e \sim 3.5$, so the peaks in $J_c(\theta)$ appear at higher frequencies (inverse magnetic flux) compared to the ballistic case. The effect of $J_{\max}(\theta)$, calculated from the Usadel equations, is taken into account. It suppresses the higher frequency peaks of J_c, since these correspond to longer classical paths of the carriers that will experience greater dephasing. Intuitively, one expects a broader distribution of $J_c(\theta)$ about each θ_l-centered peak when back-scattering occurs, and this broadening is parametrized by σ. A finite σ suppresses the recurrences in I_c; as σ is increased, the maxima in I_c drop off with increasing magnetic flux. The experimental data is fit below using this quasiballistic model. It is shown in Sec. 2.6.6 that the interference effect is not sensitive to the radial position of the carriers, $d/2$, up to a rescaling of the broadening parameter σ, and of the envelope function $J_{\max}$.

2.3.6 Fitting to the Data

In Eq. 2.3 we have modelled $J_c(\theta)$, the spectral density of I_c. In order to fit the model to the experimental data, spectral densities are calculated numerically from the $I_c(B)$ data shown in Figure 2.3, for three values of gate voltage V_3. A fast-Fourier transform is taken of a signal which is identical to $I_c(B)$, except that it changes sign at each node so that each becomes a zero crossing. Eq. 2.3 is then fitted to this Fourier transform, with results shown in Figure 2.3, and discussed below.

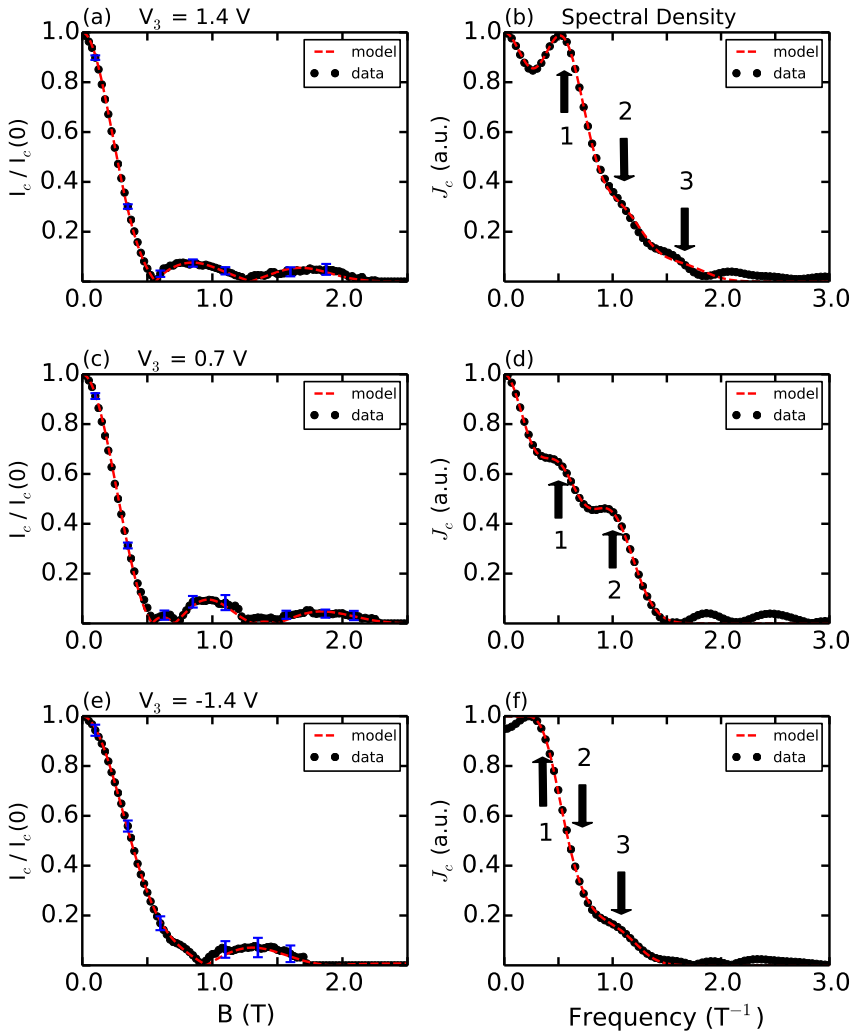

Figure 2.3: Theoretical fits to the experimental data for (a, b) $V_3 = 1.4$ V, (c, d) $V_3 = 0.7$ V and (e, f) $V_3 = -1.4$ V. (a, c, e) The experimental critical current (solid circles) and model fits (dashed lines) are overlaid. The data is truncated above magnetic fields for which the switching transition becomes too weak for I_c to be determined. (b, d, f) Spectral densities of the experimental data determined by Fourier transformation of I_c (solid circles), and the best-fit spectral densities from the model (dashed lines) are shown. To produce the model curves, Eq. 2.3 is fitted to the low-frequency region < 2 T^{-1} with the parameters given in Table 2.1. Arrows indicate the frequencies of the peaks corresponding to each subband of orbital angular momentum $\hbar|l|$, for $|l| = 1, 2, 3$ ($l = 0$ gives a peak at zero frequency). For clarity, we only show every fourth experimental data point, and representative error bars on selected data points.

2.4 Discussion

Here we discuss the best-fit parameters we obtained by fitting the model to the experimental data (Table 2.1). The most important variation between the three data sets is the occupation number of angular momentum subbands, n_l, which is modulated by the applied gate voltage. As V_3 is made more negative, the fits are consistent with fewer subbands being occupied. The subbands with higher l values depopulate first, in a manner roughly consistent with the expected shell-filling structure of the nanowire [36, 131, 156]. For a given data set, only the ratios n_l/n_{l+1} matter when calculating $I_c(B)/I_c(0)$. We have adjusted the n_l so that the experimental normal state conductance G_N at each gate voltage is consistent with the estimated number of occupied subbands. Another notable feature in Table 2.1 is an apparent increase in elastic mean free path l_e as the gate voltages are made more negative. In the real nanowire junction, the radial wavefunction is not confined to a shell but rather is distributed through the nanowire cross section, with some bias towards the surface due to surface band bending. Higher l states have a radial expectation value closer to the nanowire surface and are expected to scatter more frequently due to surface defects, which could explain a shorter mean free path when more channels contribute to transport. Note that the fitting involves several free parameters, and the set of best-fit parameters is not generally unique. The model is based on simplifying assumptions and considers shell conduction only, and also neglects spin-orbit and Zeeman effects. We therefore do not expect this model to capture the complete physics of the junction; however, it appears to explain the dominant mechanism of the critical current oscillations in the InAs device studied here.

In conclusion, a nanowire SNS junction was investigated that showed an unexpected modulation of critical current in an axial magnetic field. This result is understood by considering a novel type of Josephson interference due to orbital states in the multi-band InAs nanowire. Although we restricted the model to a cylindrical shell, the interference effect does not depend on the diameter d, up to a rescaling of the spectral density broadening parameter σ. The effect is therefore expected to be present for more general radial wavefunctions, including when electrons and holes forming Andreev pairs have different radial wavefunctions. For a more realistic model, it will be necessary to calculate the Josephson interference based on quasiparticle wavefunctions rather than classical trajectories. Despite the simplicity of the semi-classical model considered here, it is able to reproduce the main features of the experimental data. Therefore, the interplay of orbital and magnetic effects should be carefully considered for semiconductor nanowire Josephson junctions, especially when searching for signatures of topological states.

2.5 Methods

The bottom gate pattern was defined by electron beam lithography (EBL) on an undoped Si substrate with a 300 nm thermal oxide layer. 7 nm/14 nm layers of Ti/Au were deposited by electron beam evaporation to realize the gates, followed by atomic layer deposition of a 7 nm layer of dielectric Al_2O_3, and plasma-enhanced chemical vapour deposition of a 13 nm layer of dielectric SiN_x. Next, molecular beam epitaxially grown InAs nanowires were mechanically deposited on the substrate. Details of the nanowire growth can be found in Ref. [157]. Using scanning electron microscopy, we selected a nanowire positioned on the predefined gate pattern. The pattern for the superconducting contacts was defined by EBL. A 50 nm layer of Nb was deposited by dc sputtering at room temperature, preceded by Ar ion milling to achieve transparent InAs/Nb interfaces.

The sample was wirebonded to a chip carrier and thermally anchored to the mixing chamber of a dilution refrigerator with a base lattice temperature of 25 mK. The junction was connected in a four-probe (current-voltage) setup. A dc current bias was applied using a homemade voltage source, by dropping the output voltage across two sets of resistors, anchored at room temperature, and the mixing chamber temperature of the dilution refrigerator, respectively. The voltage response of the junction was measured using a voltage preamplifier.

2.6 Details of Experiment and Numerical Analysis

2.6.1 Junction Characteristics

Tunability of the Supercurrent with Local Gate Voltages

Figure 2.4 shows the differential resistance dV/dI of the junction vs. the bias current I and the local gate voltage V_3 (see Figure 2.1.) A clear zero-resistance regime can be seen at low bias. A voltage drop of magnitude $\lesssim 5$ μeV develops across the junction as I approaches the critical current I_c. This voltage has an exponential dependence on the bias current I, and is consistent with the occurrence of a combination of thermally activated phase slip events and quantum phase slip events, similar to the effect observed in Ref. [158].

The voltages on the local gates can be used to tune the critical current of the junction. Of these, V_3 is the most effective. The variations of I_c with V_3 are reproducible. A general trend is observed that I_c is larger for more positive V_3. In Section 2.6.1 we show that these variations are correlated with the variations of the normal state conductance, G_N, with V_3. We conclude

that the normal section of the SNS junction is indeed semiconducting, and the gate voltages tune the local potential in the nanowire, simultaneously tuning I_c and G_N.

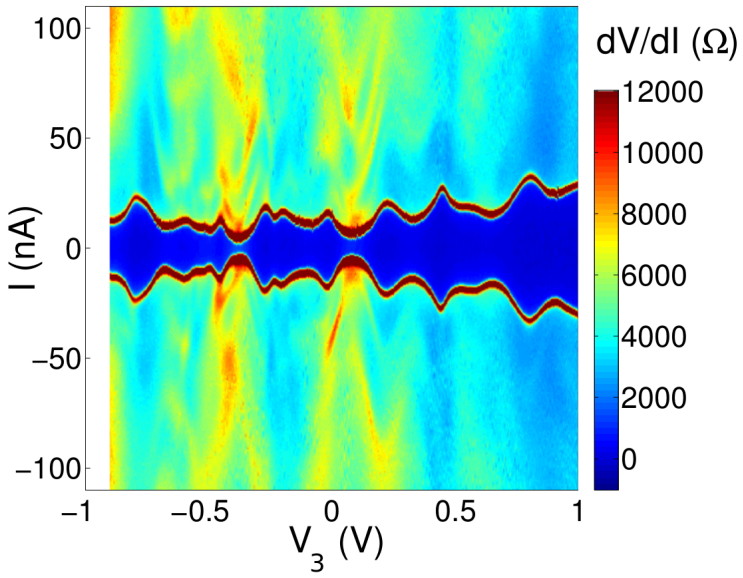

Figure 2.4: Differential resistance dV/dI in Ohms, vs. bias current I and local gate voltage V_3 at $T = 25$ mK. A supercurrent up to ~ 30 nA is observed (Dark blue region). Here, the voltages on the two gates V_3, V_4 are being swept together from negative to positive values. The critical current shows reproducible variations with V_3.

Contact Resistances

In order to correctly identify the resistance of the nanowire section of the junction, the resistances of the Nb-InAs contacts need to be subtracted from the total measured resistance. Since the nanowire is contacted by two Nb leads, a four-point measurement of the contact resistances was not possible. Using the results in [159], the barrier resistance R_b was estimated to be no greater than 1 kΩ. In what follows, we consistently use the value $R_b = 800\ \Omega$ for each contact. The normal state resistance of the junction R_N is related to the measured high bias current resistance value R by the relation $R = (1 + 2r)R_N$, where $r = R_b/R_N$. Typically for this device, the value for the ratio r is $r \sim 0.15$.

Correlation of the Critical Current and Normal State Conductance

The resistance R of the junction was measured at a high bias voltage $V = 5$ mV $> 2\Delta_{Nb}/e$, where $\Delta_{Nb} = 1.2$ meV is the superconducting gap in the Nb leads. The normal state resistance R_N of the junction was obtained using the relation $R = R_N + 2R_b$, where $R_b = 800\ \Omega$ is the resistance of the Nb-InAs barriers (see Section 2.6.1).

In Figure 2.5 we show the normal state conductance $G_N = 1/R_N$ and the critical current I_c of the junction vs. the local gate voltage V_3. The variations of G_N and I_c with V_3 are correlated, suggesting a common physical origin. This has been previously observed for semiconductor nanowire SNS junctions [135, 160, 140, 139, 161]. For a nanowire junction in the ballistic regime, I_c and G_N are directly proportional [161]. This is not the case for the junction studied here, and can be attributed to non-ideal Nb-InAs interfaces (i.e., a contact transparency less than 1), which suppress the mini-gap and therefore the critical current of the junction [143]. The relative fluctuations in I_c are larger than those in G_N, as seen in Doh, et al [135]. This can be attributed to an interplay between the phase coherent Andreev processes and conductance fluctuations resulting from potential fluctuations in the nanowire.

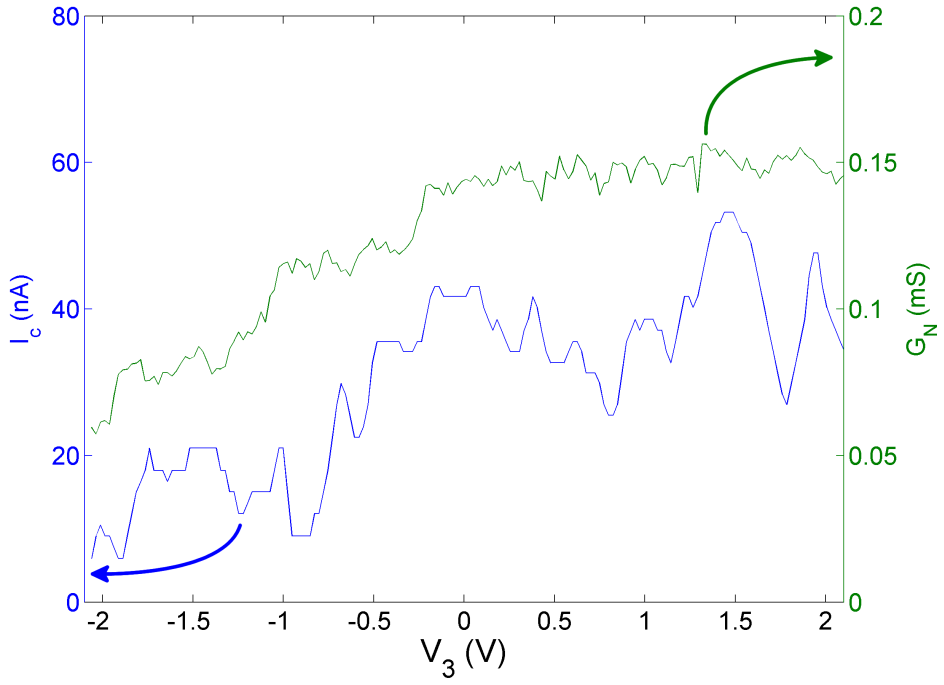

Figure 2.5: Junction critical current I_c (blue) and high bias current normal state conductance G_N (green) vs. the local gate voltage V_3. The variations of I_c and G_N with V_3 are correlated, typical of high-transparency SNS junctions. A direct proportionality relation does not hold, likely due to the non-ballistic nature of the device.

Multiple Andreev Reflections

Signatures of Multiple Andreev Reflections (MAR) [162] are visible as peaks in the differential resistance dV/dI of the junction, at bias voltages $V_n = 2\Delta_{Nb}/en$ for integer n. Here, $\Delta_{Nb} = 1.2$ meV is the superconducting energy gap in the Nb leads. The size of the peak at each V_n varies with the local gate voltages, but the peaks are visible whenever there is a supercurrent present at zero bias voltage. The presence of this subharmonic gap structure [134] indicates phase coherence across the junction.

In Figure 2.6 the junction differential resistance vs. bias voltage is shown for $V_3 = +2.1$ V. A supercurrent branch is present at zero bias voltage, and signatures of MAR are clearly visible at higher bias. As the bias voltage is increased, the Andreev process at the Nb-InAs interfaces is suppressed, increasing the junction resistance. The current-voltage (I-V) trace corresponding

to Figure 2.6 can be used to extract the excess current [134] due to the Andreev process, by making a linear fit to the high bias voltage regime. This yields $I_{exc} = 40.2$ nA (Figure 2.7). This value, and the value for the high-bias conductance of the junction, are used to calculate the figure of merit product $eI_{exc}R_N/\Delta_{Nb} \simeq 0.5$. This value is inserted into the OTBK model [134] for the subharmonic gap structure, in order to get the scattering parameter Z at the Nb-InAs interfaces. For Z we get a value ~ 0.75, indicating a Nb-InAs contact transparency of $t \sim 0.65$.

Notice in Figures 2.6, 2.7 the bias voltage was not increased to $V > 2\Delta_{Nb}/e$, or else the low resistance of the junction would have resulted in a large current, and therefore a high Joule heating. However, for $V > 2\Delta_{Nb}/e$ we would expect the excess current to be even higher than the measured value. Therefore, the reported value $t \sim 0.65$ is a lower bound of the actual contact transparency of the junction. For other values of the gate voltage V_3, the MAR signature at $V = 2\Delta_{Nb}/e$ can be observed.

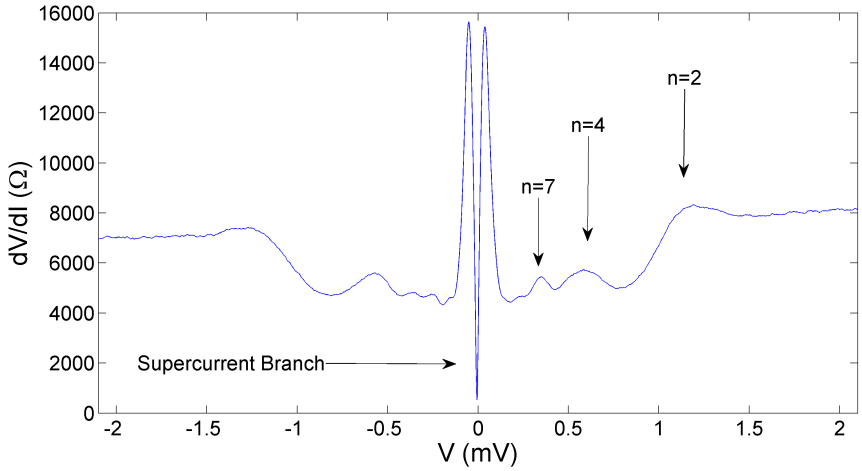

Figure 2.6: Junction differential resistance dV/dI vs. bias voltage V. A supercurrent branch can be seen at zero bias. Signatures of Multiple Andreev Reflections (MAR) are seen higher bias as peak in dV/dI. This indicates phase coherence across the junction. The arrows indicate the position and the number of MAR peak. For this value of the gate voltage, $V_3 = +2.1$ V, the bias voltage was not raised to $V > 2\Delta_{Nb}/e$ because of the low resistance of the junction. For other values of V_3, the $n = 1$ MAR signature can be observed.

Superconducting Coherence Length

Thermal fluctuations and inelastic scattering result in the dephasing of Andreev pairs, limiting the superconducting coherence length in the normal section of an SNS junction [163, 143]. For the junction studied here, the superconducting coherence length in the InAs nanowire is $\xi_{\text{InAs}} = \min(l_T, l_{in})$, where $l_T = \sqrt{\hbar D/(2\pi k_B T)}$ is a characteristic thermal length, D the diffusion coefficient, k_B the Boltzmann constant, T the (electron) temperature, and l_{in} the inelastic scattering length. Using an estimated $T \sim 100$mK, we calculate l_T on the order of a micrometer.

The inelastic scattering length in InAs nanowires, similar to the one studied here, was measured in Ref. [138] to be $l_{in} \sim 250 - 500$ nm. This indicates that ξ_{InAs} is limited by l_{in}. In our calculations we consistently use $\xi_{InAs} = 400$ nm, longer than the junction length $L \simeq 200$ nm.

2.6.2 Junction Critical Current in a Perpendicular Magnetic Field

The Junction critical current exhibits a monotonic, quasi-Gaussian decay as the perpendicular magnetic field, $B_\perp$, increases (see Figure 2.1). Here we concentrate on the theoretical description of this behaviour.

In Ref. [143], the behaviour of the critical current of a long, diffusive planar SNS junction in a perpendicular field was studied using the quasiclassical Green's function method. The roles of non-ideal N-S interfaces were considered. The perpendicular field results in a pair-breaking mechanism equivalent to spin-flip scattering, which is responsible for the decay of the critical current I_c with $B_\perp$. For a narrow junction (with width w smaller than the superconducting coherence length ξ) with perfect interfaces, the following regimes were found: (i) When the junction is very long, $w \ll L$, the Usadel equation for the Green's function can be solved analytically, resulting in a Gaussian decay as a function of the magnetic flux Φ through the junction: $I_c(\Phi) = I_c(0)\exp(-0.238(\Phi/\Phi_0)^2)$. Here, Φ_0 is the (superconducting) flux quantum. (ii) If the width is lesser but of the order of the length, numerical methods are required; however, I_c still decays, and the decay is approximately Gaussian. Aside from the interplay of the orbital states and the perpendicular field (see Section 2.6.3), the nanowire junction studied here is analogous to a planar junction with w given by the diameter $d = 63$ nm. The junction is narrow, $d \lesssim \xi_{InAs} \sim 250 - 500$ nm. The junction length is given by $L = 200$ nm. Thus, the model for a planar junction with $w \lesssim L$ applies. Calculations reported in Ref. [164] indicate that in this limit, a quasi-Gaussian decay of I_c with $B_\perp$ is expected, with a tail at high $B_\perp$ slightly above the Gaussian curve. This may explain why the experimental critical current in figure 1b develops a tail when $B_\perp > 0.3$ T.

The experimental I_c is fit to a Gaussian $I_c(\Phi) = I_c(0)\exp(-0.499(\Phi/\Phi_0)^2)$, which decays

faster by a factor of 2.1 than theoretically predicted in case (i) above. This can be explained by taking into account non-ideal Nb-InAs interfaces. As discussed in [143], the behaviour of the junction is critically dependent on contact resistances. The main effect of non-ideal interfaces is to increase the dwell time of the Andreev pair in the semiconducting section of the junction. The cumulative spin-flip depairing effect causes I_c to decay faster. We use an estimated $R_b = 800\ \Omega$ for each contact, as discussed in Section 2.6.1. This implies a resistance ratio of $r = R_b/R_N = 0.15$, which can account for rescaling the decay by a factor of 1.6, see Ref. [143]. An additional contribution can come from an asymmetry between the contacts, which would further increase the decay rate.

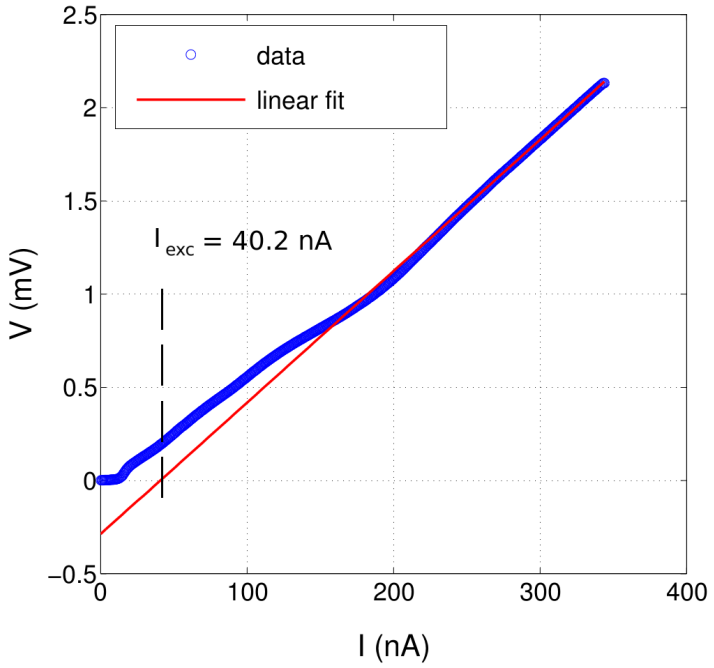

Figure 2.7: Current-Voltage trace of the junction (blue circles), at the gate voltage $V_3 = +2.1$ V. A linear fit to the high bias voltage regime (solid red line) is used to extract the excess current $I_{exc} = 40.2$ nA. Using the analysis given in ref. [134], a Nb-InAs contact transparency $t \sim 0.65$ is extracted.

2.6.3 Interplay of Orbital States and the Perpendicular Magnetic Field

A natural question to ask is if the interference effect due to the interplay of orbital states and the external field appears when the magnetic field is applied in a perpendicular rather than an

axial direction.

Let the nanowire axis be along the $\hat{\boldsymbol{x}}$ direction (Fig. 2.1). Let a magnetic field $\boldsymbol{B} = -B_\perp \hat{\boldsymbol{y}}$ be applied. For the vector potential we choose $\boldsymbol{A} = (B_\perp z/2)\hat{\boldsymbol{x}}$. The main effect of this field is to attenuate the critical current with $B_\perp$ through a depairing mechanism (Section 2.6.2). We ask here if the phase picked up by spiral paths on the circumference of the nanowire can result in an oscillatory behaviour on top of this attenuation.

Consider a spiral path with winding angle θ. Let us assume no back-scattering for the moment (ballistic regime). The phase picked up by this path is $\phi = 2e/\hbar \int \boldsymbol{A} \cdot \mathrm{d}\boldsymbol{l}$, where the line integral is taken along the path. Since the path is a simple spiral, the height z can be determined as a function of the position x along the junction length as $z = r\,\cos(x\theta/L)$. Here, $r = d/2$ is the radius of the nanowire and L the length of the junction. So the phase is

$$\phi = (eB_\perp r/\hbar)\int_0^L \cos(x\theta/L)\mathrm{d}x = 2\pi\,(\Phi/\Phi_0)\left(\frac{\sin(\theta)}{\theta}\right), \tag{2.6}$$

where $\Phi = B_\perp dL$ is the flux through the junction and Φ_0 is the (superconducting) flux quantum. Eq. 2.6 indicates a qualitative difference versus the case of an axial magnetic field: as the perpendicular component of the momentum changes direction with respect to the applied field, the phase picked up by the spiral path changes sign, so the accumulated phase cancels with itself. Specifically, the phase accumulated on parts of the spiral path with $z > 0$ cancels out with that of parts with $z < 0$. Whereas the phase picked up by long spiral paths is suppressed, for a junction in the ballistic regime, the winding angles of the angular momentum subbands with $l = -3, -2, \ldots, 3$ are in the range $(-\pi, \pi)$, i.e. on the main lobe of the sinc function in Eq. 2.6 (l is the angular momentum quantum number). This means that angular momentum subbands can pick up an appreciable phase. Therefore, the occurrence of an interference effect may be possible for a short, ballistic junction.

Now let us consider the quasiballistic regime by introducing back-scattering. Notice that $\boldsymbol{A} \cdot \mathrm{d}\boldsymbol{l}$ changes sign upon each back-scattering event. This has a randomizing effect on the total phase, as the phase now depends on the details of the scattering events. Since the phase ϕ picked up between two scattering events is not small ($|\phi| \sim \pi/2$), after several scattering events we expect the phase to be completely randomized, and no interference effect to survive. Similar to previously studied cases of a randomly distributed phase due to diffusive paths [165, 164], the effect of this random phase is estimated to be a suppression of the total supercurrent, contributing the suppression of I_c with $B_\perp$ on top of the pair-breaking mechanism discussed in Section 2.6.2.

In summary, for the quasiballistic junction studied experimentally we do not expect an interference effect due to the interplay of orbital states and a perpendicular field, because of the

randomizing effect of back-scattering. However, in a ballistic junction short enough that the self-cancelling of the phase does not dominate, an interference effect may occur.

2.6.4 Spin-Orbit and Zeeman Effects in the Josephson Junction

Yokoyama et al. [144] theoretically studied the interplay of spin-orbit and Zeeman effects in an InSb nanowire SNS junction. They found that, in the presence of a magnetic field B, the different spin components of Andreev pairs pick up different amounts of superconducting phase, resulting in the splitting of the Andreev Bound States in the junction. Consequently, as B is increased from zero, the junction critical current I_c is reduced. At a certain value for B, the junction abruptly undergoes a so-called 0-π transition, wherein the phase ϕ across the junction in its ground state shifts from $\phi = 0$ to $\phi = \pi$. This results in a cusp (minimum) in the critical current, and, upon further increasing the field B, I_c increases until it recovers value close to its original value at $B = 0$. The cycle repeats upon further increasing B, resulting in an oscillatory I_c. This effect can dominate the behaviour of I_c for InSb nanowire junctions in the presence of a magnetic field. We ask if a similar physical picture can be responsible for the observed oscillations of I_c vs. $B_{\|}$, in the InAs nanowire junction studied here.

In terms of a magnetic parameter $\theta_B = |g\mu_B B|L/(\hbar v_F)$, the cusps of the critical current are predicted to happen at fields corresponding to $\theta_B = (2n+1)\pi/2$, for integer n. Here, g is the Landé g-factor, μ_B the Bohr magneton, L the junction length, and v_F the Fermi velocity. For an InSb nanowire of length $500 - 1000$ nm, the first cusp ($\theta_B = \pi/2$) is estimated in Ref. [144] to be at $B = 0.2$ T. However, using the values for our InAs nanowire device, which is shorter ($L \simeq 200$ nm), and has a g-factor that is roughly a factor of 5 smaller than that of InSb, we estimate $B \sim 7$T for the position of the first cusp. This is an order of magnitude larger than the observed value of $B \sim 0.6$ T. Furthermore, the regularity of positions, in B, of I_c minima predicted by the relation $\theta_B = (2n+1)\pi/2$ does not hold for the InAs junction. In fact, we find the positions of the minima can be tuned using the voltages on the local gates, see Figure 2.3. Also, the observed value of I_c at the first antinode (e.g. at $B_{\|} \simeq 0.8$ T in Figure 3a) is roughly 0.15 times the value of I_c at zero field, whereas in [144] this ratio is predicted to be close to 1.

Therefore, it is concluded that the I_c vs. $B_{\|}$ oscillations observed in the InAs nanowire junction are not due to the interplay of spin-orbit and Zeeman effects. We neglect these effects in our analyses for simplicity. Observing 0-π transitions in an InAs nanowire junction may be difficult, because the high magnetic field required to drive the transition will likely destroy superconductivity in the leads.

2.6.5 Magnetic Field Misalignment

The perpendicular magnetic field, $B_\perp$, was applied in the plane of the device substrate (xy-plane in Fig. 2.1). The deviation angle of the field from the perpendicular ($\hat{\boldsymbol{y}}$) direction is $2^\circ \pm 3^\circ$. Since $\tan(2^\circ) \simeq 0.03$, this misalignment was neglected.

The axial magnetic field, $B_\parallel$, was applied in the xy-plane, at an angle $\alpha = 8^\circ \pm 4^\circ$ with respect to the nanowire axis $\hat{\boldsymbol{x}}$. The axial component of the field is $B_\parallel \times \cos\alpha$. Since $\cos\alpha > 0.98 \simeq 1$, the axial component is very close in magnitude to $B_\parallel$.

The perpendicular ($\hat{\boldsymbol{y}}$) component of $B_\parallel$ is of magnitude $B_\parallel \times \sin\alpha$. This results in a quasi-Gaussian decay of the critical current I_c with $B_\parallel$, due to a pair-breaking mechanism effectively equivalent to spin-flip scattering (see Section 2.6.2). Let us quantify this quasi-Gaussian decay by a suppression factor $s(B_\parallel) = I_c(B_\parallel)/I_c(B_\parallel = 0)$. Given that $\sin\alpha$ is in the range $0.07 - 0.2$, with an average value 0.13, we estimate s is close to 1 ($s > 0.75$) for $B_\parallel < 1.5$ T, covering a large range of the measured magnetic fields. However, for the highest field measured, $B_\parallel = 2.5$ T, the s can be as severe as 0.3.

A similar field dependence can be defined for the critical current density, by generalizing $J_c(\theta)$ to $J_c(B_\parallel, \theta) = s(B_\parallel)J_c(\theta)$. The $B_\parallel$- and θ-dependent parts of J_c are separable, and the pair breaking effect of $B_\parallel$ has been neglected (i.e. $s(B_\parallel) = 1$ for all $B_\parallel$). Including the field dependence of J_c will not qualitatively change the interference pattern (see also discussion in Section 2.6.3). However, I_c and a field-dependent J_c will no longer be simply related as a Fourier pair. The broadening parameter σ, which influences the attenuation of I_c at high fields (see Section 2.6.6), is expected to be sensitive to the field dependence of J_c. We leave the treatment of a model with a field dependant critical current density to future work.

2.6.6 The Effect of Broadening the Peaks in the Spectral Density

In the quasi-ballistic regime, the width of the Gaussian peaks in the modelled critical current density, $J_c(\theta)$, is parametrized by σ (see Eq.2.3). The broadening of the peaks determines the qualitative behaviour of $I_c(B_\parallel)$. To illustrate this we use the example developed above, where $n_l = 1$ for $l = -3, -2, \ldots, 3$, and zero otherwise. We show in Figure 2.8 the critical current density J_c vs. the magnetic frequency Φ_0/Φ_{nw}, and the resulting I_c vs. Φ_{nw}/Φ_0, for two different values of σ. When the spectral density J_c shows sharp peaks in its distribution vs. winding angle θ (i.e., when $\sigma \ll \mathrm{d}\theta_l/\mathrm{d}l$), I_c oscillates. However, when the distribution of J_c is very broad ($\sigma \gg \mathrm{d}\theta_l/\mathrm{d}l$), I_c shows a monotonic, quasi-Gaussian decay. The model was fit to the experimental data using an intermediate regime of broadening.

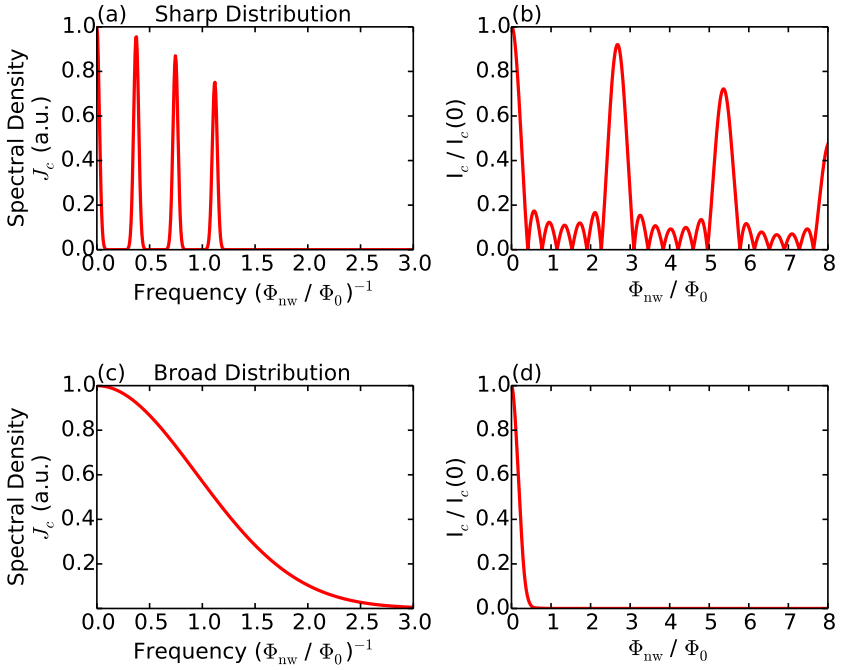

Figure 2.8: Spectral densities (left) critical currents (right) in the quasiballistic regime, as a function of the broadening parameter σ. The spectral density J_c is plotted vs. the magnetic frequency (Φ_0/Φ_{nw}), see Figure 2.2. The envelope function $J_{\max}(\theta)$ has been taken into account, assuming $l_{in} = 400$ nm as the inelastic scattering length (see Section 2.6.8). (a,b) $\sigma = 0.15$. Sharp peaks in J_c compared to the peak spacing, $\sigma \ll \mathrm{d}\theta_l/\mathrm{d}l$, results in an oscillatory I_c. The oscillations in (b) attenuate with increasing magnetic flux, due to the finite σ. Panels (a,b) are reproduced in the bottom row of Figure 2.2. (c,d) $\sigma = 5.0$. Broad peaks in J_c compared to the peak spacing, $\sigma \gg \mathrm{d}\theta_l/\mathrm{d}l$. The peaks in (c) overlap, creating a bell shaped curve. The attenuation of critical current with increasing magnetic flux is strong enough that no oscillations are seen in (d), resulting in a monotonic, quasi-Gaussian decay. The following parameters were used in these examples: $d = 63$ nm, $L = 200$ nm, $l_e = 80$ nm, $E_F = 150$ meV. $n_l = 1$ for $l = -3, -2, \ldots, 3$, and zero otherwise. The experimental data is best fit to an intermediate regime, with $\sigma \sim 0.9$.

2.6.7 Varying the Nanowire Diameter

We discuss the effect of changing the nanowire diameter d on the interference effect in the quasi-ballistic model, where all carriers are on a cylindrical shell at a radius $d/2$ from the nanowire center. Consider the critical current of the junction as a function of the axial magnetic

field, $B_\parallel$. Eq. 2.2 can be written as

$$I_c(B_\parallel) = \left| \int_{-\infty}^{\infty} J_c(\theta) \mathrm{e}^{\left(i \frac{\Phi_{\mathrm{nw}}}{\Phi_0} \theta\right)} \mathrm{d}\,\theta \right|, \tag{2.7}$$

with $\Phi_{nw} = \pi d^2 B_\parallel / 4$. The critical current density, J_c, is given by Eq. 2.3.

Let us change the diameter from d to a value d', resulting in $\Phi_{nw} \to \Phi'_{nw} = (\frac{d'^2}{d^2})\Phi_{nw}$, and $J_c(\theta) \to J'_c(\theta)$, $I_c(B_\parallel) \to I'_c(B_\parallel)$. We calculate $J'_c(\theta)$ below, and show that $I'_c(B_\parallel) = I_c(B_\parallel)$, up to a rescaling of the broadening parameter σ, and a rescaling of the envelope function $J_{\mathrm{max}}(\theta)$. We make the substitution of variables $\theta = (d^2/d'^2)\theta'$ in Eq. 2.7 to write

$$\begin{aligned} I_c(B_\parallel) \to I'_c(B_\parallel) &= \left| \int_{-\infty}^{\infty} J'_c(\theta) \mathrm{e}^{\left(i \frac{\Phi'_{\mathrm{nw}}}{\Phi_0} \theta\right)} \mathrm{d}\,\theta \right| \\ &= \frac{d^2}{d'^2} \left| \int_{-\infty}^{\infty} J'_c \left(\left(\frac{d^2}{d'^2} \right) \theta' \right) \mathrm{e}^{\left(i \frac{\Phi_{\mathrm{nw}}}{\Phi_0} \theta'\right)} \mathrm{d}\,\theta' \right|. \end{aligned} \tag{2.8}$$

In the above integral, θ, θ' are dummy variables, and it suffices to have $J'_c(\theta) = (d'^2/d^2) J_c(\theta')$ in order to get $I'_c(B_\parallel) = I_c(B_\parallel)$. Let us use a constant envelope function $J_{\mathrm{max}}(\theta) = J_0$ for now. Notice that in Eq. 2.5, $v_\theta \propto 1/d$, so the positions of the peaks, θ_l have an inverse-square dependence of d, so when $d \to d'$, $\theta_l \to \theta'_l = (d^2/d'^2)\theta_l$. Using Eq. 2.3 we write

$$\begin{aligned} J'_c \left(\left(\frac{d^2}{d'^2} \right) \theta' \right) &= J_0 \sum_l \frac{n_l}{\sigma\sqrt{2\pi}} \exp\left(-\frac{((d^2/d'^2)\theta' - \theta'_l)^2}{2\sigma^2} \right) \\ &= J_0 \sum_l \frac{n_l}{\sigma\sqrt{2\pi}} \exp\left(-\frac{(d^2/d'^2)^2(\theta' - \theta_l)^2}{2\sigma^2} \right). \end{aligned} \tag{2.9}$$

If we rescale σ as $\sigma \to \sigma' = (d^2/d'^2)\sigma$, the factors in the exponent cancel, and we get the result $J'_c\left((d^2/d'^2)\theta'\right) = (d'^2/d^2) J_c(\theta')$, or equivalently $I'_c(B_\parallel) = I_c(B_\parallel)$.
Let us consider the case of a generic $J_{\mathrm{max}}(\theta)$. Using similar analysis we see that, if the angle argument of J_{max} is rescaled such that $J_{\mathrm{max}}(\theta) \to J'_{\mathrm{max}}(\theta) = J_{\mathrm{max}}((d'^2/d^2)\theta)$, then the relation $J'_c\left((d^2/d'^2)\theta'\right) = (d'^2/d^2) J_c(\theta')$ holds true (up to rescaling σ). This follows from the dependence of J_{max} on the length of the spiral paths $l_\theta = \sqrt{L^2 + (d\theta/2)^2}$, as discussed in Section 2.6.8. When the diameter of the nanowire becomes very large, the spiral paths on its circumference become very long, and the supercurrent is suppressed due to inelastic scattering.

In summary, we have shown that if the radial position of the carriers is changed, the spectral density $J_c(\theta)$ is unaffected up to a rescaling of the envelope function (J_{max}) and the width of

its peaks (σ). Crucially, the frequencies at which the peaks of J_c appear, i.e. the frequencies of oscillations of I_c vs. $B_\parallel$, are unaffected. We suggest that, for general radial wavefunctions of the carriers, a Josephson interference effect similar to that discussed above, and with the same periods of oscillations in $B_\parallel$, should appear. However, a detailed calculation is required to verify this, using Usadel equations and taking into account the complete Hamiltonian for the system, including the radial confinement potential.

2.6.8 Maximum Supercurrent Calculated via Usadel Equations

We use the quasi-classical Green's functions theory [150] to describe the proximity effect superconductivity in the InAs nanowire junction. Further details on this approach can be found in [166], on which this section is based.

The starting point is a field operator

$$\Psi = \begin{pmatrix} \Psi_\uparrow(x,t) \\ \Psi_\downarrow^\dagger(x,t) \end{pmatrix}$$

acting on the electron-hole Nambu space. $\Psi_\uparrow(x,t)$ and $\Psi_\uparrow^\dagger(x,t)$ are annihilation and creation operators for a fermionic quasiparticle with spin $\uparrow$ at position x and time t.

The basic objects in terms of which the theory is developed are the Retarded, Advanced, and Keldysh Green's functions ($\hat{R}$, $\hat{A}$, and $\hat{K}$, respectively) defined in terms of the field operator Ψ. We consider the nanowire to be in thermal equilibrium, so the function $\hat{K}$ is redundant and holds no further information about the system than $\hat{R}$, $\hat{A}$. Being metallic superconductors, the Nb leads exhibit electron-hole symmetry. We assume electron-hole symmetry in the normal section as well, so $\hat{A}$ is also redundant. We concentrate on $\hat{R}$. Using the standard angular (Θ, ϕ) parametrization on the unit sphere, we write

$$\hat{R} = \cos\Theta\tau_z + \sin\Theta(\cos\phi\tau_x + \sin\phi\tau_y) = \begin{pmatrix} \cos\Theta & e^{-i\phi}\sin\Theta \\ e^{i\phi}\sin\Theta & -\cos\Theta \end{pmatrix},$$

where $\tau_{x,y,z}$ are Nambu spinors acting on the electron-hole degree of freedom. Here, $\Theta = \Theta(x,E)$ is the complex pairing angle which quantifies the strength of superconducting-like correlations (off-diagonal elements of $\hat{R}$) and normal-like correlations (diagonal elements of $\hat{R}$). We use the capital symbol Θ instead of the more standard θ to avoid confusion with winding angles. $\phi = \phi(x,E)$ is the real superconducting phase. We have considered only one spatial dimension x, along the axis of the nanowire. This one dimensional (1D) formulation is in anticipation of reducing the description of the nanowire to a quasi-1D model, see below.

Our goal here is to calculate $\Theta(x,E)$ and $\phi(x,E)$ for all positions and energies, for the geometry of the junction. The equilibrium Usadel equations, governing Θ, ϕ, can be derived from the equation for $\hat{R}$. The 1D set of coupled equations reads:

$$\frac{\hbar D}{2}\frac{\partial^2\Theta}{\partial x^2} + \left(iE - \frac{\hbar}{\tau_{in}} - \left(\frac{\hbar}{\tau_{sf}} + \frac{\hbar D}{2}\left(\frac{\partial\phi}{\partial x} + \frac{2e}{\hbar}A_x\right)^2\right)\cos\Theta\right)\sin\Theta + \Delta(x)\cos\Theta = 0, \tag{2.10a}$$

$$\frac{\partial}{\partial x}\left(\left(\frac{\partial\phi}{\partial x} + \frac{2e}{\hbar}A_x\right)\sin^2\Theta\right) = 0. \tag{2.10b}$$

Here, $D = l_e v_F/3$ is the diffusion coefficient of electrons, l_e is the elastic mean free path and v_F the Fermi velocity. The timescales for inelastic and spin-flip scatterings are denoted by τ_{in} and τ_{sf}, respectively. A_x is the axial component of the magnetic vector potential, due to a perpendicular external magnetic field, $B_\perp$. Spin-flip scattering off of magnetic impurities is ignored, so the only contribution to the spin-flip rate is the narrow-junction limit depairing term $\hbar/\tau_{sf} = e^2d^2DB_\perp^2/(6\hbar)$, as discussed in [143]. The quasi-1D depairing term is valid because the width of the junction is on the same order as the superconducting coherence length in Nb, $d = 63$ nm $\sim \xi_{Nb}$. The parallel component of the magnetic field does not enter the 1D Usadel equations. We use Δ for the superconducting energy gap due to electron-phonon coupling. In the Nb leads, this equals $\Delta_{Nb} = 1.2$ meV, and in the normal section of the junction we have $\Delta = 0$.

All physical quantities related to the junction can be derived from Θ and ϕ. In particular, the supercurrent density in the N (S) section of the junction is

$$J_{N(S)} = -(\sigma_{N(S)}/e)\int_0^\infty \mathrm{d}E\,\tanh\left(E/2k_BT\right)\mathrm{Im}\left(\sin^2\Theta\right)\left(\frac{\partial\phi}{\partial x} + (2e/\hbar)A_x\right). \tag{2.11}$$

Here, $\sigma_{N(S)}$ is the normal state conductivity of the normal (superconducting) section of the junction, k_B the Boltzmann constant and T the temperature. By comparison with the Ginzburg-Landau (GL) result $\mathbf{J} = (-\hbar e/m^*)|\psi_{GL}|^2(\boldsymbol{\nabla}\phi + (2e/\hbar)\mathbf{A})$, we identify the modulus squared of the GL order parameter in the normal section as

$$|\psi_{GL}|^2 = (m^*\sigma_N/e^2\hbar)\int_0^\infty \mathrm{d}E\,\tanh\left(E/2k_BT\right)\mathrm{Im}\left(\sin^2\Theta\right), \tag{2.12}$$

where m^* is the effective mass. The energy dependence of the phase ϕ has been neglected. This is justified because the Nb reservoirs at the ends of the junction are bulk superconductors, with

an energy independent phase difference γ determined by the bias current. The N-S interface are transparent with $t \sim 0.65$, so the phase gradient in the normal section of the junction is also energy independent [167].

In the model for the InAs nanowire junction, orbital effects are the dominant mechanism for Josephson interference. However, the field operator Ψ contains no information on the orbital structure of the nanowire, such as angular momentum subbands — in fact, it acts to create/annihilate a fermion of angular momentum zero. This is because the effects of quantum confinement are neglected in the standard treatment of Green's functions that leads to Eq. 2.10, e.g. the treatment given in [166]. It is possible, in principle, to generalize the Green's functions method by starting from a Hamiltonian for the junction which contains the quantum confinement potential, then deriving the orbital subband structure of the nanowire, and the effects of its interplay with superconductivity. However, such treatment is beyond the scope of this chapter. Instead, we assume a sinusoidal current-phase relationship and model the orbital effects using a semi-classical approach based on the spiral trajectories of particles. What we wish to calculate here is the suppression of the supercurrent, for long trajectories, due to inelastic scattering.

Consider a spiral trajectory on the circumference of the nanowire with winding angle θ. The length of this trajectory is $l_\theta = \sqrt{L^2 + (d\theta/2)^2}$, where $L = 200$ nm is the length of the junction and $d = 63$ nm the diameter of the nanowire. We approximate the supercurrent density of this trajectory by that of a planar junction (Eq. 2.11) of length $L' = l_\theta$. In doing so we are modelling the nanowire as a set of parallel, narrow (quasi-1D) planar junctions, each with a length $L' = l_\theta$, corresponding to a winding angle θ. What limits the supercurrent in the planar junction is the magnitude squared of the GL order parameter at the "bottleneck" in the normal section midway between the Nb leads. Since $|\psi_{GL}|^2$ does not depend on the phase, we set ϕ equal to zero everywhere, and the Usadel equations (Eq. 2.10) simplify to

$$\frac{\hbar D}{2}\frac{\partial^2 \Theta}{\partial x^2} + \left(iE - \frac{\hbar}{\tau_{in}}\right)\sin\Theta + \Delta(x)\sin\Theta = 0. \tag{2.13}$$

Here we have set the spin-flip scattering rate τ_{sf} equal to zero, i.e. no external magnetic field applied. We discuss this assumption below. Let the N-S boundaries be at $x = 0, x = L'$. We have

$$\Delta(x) = \begin{cases} \Delta_{Nb} = 1.2 \text{ meV} & x < 0 \text{ or } x > L' \\ 0 & \text{otherwise} \end{cases}$$

The pairing angle in the superconducting Nb leads, Θ_S, tends to its BCS value for Nb at positions

far from the N-S interfaces, $\Theta_S = \Theta_{BCS}$, for $x \to \pm\infty$. Here,

$$\Theta_{BCS}(E) = \begin{cases} \pi/2 + i \text{ argtanh}(E/\Delta_{Nb}) & \text{if } |E| < \Delta_{Nb}, \\ i \text{ argtanh}(\Delta_{Nb}/E) & \text{if } |E| > \Delta_{Nb}. \end{cases}$$

At the N-S interfaces, the pairing angle in the normal section, Θ_N, and the superconducting section, Θ_S, are subject to the following continuity condition:

$$\sigma_N \frac{\partial \Theta_N}{\partial x}\bigg|_{x=x_i} = \sigma_S \frac{\partial \Theta_S}{\partial x}\bigg|_{x=x_i} = g_b \sin\left(\Theta_S(x_i, E) - \Theta_N(x_i, E)\right),$$

for $x_i = 0, L'$. This expresses the conservation of spectral current at the boundaries. Here, $g_b = G_b/\mathcal{A}_b$ is the conductance of an interface normalized by its area. We can further simplify the situation by noticing the high conductance at the interfaces, $r = R_b/R_N = G_N/G_b \sim 0.15 \ll 1$, see Section 2.6.1. So, we use the transparent interface limit [168] to write

$$\Theta_S(x = x_i) = \Theta_N(x = x_i) = \Theta_{BCS}, \quad \text{for } x_i = 0, L'. \tag{2.14}$$

We solve Eq. 2.13 for the complex quantity Θ_N numerically, subject to the boundary conditions in Eq. 2.14. We insert the solution Θ_N into Eq. 2.12 to calculate $|\psi_{GL}|^2$ at middle of the junction, i.e. $x = L'/2$. We do this calculation for different values of the junction length L'. The decay of the supercurrent with trajectory length l_θ is captured by the envelope function

$$J_{\max}(\theta) = \frac{|\psi_{GL}\left(L' = l_\theta, x = L'/2\right)|^2}{|\psi_{GL}\left(L' = L, x = L'/2\right)|^2}, \tag{2.15}$$

where $L = 200$ nm is the length of the shortest path across the junction, with $\theta = 0$, i.e. a straight trajectory.

In Figure 2.9 we show $J_{\max}$ vs. L'/l_e as a function of the inelastic scattering length l_{in}. As expected, $J_{\max}$ decays as the length of the trajectory is increased, and the decay is faster for shorter l_{in}. For L' much longer than l_e, and longer than l_{in}, the $J_{\max}$ curves can be fitted to exponential curves. The length scale of the exponential decay depends on l_e as well as l_{in}. For short lengths, $L' \lesssim l_e$, the $J_{\max}$ curves saturate (not shown). The parameters used for this calculation are the same as those used in Figure 2.2: $d = 63$ nm, $L = 200$ nm, $l_e = 80$ nm, $l_{in} = 400$ nm, $E_F = 150$ meV, $m^* = 0.023 m_e$, and $T = 100$ mK is taken as the (electron) temperature.

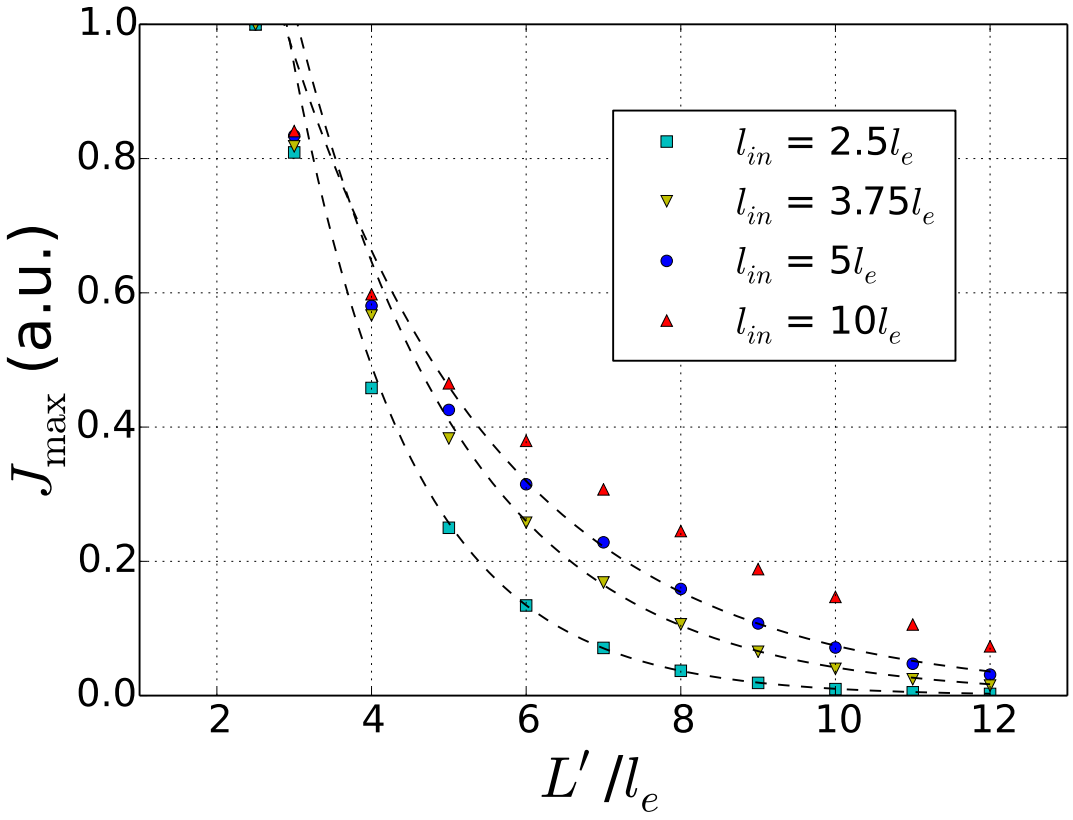

Figure 2.9: The envelope function $J_{\max}$ (Eq. 2.15) vs. the normalized planar junction length L'/l_e, as a function of the inelastic scattering length l_{in}. Here, $l_e = 80$ nm is the elastic scattering length. The supercurrent density decays as the length of the trajectory is increased, and the decay is faster for shorter l_{in}. The dashed lines are exponential fits to the region $L'/l_e > 5$, for the cases $l_{in}/l_e = 2.5,\ 3.75,\ 5$. Each curve is normalized to its value at $L' = 200$ nm (i.e. $L'/l_e = 2.5$). For a trajectory with winding angle θ on the circumference of the nanowire, $J_{\max}(\theta)$ can be calculated by setting $L' = l_\theta = \sqrt{L^2 + (d\theta/2)^2}$. The curve corresponding to $l_{in} = 5l_e$ is used in the inset of Figure 2.2.

Finally, we comment on setting the spin-flip scattering rate $\Gamma_{sf} = \hbar/\tau_{sf}$ equal to zero in the above calculation. The axial magnetic field $B_\parallel$ can create a pair-breaking mechanism (i.e. an effective spin-flip mechanism similar to that in Section 2.6.2) for Andreev pairs on spiral paths, because the azimuthal ($\hat{\boldsymbol{\theta}}$) component of their velocity is perpendicular to $B_\parallel$. However, this effect is overshadowed by the pair-breaking due to the misalignment of $B_\parallel$ with respect to

the nanowire axis, as discussed in Section 2.6.5. This is because the $\hat{\boldsymbol{\theta}}$ component of the pair velocity is small compared to its total (Fermi) velocity between scattering events: $v_\theta \lesssim 0.3 v_F$. A typical value is $v_\theta \sim 0.1 v_F$, for a subband with angular momentum quantum number $l = 1$. Furthermore, the axial cross section of the nanowire, $\pi d^2/4$, is a factor of 4 smaller than its perpendicular cross section, $d \times L$. Estimates give $J_{\max}(\Gamma_{sf})/J_{\max}(\Gamma_{sf} = 0) \gtrsim 0.8$ for the largest magnetic field measured, $B_\parallel = 2.5$ T. As in Section 2.6.5, we neglect such field dependence of J_c.

Chapter 3

Theory of Orbital Josephson Interference in a Nanowire Proximity Effect Junction

3.1 Introduction

In Chapter 2 we saw an oscillation of the critical current I_c of our first generation proximitized Josephson junctions with respect to an axially applied magnetic field $B_{||}$. We argued that the observed effect cannot be fully explained by using a combination of spin-orbit and Zeeman effects in the nanowire, because the positions of the nodes of the oscillation with respect to the field do not agree with that the spin-orbit + Zeeman theory predicts. Later on, in chapters 4 and 5 we will see that a similar oscillation or modulation of I_c is observed versus $B_{||}$ for the second and third generation Josephson junctions, suggesting that the observed phenomenon is a typical occurrence in nanowire based proximity junctions, and deserves further study.

It is especially interesting to fully understand the behaviour of I_c versus $B_{||}$ because applying an axial magnetic field is exactly the condition required to tune the device into a topological regime that can host Majorana Bound states [76, 44], and that any signatures of the topological transition in the critical current [85] need to be distinguishable from the non-topological physics that cause the oscillations of I_c. Furthermore, and on a more fundamental level, the critical current of a junction appears to be very sensitively dependent on the potential landscape inside of the nanowire — this point is further expanded on in Chapter 4. So, understanding the magnetic field dependence of I_c may provide a sensitive tool to study the electric potential and the subband structure inside the nanowire, and may provide more information than, e.g., normal-state magneto-resistance studies [156, 169] of the nanowire junction.

In this chapter we provide a rigorous model for Orbital Josephson interference [170], the phenomenon alluded to in Chapter 2. From first principles we solve the $B_{||}$ dependence of the critical current of an idealized Josephson junction while taking into account the subband structure of the nanowire. Numerical simulations show that a qualitative agreement can be reached between our experimental data and the predictions of this model, even though the model describes an idealized junction in the sense that (i) the mean free path is assumed to be longer than the junction channel length, (ii) the junction is assumed to be exactly cylindrically symmetric, and (iii) there is no scattering at the superconductor/semiconductor interface due to Fermi wave-vector mismatch. We argue that spin-orbit and Zeeman effects, while present, are a smaller effect on the magnetic field dependence of I_c that Orbital Josephson interference. To our knowledge, this model provides the most likely explanation for the observed behaviour of I_c versus $B_{||}$. Future potential expansions of this model are discussed.

A semiconductor nanowire based superconductor-normal-superconductor (SNS) junction is modeled theoretically. A magnetic field is applied along the nanowire axis, parallel to the current. The Bogoliubov-de Gennes equations for Andreev bound states are solved while considering the electronic subbands due to radial confinement in the N-section. The energy-versus-phase curves of the Andreev bound states shift in phase as the N-section quasiparticles with orbital angular momentum couple to the axial field. A similar phase shift is observed in the continuum current of the junction. The quantum mechanical result is shown to reduce to an intuitive, semi-classical model when the Andreev approximation holds. Numerical calculations of the critical current versus axial field reveal flux-aperiodic oscillations that we identify as a novel form of Josephson interference due to this orbital subband effect. This behavior is studied as a function of junction length and chemical potential. Finally, we discuss extensions to the model that may be useful for describing realistic devices.

3.2 Motivation

The Josephson effect is characterized by a current-phase relationship (CPR) linking macroscopic current flow to the phase gradient of the superconducting order parameter [171]. The precise form of the CPR for a superconducting weak link depends on intrinsic factors such as junction geometry, material properties, coherence lengths, etc., in addition to extrinsic variables like temperature and magnetic field. In superconductor-normal-superconductor (SNS) junctions in which the N-section is long enough to suppress direct tunnelling of Cooper pairs, but shorter than the N-section phase coherence length, a supercurrent may be carried by quasiparticles undergoing Andreev reflection at the S-N interfaces [172, 173, 132, 137]. Planar SNS junctions of a larger width compared to the S-section superconducting coherence length have been studied

in great detail [153] (width refers to the dimension perpendicular to the current). These have revealed, for example, Fraunhofer oscillations of the critical current I_c with respect to an externally applied out-of-plane magnetic field [164, 174, 175]. For junction widths comparable to the S-section coherence length, i.e. the narrow junction limit, this becomes a quasi-Gaussian, monotonic decay of the critical current [164, 141, 176]. Recently, attention has been given to nanoscale, quasi one-dimensional (1D) SNS junctions, such as those readily engineered by contacting semiconductor nanowires with superconducting leads [135, 140, 139, 177, 178]. Gating the semiconducting N-section allows for modulating the supercurrent by controlling the chemical potential [135, 177]. The oscillations of the magnetoresistance of a nanowire SNS junction in the voltage-biased state (i.e. no dc supercurrent) versus an axial magnetic field have been studied [178]. Efforts to realize Majorana fermion quasiparticles in 1D semiconductors with strong spin-orbit interaction and proximity coupling to a superconductor [6, 76, 77, 78, 77] have further raised interest in this type of junction. Theoretical results have indicated that the behaviour of the critical current in such a junction versus magnetic field and chemical potential can be used to identify topological phases [133].

Previous theoretical descriptions of quasi-1D SNS junctions [141, 142, 143, 176] have not fully considered the effects of nanoscale confinement on the CPR, in particular the implications of orbital angular momentum coupling to an external magnetic flux. Here we provide a quantum mechanical description of an idealized junction with a flux applied along the nanowire axis (parallel to the current). For a planar junction, no significant modification of the CPR with an axial flux is expected, as azimuthal motion of the carriers is absent. However, for a cylindrical geometry, azimuthal motion leads to a non-trivial effect which we identify as a previously unstudied form of Josephson interference. This is due to the coupling between Andreev quasiparticles (bound states and continuum states) with orbital angular momentum and the axial flux, which results in phase shifts of the energy-versus-phase for these current carrying states. The total current summed over all channels (occupied orbitals) can display interference. In contrast to Fraunhofer interference in wide planar junctions, the flux is aligned *with* the current and the oscillations are *not* periodic in the flux quantum. This effect is only present in nanoscale junctions with lateral dimensions (i.e. diameter) smaller than the London penetration depth. This is a regime in which the general theorem of Byers and Yang [179] does not apply. It is shown that the supercurrent from continuum states also contributes to this interference. For certain junction parameters, the interference effect can dominate the I_c vs. Φ characteristics. Semiclassically, the effect is intuitively understood by the pickup of a magnetic phase by Andreev pairs with an azimuthal velocity component as they cross the junction ballistically. The aim of this paper is to theoretically describe this type of Josephson interference in a fully quantum mechanical way. In particular, we are interested in understanding the effect in isolation from the additional complications of real devices, such as non-cylindrical contact geometry, inter-

facial potential barriers, etc. We consider in the discussion section how to modify the present model to better describe realistic devices. Here, we consider the case where the diameter is smaller than the superconducting coherence length in the S-section, so that the phase of the order parameter is uniform around the S-section circumference in any magnetic field up to the critical field of the leads, H_c. Spin-orbit and Zeeman effects in the N-section (e.g. relevant to III-V semiconductor nanowires) are neglected, and we assume no barriers at the S-N interfaces. Furthermore, we neglect magnetic depairing effects.

3.3 Model

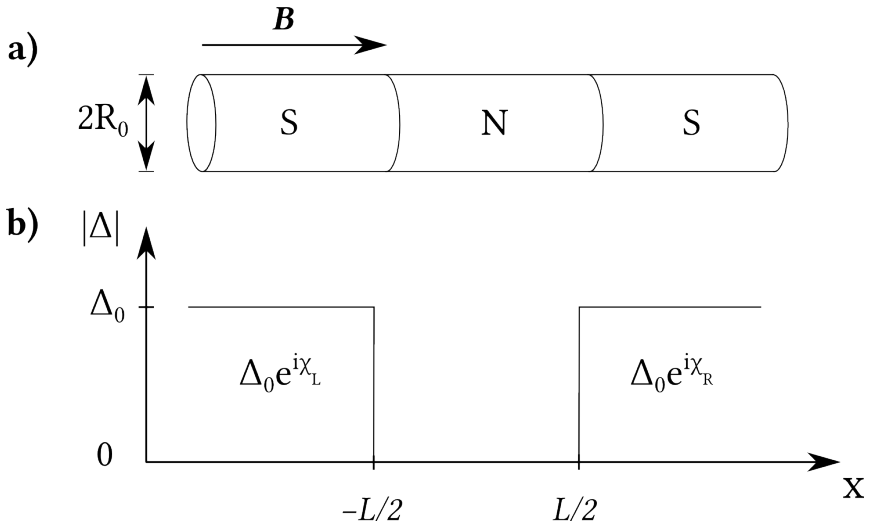

Figure 3.1: (a) Schematic of the nanowire SNS junction of length L. It is modelled as a cylinder with a nanoscale diameter d smaller than both the London penetration length and the S-section phase coherence length. An axial magnetic field $\boldsymbol{B} = B_{\|}\hat{\boldsymbol{x}}$ penetrates the cylinder. (b) The superconducting order parameter has the magnitude Δ_0 in the S-section, and is zero in the normal section, with a jump-like variation at the boundaries.

Consider an SNS junction created by a semiconducting nanowire contacted by superconducting leads. A cylindrical coordinate system $\boldsymbol{r} = (x, \rho, \theta)$ is used, with the nanowire axis along $\hat{\boldsymbol{x}}$. The junction is modelled as a cylinder of radius R_0. The diameter $d = 2R_0$ of the cylinder is assumed smaller than the S-section London penetration depth λ_S, and the S-section superconducting coherence length ξ_S. In Figure 3.1a, we divide the cylinder into three regions,

with region 1 the superconducting section corresponding to the left lead ($x < -L/2$), region 2 the normal section corresponding to the nanowire ($|x| < L/2$), and region 3 the S-section corresponding to the right lead ($x > L/2$). The leads are connected to bulk superconductors at temperature T. Figure 3.1b shows the corresponding variation of the superconducting order parameter inside the nanowire.

We assume uniform electrostatic potentials in each section (i.e. no scattering potential is included and transport is ballistic), and no potential barrier at the S-N interfaces. The effective mass of the electron is assumed to have the same value m^* in both S- and N-sections so that there is no Fermi wavevector mismatch (FWVM) at the S-N interfaces. This assumption allows us to use Kulik's method [180] to calculate the supercurrent of the junction. The advantage of this method is that it gives an analytical expression for the bound state energies, which provides us an intuitive way to understand the interference effect and connects our model to an approximate semiclassical picture. We note that inclusion of FWVM or interfacial barriers would not alter the basic mechanism of orbital Josephson interference that is demonstrated by this simpler model, but would require use of a more complicated transmission matrix formalism to calculate supercurrents. Our expectations for the qualitative effects of barriers are discussed in Section 3.7.

An axial magnetic field $\boldsymbol{B} = B_{\parallel}\hat{\boldsymbol{x}}$ penetrates the cylinder. Any screening of the magnetic field in the S-sections is neglected, as we have $d < \lambda_S$. In the Coulomb gauge, the vector potential is $\boldsymbol{A} = A_\theta\hat{\boldsymbol{\theta}} = (B_{\parallel}\rho/2)\hat{\boldsymbol{\theta}}$. Using the superscript $\alpha = 1, 2, 3$ to refer to the three sections of the junction (with the N-section corresponding to $\alpha = 2$), the single-electron Hamiltonian (excluding the superconducting pairing potential) in the presence of the magnetic field can be written as:

$$H_0 = -\mu + H_x + H_\theta + \sum_{\alpha=1,2,3} V^\alpha(\rho); \tag{3.1a}$$

$$H_x = -\frac{\hbar^2}{2m^*}\frac{\partial^2}{\partial x^2}, \tag{3.1b}$$

$$H_\theta = \frac{1}{2m^*}\left(-i\hbar\frac{1}{\rho}\frac{\partial}{\partial\theta} - eA_\theta\right)^2. \tag{3.1c}$$

Here, H_x describes the kinetic energy of motion along the axis of the cylinder, H_θ the kinetic and magnetic energies of the azimuthal motion around the cylinder, and $V^\alpha(\rho)$ the radial confining potential of the cylinder in section α.

Radial confinement results in charge carriers occupying transverse subbands denoted by a pair of quantum numbers. We use the pair (n, l) in the N-section, and (p, l') in the S-sections, where n and p are the radial quantum numbers, and l, l' the orbital angular momentum quantum

numbers. The chemical potential in the cylinder is defined as the energy difference between the bottom edge of the lowest subband and the Fermi energy, and is denoted by μ (Figure 3.2). The numerical calculations were performed using the electron effective mass $m^* = 0.023m_e$ corresponding to InAs. Zeeman and spin-orbit effects on the critical current of the junction (studied in Ref. [144]) are not considered here, in order to focus on the effects of orbital angular momentum. In Section 3.7, we discuss the conditions under which either the orbital effect or the Zeeman + spin orbit effects could be more dominant.

In this paper, we do not write out an explicit form for $V^{\alpha}(\rho)$, and do not solve for the radial wavefunctions corresponding to the subbands (n, l) in any section of the cylinder. Instead, we use a shell conduction model for the N-section. This is appropriate for certain III-V nanowires (such as InAs or InN), where the charge carriers are typically confined near the surface due to a positive surface potential, forming a surface accumulation layer [146, 181]. Assuming a strong downward surface band bending ($\sim 100 - 200$ meV) [145], the radial position of the carriers in all subbands (n, l) is taken to be $R \lesssim R_0$. This greatly simplifies the calculation of the eigenvalues of H_θ (Eq. 3.1c). However, we emphasize that the qualitative results obtained here should not be limited to this shell conduction model, particularly since we find a weak dependence of the interference effect on R.

Superconductivity in the leads is described by the order parameter (pairing potential) $\Delta(\boldsymbol{r})$, which in the general case, must be calculated self-consistently. We use a simplified model in which Δ is constant, so that proximity effects such as the reduction of Δ near the S-N interfaces due to 'reverse' proximity are neglected. For $\rho < R_0$, there is a jump-like variation at the boundary of each section (Figure 3.1b):

$$\Delta(\boldsymbol{r}) = \begin{cases} \Delta_0 e^{i\chi_L}, & x < -L/2 \\ 0, & |x| < L/2 \\ \Delta_0 e^{i\chi_R}. & x > L/2 \end{cases} \tag{3.2}$$

Outside the radius of the cylinder, the order parameter is zero: $\Delta(\boldsymbol{r}) = 0$ when $\rho > R_0$. Here, Δ_0 is the superconducting energy gap value in the leads, and $\chi_{L(R)}$ is the phase of the superconducting condensate in the left (right) lead. The order parameter is zero in the N-section because of the lack of attractive electron-electron interactions (repulsive interactions are present in general, but neglected here.)

In Eq. 3.2, a spatially uniform Δ is assumed in the S-sections in all magnetic fields up to H_c. This is justified if the following two conditions hold: (i) the diameter of the cylinder is smaller than the superconducting coherence length in the S-section, $d < \xi_S$. The change in the phase of the order parameter around the circumference of the cylinder, $\delta\chi$, is constrained to integer multiples of 2π, because Δ has to be single valued (i.e. due to fluxoid quantization [152]).

When $d < \xi_S$, one can assume $\delta\chi = 0$, since ξ_S sets the length-scale for the spatial variations of the order parameter [41], so Δ must be uniform. The validity of the assumption $d < \xi_S$ in experimental devices is discussed in Section 3.7. (ii) The injected current in the SNS junction is much smaller than the critical current of the superconducting leads. Otherwise, the superfluid flow in the S-sections cannot be neglected, and a self-consistent determination of Δ is required, as performed in Ref. [182]. Here, we assume the critical current of the junction is bottle-necked in the N-section, which is reasonable given that the critical currents of nanowire junctions are typically small compared to those of the S leads.

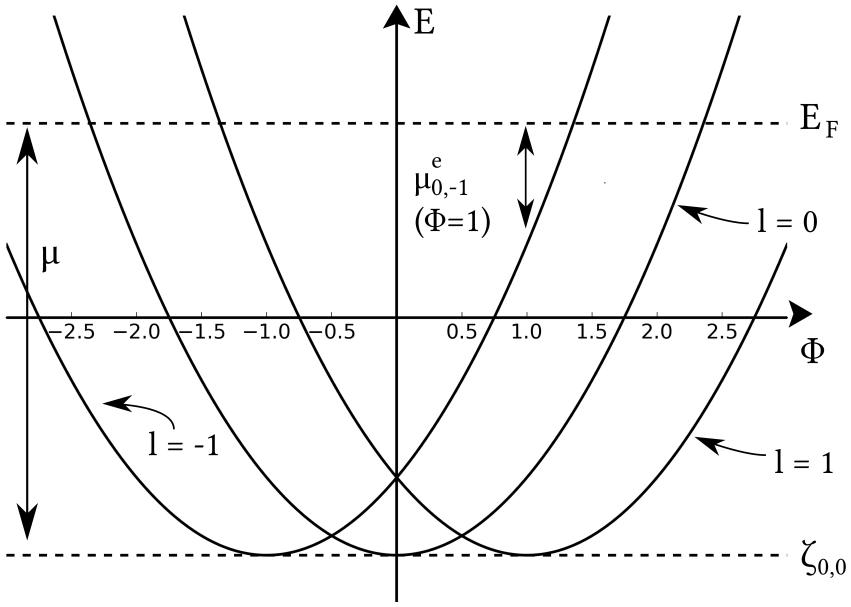

Figure 3.2: Subband energies for the electrons in the N-section (i.e. the eigenenergies of H_0 in Eq. 3.1 at $k = 0$) versus the normalized magnetic flux $\Phi = (\pi B_\parallel R^2)/(h/e)$. The $l = 0$ and $l = \pm 1$ subbands with $n = 0$ are shown. The energies are parabolic because of the $\frac{\hbar^2}{2m^* R^2}(l - \Phi)^2$ contribution to the energy by H_θ (see Eqs. 3.1c, 3.4a). The upper dashed line is the Fermi energy. The chemical potential μ is the Fermi energy measured from the bottom of the lowest subband, $\zeta_{0,0}$ (lower dashed line). We have assumed $\zeta_{0,\pm 1} = \zeta_{0,0}$, so the bottoms of the $n = 0$ subbands have the same energy. The effective chemical potential for electrons at flux Φ, $\mu^e_{n,l}(\Phi)$, is the difference between the subband energy and the Fermi energy at that flux. This is shown for the subband $(n, l) = (0, -1)$ at $\Phi = 1$. For the hole-like states (not shown), the subband energies (Eq. 3.4b) are inverted (mirrored) with respect to the $E = E_F$ line, and the l quantum number negated ($l \to -l$). The effective chemical potential for holes is given by $\mu^h_{n,l}(\Phi) = \mu^e_{n,-l}(\Phi)$.

3.4 Theory

We wish to calculate the current-phase relationship (CPR) of the junction in the presence of an axial magnetic field. First, the spectrum of discrete levels (Andreev bound states) in the junction is obtained. Next, the current from the discrete levels, as well the "continuum" levels with energy $|E| > \Delta_0$ is calculated. It is shown that energy eigenstates corresponding to these energy levels (both the bound states and the continuum states) follow the single-electron subband structure imposed by the Hamiltonian H_0 (Eq. 3.1). In particular, we show that the CPR is modified by the axial magnetic flux in a way that depends on the orbital angular momentum of the subbands. This leads to a form of Josephson interference when one or more subbands with orbital angular momentum are occupied.

3.4.1 Bogoliubov-de Gennes Equations

The wavefunctions of the elementary excitations of the SNS junction are identified as the solutions to the Bogoliubov-de Gennes [41] (BdG) equations:

$$\begin{pmatrix} H_0 & \Delta(\boldsymbol{r}) \\ \Delta^*(\boldsymbol{r}) & -H_0^* \end{pmatrix} \begin{pmatrix} u(\boldsymbol{r}) \\ v(\boldsymbol{r}) \end{pmatrix} = E \begin{pmatrix} u(\boldsymbol{r}) \\ v(\boldsymbol{r}) \end{pmatrix}, \tag{3.3}$$

where H_0 is given by Eq. 3.1, and $u(\boldsymbol{r})$ and $v(\boldsymbol{r})$ are particle- and hole-like wavefunctions. The asterisk (*) denotes complex conjugation.

The solution strategy for Eq. 3.3 starts with finding the solutions to H_0. Let us first consider the N-section. Given the simple forms of H_x and H_θ in Eq. 3.1, it is clear that the single-particle eigenfunctions are plane-waves in the x, θ directions of the form $e^{ikx}e^{il\theta}\phi_{n,l}(\rho)$. The linear momentum along the axis of the cylinder is given by $\hbar k$, and the radial eigenfunction in the subband (n, l) is given by $\phi_{n,l}(\rho)$. As discussed above, we use a shell conduction model for the N-section, so $\phi_{n,l}$ is not written out explicitly, but assumed to result in a radial position $R \lesssim R_0$ for the carriers. The most general solutions $u(\boldsymbol{r}), v(\boldsymbol{r})$ to Eq. 3.3 are expansions over these single-particle solutions [183, 184]. However, since $\Delta^*(\boldsymbol{r}) = 0$ in the N-section, (k, n, l) are good quantum numbers and the single particle energies are given by:

$$\begin{aligned} H_0 u(\boldsymbol{r}) = &\left\{\hbar^2 k^2/(2m^*) + \left[\hbar^2/(2m^* R^2)\right](l^2 + \Phi^2)\right. \\ &\left. -\varepsilon_l + \zeta_{n,l} - \mu\right\} u(\boldsymbol{r}), \end{aligned} \tag{3.4a}$$

$$\begin{aligned} -H_0^* v(\boldsymbol{r}) = &\left\{-\hbar^2 k^2/(2m^*) - \left[\hbar^2/(2m^* R^2)\right](l^2 + \Phi^2)\right. \\ &\left. -\varepsilon_l - \zeta_{n,l} + \mu\right\} v(\boldsymbol{r}). \end{aligned} \tag{3.4b}$$

Here, $\Phi = (\pi B_{\parallel} R^2)/(h/e)$ is the normalized magnetic flux enclosed by the charge carriers, $\varepsilon_l = \left[\hbar^2/(2m^* R^2)\right](2l\Phi)$, and $\zeta_{n,l}$ is the radial confinement energy associated with $\phi_{n,l}(\rho)$. The electron subband energies (i.e. the eigenvalues of u at $k = 0$) are plotted in Figure 3.2, and are parabolic in shape versus the magnetic flux. For the corresponding eigenvalues for v, the parabolas are inverted (mirrored with respect to the Fermi energy, E_F). This gives $v(\boldsymbol{r})$ its hole-like character: its group velocity $\boldsymbol{v}_g = \frac{1}{\hbar}\boldsymbol{\nabla}_{\boldsymbol{k}} E$ is opposite to its wave vector $\boldsymbol{k}$ (i.e. it is retroreflected — see Ref. [40]). Note, however, that for a given k, charge is transported in the same direction by the two wavefunctions, as the retroreflected hole has opposite charge to the electron. The eigenvalues associated with $u(\boldsymbol{r}), v(\boldsymbol{r})$ are not equal in magnitude, as the term ε_l has the same sign in both lines of Eq. 3.4. This follows because of the complex conjugation of the diagonal term on the second row of Eq. 3.3, and is a manifestation of the breaking of time-reversal symmetry in the presence of a magnetic field: the retroreflected particle sees the same magnetic field as the incident particle, rather than a time-reversed field $A_\theta \to -A_\theta$.

3.4.2 Andreev Bound States

Following the original work of Kulik [180] we calculate the spectrum of the bound states of the nanowire SNS junction, however, here we allow the solutions to carry finite orbital angular momentum.

Suppose there is a solution $\Psi(\boldsymbol{r}) = (u(\boldsymbol{r}), v(\boldsymbol{r}))^T$ to Eq. 3.3, with energy E within the gap, $|E| < \Delta_0$. Since we assume no FWVM or barriers at the S-N interface, the right- and left-moving solutions $\Psi^{\pm}$ can be separated [180]. We disallow superpositions of (n, l) subbands in the N-section. This is justified because: (i) we have assumed the ballistic regime, so no scattering-induced subband-mixing occurs, and (ii) the pairing potential, Eq. 3.2, is zero in the N-section, and so it does not mix the (n, l) states (see Ref. [184]).

In the S-sections, Cooper pairing generally mixes subbands with different radial quantum numbers p, but the orbital angular momentum number l remains a good quantum number [183]. The latter follows from the cylindrical symmetry of Eq. 3.3, which in turn follows from a cylindrically symmetric H_0 and a spatially uniform Δ. For a given quantum number l and energy E, the most generic single-particle wavefunction in the leads is given by $e^{il\theta}\sum_p \beta_{p,E} e^{ik_{p,E}x}\phi_{p,l} = e^{il\theta}Y_{l,E}(x,\rho)$. In each term of the sum, $k_{p,E}$ adjusts itself such that the energy of that term is E. For $|E| < \Delta_0$ considered here, $k_{p,E}$ also has an imaginary component, resulting in an exponential decay of the wavefunction inside the S-Section [40]. In general, there is significant freedom in the choice of the expansion coefficients $\beta_{p,E}$ which will allow matching of the radial wavefunctions in the N and S sections.

The wavefunctions $\Psi^{\pm}$ can be written as:

$$\Psi^{\pm}_{n,l,E} = \begin{cases} A^{\pm} e^{il\theta} e^{\pm i k^{e}_{n,l} x} \phi_{n,l}(\rho) \begin{pmatrix} 1 \\ 0 \end{pmatrix} + \\ B^{\pm} e^{il\theta} e^{\pm i k^{h}_{n,l} x} \phi_{n,l}(\rho) \begin{pmatrix} 0 \\ 1 \end{pmatrix}, & |x| < L/2 \\ C^{\pm} e^{il\theta} \psi^{R}_{l}(x,\rho) \begin{pmatrix} e^{i\chi_R} \\ \gamma^{\pm} \end{pmatrix}, & x > L/2 \\ D^{\pm} e^{il\theta} \psi^{L}_{l}(x,\rho) \begin{pmatrix} \gamma^{\pm} \\ e^{-i\chi_L} \end{pmatrix}. & x < -L/2 \end{cases} \tag{3.5}$$

The wavenumbers $k^{e}_{n,l}$ and $k^{h}_{n,l}$ represent the momenta of the electron-like and hole-like components in the N-section, respectively. $\gamma^{+} = \Delta_0 \left(E + i\sqrt{\Delta_0^2 - E^2} \right)^{-1}$ is the BCS coherence factor in the leads, and γ^{-} is its complex conjugate. $\psi^{L,(R)}_{l}$ are, in general, superpositions of the $Y_{l,E}$ functions with different E, due to the inter-subband mixing induced by Δ. Since there is no FWVM or barrier at the S-N interfaces, $\Psi^{\pm}$ has to be continuous at $|x| = L/2$. In order for this to be possible, we must have $\psi^{R}_{l}(L/2,\rho) = \psi^{L}_{l}(-L/2,\rho) = \phi_{n,l}(\rho)$. A solution can always be achieved by a correct choice of the expansion coefficients $\beta_{p,E}$, so the form given in Eq. 3.5 for $\Psi^{\pm}$ is valid.

We now concentrate on the N-section, and derive the quantization rules for the energies of the bound states. Asserting that each term of $\Psi^{\pm}$ in the N-section has energy E, the wavenumbers $k^{e}_{n,l}, k^{h}_{n,l}$ are obtained as a function of energy:

$$k^{e}_{n,l}(E) = \frac{\sqrt{2m^*}}{\hbar} \sqrt{\mu^{e}_{n,l} + E}, \tag{3.6a}$$

$$k^{h}_{n,l}(E) = \frac{\sqrt{2m^*}}{\hbar} \sqrt{\mu^{h}_{n,l} - E}, \tag{3.6b}$$

where we have defined an effective chemical potential for an electron-like (hole-like) particle in the subband (n,l) in the N-section $\mu^{e(h)}_{n,l} := \mu - \frac{\hbar^2}{2m^* R^2}(l \mp \Phi)^2 - \zeta_{n,l}$. The minus (plus) sign in the parentheses refers to the electron-like (hole-like) particle, and $\zeta_{n,l}$ is the radial confinement energy due to $\phi_{n,l}$. The effective chemical potential is the difference between the energy of the subband (n,l) and the Fermi energy at a given magnetic field (see Figure 3.2), and is a positive quantity for any subband that is occupied.

The energy quantization rules can be obtained [180] by finding a set of coefficients $\{A^{\pm}, \ldots, D^{\pm}\}$ that make the solution $\Psi^{\pm}$ of Eq. 3.5 continuous at $|x| = L/2$. This is only possible if the

following relation holds:

$$\gamma^2 e^{i(k^e_{n,l}-k^h_{n,l})L} e^{\mp i\chi} = 1, \tag{3.7}$$

where the junction phase $\chi = \chi_R - \chi_L$ enters with a minus sign when for Ψ^+, and a plus sign for Ψ^-. Note that the superscript $s = +, -$ denotes the right- and left-moving solutions, respectively. The complex phase of the right-hand side of Eq. 3.7 must equal $2m\pi$, with $m = 0, \pm1, \pm2$, etc. Since $k^e_{n,l}, k^h_{n,l}$ depend explicitly on the bound state energy E (Eq. 3.6), this results in a quantization rule for E, and yields the bound state spectrum. This procedure is carried out in Section 3.5 to numerically solve for E as a function of χ.

Quite generally, if $\Psi^s = (u, v)^T$ is an eigensolution of the BdG equation (Eq. 3.3) with energy E, then $\overline{\Psi}^s = (-v^*, u^*)^T$ is also an eigensolution[41] with energy $-E$. If Ψ^s is a right-moving solution, then $\overline{\Psi}^s$ is left-moving, and vice versa. Let $\bar{s}$ denote the conjugate of s. The wavefunctions $\overline{\Psi}^s$ and $\Psi^{\bar{s}}$ are degenerate at zero field, for all χ (Figure 3.3a). This degeneracy is lifted in the presence of the magnetic field, which induces a finite phase shift, as will be discussed below. The pair of solutions $(\Psi^+, \overline{\Psi}^+)$ are phase shifted *together* in one direction, while the opposite pair $(\Psi^-, \overline{\Psi}^-)$ are phase shifted in the *opposite* direction (Figure 3.3b).

3.4.3 Andreev Approximation

Deriving an analytical expression for the bound state spectrum by inserting Eq. 3.6 into Eq. 3.7 becomes intractable, because of the complicated dependence of $k^e_{n,l} - k^h_{n,l}$ on E. In order to gain insight into the behaviour of the bound states, we invoke below the well-known Andreev approximation [172, 173, 185], in which $|k^e_{n,l} - k^h_{n,l}|$ is considered a small quantity compared to $|k^e_{n,l}|$ and $|k^h_{n,l}|$. This approximation is widely used in the literature for a variety of situations [180, 186, 185, 187], but can be violated in some regimes of our SNS junction. In particular, when the subband energy is close to the Fermi energy, $k^e_{n,l}$ and $k^h_{n,l}$ become small and the assumption $|k^e_{n,l} - k^h_{n,l}| \ll |k^e_{n,l}|, |k^h_{n,l}|$ is not justified. Keeping these restrictions in mind, we now look at how the CPR of the junction is modified in the presence of the axial magnetic field.

The effective chemical potential for electron-like (hole-like) particles in the subband (n, l) in the N-section can be written $\mu^{e(h)}_{n,l} = \mu - \frac{\hbar^2}{2m^* R^2}(l^2 + \Phi^2) \pm \varepsilon_l - \zeta_{n,l}$, where $\varepsilon_l = \left[\hbar^2/(2m^* R^2)\right] \times (2l\Phi)$ enters with a plus sign for electron-like particles. It reflects the coupling of the orbital motion and the axial field. The Andreev approximation translates to the following condition: $E + \varepsilon_l \ll \mu^e, \mu^h$, i.e. the quasi-particle energy and the coupling to the field are small perturbations on the single-particle energies. Eq. 3.6a, 3.6b can be expanded in a Taylor series in the powers of $(E + \varepsilon_l)$. We calculate $k^e_{n,l} - k^h_{n,l}$ to first order:

$$k^e_{n,l} - k^h_{n,l} \simeq \frac{2}{\hbar} \frac{E + \varepsilon_l}{v_{n,l}}, \tag{3.8}$$

where $v_{n,l} = \sqrt{2\left(\mu - \frac{\hbar^2}{2m^*R^2}(l^2+\Phi^2) - \zeta_{n,l}\right)/m^*}$ is the velocity of a particle in the subband (n,l) traveling along the cylinder axis in the N-section.

By inserting $(k^e_{n,l} - k^h_{n,l})$ into Eq. 3.7 and equating the complex phase of the left hand side of Eq. 3.7 with $2m\pi$, where $m = 0, 1, 2$, etc., we obtain the following expression for the spectrum of bound states:

$$\left(\frac{L}{\xi^0_{n,l}}\right)\left(\frac{E^{\pm}_{n,l,m}}{\Delta_0}\right) - 2\arccos\left(\frac{E^{\pm}_{n,l,m}}{\Delta_0}\right) \mp \chi + \left(\frac{L}{\xi^0_{n,l}}\right)\left(\frac{\varepsilon_l}{\Delta_0}\right) = 2\pi m, \tag{3.9}$$

where $\xi^0_{n,l} = \hbar v_{n,l}/(2\Delta_0)$ is the healing length [186] for the subband (n,l), and the energy of the bound state depends on three quantum numbers n, l, m, and the junction phase difference χ. $E^+(E^-)$ refers to the eigenenergy of the right-moving (left-moving) solution. Note that the energy corresponding to $\overline{\Psi}^+$ is $-E^+$, for example.

In a short junction, $L \ll \xi^0_{n,l}$, Eq. 3.9 allows only one m value per solution, and there are four bound states ($\Psi^+, \overline{\Psi}^+, \Psi^-, \overline{\Psi}^-$) per subband (n,l). At zero field, there are two positive, and two negative solutions at any given χ (Figure 3.3a). For long junctions there are more than four bound state energies per subband, with different m numbers [186, 188, 189, 190, 191].

The bound state spectrum Eq. 3.9 gives, for the case of no magnetic field (ε_l = 0), a result similar to the well known Andreev levels of a ballistic SNS junction [180, 186], but with a different value of the healing length for each subband. An example is shown in Figure 3.3a for subband $(n,l) = (0,1)$ in a short junction with $L = 25$ nm $\ll \xi^0_{n,l} \sim 200$ nm. Figure 3.3b shows the energy-versus-phase curves of the bound levels at a finite flux, $\Phi = 2.5$. The curves are now phase shifted by an amount $\delta_{n,l} = \left(\frac{L}{\xi^0_{n,l}}\right)\left(\frac{\varepsilon_l}{\Delta_0}\right)$, where $\varepsilon_l = \left[\hbar^2/(2m^*R^2)\right](2l\Phi)$. That is, $E^{\pm}_{n,l,m}(\chi) \to E^{\pm}_{n,l,m}(\chi \mp \delta_{n,l})$.

3.4.4 Reduction to a Semiclassical Model

The phase shift $\delta_{n,l}$ can be understood semiclassically as the phase picked up by azimuthal travel around the circumference of the cylinder in the presence of the magnetic field. In this picture, for a subband (n,l) with $l \neq 0$, the particles (both electron- and hole-like) travel in a spiral (helical) path as they traverse the junction length L. In the shell-conduction model the spiral has radius R. The velocity along the axis is $v_{n,l}$, while the azimuthal velocity is $v_\theta(l) = \hbar l/(m^*R)$.

The semiclassical phase δ_{sc} is due to the coupling of v_θ and the vector potential $\boldsymbol{A} = (B_\parallel \rho/2)\hat{\boldsymbol{\theta}}$, and is calculated from the Ginzburg-Landau formula for the phase:

$$\delta_{sc} = (2e/\hbar) \int \boldsymbol{A} \cdot \mathrm{d}\boldsymbol{l} = (2e/\hbar) \int \boldsymbol{A} \cdot \boldsymbol{v} \mathrm{d}t, \tag{3.10}$$

where the differential element $\mathrm{d}\boldsymbol{l}$ is along the spiral path, $\boldsymbol{v} = v_{n,l}\hat{\boldsymbol{x}} + v_\theta \hat{\boldsymbol{\theta}}$ is the velocity, t is time, and the second integral is taken from $t = 0$ corresponding to the particle leaving one S-section, to $t = L/v_{n,l}$, when it arrives at the other S-section. The result is $\delta_{sc} = elLB_\parallel/(m^* v_{n,l})$, which equals $\delta_{n,l}$. This shows that when the Andreev approximation holds and there is shell conduction, the semiclassical result coincides with the quantum mechanical one. Note that in the expression for δ_{sc} there is no explicit dependence on R. The dependence of the phase shift on R comes only through $v_{n,l}$, and is a weak dependence within the Andreev approximation. More generally, we numerically calculate the energy spectra using Eq. 3.6 without the Andreev approximation and find similar phase shifts that are always proportional to the junction length L and to the angular momentum quantum number l.

3.4.5 Bound State and Continuum Currents

The current due to the Andreev bound states in the subband (n, l) at temperature T is calculated [190, 186, 192] from the formula

$$I_{n,l}(\chi) = \frac{e}{\hbar} \sum_{s,m} f(E^s_{n,l,m}) \frac{\mathrm{d}E^s_{n,l,m}(\chi)}{\mathrm{d}\chi}, \tag{3.11}$$

where $f(E^s_{n,l,m}) = 1/(\exp(E^s_{n,l,m}/(k_B T)) + 1)$ is the Fermi-Dirac occupation probability of a given energy level (k_B is the Boltzmann constant). Energies corresponding to both types of wavefunctions $\Psi^s_{n,l}$ and $\overline{\Psi}^s_{n,l}$ must be inserted into Eq. 3.11. The total bound state current is the sum of supercurrent amplitudes from all occupied subbands [193] ('open channels' in the language of Ref. [194]):

$$I_{\text{total}}(\chi) = \sum_{n,l} I_{n,l}(\chi). \tag{3.12}$$

The continuous spectrum of states with energies $|E| > \Delta_0$ also contributes to the junction current. A continuum level can be viewed as a "leaky" solution [186, 188] to the Andreev bound state problem described above, with a complex-valued eigenenergy $E = E_R + iE_I$, with $|E_R| > \Delta_0$. The leaky level follows the same subband structure as the Andreev bound states.

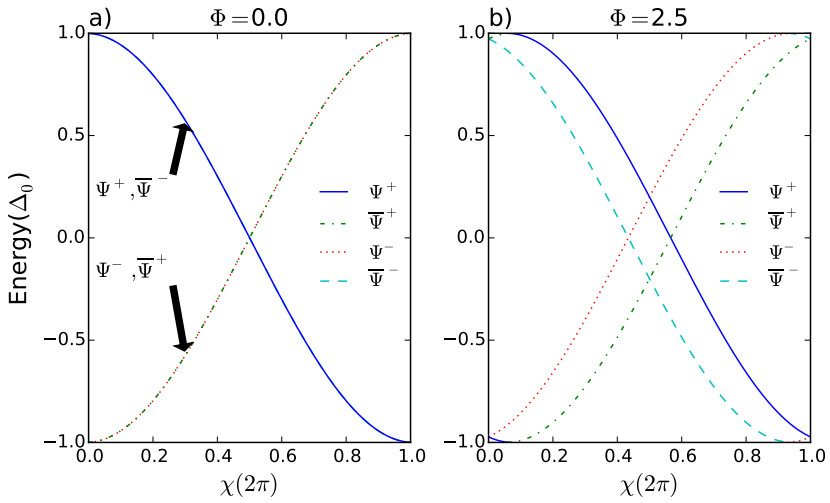

Figure 3.3: Eigenenergies of the Andreev bound states of a short ($L = 25$ nm $\ll \xi^0_{n,l} \sim 200$ nm), cylindrical SNS junction with no barriers at the S-N interfaces, vs. the superconducting phase difference χ of the leads. Two values of normalized magnetic flux, $\Phi = \pi R^2 B_{\parallel}/(h/e) = 0, 2.5$, are shown. We concentrate on one subband (n, l) with $n = 0$ and $l = 1$. (a) Zero magnetic field, $\Phi = 0$. The energies correspond to the four allowed wavefunctions (defined in the main text), and the states are pairwise degenerate for all χ. (b) $\Phi = 2.5$, where the degeneracies are lifted, and there is a phase shift with opposite directions for each pair of states. The phase shift is small because of the short length of the junction. The following parameters were used for both panels: $\mu = 200$ meV, $R = 30$ nm, $T = 100$ mK.

The imaginary component of energy results in a finite lifetime for the continuum level, reducing its contribution to the junction current, but for a long junction $L \gtrsim \xi^0_{n,l}$, this contribution is significant, and cannot be ignored [186].

The continuum current due to the subband (n, l), $J_{n,l}(\chi)$, is calculated using the transmission formalism [186, 191, 195]. We calculate the transmission coefficients for the electrical currents carried by electron-like and hole-like excitations incident on the S-N interfaces, resulting in leaky solutions in the N-section. The details of the calculation are given in Appendix 3.6. For the rest of this section the subscripts n, l are dropped for the sake of simplicity; it is implicitly assumed that all quantities pertain to the subband (n, l). The result for the continuum current

is:

$$J(\chi) = \frac{e}{h}\left(\int_{-\infty}^{-\Delta_0} + \int_{\Delta_0}^{\infty}\right)|u_0^2 - v_0^2|\left(\frac{1}{F^+(E,-\chi)}\right.$$
$$\left. - \frac{1}{F^-(E,-\chi)} - \frac{1}{F^+(E,+\chi)} + \frac{1}{F^-(E,+\chi)}\right) f(E)\mathrm{d}E, \tag{3.13}$$

where E is the real part of the energy of the continuum level and $f(E)$ is the Fermi-Dirac distribution at temperature T, and u_0, v_0 are real-valued BCS coherence factors:

$$u_0^2 = \frac{1}{2}\left(1 + \sqrt{E^2 - \Delta_0^2}/E\right), \tag{3.14a}$$

$$v_0^2 = \frac{1}{2}\left(1 - \sqrt{E^2 - \Delta_0^2}/E\right). \tag{3.14b}$$

The functions $F^{\pm}(E,\chi)$ depend on energy, through the wavenumbers k^e and k^h (Eq. 3.6) as well as the coherence factors u_0, v_0: $F^{\pm}(E,\chi) = u_0^4 + v_0^4 - 2u_0^2v_0^2\cos\left[(k^e(\pm E) - k^h(\pm E))L + \chi\right]$. Equation 3.13 can be intuitively understood in terms of the leaky solutions to the BdG equation: the terms containing F^+ pertain to the contribution of leaky states of type $\Psi^s_{n,l,m}$, while those containing F^- pertain to $\overline{\Psi}^s_{n,l,m}$. The junction phase χ enters with a plus (minus) sign for left (right) moving solutions. At zero magnetic field, $F^+(E,\chi) = F^-(E,-\chi)$. This is analogous to the degeneracy of Ψ^+, $\overline{\Psi}^-$ in Figure 3.3a. Therefore, Eq. 3.13 reduces to Eq. 17 in Ref. [186], up to an application of the Andreev approximation.

In the presence of the magnetic field, the terms $(k^e - k^h)L$ shift the functions $F^{\pm}(E,\chi)$ in phase relative to the zero-field case, in the same manner as the phase shifts found previously for the bound states. Employing the Andreev approximation (Eq. 3.8), we obtain

$$F^{\pm}(E,\chi) = u_0^4 + v_0^4 - 2u_0^2v_0^2\cos\left[\left(\frac{E \pm \varepsilon_l}{\Delta_0}\right)\left(\frac{L}{\xi^0}\right) + \chi\right], \tag{3.15}$$

which is shifted in phase with respect to the zero-field case. Explicitly for the subband (n,l) we have $F^{\pm}_{n,l}(E,\chi) \to F^{\pm}_{n,l}(E,\chi \pm \delta_{n,l})$, with the phase shift $\delta_{n,l}$ defined previously.

The total continuum current of the junction is

$$J_{\text{total}}(\chi) = \sum_{n,l} J_{n,l}(\chi). \tag{3.16}$$

The critical current I_c of the junction is defined as the maximum of total bound state + continuum currents with respect to χ:

$$I_c = \max_{\chi\in[0,2\pi)}\left[I_{\text{total}}(\chi) + J_{\text{total}}(\chi)\right]. \tag{3.17}$$

3.5 Numerical Results

We numerically solve the continuum and bound state currents of an SNS junction at finite magnetic fields, using the shell conduction approximation with the shell at a radius $R = 30$ nm. Temperature is set to $T = 100$ mK in all calculations. From this point on, only (n, l) subbands with $n = 0$ are assumed to be occupied in the N-section. The Andreev approximation is not used in calculating the CPR. The critical current of the junction is calculated from Eq. 3.17, and its behaviour versus axial magnetic flux $\Phi = \pi R^2 B_{\parallel}/(h/e)$ is studied. Note that our assumption of no barriers at the S-N interfaces also implies full Andreev reflection.

3.5.1 Single Subband

As an illuminating example we study a 500 nm long junction with a chemical potential of $\mu = 8.5$ meV. This value for μ is chosen because it allows $l = -1, 0, 1$ subbands to be occupied at $\Phi = 0$; at $\Phi = 1$ the $|l| = 1$ subbands depopulate[1]. In this section we concentrate on the CPR obtained for one subband, namely $l = 1$, and discuss how the coupling of the finite angular momentum with the axial field modifies the subband CPR.

Since the junction length is greater than the healing length of the populated subbands ($L = 500$ nm $\gtrsim \xi^0_{n,l}$), the long junction limit applies. Many bound states are present in the junction (~ 12). In Figure 3.4a we show the bound state current $I_{n,l}$, continuum current $J_{n,l}$, and their sum, for the subband $(n, l) = (0, 1)$ at zero magnetic field. As expected of a long junction [188, 186], $I_{n,l}$ and $J_{n,l}$ are of the same order of magnitude, and the CPR is triangular in shape. An additional group of 4 bound states ($\Psi^+, \Psi^-, \overline{\Psi}^+, \overline{\Psi}^-$) appear in the junction at $\chi = 0.05$, and exit at $\chi = 0.95$, giving rise to discontinuities in $I_{n,l}$, $J_{n,l}$. However, the total subband current $I_{n,l} + J_{n,l}$ is always a smooth function of χ. It is maximal near $\chi = \pi$, (exactly at $\chi = \pi$ at zero temperature) regardless of the junction length [186]. Note that the continuum current is zero at $\chi = \pi$.

In Figure 3.4b we show the subband current $I_{n,l} + J_{n,l}$ as a function of the magnetic flux. As the flux is increased from zero, two discontinuities develop in the subband current (shown for $\Phi = 0.10$). The bound state current is modified as the eigenenergies corresponding to states $(\Psi^+, \overline{\Psi}^+)$ are shifted in phase in the opposite direction to those of states $(\Psi^-, \overline{\Psi}^-)$, similarly to Figure 3.3b. An equivalent process happens for the continuum current, as explained in Eq. 3.15. As a result, the subband current $I_{n,l} + J_{n,l}$ also shows two discontinuities, and is no longer necessarily maximal near $\chi = \pi$.

[1] The effective chemical potentials follow $\mu^e_{n,l}(\Phi) = \mu^h_{n,-l}(\Phi)$, see Figure 3.2. In this example, as Φ approaches 1, $\mu^e_{0,1}, \mu^h_{0,-1}$ go to zero, at which point Andreev quasiparticles can no longer be supported by the $|l| = 1$ subbands.

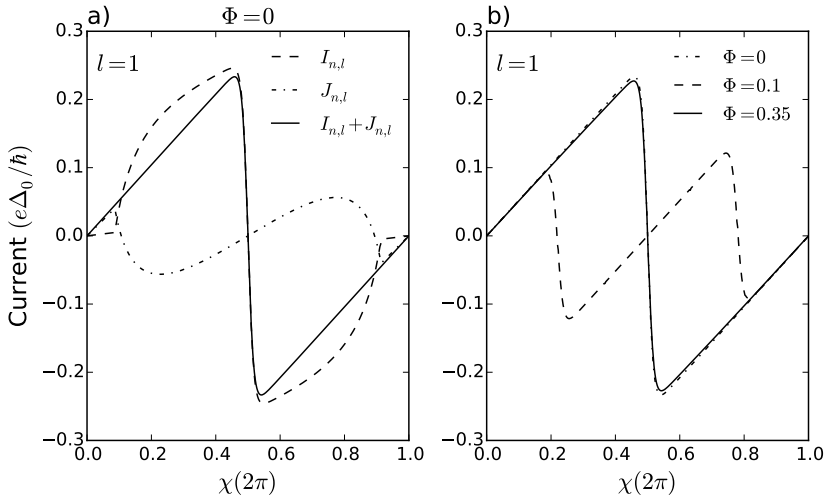

Figure 3.4: (a) Bound state current $I_{n,l}$, continuum current $J_{n,l}$, and the sum $I_{n,l} + J_{n,l}$ for the subband $(n, l) = (0, 1)$ vs. the superconducting phase χ at zero magnetic field, $\Phi = 0$. Since the junction is long, $L = 500$ nm $\gtrsim \xi^0_{n,l}$, the CPR is triangular. The kinks in $I_{n,l}, J_{n,l}$ at $\chi = 0.05, 0.95$ are due to Andreev bound states crossing the gap edge into the continuum levels, but the total subband current is a smooth function of χ. (b) Total subband current $I_{n,l} + J_{n,l}$ vs. the superconducting phase as a function of the normalized axial magnetic flux Φ. At zero flux the maximal value occurs near $\chi = \pi$. At finite flux, the bound state and continuum currents are phase shifted. For $\Phi = 0.1$, two discontinuities can be seen in $I_{n,l} + J_{n,l}$ because of the phase shifts, and the maximal value no longer occurs near $\chi = \pi$. At $\Phi = 0.35$, the phase shifts amount to 2π and the zero-field curve is recovered. The maximal current at this flux is slightly smaller than the zero field case, due to a decrease in the average momentum of the Andreev quasiparticles with increasing flux. The following parameters were used in both panels: $L = 500$ nm, $\mu = 8.5$ meV, $R = 30$ nm, $T = 100$ mK.

The amounts of the phase shifts in $I_{n,l}$ and $J_{n,l}$ depend on the quantity $(k^e_{n,l} - k^h_{n,l})L$. The wavenumbers $k^e_{n,l}, k^h_{n,l}$ are subband parameters defined in Eq. 3.6, and the length L is device dependent. Therefore, the fluxes at which phase shifts equal integer multiples of 2π need not occur at integer multiples of $\Phi_0 = (h/e)$ or $\Phi_0/2$; they can occur at any value of Φ. An example is shown in Figure 3.4b for $\Phi = 0.35$, where the phase shifts equal 2π and the CPR recovers its shape at $\Phi = 0$. Notice, however, that the maximal value of the subband current at $\Phi = 0.35$ is smaller than at $\Phi = 0$. This can be intuitively understood as follows: as the flux increases, the effective wavenumbers of the electrons and holes change according to Eq. 3.6. It can be

seen that the average momentum of the electron-hole pair and therefore the healing length $\xi^0_{n,l}$ are always smaller for higher fluxes. Since the magnitude of Josephson current in a long junction scales approximately linearly [196] with $\xi^0_{n,l}/L$, it is suppressed at higher fluxes. This suppression is stronger near the depopulation point of a given subband, where the average momentum decreases significantly.

3.5.2 Interference Due to a Few Subbands

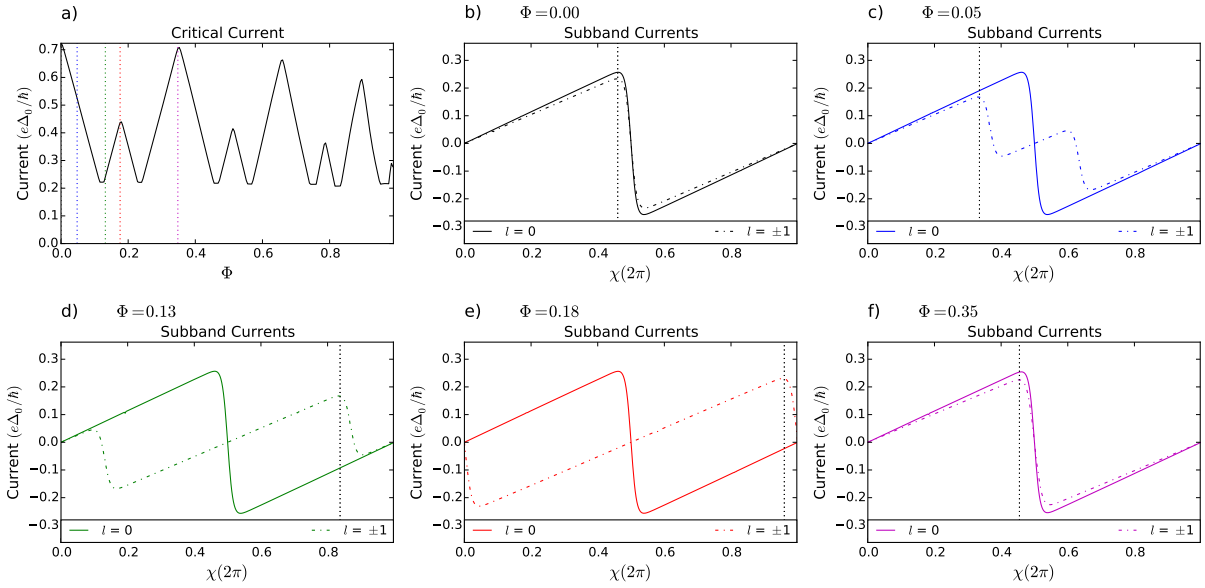

Figure 3.5: (a) Critical current I_c vs. normalized axial magnetic flux Φ of a 500 nm junction with $\mu = 8.5$ meV. The subbands with $l = -1, 0, 1$ are occupied and contribute to I_c. Oscillation of I_c with Φ is observed, which is not periodic in Φ: the positions of the peaks get closer together as Φ is increased. At flux points indicated with vertical dotted lines, individual subband currents are plotted in panels b-f vs. the superconducting phase χ. (b-f) CPR for $l = 0$ (solid lines) and $l = \pm 1$ (dash-dotted lines) subbands. The current due to the $l = 1$ subband is equal to that of the $l = -1$ subband for all χ and Φ values. Here, the contribution due to only one of the two subbands is shown for clarity. The vertical dotted lines indicate the phase χ at which the critical current occurs. Note the difference in the y-axis scale between panel a and the other panels. The following parameters were used in all plots: $L = 500$ nm, $\mu = 8.5$ meV, $R = 30$ nm, $T = 100$ mK.

In order to elucidate the mechanism of the Josephson interference between subbands, we show in Figure 3.5a the critical current versus axial flux of the junction studied in Section 3.5.1. The length $L = 500$ nm is chosen because it allows for a relatively large amount of phase pickup, since the phase pickup is proportional to the length of the junction ($(k^e_{n,l} - k^h_{n,l})L$ in Eq. 3.7). Hence, several oscillations of the critical current occur prior to the depopulation of the $|l| = 1$ subbands at $\Phi = 1$.

The supercurrent of each subband is shown versus the phase difference χ in Figure 3.5 panels b-f, at particular values of the magnetic flux. The $l = 1$ subband current equals that of $l = -1$ at all fluxes. At zero flux the current of each subband is maximal near $\chi = \pi$ (exactly $\chi = \pi$ for zero temperature), as discussed in Section 3.5.1. This can be clearly seen in panel b. The total current of the junction is the sum of the contributions from the $l = -1, 0, 1$ subbands, and is therefore roughly three times the contribution of each. The dotted vertical lines show the phase at which the critical current occurs.

As the flux is increased, the CRP of the $|l| = 1$ subbands are modified, similarly to Figure 3.4a. The critical current of the junction decreases, since the $|l| = 0, 1$ subbands no longer interfere constructively (panel c). At $\Phi = 0.13$ the maximal current switches from a phase $\chi < \pi$ to $\chi > \pi$, as shown in panel d. This is a feature of the triangular CPR. The critical current increases until $\Phi = 0.18$ (panel e), at which point the junction current is maximal near $\chi = 2\pi$. We call this a peak a secondary peak as it occurs roughly in the middle of the main period of oscillations (see discussion below on periodicity), when the magnetic phase pickup of the $|l| = 1$ subbands equals roughly π. The magnitude of this peak is roughly two thirds the total current as zero field, as the $l = \pm 1$ subbands contribute maximally, and the $l = 0$ subband current is close to zero. The process reverses itself for $\Phi > 0.18$, until at $\Phi = 0.35$ the phase pickup of the $|l| = 1$ subbands equals 2π and all subbands interfere constructively again (panel f). We refer to the peak at $\Phi = 0.35$ a primary peak. Other primary peaks occur at $\Phi = 0.66, 0.89$. As in Figure 3.4, the contribution of the $|l| = 1$ subbands decrease as Φ is increased, because the decrease in the average quasiparticle momentum. This is the mechanism behind the slow decay of the magnitude of the primary peaks as flux increases.

Aperiodicity – The $|l| = 0, 1$ subbands interfere constructively when the magnetic phase pickup of the $|l| = 1$ subbands equals an integer multiple of 2π. This corresponds to the main period of the critical current oscillations with Φ, which we estimate below. In other words, we want to find Φ such that

$$(k^e_{n,l} - k^h_{n,l})L\big|_{\Phi} - (k^e_{n,l} - k^h_{n,l})L\big|_{\Phi=0} = 2j\pi, \tag{3.18}$$

for integer j. The wavenumbers $k^e_{n,l}, k^h_{n,l}$ are defined in Eq. 3.6. For the general case this is not easy to do analytically, as $k^e_{n,l}, k^h_{n,l}$ themselves depend on the flux through the effective

chemical potentials $\mu^{e,h}_{n,l}$. However, we can get an estimate of the expected period by invoking the Andreev approximation (Eq. 3.8), and assuming the effective Fermi velocities do not depend on the flux, so can be evaluated at some fixed Φ, e.g. $\Phi = 0$. These are reasonable assumptions when the flux is much smaller than the depopulation point of a given subband (e.g., $\Phi = 1$ for $|l| = 1$ subbands in the example of Figure 3.5). The result for the position of the first primary peak Φ_1 is:

$$\Phi_1 = \pi v_{n,l} m^* R^2/(\hbar l L), \tag{3.19}$$

where $v_{n,l}$ is defined below Eq. 3.8. For the example of Figure 3.5, this evaluates to $\Phi_1 = 0.36$, deviating from the numerically calculated value by only 3%. However, we see that the numerical positions of the next primary peaks at 0.66 and 0.89 cannot be accurately approximated as integer multiples of Φ_1: the period becomes shorter as Φ is increased. This is because the field dependence of $v_{n,l}$ cannot be ignored at higher values of Φ, and the Andreev approximation breaks down. Intuitively, the effective Fermi velocity is noticeably lower at higher fields, resulting in more time spent in the junction by the Andreev pair and more phase pickup, therefore a smaller period for I_c oscillations. Consequently, even in the simple case of a few subbands, the oscillations of I_c versus Φ are not strictly periodic.

3.5.3 Interference Due to Many Subbands

A higher chemical potential results in the occupation of a greater number of angular momentum subbands. The rich interplay between the different l-subbands results in a complex pattern of the oscillation of I_c with Φ. Assume subbands with $|l|$ up to $\tilde{l}$ are occupied. Each $|l|$ subband's supercurrent oscillates with a flux dependent 'period' approximated by Eq. 3.19, which depends on the subband velocity $v_{n,l}$, and is therefore generally anharmonic with other subbands. Typically, a peak in I_c as a function of Φ occurs under one of two circumstances: (i) when some (at least two) of the subbands with different $|l|$ values interfere constructively, or (ii) when the critical current occurs near $\chi = 2\pi$, a secondary peak is formed as described in Figure 3.5. There are $\mathcal{C}(\tilde{l}, 2)$ choices for pairs of constructively interfering subbands, where $\mathcal{C}(n, k)$ is the combination function (a.k.a. the binomial coefficient function). As each $|l|$ subband's oscillations can be anharmonic with those of all other subbands, it follows that there are $\mathcal{C}(\tilde{l}, 2)$ different flux-dependant 'periods' in the I_c oscillations due to condition (i), plus another $\tilde{l}$ due to condition (ii). The I_c curves can therefore display complex, aperiodic structures.

In Figure 3.6a we plot an example of an I_c versus Φ curve for a junction with the same parameters as that of Figure 3.5, except the chemical potential is raised from 8.5 meV to 20 meV. At zero flux, subbands up to $|l| = 3$ are occupied. The $|l| = 3$ states depopulate at $\Phi = 0.2$, and the $|l| = 2$ states at $\Phi = 1.2$. As an example of configurations that can give rise to a peak in I_c,

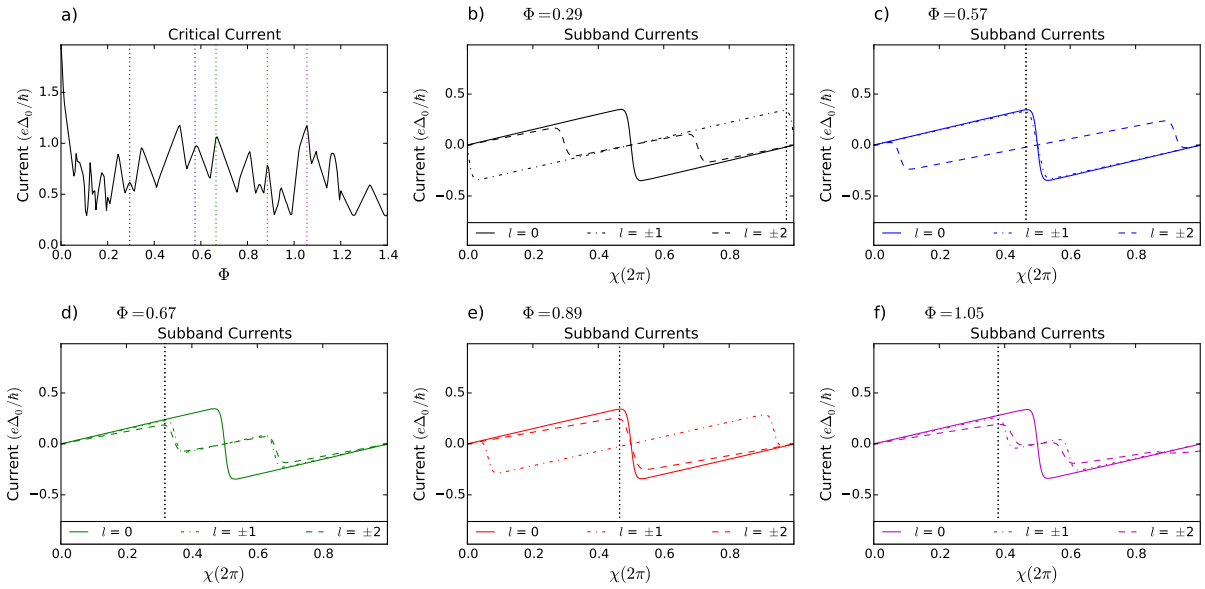

Figure 3.6: (a) Critical current I_c vs. normalized axial magnetic flux Φ of a 500 nm junction with $\mu = 20$ meV. The subbands with $|l| \leq 3$ are occupied at zero flux. The subbands with $|l| = 3, 2$ depopulate at $\Phi = 0.2, 1.2$, respectively. An aperiodic oscillation of I_c vs. Φ is observed. At flux points indicated with vertical dotted lines, individual subband currents are plotted in panels b-f vs. the superconducting phase χ. (b-f) CPR for individual subbands, displaying different configurations which can lead to a peak in I_c vs. Φ. The vertical dotted lines indicate the phase χ at which the critical current occurs. Note the difference in the y-axis scale between panel a and the other panels. The following parameters were used in all panels: $L = 500$ nm, $\mu = 20$ meV, $R = 30$ nm, $T = 100$ mK.

subband CPRs are shown in Figure 3.6 panels b-f, for 5 peaks indicated in panel a with vertical dotted lines. The peak at $\Phi = 0.29$ (panel b) satisfies condition (ii), while the other examples are due to constructive interference of two subbands, i.e. condition (i): subbands with $|l| = 0, 1$ at $\Phi = 0.57$ (panel c), $|l| = 0, 2$ at $\Phi = 0.89$ (panel e), and $|l| = 1, 2$ at $\Phi = 0.67$ and $\Phi = 1.05$ (panels d,f).

3.5.4 Effect of Junction Length

We now discuss the effect of the junction length L on the pattern of I_c oscillations. The left column in Figure 3.7 (panels a-d) shows the numerically obtained I_c versus Φ for a junction with $\mu = 8.5$ meV, as L is varied. All other junction parameters are the same as in Figure 3.5. The critical current is normalized to its value at zero magnetic flux. Two processes affect the behaviour of I_c: (i) the depopulation of the $|l| = 1$ subbands at $\Phi = 1$, shown by vertical dotted lines in panels a-d, and (ii) the Josephson interference effect described above. The first of these processes results in step-like discontinuities in I_c at $\Phi = 1.0$, a drop to roughly one-third of the zero-field I_c value as the $l = -1, 1$ subbands depopulate. Since the $l = 0$ subband does not couple to the axial flux, I_c is almost constant above $\Phi = 1$. The slow decay of the primary peak heights below $\Phi = 1$, and of I_c above $\Phi = 1$, are both due to the decreasing average momentum at higher fluxes, as discussed in Section 3.5.1. For a short junction with $L = 25$ nm (panel a) and for $\Phi < 1.0$, the phase shifts in the CPR of the $|l| = 1$ subband are small (the phase shifts are dependent on $(k^e_{n,l} - k^h_{n,l})L$), but become more significant close to $\Phi = 1$, where the axial velocities of the quasiparticles are smaller and the time of flight across the junction longer. This results in the observed decrease in I_c before the step-like discontinuity. As L is increased to 50 nm, the value of this phase shift increases and modulation due to interference starts to emerge. For $L = 200$ nm (Figure 3.7 panel c), the first primary peak occurs at $\Phi = 0.79$, and for $L = 500$ nm (panel d) at $\Phi = 0.35$. The decrease by a factor of 2.26 in the position of the first primary peak is approximately equal (within 11%) to the reciprocal ratio of lengths L, as expected from the estimate in Eq. 3.19.

The right column of Figure 3.7 (panels e-h) shows the I_c versus Φ curves for a junction with $\mu = 20$ meV. The subbands with $|l| = 3, 2, 1$ depopulate at $\Phi = 0.2, 1.2, 2.2$ respectively (vertical dotted lines in panels e-h), resulting in step-like discontinuities in I_c at those flux values. Similarly to above, the behaviour of I_c is dominated by this effect for a 25 nm junction (panel e), but as L is increased the Josephson interference becomes visible (panels f-h). Note that between the flux values $\Phi = 1.2$ and $\Phi = 2.2$ the I_c curves in the right column of Figure 3.7 are qualitatively similar to their counterparts in the left column, because similarly to the $\mu = 8.5$ meV case, subbands with $|l| \leq 1$ are occupied within this flux window. Note that for $\mu = 20$ meV, $I_c(0)$ is much larger than for the $\mu = 8.5$ meV case; the oscillation amplitude appears to be smaller in panels (e-h) only because the relative contribution of each subband to the total current is smaller when there are more subbands occupied.

In summary, for a short junction, the depopulation of subbands is more visible than the Josephson interference effect. However, as the junction length is increased, the interference effect becomes apparent. The periods of oscillation decrease slightly as flux is increased. For a junction with a low chemical potential (only a few transverse subbands occupied, e.g. an SNS

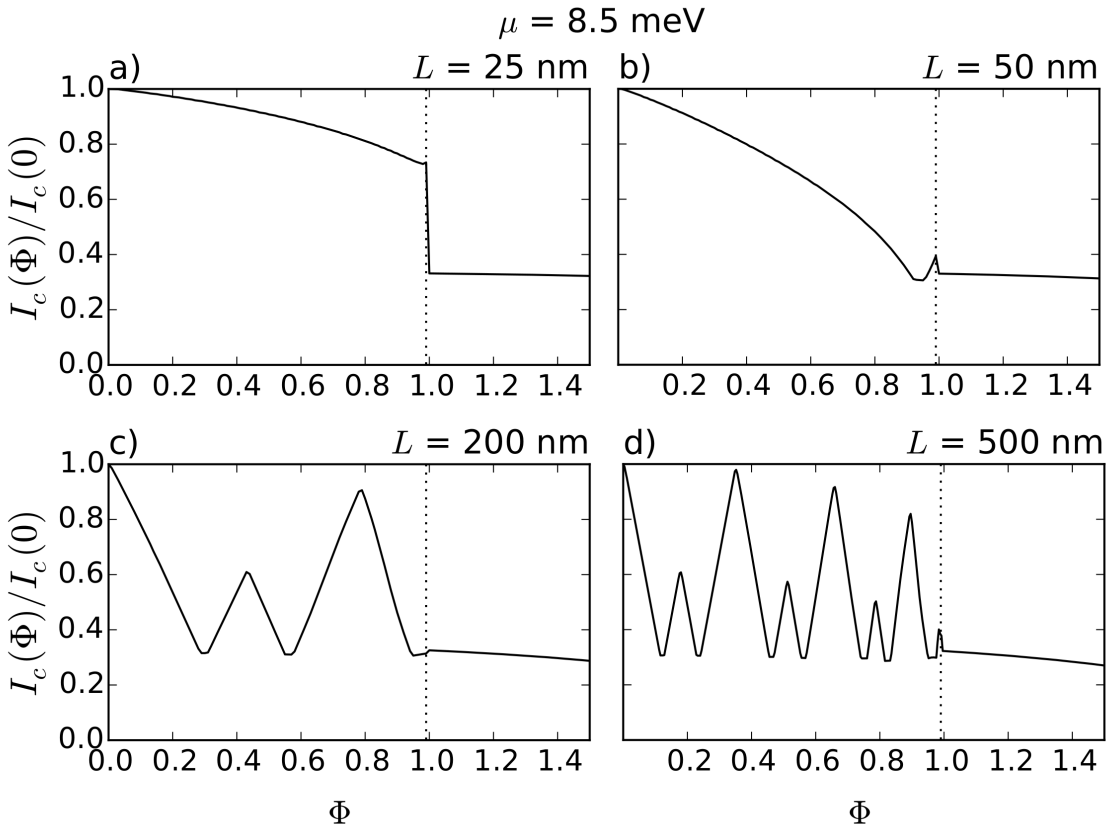

Figure 3.7: *(N.b. two-page figure & caption.)* Normalized critical current of the junction versus the normalized magnetic flux $\Phi = (\pi B_{\parallel} R^2)/(h/e)$, for $\mu = 8.5$ meV (panels a-d) and several values of the junction length L. The vertical line at $\Phi = 1.0$ indicates the depopulation of the $|l| = 1$ subbands.

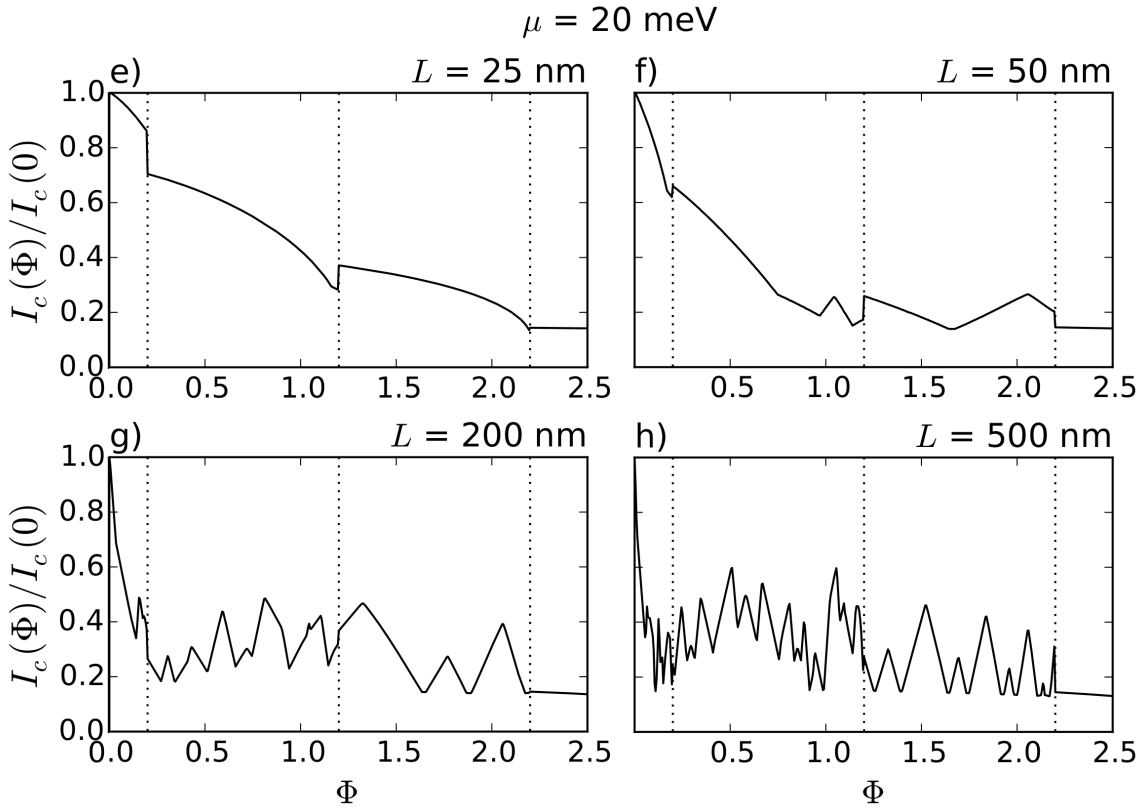

Figure 3.7: *(Cont. from prev. page.)* (Panels e-h) Same as the previous page, but with $\mu = 20$ meV. The vertical lines at $\Phi = 0.2, 1.2, 2.2$ indicate the depopulation of the $|l| = 3, 2, 1$ subbands, respectively. The occupation of more subbands results in more complex behaviour vs Φ. The following parameters were used for all panels: $R = 30$ nm, $T = 100$ mK.

point-contact [197, 198, 182]), the pattern of I_c modulation is simpler and the period longer than the case of a high chemical potential (many transverse subbands occupied). A long, low-μ junction is optimal for experimental observation of this Josephson interference effect.

3.6 Transmission Formalism for the Continuum Current

The electrical current transmission amplitudes for the continuum states are obtained by matching the solutions of the BdG equation (Eq. 3.3) in the three regions of the cylinder ($x < -L/2$, $|x| < L/2$, $x > L/2$) while assuming an incident "source term" on the S-N interface at $x = -L/2$ with energy $|E| > \Delta_0$. These transmission amplitudes are then used to calculate the continuum current. This section follows appendices A,B in Ref. [186], but is generalized to account for finite magnetic field and orbital angular momenta.

Hereafter all quantities are presumed to pertain to one subband, (n, l), unless explicitly stated otherwise. We drop the subscripts n, l for simplicity. Consider the quasiparticle excitation spectrum of the BdG Hamiltonian. In the left S-section ($x < -L/2$), the electron-like solutions with energy $E > \Delta_0 > 0$ are given by

$$\Psi^e = \begin{pmatrix} u(x,\rho,\theta) \\ v(x,\rho,\theta) \end{pmatrix} = \begin{pmatrix} u_0 e^{i\chi_L} \\ v_0 \end{pmatrix} \psi^{L,e}(x,\rho) e^{il\theta}, \tag{3.20}$$

and the hole-like solutions by

$$\Psi^h = \begin{pmatrix} u(x,\rho,\theta) \\ v(x,\rho,\theta) \end{pmatrix} = \begin{pmatrix} v_0 e^{i\chi_L} \\ u_0 \end{pmatrix} \psi^{L,h}(x,\rho) e^{il\theta}. \tag{3.21}$$

Here, u_0, v_0 are given in Eq. 3.14, and $\psi^{L,e}, \psi^{L,h}$ have the form given above Eq. 3.5, with different expansion coefficients β_p for the electron- and hole-like wavefunctions. We do not reproduce these coefficients here as they do not enter the calculation. Let the source term Ψ^e be incident from the left on the S-N interface at $x = -L/2$. The wavefunctions generated due to this source term are grouped into two categories (depending on which S-section they belong to), with coefficients B, C, following Bagwell's notation [186]. The first group pertains to the left S-section. The electron-like source term incident on the S-N interface is

$$\begin{pmatrix} u_0 e^{i\chi_L} \\ v_0 \end{pmatrix} \psi^{L,e}(x + \frac{L}{2}, \rho) e^{il\theta} \quad (x < -\frac{L}{2}). \tag{3.22}$$

The Andreev reflected hole-like wavefunction is

$$\left(B - \frac{v_0}{u_0}\right) \begin{pmatrix} v_0 e^{i\chi_L} \\ u_0 \end{pmatrix} \psi^{L,h}(x + \frac{L}{2}, \rho) e^{il\theta} \quad (x < -\frac{L}{2}). \tag{3.23}$$

For the electrons in the normal region, the wavefunction is

$$\left(B - \tfrac{v_0}{u_0} + \tfrac{u_0}{v_0}\right) \begin{pmatrix} v_0 e^{i\chi_L} \\ 0 \end{pmatrix} e^{i(k^e(E))\times(x+\frac{L}{2})} \quad \phi(\rho)e^{il\theta} \quad (|x| < \tfrac{L}{2}), \tag{3.24}$$

and for the holes

$$B \begin{pmatrix} 0 \\ u_0 \end{pmatrix} e^{i(k^{h(E)})\times(x+\frac{L}{2})}\phi(\rho)e^{il\theta} \quad (|x| < \frac{L}{2}). \tag{3.25}$$

Here, ϕ is radial part of the wavefunction in the N-section, defined below Eq. 3.3. The explicit energy dependence of the wavenumbers k^e, k^h is given in Eq. 3.6.

The transmitted wavefunction into the right contact is

$$C \begin{pmatrix} u_0 e^{i\chi_R} \\ v_0 \end{pmatrix} \psi^{L,e}(x - \frac{L}{2}, \rho)e^{il\theta} \quad (x > \frac{L}{2}). \tag{3.26}$$

This is supported by electrons in the N-section with the wavefunction

$$C \begin{pmatrix} u_0 e^{i\chi_R} \\ 0 \end{pmatrix} e^{i(k^{e(E)})\times(x-\frac{L}{2})}\phi(\rho)e^{il\theta} \quad (|x| < \frac{L}{2}), \tag{3.27}$$

and holes

$$C \begin{pmatrix} 0 \\ v_0 \end{pmatrix} e^{i(k^{h(E)})\times(x-\frac{L}{2})}\phi(\rho)e^{il\theta} \quad (|x| < \frac{L}{2}). \tag{3.28}$$

The normal reflection processes have not been considered, as no FWVM or barriers are assumed at the S-N interfaces.

The coefficients B, C can be found by connecting together Eqs. 3.24, 3.27, and Eqs. 3.25, 3.28 at any point $x = a$ within the N-section or at the S-N interfaces. We use $a = -L/2$. The result is

$$C = \frac{1 - \frac{v_0^2}{u_0^2}}{e^{i\chi}e^{-ik^e(E)L} - \frac{v_0^2}{u_0^2}e^{-ik^h(E)L}}, \tag{3.29}$$

where $\chi = \chi_R - \chi_L$. By definition, C is the transmission amplitude from the left contact to the right contact due to an electron-like incident source term with energy $E > 0$. The corresponding transmission coefficient $T^e_{L\to R}(E, \chi)$ is

$$T^e_{L\to R}(E, \chi) = |C|^2 = \frac{|u_0^2 - v_0^2|^2}{F^+(E, -\chi)}, \tag{3.30}$$

with the function F^+ given below Eq. 3.14.

The coefficient for transmission from right to left (due to a left-moving source) can be found by making the transformation $\chi \to -\chi$ in the above formula. That is,

$$T^e_{R\to L}(E,\chi) = \frac{|u_0^2 - v_0^2|^2}{F^+(E,\chi)}. \tag{3.31}$$

Repeating these calculations for an electron-like source term with energy $E < -\Delta_0 < 0$ shows that Eqs. 3.30, 3.31 give the correct transmission coefficients for the negative energy case as well.

Similar to the case of the bound states, if $(u,v)^T$ is a solution at energy E, then $(-v^*,u^*)^T$ gives a solution at energy $-E$. Both types of solutions must be taken into account when calculating the total transmission coefficients. Consider the (left-moving) source term $\overline{\Psi^e}$ obtained by applying the above transformation on Eq. 3.20:

$$\overline{\Psi^e} = \begin{pmatrix} -v_0 \\ u_0 e^{-i\chi_L} \end{pmatrix} \left(\psi^{L,e}(x,\rho)\right)^* e^{-il\theta}. \tag{3.32}$$

All relevant wavefunctions due to this source term (i.e. the Andreev reflected in the S-section, electron- and hole-like in the N-section, and transmitted to the other S-section wavefunctions) can be constructed by applying the transformation $(u,v)^T \to (-v^*,u^*0)^T$ to Eqs. 3.23 – 3.28. Crucially, the resulting wavefunctions contain the wavenumbers $k^e(E), k^h(E)$, while having energy $-E$. Repeating the above calculation, the transmission coefficient $\overline{T^e_{R\to L}}$ due to the source term $\overline{\Psi^e}$ is found:

$$\overline{T^e_{R\to L}}(-E,\chi) = \frac{|u_0^2 - v_0^2|^2}{F^+(E,-\chi)}, \tag{3.33}$$

or equivalently,

$$\overline{T^e_{L\to R}}(E,\chi) = \frac{|u_0^2 - v_0^2|^2}{F^-(E,\chi)}, \tag{3.34}$$

$$\overline{T^e_{R\to L}}(E,\chi) = \frac{|u_0^2 - v_0^2|^2}{F^-(E,-\chi)}, \tag{3.35}$$

with $F^-(E,\chi) := F^+(-E,\chi)$.

The current J^e due to electron-like excitation source terms is calculated [186] using the formula

$$\begin{aligned} J^e(\chi) = &\frac{e}{h}\left(\int_{-\infty}^{-\Delta_0} + \int_{\Delta_0}^{\infty}\right) \frac{1}{|u_0^2 - v_0^2|} \\ &\times \left[T^e_{L\to R}(E,\chi) - T^e_{R\to L}(E,\chi) + \overline{T^e_{L\to R}}(E,\chi)\right. \\ &\left. -\overline{T^e_{R\to L}}(E,\chi)\right] f(E)\mathrm{d}E. \end{aligned} \tag{3.36}$$

Here, $f(E)$ is the Fermi-Dirac distribution at temperature T. It can be seen that Eq. 3.36 is equal to Eq. 3.13. In deriving Eq. 3.36 we used only the electrical current transmitted due to electron-like source terms. Repeating the above calculations for hole-like source terms results in a current J^h which is equal to J^e. Naively, one might then think the total continuum current obtained is too large by a factor of two. However, note that the density of excitations (electron- plus hole-like) in the S-section is twice as large as the density of states in the N-section. Consequently, the subband's continuum current is

$$J(\chi) = \frac{1}{2}\left(J^e(\chi) + J^h(\chi)\right), \tag{3.37}$$

and we recover Eq. 3.13. This disparity in the density of states in the S- and N-sections was noted in Ref. [186], see Eq. B8 in that paper.

Equation 3.36 is used in Section 3.5 to numerically calculate the continuum current J due to each subband. For a junction much shorter than the subband's healing length, $L \ll \xi^0$, the bound state current I is much larger than J. When $L \gtrsim \xi^0$, $I_{n,l}$ and $J_{n,l}$ are of the same order of magnitude, and we obtain a triangular CPR. At finite magnetic fields, phase shifts appear in both I and J as described in Section 3.5.1, but the CPR retains its triangular shape.

Notice that at zero magnetic field, we have $k^e(-E) = k^h(E)$, so J simplifies and can be written as

$$\begin{aligned} J(\chi) =& \frac{2e}{h}\left(\int_{-\infty}^{-\Delta_0} + \int_{\Delta_0}^{\infty}\right)\frac{1}{|u_0^2 - v_0^2|} \\ &\times \left[T^e_{L\to R}(E,\chi) - T^e_{R\to L}(E,\chi)\right] f(E)\mathrm{d}E. \end{aligned} \tag{3.38}$$

The extra factor of 2 here is usually attributed to the spin degree of freedom of the electrons/holes. By including both types of coefficients $T^e, \overline{T^e}$ in Eq. 3.36 we are taking into account this degree of freedom. This can be further elucidated by noting that in the spinful version of this problem, the particle-hole symmetry is manifested as two (Nambu-spinor type) solutions $\mathbf{\Psi}$ and $(\sigma_y\tau_y\mathbf{\Psi})^*$ with opposite energies, spins, and coherence factors (the Pauli matrices σ, τ act on the spin and particle-hole manifolds, respectively). That is, $(u, v)^T$ and $(-v^*, u^*)^T$ generalize to states of opposite spin, and the spin degree of freedom is correctly accounted for by considering both types of solutions.

3.7 Discussion

We have described the theory of a previously unstudied form of the Josephson interference effect that can occur in nanoscale SNS junctions due to the coupling of the orbital angular

momentum of transverse electronic subbands with an axial magnetic flux. We found in Section 3.5.4 the regimes in which this interference effect dominates the I_c vs. Φ characteristics of the junction. An idealized model of an SNS junction was used, with several simplifying assumptions, in order to elucidate the mechanism of the effect. We discuss generalizations of the model below, in particular those modifications that may be necessary to directly model experimental devices.

FWVM and barriers at the interfaces — No barriers were assumed at the S-N interfaces, and FWVM was neglected. The effective mass for electrons m^* was assumed to be uniform throughout the junction. These assumptions allowed Kulik's method of matching the wavefunctions at the interfaces to be used to calculate the bound state and the continuum currents. We stress that the basic mechanism of the orbital interference effect, i.e. the modification of the N-section wavenumbers in the presence of the axial field, is independent of FWVM and interfacial barriers. Therefore, the main features of the I_c oscillations (periodicity, amplitude) should only be modified by FWVM and barriers as higher order corrections. The exact shape of the junction CPR and the I_c vs. Φ curves, however, depends on the details of the interfaces. Accurate modeling of experiments must take this into account, based on the material and interfacial properties specific to a particular experimental implementation.

As was discovered in studies of Andreev reflection at Nb-InAs interfaces [189, 193], FWVM modifies the CPR of Superconductor/Semiconductor/Superconductor junctions. In the general case, where FWVM and barriers are included at the S-N interfaces, the bound state energies and the continuum current must be calculated from the transmission matrix formalism [195], in which the transmission matrix includes a normal (specular) reflection coefficient as well as an Andreev (retro) reflection coefficient. The values of these coefficients depend on the material details of the junction. The CPRs of junctions with FWVM [195] and barriers [198, 199, 186] have been previously calculated (numerically) at zero magnetic field. The effect of both mechanisms is to make the CPR more closely resemble a sinusoidal curve. Since the N-section wavenumbers have the same coupling to the axial field shown in Eq. 3.6 regardless of FWVM or barriers, we expect the phase-shift mechanism leading to interference to remain. However, the shape of the oscillations in I_c should appear more sinusoidal, following the shape of the CPR.

Normal reflection of the quasiparticle wavefunctions from the S-N barriers will result in a higher order correction to the periodicity of the interference effect. This is due to an increased average phase pickup as the quasiparticle spends more time in the junction. On the other hand, this should also lead to some randomization of the phase. The former would lead to shorter period oscillations (i.e the effect occurs at lower fields), while the latter will partially smear out the interference effect, reducing the amplitude of oscillations. Similar effects are expected from elastic backscattering occurring in the N-section in non-ballistic junctions. These considerations are beyond the scope of this paper, and are left to future work.

General form of Δ — A spatially uniform pairing potential was assumed in the S-sections at all magnetic fields (Eq. 3.2). This was justified by assuming cylindrical S-sections, and restricting the cylinder diameter to be smaller than the superconducting coherence length in the S-sections. However, experimental fabrication of nanoscale SNS junctions is usually done by evaporating or sputtering metallic (e.g. Al or Nb) thin film contacts onto a semiconducting nanowire. In this case, the geometry of the S-section is not cylindrical but Ω shaped. The lack of cylindrical symmetry necessitates, in principle, a 3-dimensional numerical calculation of $\Delta(\boldsymbol{r})$ using self-consistent methods. However, as long as the N-section can be assumed to be cylindrically symmetric, our model should closely approximate the experimental situation. This is because the interference effect depends mainly on the eigensolutions in the N-section, particularly the orbital angular momentum states and their coupling to the flux. The details of the eigensolutions in the S-section do not play a direct role, other than asserting the form of the wavefunction ansatz (Eq. 3.5) is valid. Similarly, the axial field can induce a non-uniformity in Δ. If the thickness of the metallic film becomes larger than the S-section coherence length, fluxoid quantization can result in a θ-dependent phase for Δ in the presence of the field. Inserting a θ-dependent Δ in the BdG equations (Eq. 3.3) will affect the bound state solutions, likely requiring a 3-dimensional numerical solution. However, we still expect the interference effect to depend mainly on the states in the N-section.

General radial wavefunctions — The shell-conduction model was used in order to simplify computations, and to help gain intuitive insight into the problem; it is not strictly necessary for the main arguments of the paper. Indeed, we found in Section 3.4.4 that the semiclassical phase shift δ_{sc} is only weakly dependent on the radius R, so the interference effect should be present for general radial wavefunctions. In future work, the radial wavefunctions in the N-section, $\phi_{n,l}$, and the corresponding single particle energies in the presence of the field will be numerically calculated, yielding the appropriate wavenumbers $k^e_{n,l}, k^h_{n,l}$ for electron- and hole-like solutions. We expect the term $(k^e_{n,l} - k^h_{n,l})L$ appearing in Eqs. 3.7, 3.13 will continue to result phase shifts similar to those seen in the present model.

Zeeman and Spin-orbit effects — In order to study the orbital Josephson interference effect in isolation, Zeeman and spin-orbit effects were neglected in our analysis. It is useful to ask under what circumstances should the orbital effects or the Zeeman + spin-orbit effects dominate? The critical current of a short, InSb SNS junction, including spin-orbit and Zeeman effects, was studied in Ref.[144]. The bound state energies were solved, and a phase-shift was observed in the energy-versus-phase curves due to the Zeeman effect. Similar to the mechanism described in our analysis, the Zeeman effect modifies the N-section wavenumbers, but based on the spin state rather than the orbital state. This results in an oscillation of I_c, with the first minimum occurring at $B_{\text{min}} = \hbar v_F/(g\mu_B L)$, where v_F is the Fermi velocity, g is the effective Landé g-factor, and μ_B is the Bohr magneton. For a 200 nm InSb junction with $|g| = 50$, this evaluates

to $B_{\text{min}} = 0.5$ T for v_F corresponding to $\mu = 10$ meV, but for other materials B_{min} is typically much larger. Considering InAs with a moderately large $|g| = 10$ gives $B_{\text{min}} = 2.1$ T (again for $L = 200$ nm and $\mu = 10$ meV). Since we used the effective mass for InAs in our calculations, we can directly compare with the results of Figure 3.7c for a 200 nm long junction. The orbital effect should dominate in this case, as the first minimum of I_c is at a flux corresponding to $B_{\parallel} \simeq 0.4$ T. The consequence of the inclusion of the spin-orbit coupling is a smaller correction: the so called anomalous Josephson effect, in which the current is no longer an even function of the superconducting phase: $I(\chi) \neq I(-\chi)$.

We conclude that for InSb devices, the Zeeman effect could easily dominate. This is especially true if either of the following conditions hold: (i) If only $l = 0$ subbands are occupied (i.e. small chemical potential), or (ii) in a perpendicular field, where the Zeeman effect is present but the orbital effect is suppressed. On the other hand, for most low spin-orbit semiconductor materials, $g \sim 2$ and we would expect the orbital subband effect to dominate in an axial field experiment, unless only $l = 0$ subbands are occupied.

Magnetic depairing — Field-induced depairing suppresses both superconductivity in the S-sections and proximity superconductivity in the N-Section [140, 139]. For a type-II superconductor with a relatively large gap such as Nb, we can assume depairing in the N-section should dominate. For diffusive junctions in the narrow junction limit, the Usadel equations predict a monotonic Gaussian decay $I_c \propto \exp(-\alpha\Phi^2/\Phi_0^2)$ for a perpendicular magnetic flux Φ through the N-Section [143], where $\alpha \approx 0.24$ is a numerical constant. A similar effect should apply to the axial field case, except with a slower magnetic field decay due to a smaller cross-sectional area (smaller flux). This is expected to produce a monotonic decay envelope superimposed on the critical current oscillations, and should be taken into account when modeling experimental data.

Summary — The idealized model studied here serves to demonstrate a novel form of Josephson interference due to orbital angular momentum states, with the unusual property of flux-aperiodic oscillations. Extensions to the model discussed above, most importantly FWVM and barriers at the S-N interfaces, will be useful for describing experimental implementations.

Chapter 4

Nb/InAs Nanowire Proximity Junctions from Josephson to Quantum Dot Regimes

4.1 Introduction

In this chapter we explore the second generation of nanowire Josephson devices which were fabricated using a much improved recipe compared to the first generation. The details of this fabrication recipe can be found in Appendix A. This resulted in an improvement in the Nb/InAs interface transparency t; values as large as 0.7 were observed. The electronic phase coherence length at low temperatures exceeds the channel length, and almost all devices in this fabrication batch show signatures of proximity superconductivity in some form; mostly as Andreev Bound state (ABS) associated with spontaneous quantum dots in the channel of the junction. Roughly a quarter of the devices are estimated to show a large supercurrent ~ 100 nA. The field effect mobility was found to be a good predictor of whether a particular device will show a large supercurrent: if the elastic scattering length derived from the field effect mobility is at least $\sim \frac{1}{3}$ times as long as the channel length or longer, then electrical measurements reveal the device to be in the Josephson regime, characterized by a dissipationless current; otherwise, the device is in the quantum dot regime, characterized by ABS resonances interplaying with a Coulomb diamond (see Section 4.3.3) structure.

4.1.1 Background

As discussed in Chapter 1, Andreev reflection at an interface between a superconductor and a normal metal (or semiconductor) leads to a number of surprising transport phenomena, in-

cluding a subharmonic gap structure due to multiple Andreev reflection (MAR) [134], Andreev Bound States (ABS) [180, 200], and supercurrent in superconductor-normal-superconductor (SNS) junctions [132, 135]. At low temperature, the normal section length that can support a supercurrent is limited by the phase coherence length of conduction electrons in that section, and in semiconductors this can far exceed the superconducting coherence length that characterizes the superconductor. While planar SNS junctions are well studied [153] and have revealed interesting phenomena such as Fraunhofer interference in a magnetic field [164], there are fewer studies on semiconductor nanowire-based SNS junctions. The latter are especially relevant in light of recent advances in the search for Majorana fermions, zero-energy quasiparticles at the boundaries of one-dimensional topological superconductors [32, 63]. There are several reported observations of signatures of Majorana fermions based on proposals for their detection in semiconducting nanowires contacted with superconductors [47, 85, 76, 78, 77]. The semiconductor must have a large spin-orbit coupling and make high transparency contacts with a superconductor, properties shared by InAs and InSb nanowires. While Al/InAs junctions are relatively well studied [201, 47, 202], Nb/InAs is less well characterized, but potentially advantageous due to a significantly larger superconducting gap Δ and that Nb is a type II superconductor, with an upper critical field $H_{c2} \sim 2.8$ T, allowing superconductivity in the device to be studied up to that magnetic field. Given that nanowire junctions are typically in the diffusive transport regime, a key question relevant to Majorana and other research is how (static) disorder in the nanowire is manifested in quantum transport experiments on SNS devices, and one method by which disorder (specifically, elastic scattering) can be quantified is via field effect mobility.

4.1.2 Field Effect Mobility and Distict Transport Regimes

Here, we report on proximity effect Josephson junctions made with InAs nanowires contacted by Nb leads. The junctions have channel lengths $L \sim 200$ nm, shorter than the estimated electronic phase coherence length $\xi \sim 250 - 350$ nm at low temperature, but longer than the estimated elastic scattering length by a factor of $3 - 5$. Data is presented for 5 different devices (d1–d5) falling within two distinctive regimes of quantum transport: devices with higher electron mobilities $\mu \sim 18,000$ cm^2/(V.s) are characterized by the observation of a dissipationless current ('Josephson regime'), whereas devices with lower mobilities $\mu \lesssim 10,000$ cm^2/(V.s) typically show signatures of spontaneous, unintentional quantum dots ('quantum dot regime') and signatures of induced superconductivity in the form of Andreev Bound States (ABS).

In the Josephson regime, the diffusive nature of the nanowire transport is manifested by a critical current that is modulated as the nanowire chemical potential is varied, closely following the normal state conductance fluctuations, but with enhanced sensitivity. Transmission

coefficients in the OTBK model [134] are found to be in the range $\sim 0.4 - 0.7$, indicating sufficiently good contact transparencies to observe Andreev physics. The junction phase dynamics are typically overdamped. The supercurrent versus axial magnetic field data shows modulations (reminiscent of those seen in Chapter 2) to fields > 2 T, and a combination of Orbital Josephson interference and spin-orbit + Zeeman effects may best describe their behaviour.

In devices with more disorder in the potential landscape, the quantum dot (QD) regime is observed and reveals resonances associated with ABS up to temperatures ~ 2 K. Unlike previously reported observations [201, 202, 80, 203, 129, 204, 205, 206, 207, 200, 208], the gate dependence of the ABS resonances does not appear to depend strongly on whether the QD is in an even- or odd-electron state. In order to explain this, we adapt an Anderson-type mode [209] originally developed for a phase-biased S-QD-S configuration to our experiment, which behaves as a current-biased S-N-QD-N-S configuration. The model qualitatively explains how the observed patterns of ABS resonances depend on a competition between the strength of the coupling to superconductivity and the dot addition energy E_{add}. The presence of ABS associated with either spontaneous or engineered QDs could be useful as energy filters in transport spectroscopy of zero modes.

4.1.3 Structure of this Chapter

In Section 4.2, we discuss fabrication methods and basic device characteristics. Section 4.3 presents the low temperature transport results in the Josephson and QD regimes, and introduces a model for the ABS associated with QDs. In Section 4.4, we discuss these results in the context of related observations in the literature, and with regard to the relevance of these types of devices in exploring Majorana fermion physics. Conclusions are given in Section 4.5.

4.2 Experiment

The devices d1–d5 reported on here are based on a single batch of undoped InAs nanowires grown in a gas-source molecular beam epitaxy system, starting from a gold nanoparticle. The diameter of the selected nanowires is in the range $40 - 65$ nm. Details of the nanowire growth can be found in Refs. [210, 211]. Devices d3 and d5 were on the same chip; otherwise each device is representative of a distinct fabrication run. Thirty-six devices were measured in total; all of the devices not reported on explicitly here were measured at a temperature of 1.5 K and showed characteristics similar to the ones reported. While none of these devices show a supercurrent at 1.5 K, we estimate from the minimum resistances that $\sim 1/4$ of the devices would show a supercurrent in the range of $10 - 100$ nA at dilution refrigerator temperatures.

For devices d1, d3 and d5, an 8 nm thick Al_2O_3 shell was deposited via atomic layer deposition onto the nanowires on their growth substrate, covering all facets of the nanowires. Our previous studies have found [212] that the desirable transport characteristics of these nanowires — such as mobility, low gate hysteresis, stability at low temperature, etc. — can be maintained with an optimized process of chemical surface passivation (using octadecanethiol [213, 214, 215]) followed by a conformal Al_2O_3 shell deposition. These coated nanowires, as well as bare nanowires, are moved to n++ Si / 300 nm SiO_2 device substrates via dry deposition. Before nanowire deposition, preparatory fabrication steps are performed, such as placing Ti/Au bonding pads and alignment markers. Other steps varied across the devices studied. Device d2 has a set of five evenly spaced bottom gates in the channel region, covered by a 20 nm SiN_x dielectric layer. Device d4 is an entrenched nanowire, where reactive ion etching was used to etch a ~ 60 nm wide and deep trench in SiO_2. A nanowire which (randomly) fell into this trench after mechanical deposition was identified via SEM (this occurs for roughly 5% of all the deposited nanowires.) The n++ Si substrate serves as a global backgate for all devices except d2. Superconducting contacts are defined using electron beam lithography on a bilayer PMMA resist of thickness ~ 500 nm. Following a short $5 - 12$ s HF etch to remove the Al_2O_3 shell and/or the native oxide of InAs, the device substrate is quickly moved to the deposition chamber. In-situ Ar ion milling (rf reverse sputtering) is performed at Ar pressures listed in table 4.1 using an rf power 50 W for a duration of ~ 10 minutes, followed by deposition of Nb or Ti/Nb contacts via dc magnetron sputtering. Table 4.1 summarizes the contacting recipes for the 5 devices, as well as other junction properties. After lift-off of the contacts, transport measurements are carried out at low temperature in one of two cryostats: a dilution refrigerator with a base lattice temperature $T_{\rm L} = 25$ mK (for all Josephson and some QD devices), and a pumped ^{4}He system with base $T_{\rm L} = 1.5$ K (for QD devices). The electron temperatures are ~ 100 mK and 1.5 K, respectively. Electrical measurements are made by applying a dc bias voltage (or current) using a custom high-resolution source, and the dc voltage and current responses of the device measured with low-noise preamplifiers.

Table 4.1 reports the field effect mobilities μ obtained from transconductance measurements at $T \simeq 50$ K via the analysis given in Ref. [210]. The capacitance between the nanowire and the global backgate is estimated using a COMSOL model. The model shows the effect of the metallic leads of the short channel junction is to screen the electric field of the gate, reducing the effective capacitance by a factor $4 - 5$ for channel lengths $L \sim 200$ nm. Uncertainty in this screening factor is the main source of uncertainty in the values of μ reported in table 4.1.

The field effect mobility μ can predict whether a particular device will exhibit a large supercurrent (i.e. the Josephson regime) at base temperature. Most devices display $\mu \leq 10^4$ $\mathrm{cm}^2/(\mathrm{V.s})$, corresponding to an elastic mean free path $l_e \lesssim 40$ nm, and show signatures of unintentional quantum dots forming inside the nanowire channel (i.e. the QD regime). Such

	Nanowire type	P_{Ar} (Pa)	Contact Recipe	Gate Layout	L (nm)	μ $m^2/(V.s)$	Device regime
d1	Al_2O_3/InAs	0.2	Ti/Nb (2 nm/80 nm)	Global BG	170 nm	1.8 ± 0.3	Josephson
d2	InAs	0.6	Nb (50 nm)	5 local gates	200 nm	1.6 ± 0.3	Josephson
d3	Al_2O_3/InAs	0.6	Ti/Nb (2 nm/80 nm)	Global BG	170 nm	0.8 ± 0.2	QD
d4	InAs	1.3	Ti/Nb (2 nm/50 nm)	Global BG	200 nm	0.6 ± 0.2	QD
d5	Al_2O_3/InAs	0.6	Ti/Nb (2 nm/80 nm)	Global BG	170 nm	0.9 ± 0.2	QD

Table 4.1: Basic device characteristics. P_{Ar} is the Ar ion milling pressure prior to contact deposition. L is the channel length after lift-off of contacts, typically ~ 30 nm shorter than the channel length written on PMMA from the lithography stage. The field-effect mobility μ (measured at ~ 50 K) can serve as a predictor as to whether a junction will be in the Josephson or the QD regime, with $\mu \lesssim 1.0$ $m^2/(V.s)$ typical of the QD regime.

devices have not been observed to sustain a supercurrent larger than 2 nA at $T_L = 25$ mK. However, devices such as d1 and d2 with $\mu \gtrsim 1.5 \times 10^4$ $cm^2/(V.s)$, i.e. $l_e \gtrsim 60$ nm, typically do not show Coulomb diamonds (see Section 4.3.3) in the low temperature I-V data. Given channel lengths $L = 170 - 200$ nm, these devices are in the diffusive regime, but a lack of Coulomb blockade allows for resistances as low as 3 kΩ at $V_g \simeq 10$ V. These Josephson regime junctions carry supercurrents up to ~ 100 nA at $T_L = 25$ mK. We expect that optimizing the InAs surface preparation recipe prior to the sputtering of the Nb contacts and improving the Nb/InAs contact transparency should increase the likelihood for a device to exhibit Josephson behavior. No signatures of proximity superconductivity were observed in devices fabricated without Ar ion milling. Lower Ar ion milling pressure (such as for d1) has been found to correlate with reduced Nb/InAs contact resistance; however, one must also consider the natural variation between different nanowires when interpreting this observation, since a total sample size of ~ 10 devices per fabricated chip is relatively small. Even for devices with high Nb/InAs contact transparency, it is the potential landscape in the nanowire channel that plays a dominant role in determining which regime of quantum transport is observed. The salient features of these two regimes are presented in the next section.

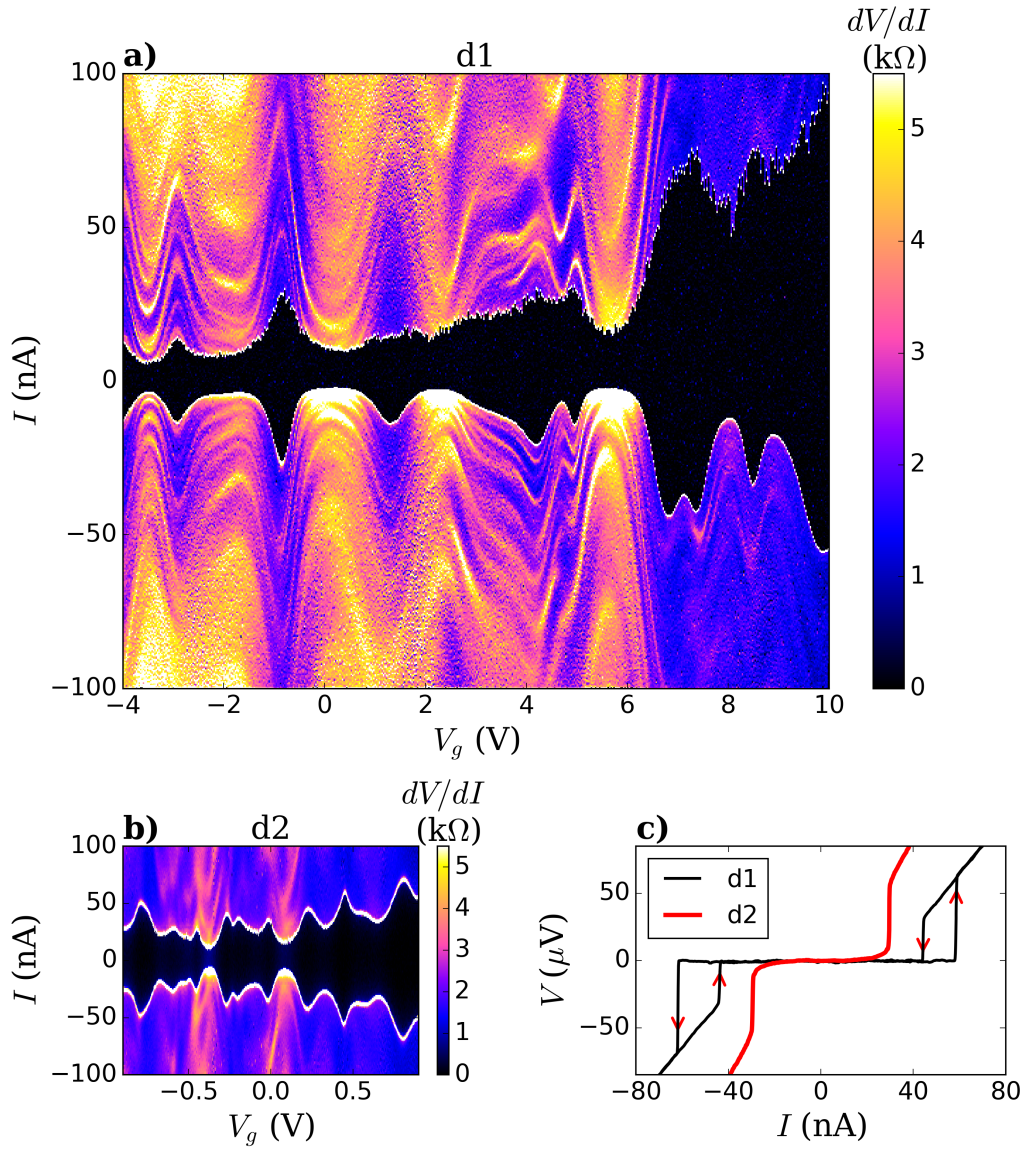

Figure 4.1: *(N.b. two-page figure & caption.)* Josephson regime devices d1 and d2. (a,b) Differential resistance dV/dI versus bias current I and gate voltage V_g for d1 and d2, respectively. The supercurrent magnitude is modulated by the gate voltage. (c) Typical I-V traces for d1 (black) and d2 (blue/dark grey). The residual resistance observed for d2, compared to sharp normal to dissipationless transitions for d1, suggest that the Nb/InAs interface may be of higher quality in d1.

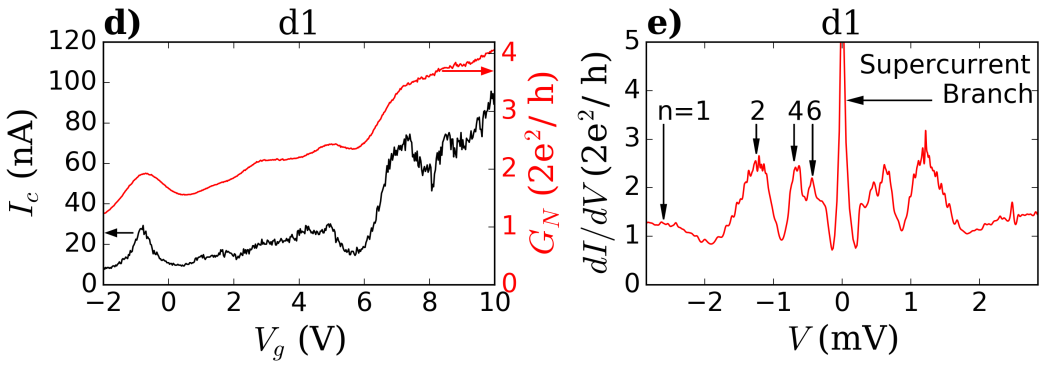

Figure 4.1: *(Cont. from prev. page.)* (d) A strong correlation is observed between the critical current I_c and the normal state resistance G_N versus gate voltage V_g (device d1). (e) Multiple Andreev reflection (MAR) signatures of order n are observed in d1 as peaks in dI/dV, indicated by arrows. Here, $V_g = 0.9$ V. The Josephson junction is phase-coherent across the channel. Similar data is observed for d2 (not shown). For all panels, data is measured at $T_{\mathrm{L}} = 25$ mK, except G_N, which is measured at 8 K.

4.3 Results

4.3.1 Josephson Regime

We first focus on devices d1 and d2 that are representative of the Josephson regime. Figure 4.1a shows the numerically calculated differential resistance dV/dI of d1 versus gate voltage and bias current at a base lattice temperature $T_{\mathrm{L}} = 25$ mK and zero magnetic field. As the bias current I is swept from negative to positive values, the dc voltage response V of the device is recorded. A dissipationless current (black region) is observed, with a critical current I_c whose value can be tuned with the back gate voltage V_g, and can assume a value as large as $I_c = 97$ nA at gate voltage $V_g = 10$ V. A similar plot is shown in Figure 4.1b for d2, where all five bottom gates are swept together but V_g refers to the value of the middle gate which was most effective. A maximum critical current of $I_c = 55$ nA is observed for d2. Figure 4.1c shows the I-V traces for both junctions; d1 typically shows a sharp supercurrent transition and a hysteretic behaviour with respect to sweep direction due to quasiparticle heating [216], as is typical of nanowire based Josephson junctions. The device d1 was measured at temperatures in the range $T_{\mathrm{L}} = 25$ mK to $T_{\mathrm{L}} = 1.2$ K, as well as at $T_{\mathrm{L}} = 8$ K, inside the dilution refrigerator. The hysteretic behaviour is suppressed at higher temperatures; at $T_{\mathrm{L}} = 1.2$ K, the retrapping current I_r is reduced by about 20% (averaged over V_g) compared to $T_{\mathrm{L}} = 25$ mK, but there is

negligible difference between the retrapping and critical switching currents. Hence, the local Joule heating that reduces I_r compared to I_c, causing hysteresis at $T_{\mathrm{L}} = 25$ mK, is overshadowed by thermal energy at $T_{\mathrm{L}} = 1.2$ K.

The critical temperature of the junction is extrapolated from I_c versus T data to be approximately $T_c = 1.6$ K. On the other hand, d2 shows residual resistance on the order of 100 Ω near its switching point, and negligibly small hysteresis. This difference in the I-V behaviour of the junctions could be due to two effects: higher electron temperature and/or the quality of the Nb/InAs interfaces. First, while d2 was measured at the lattice temperature $T_{\mathrm{L}} = 25$ mK, we suspect the effective electron temperature might have been higher than ~ 100 mK due to high-frequency noise on the five local bottom gates. Secondly, the interface quality can be estimated from the OTBK [134] transmission coefficient t. The high-bias I-V traces for both devices extrapolate to a finite excess current [135, 134] $I_{\mathrm{exc}} \sim 10 - 100$ nA at zero voltage bias, depending on the gate voltage. This excess current can be used to calculate t. In a non-ballistic junction, t can be influenced by scattering processes inside the semiconducting channel. Indeed, the calculated t follows the gate voltage dependence I_{exc}. However, t can serve as a (conservative) estimate of the sputtered Nb/InAs contact transparency. The obtained value is generally higher when the device is more conductive. For d1, t is within the range $t = 0.56$ to $t = 0.72$ with an uncertainty ± 0.02 at each point within that interval. This is a relatively good value for Nb/InAs devices [139, 217]. For device d2, lower values are observed, $t = 0.41$ to $t = 0.55$ with uncertainty ± 0.02.

The phase dynamics of both junctions are overdamped. With both devices tuned to the regime of maximal supercurrent, the quality factor $Q = R_N \sqrt{2eI_cC/\hbar}$ is calculated using the resistively and capacitively shunted junction model [218]. Here R_N is normal state resistance and C the source-drain capacitance. For d1, $Q \cong 0.9$. Thus, d1 is close to the transition point between overdamped and underdamped regimes. For d2, $Q \cong 0.1$. This difference is due to a higher critical current in d1 and a larger source-drain capacitance due to thicker sputtered contacts. It should be possible to engineer similar nanowire junctions to be in the underdamped regime by making the Nb contacts with larger cross-sectional area. In a SQUID geometry, this would allow phase dynamics experiments, such as measurement of the current-phase relation [219], to be performed.

Figure 4.1d shows the critical current I_c (black curve) and normal state conductance G_N (red/grey curve) of d1 versus the backgate voltage V_g. The I_c curve is extracted from Figure 4.1a using a threshold resistance: the current bias point at which the numerical dV/dI first goes from $\simeq 0$ (supercurrent branch) to above a threshold resistance $\sim 100\ \Omega$ is identified as the switching point. G_N is measured directly using a standard lock-in technique, with a 2 nA bias current signal at 17 Hz and a temperature $T_{\mathrm{L}} = 8$ K, during the same cooldown. The two quantities show a strong positive correlation, typical of SNS junctions [220, 139, 177, 135,

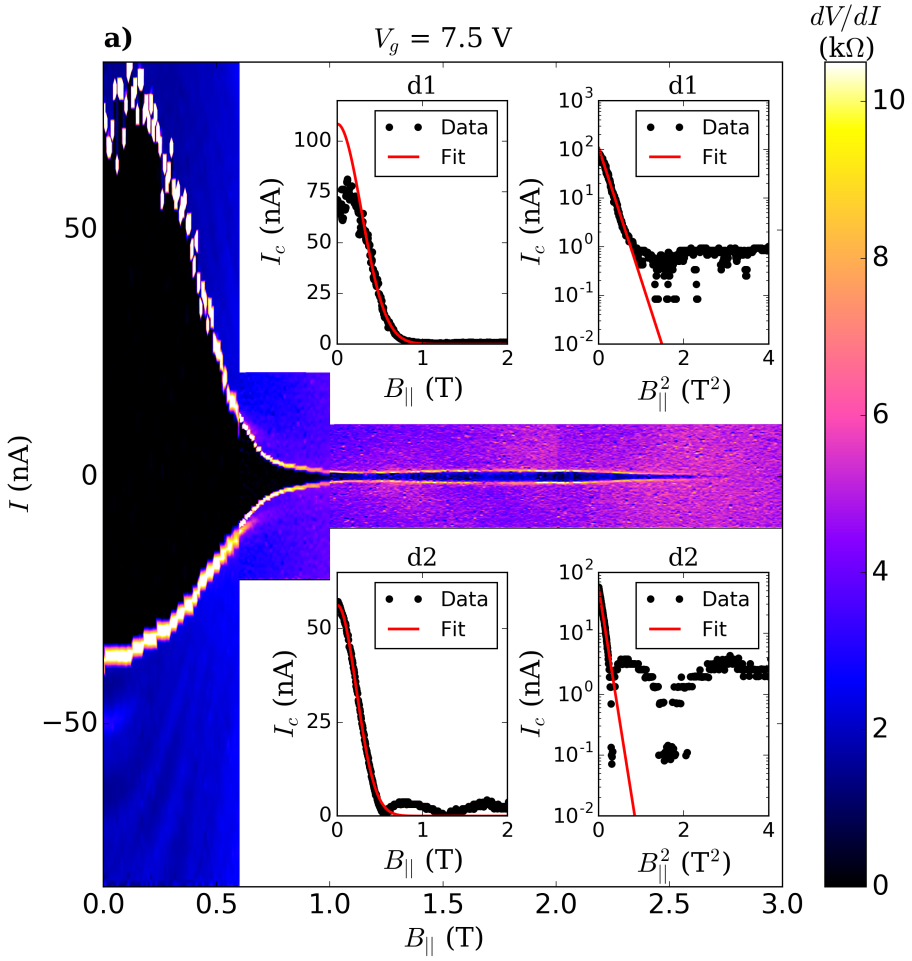

Figure 4.2: *(N.b. two-page figure & caption.)* Magnetic field dependence of the critical current I_c for d1 and d2 at $T_{\mathrm{L}} = 25$ mK. (a) Differential resistance dV/dI of d1 versus bias current I and axial magnetic field $B_{||}$ at $V_g = 7.8$ V. Above 0.8 T, I_c does not follow a Gaussian decay and is weakly modulated with the field, persisting until ~ 2.8 T. Inset, Upper: Gaussian fit (red/grey) to extracted I_c vs. $B_{||}$ data for d1 on linear and logarithmic scales (left, right, respectively). Depairing mechanisms are accounted for by the Gaussian curve, as discussed in the text. Lower insets: data for device d2 plotted in a similar format as the upper insets. Above ~ 0.6 T, d2 shows a stronger oscillation-like modulation with field compared to d1.

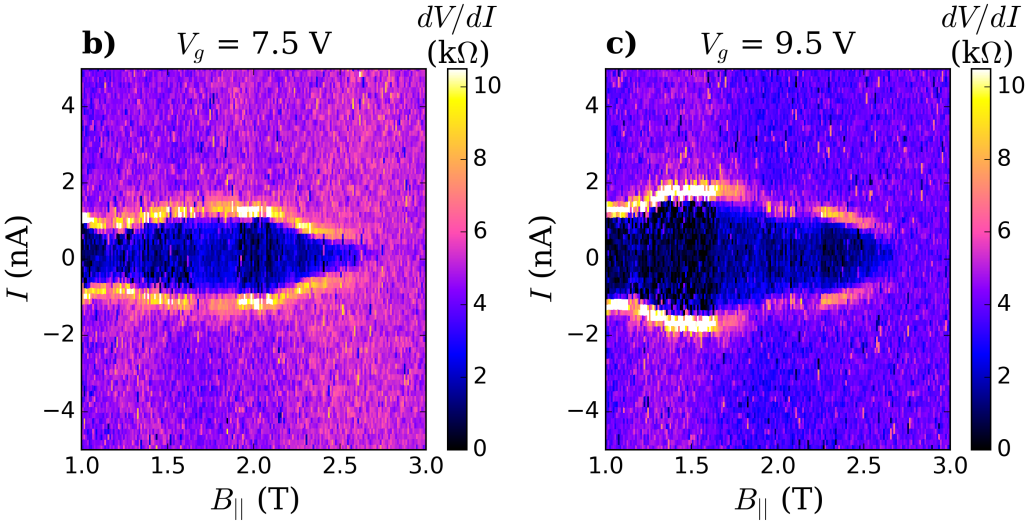

Figure 4.2: *(Cont. from prev. page.)* (b,c) High field data for d1 ($B_{||} > 1$ T) for two values of V_g show that the I_c variation is not monotonic, and the detailed behaviour depends on gate voltage.

217]. The rms value of universal conductance fluctuations [160, 135, 221] in G_N versus gate voltage can be calculated by first subtracting a baseline curve from the G_N versus V_g data, then calculating the standard deviation. The baseline is obtained by smoothing the G_N data over intervals $\delta V_g \sim 50$ mV. We obtain $\delta_{G_N} = 4.8 \times 10^{-7}$ S, whereas the fluctuations in I_c display an rms value 3.8 nA with respect to a similarly obtained baseline. These values are consistent across gate voltage values for each device. Note that the device is in the overdamped regime, so values extracted for I_c at any gate voltage is reproducible over repeated measurements to within $\pm \sim 0.5$ nA. Comparing the fluctuation ratios of the two quantities shows $\delta_{G_N}/G_N = 0.2\% \ll \delta_{I_c}/Ic = 4\%$, suggesting that the critical current is a more sensitive probe of mesoscopic fluctuations in the junction compared to normal state conductance, as first noticed in Ref. [135] for an InAs nanowire junction. These ratios are generally consistent across multiple devices. The 'figure of merit' product $I_c R_N$ has a value in the range $0.2-0.4$ mV. Here, R_N is the normal state resistance of the junction. Figure 4.1e shows differential conductance dI/dV of d1 versus bias voltage V at $V_g = 0.9$ V. Signatures of multiple Andreev reflection (MAR) are observed at voltages $V_n = 2\Delta/(en)$ as peaks in conductance for integer n, as indicated by arrows. Here, e is the electronic charge and $\Delta = 1.25$ meV is the superconducting gap of the Nb contacts. It is seen that the product eI_cR_N is factor of $3-4$ smaller than Δ. Whereas in an ideal, ballistic SNS junction a value $I_c = \Delta/(eR_N)$ is expected, the observed supercurrent is smaller due to a

combination of the diffusive nature of the junction, as well as a residual resistance present at the Nb/InAs interfaces.

4.3.2 Finite Magnetic Field

An axial magnetic field $B_{||}$ is a key ingredient predicted by theory to enable tuning the junction into the topological regime [47, 85, 76, 63]. Signatures of the topological phase transition have also been predicted to appear in the critical current [133]. Although we do not see explicit signatures of topological states here, we focus on the critical current I_c, which shows a non-monotonic and complex dependence on $B_{||}$, worthy of further study.

Figure 4.2a shows numerical differential resistance dV/dI of d1 versus $B_{||}$ at a backgate voltage $V_g = 7.5$ V. The current is swept from negative to positive values, so the transition at $I > 0$ ($I < 0$) indicates the critical current I_c (the retrapping current I_r). Three observations are of note here: (i) In the low-field regime, there is a slight *increase* of I_c with the magnetic field up to $B_{||} \simeq 0.14$ T. This behaviour occurs for a wide range of gate voltages, and can be understood as a manifestation of weak localization due to disorder in the diffusive nanowire channel with $l_e \simeq 60$ nm $< L = 170$ nm. As the magnetic field is increased, back-scattering is suppressed slightly due to the breaking of time-reversal symmetry. This results in an increase of the normal state conductance G_N and therefore I_c. However, it is of note that this behaviour is not directly observed in lock-in measurements of G_N vs. $B_{||}$ at $T_{\mathrm{L}} = 8$ K. This is likely explained by temperature: at $T_{\mathrm{L}} = 25$ mK, the phase coherence length ξ of the nanowire channel of the junction is estimated to be $\xi = 250 - 350$ nm, based on the suppression field $B_s = 0.2 - 0.3$ T above which the weak localization behaviour is no longer observed [222]. However, at $T_{\mathrm{L}} = 8$ K, ξ is bounded by the thermal length $L_T = \sqrt{\hbar D/2\pi k_B T} \simeq 100$ nm, shorter than the channel length $L = 170$ nm. Thus, the junction cannot be expected to be phase-coherent at 8 K; indeed no signatures of a supercurrent or MAR are observed there. N.b. similar devices with non-superconducting contacts show significant magneto-resistance effects [156] especially at high ($>\sim 2$ T) fields, making it difficult to interpret any "normal conductance" data acquired at base temperature in a high magnetic field intended to quench superconductivity. Similarly, the retrapping current I_r does not show an increase with $B_{||}$, as it is likely bound by the local Joule heating mechanism [216]. We conclude that, at $T_{\mathrm{L}} = 25$ mK, the supercurrent can serve as a sensitive probe of the mesoscopic and Fabry-Pérot type resonances of the junction. (ii) Above $B_{||} \sim 0.3$ T, the magnetic depairing mechanism [143] sets in, and the I_c vs. $B_{||}$ curve can be fit to a Gaussian, $I_c \propto \exp(-0.526\Phi^2/\Phi_0^2)$ (see insets of Figure 4.2). Here, $\Phi = \pi d^2 B_{||}/4$ is the magnetic flux through the axial cross section of the nanowire for diameter d, and $\Phi_0 = h/(2e)$ is the superconducting flux quantum. A theoretical calculation [143] of the depairing of a planar SNS junction in a perpendicular field predicts $I_c \propto \exp(-0.238\Phi^2/\Phi_0^2)$.

The reason behind the discrepancy in the numerical prefactor of the exponent between the theory and the experiment is not fully understood. A flux focusing effect is not expected to be at play here, as $B_{||}$ is applied in the device substrate and parallel to the nanowire axis. In fact, the effect of the Nb leads will be to produce a magnetic screening effect, similar to the effect seen in ref. [223]. A full description of the system may require a numerical solution of 3-dimensional Usadel equations [163, 150, 224] for the SNS junction while taking into account any screening effects due to the superconducting contacts. These considerations are beyond the scope of this chapter. (iii) Interestingly, in the high-field regime it is observed that the Gaussian suppression of I_c does not continue beyond $B_{||} \sim 0.8$ T (see Figure 4.2a insets), and a finite I_c can be resolved up to $B_{||} \sim 2.8$ T. Furthermore, in this high field regime, I_c does not decay monotonically with $B_{||}$, but is modulated with a pattern that depends on the gate voltage. These modulations are not consistent with a Fraunhofer pattern. Figure 4.2 (b, c) shows this high-field behaviour in device d1 for two values of V_g. A more oscillatory modulation of I_c vs. $B_{||}$ is observed in device d2, following an initial Gaussian decay (bottom inset of Figure 4.2a). The magnitude of I_c modulations in d2 are larger than in d1, with the ratio $I_c(B_{||})/I_c(0)$ up to 10% at high fields. Qualitatively similar modulation of I_c vs. $B_{||}$ was theoretically calculated in Chapter 3 to result from a Josephson interference due to orbital angular momentum states inside an idealized nanowire channel [170], with oscillation periods and node positions on the same scale as those in Figure 4.2. Another possible explanation is an effect due to the Zeeman splitting of the two spin channels in the presence of the axial field and spin-orbit coupling [144]. However, we estimate the first 'node' of oscillation within that theory to occur at $B_{||} \gtrsim 3$ T for an InAs nanowire with Landé g-factor close to 10, whereas the first minimum in I_c is observed at $B_{||} \sim 0.8$ T in the experiment. The modulations could also simply be due to the evolution of mesoscopic interference (universal conductance fluctuations due to static disorder) with magnetic field. None of these hypotheses, however, explain the persistence of I_c up to relatively high magnetic field. For InAs nanowires, it is well known that band bending due to surface states enhances the conductivity near the surface. It is possible that a significant fraction of I_c is carried by surface conducting channels that are not necessarily continuous around the perimeter due to the hexagonal faceted geometry. In this case, the effective flux enclosed by those channels could be very small, reducing the response to an axial magnetic field.

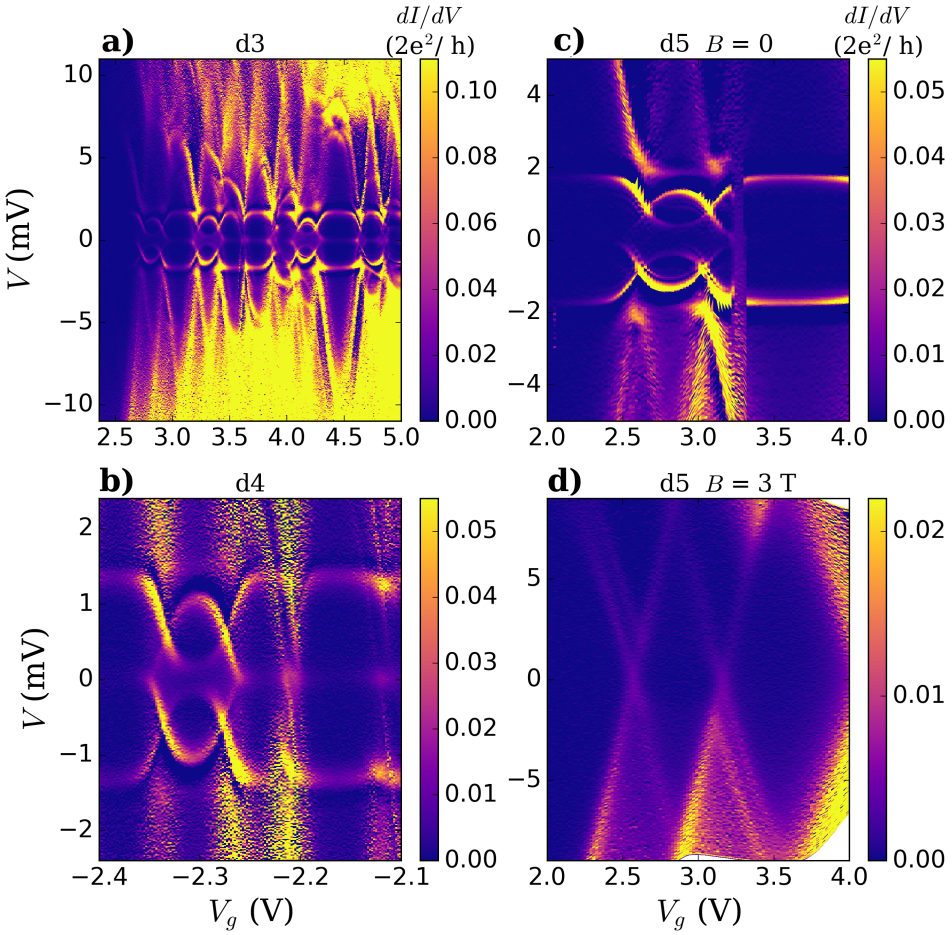

Figure 4.3: Differential conductance dI/dV of the devices d3–d5 in the QD regime. (a,b,c) Zero magnetic field dI/dV data of d3, d4, d5, respectively, versus bias voltage V and gate voltage V_g. Coulomb diamonds associated with the spontaneous quantum dots are visible, as well as resonant features identified as Andreev Bound States (ABS) at $|V| < \Delta/e = 1.4$ mV. For each value of V_g, four ABS are visible. In Coulomb diamonds with electron addition energy $E_{add} \gtrsim 10$ meV, the inner two ABS merge to form a zero bias peak (ZBP), whereas the outer two ABS are pinned at $|V| = \Delta/e$. By contrast, in Coulomb diamonds with $E_{add} \lesssim 10$ meV, four non-degenerate ABS are visible at $0 < |V| < \Delta/e$. (d) Same as panel c, but at a magnetic field $B = 3$ T perpendicular to the device substrate, which suppresses the superconductivity in the Nb leads. Comparing panels c and d allows distinguishing the ABS from the Coulomb diamond features, and allows the charge degeneracy points to be identified. For all panels, the data was acquired $T_{\mathrm{L}} = 1.5$ K.

4.3.3 Quantum Dot Regime

A majority of these devices show signatures of unintentional quantum dots formed inside the nanowire channel at low temperatures, due to random, static potential fluctuations. They are characterized by the observation of Coulomb diamonds in the $I - V$ characteristics at temperatures $T_{\mathrm{L}} \lesssim 10$ K.

Coulomb diamonds are the essential transport feature of Coulomb quantization in quantum dots, i.e. the quantization of charge states within the quantum dot due to the Coulomb repulsion of confined electrons; please see Ref. [225] for studies of quantum dots in similar devices but without superconducting contacts, and Refs. [226, 227] for reviews of this rich and broad topic. A brief summary is as follows: when conductance through a quantum dot is plotted versus gate voltage and bias voltage in a colour plot, rhombus- or parallelogram-shaped features ("diamonds") appear in conductance due to Coulomb quantization (see e.g. Figure 4.3d). The interior of the diamonds (dark purple regions) indicate when transport is disallowed ("Coulomb blockade") and conductance tends to zero. The "arms" of the diamonds indicate where charge transition first becomes possible. The sizes of the diamonds relate to the charging energy, therefore the self-capacitance, and therefore the physical size of the quantum dot, allowing us to derive estimates for the latter; and the slant (slope) of the arms relates to the strength of the capacitive coupling of the quantum dot to the metallic leads, therefore its approximate location within the channel; more on this below and in Ch. 5.

In most devices, the diamonds fully close at zero bias voltage, indicating that a single QD dominates the transport. At $T_{\mathrm{L}} \lesssim 2$ K, superconducting correlations also appear in the nanowire channel due to its proximity to the Nb leads, interplaying with the QD charging energy and resulting in Andreev Bound States (ABS) associated with the QD. Here we focus on devices d3, d4, and d5 measured at $T_{\mathrm{L}} = 1.5$ K, representative of the total of ~ 20 measured devices.

Figure 4.3a, b, c shows numerical differential conductance dI/dV measured at $T_{\mathrm{L}} = 1.5$ K for d3, d4, and d5, respectively, versus bias voltage V and the back-gate voltage V_g. The data is characterized by the appearance of resonances at or below the Nb leads' superconducting gap at $\Delta \simeq 1.4$ meV, superimposed on the Coulomb diamond structure. We shall return to these resonant features shortly. Figure 4.3d shows the same data as panel c, but at a magnetic field $B = 3$ T perpendicular to the device substrate, which suppresses the superconductivity in the Nb leads. This allows the electron addition energy E_{add} and the charge degeneracy points of the Coulomb diamonds to be measured. Lowering the field back down to 0 T, we observe that any shift of the Coulomb diamond structure versus field is small, corresponding to a change in the backgate voltage $\delta V_g \lesssim 10$ mV. The QD charging energies (i.e. the smallest observed addition energies) are typically within the range $5 - 8$ meV, from which we estimate a QD radius on

the order of $12 - 20$ nm. While based on a simple model of a spherical QD, this is nonetheless indicative that the QDs are small compared to the channel length $L = 170 - 200$ nm.

At zero magnetic field, peaks appear in conductance at resonant values of the bias voltage V, and these resonant values are modulated by changing the backgate voltage V_g. The dependence of the resonances on V_g strongly correlates with the Coulomb diamond structure, as previously seen in carbon nanotube [204, 205, 206, 207, 200, 208] and InAs nanowire devices [201, 202, 80, 203, 129]. Unlike previous studies, however, there appears to be little correlation between the shape of the resonances versus V_g and the charge state of the quantum dot; i.e. the even Coulomb valleys host similar resonances to the odd Coulomb valleys. This is in contrast with almost all previous observations in the literature, wherein the odd valleys host Yu-Shiba-Rusinov states that have a strong dependence on the gate voltage, but even valleys form resonances close to the superconducting gap Δ, with little gate dependence (an exception is part of the data reported in reference [204]). Below we use an extended Anderson-type model to qualitatively explain this behaviour. Another typical observation (see e.g. Figure 4.3a) is for the resonances to be 'pinned' to the bias voltage $|V| = \Delta$, or merge to form a zero-bias peak (ZBP) at $V = 0$; however, they can generally appear at any value $|V| < \Delta$. Importantly there are no features visible at $|V| = 2\Delta$, and contrary to observations of QDs formed in carbon nanotubes contacted with superconductors [200], there is no transport 'gap' in the low bias regime. These observations suggest that regions of the nanowire channel with finite (ungapped) density of states are connecting the QD to the Nb leads, i.e. an S-N-QD-N-S transport geometry, in which the QD is randomly placed inside the nanowire channel, with normal leads (N) connecting the QD on one or both sides to the superconducting (S) leads. The N-sections can carry superconducting correlations to the QD via the Andreev reflection process. The resonant features are identified as Andreev Bound States (ABS) associated with the QD, and a model for the ABS is presented below. Transport across the junction corresponds to energy resolved tunnelling of the ABS, with the normal sections of the nanowire corresponding to weakly coupled probes, and tunnelling occurring across the potential barriers at the edges of QD.

A good model for the ABS observed here must reproduce the following experimental observations: (i) for each value of V_g there are two pairs of resonances, where each pair consists of a resonance at $\pm V$. (ii) At the charge degeneracy points, the ABS at positive bias become degenerate at a bias value $0 < V < \Delta$, similarly for the two at negative bias, at $-\Delta < V < 0$. (iii) There is no discernible even-odd effect for the observed ZBP with respect to the electron number on the QD. This rules out Kondo correlations as a potential mechanism behind the ZBP: indeed, the Kondo temperature for the QDs is approximated, based on the Anderson model formula [228], to be $T_K \simeq 2$ K, similar to previous reports on measurements of T_K for InAs nanowire QDs [229]. The experimental data is collected at an electron temperature of 1.5 K $\sim T_K$, so it is not surprising if signatures of Kondo correlations cannot be observed. Pre-

liminary data taken at $T_{\mathrm{L}} = 25$ mK does not show signatures of Kondo effects, but further experiments are required to rule it out completely. (iv) The formation (or lack thereof) of the ZBP appears to be correlated with the addition energy E_{add} of the QD; for large E_{add} the ABS appear to be pinned at $|V| = 0, \Delta$ (for gate voltages V_g tuned away from the charge degeneracy points), whereas for small E_{add} the ABS appears at $0 < |V| < \Delta$ (see Figure 4.3b,c).

4.3.4 Model

A slightly modified version of an Anderson-type model [230, 206] detailed in Ref. [209] is used to describe the observed ABS. The elements of the model are two superconducting (S) leads with energy gap Δ, each tunnel coupled to a QD with a coupling strength Γ_i, where $i = L, R$ denote the left and right contacts. The superconducting phase difference between S-leads is denoted by ϕ. The transport geometry within the model is an S-QD-S configuration. As mentioned earlier, we believe our devices to be in an S-N-QD-N-S configuration; however, neglecting the N-sections results in a much simplified model which can be used to accurately describe the experimental data, as described below. The device channel lengths $L = 170 - 200$ nm are assumed to be smaller than the phase coherence length of the channel at 1.5 K, so the N-sections can transfer superconducting correlations to the QD through the Andreev reflection process. Within the context of the model, the presence of these N-sections have no effect on the physics of the ABS other than a rescaling of the S-QD coupling strengths Γ_i. In a full treatment of the problem, S-QD coupling will involve the details of the S-N tunnel coupling, the N-section transmission/scattering processes, and the N-QD tunnel coupling. Such considerations are left for future work, and the entire process is concisely described by the 'effective' model parameters Γ_i. The cost of this simplification is that Γ_i cannot be interpreted as tunnelling rates from which the total current can be derived, but rather as parameters describing the strength of S-QD correlations.

Lack of an Even-Odd Effect

The Anderson model can describe Yu-Shiba-Rusinov (YSR) states arising in QDs connected to superconducting leads. The mechanism for YSR states relies on a spin impurity (in this case a spin-1/2) impurity inside the QD to couple to a spinful quasiparticle in the S lead. As such, YSR states are only predicted to exist for odd-occupation states of the QD in an S-QD-S system. For an even occupation of the QD, the ABS are predicted assume a simpler character, pinned to $\pm\Delta$ with little to no gate voltage modulation. Much experimental evidence points to this even-odd effect in the ABS spectrum of InAs, InSb and carbon nanotube S-QD-S devices. However, our observations, consistent across ~ 20 devices, are different. We observe YSR-like behaviour

for both even- and odd-occupation Coulomb valleys of the QD. As mentioned above, only the addition energy E_{add} appears to control the behaviour of the ABS resonances.

The key to explaining this lack of even-odd behaviour is most likely related to the S-N-QD-N-S geometry of our devices and the nature of the N-sections. Disorder in the electrostatic potential is present in the whole nanowire, and in the N-sections it produces a 'spiky' density of states (DOS) rather than the smooth DOS of an ideal one-dimensional conductor. This can also be viewed as weak charge localization, i.e. large quantum dots with small charging energy compared to Δ and weak tunneling barriers. Since the Andreev reflections between the Nb leads result in wavefunctions spanning the entire channel, any spin impurity within the channel can couple to the Nb leads to create YSR states [231]. The presence of this non-trivial DOS in the N-sections affords the freedom to assume a spinful state inside the channel with little energy cost, regardless of the electron occupation of the primary QD. With this picture in mind, we apply analytical solutions for YSR states of an Anderson model to describe the ABS resonances in both the even- and odd-electron Coulomb valleys.

Subgap Energies

The subgap energies E are calculated versus normalized gate voltage $x = 1 + 2\varepsilon/E_{add}$. Here, ε is the chemical potential of the QD level, and $x = 1, -1$ refer to charge degeneracy points. The starting point is the analytical result obtained in Eq. 34 of Ref. [209]. For each value of x, we choose a superconducting phase ϕ_0 that will maximize the supercurrent $I_s(x, \phi)$ carried by the ABS, where $I_s(x, \phi)$ is calculated [186, 232] using the formula

$$I_s(x, \phi) = \frac{2e}{h} \sum_n \left(f(E_n(x, \phi)) \times \frac{\partial}{\partial \phi} E_n(x, \phi) \right). \tag{4.1}$$

Here, f is the Fermi-Dirac distribution at temperature $T = 1.5$ K, e is the electronic charge, h is Planck's constant, and E_n is the energy level of the ABS as calculated in Eq. 34 of Ref. [209], where n enumerates the four allowed solutions. Finding the optimal ϕ_0 as a function of x amounts to modelling the junction as *current-biased*, instead of phase-biased. This is the appropriate choice for the S-N-QD-N-S geometry of devices studied here, because ϕ is not fixed by a magnetic flux threading a SQUID loop, but rather, the ABS levels are tunnel-probed by injecting current through them via the N-leads.

Figure 4.4 (a-c) shows the theoretical energies of the subgap ABS states versus x, and as a function of the Γ/E_{add}, where $\Gamma = \sqrt{\Gamma_L^2 + \Gamma_R^2}$ is the total effective S-QD coupling strength. It is seen that a ZBP forms due to a merger of two ABS for $\Gamma/E_{add} < 0.65$, starting at around $x = 0$. Figure 4.4d shows an enlarged version of Figure 4.3a, and panel e shows the same data with the

theoretical ABS curves superimposed. A coupling asymmetry value $\Gamma_L/\Gamma_R = 0.57$ is found to produce the best fit to the data. Two characteristic electron addition energies E_{add} are seen in Figure 4.4 (d,e). The diamond with $E_{add} = 13$ meV is best fit to the model with $\Gamma/E_{add} = 0.43$ (dark blue), whereas the diamond with $E_{add} = 8$ meV is best fit to $\Gamma/E_{add} = 0.87$ (cyan). Data from d3 is shown as representative here; however, it is found that for all data sets, once model parameters Δ and the ratio Γ_L/Γ_R are fixed, good agreement with the model can be reached by finding the optimal value for Γ/E_{add} within each Coulomb diamond. We conclude that the simplified model presented here captures the basic physics of the current-biased ABS.

4.4 Discussion

Josephson regime — The interface transparency t crucially affects the proximity gap induced inside the semiconductor by the superconducting leads. Several groups have recently focused on *in-situ* grown, epitaxial Al contacts on InAs and InSb in order achieve $t \sim 1$. However, it was recently shown [85] that a hard proximity gap can be induced in InSb nanowires using sputtered NbTiN contacts, with $t \sim 0.98$, proving that epitaxial contacts are not a strict requirement for high-quality interfaces. In order to optimize t in our devices, current work is under way to improve the nanowire surface preparation process prior to the deposition of the Ti/Nb contacts, including passivation of the nanowire surface using a sulfur-rich ammonium sulfide solution [233]. We have obtained preliminary results with S-passivated devices in which a Josephson supercurrent is observed even at $T_{\mathrm{L}} = 1.5$ K. While still in the diffusive regime, such devices are well suited to the search for signatures of Majorana fermions in the supercurrent [133].

Decay of I_c versus $B_{||}$ — The decay of the critical current I_c versus the axial magnetic field can be fit to a Gaussian curve up to $B_{||} \sim 0.8$ T for both d1 and d2 (Figure 4.2), suggesting that a magnetic depairing mechanism [143] is at play. However, it is unclear why the depairing occurs $2-3$ times faster versus $B_{||}$ than predicted [143]. It is also unclear why the mechanism is not effective at suppressing the supercurrent for $B_{||} \gtrsim 0.8$ T until the upper critical field for the Nb contacts is reached at $H_{c2} \simeq 2.8$ T. An accurate description of the magnetic field depairing effect thus remains out of reach, likely requiring numerical solutions to the Usadel equations for our device geometry. Another possibility is that the initial decay is not dominated by the depairing effect, but rather a mesoscopic interference effect. For example, orbital Josephson interference [170] can result in a sharp initial decay of I_c versus $B_{||}$ if a large number of orbital angular momentum subbands are occupied.

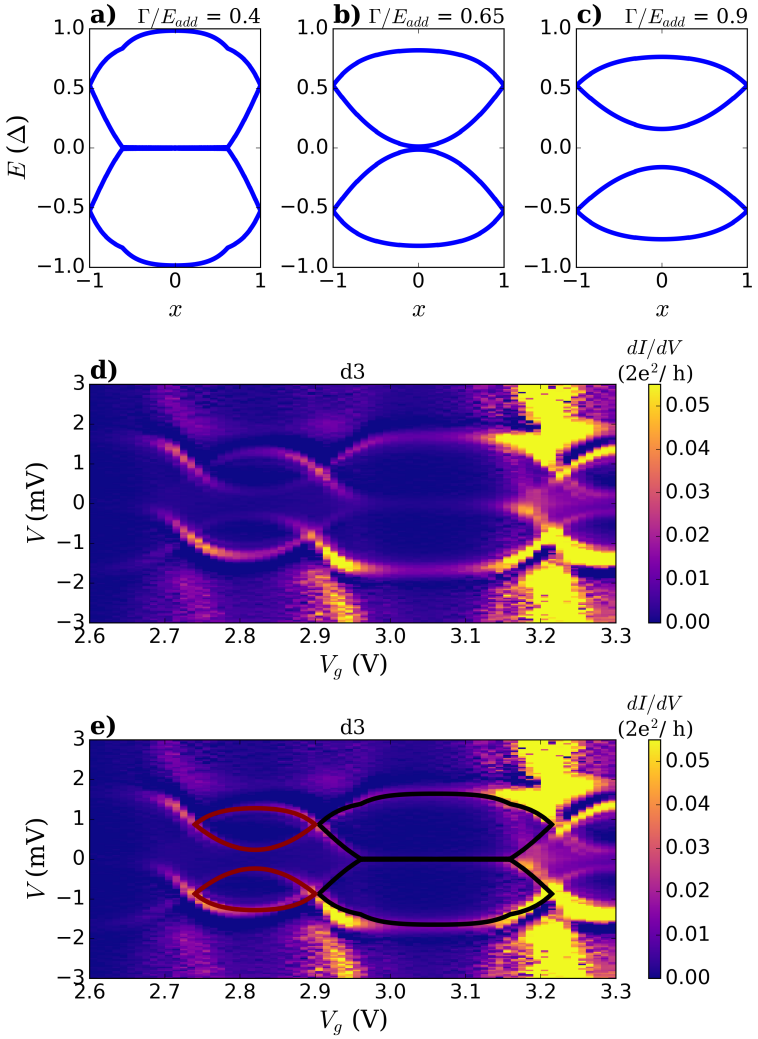

Figure 4.4: Modelled ABS energies (normalized to superconducting gap Δ) vs. normalized gate voltage x, as a function of Γ/E_{add}. For a large value of the electron addition energy E_{add} ($\Gamma/E_{add} < 0.65$) in this example, panel (a), two ABS are pinned at $|E| = \Delta$, and another ABS pair merge to form a ZBP over a large range of gate voltage x; whereas for a small value of E_{add} ($\Gamma/E_{add} > 0.65$, panel (c)), four non-generate ABS occur at $0 < |E| < \Delta$ for all x, and panel (b) shows the intermediate case. (d) Enlarged region of Figure 4.3a. (e) Same as (d), with superimposed theoretical ABS resonances. The following parameters are used in generating the theoretical curves: $\Gamma/E_{add} = 0.87$ (cyan), $\Gamma/E_{add} = 0.43$ (dark blue), $\Delta = 1.4$ meV, $\Gamma_L/\Gamma_R = 0.57$, $\Gamma/\Delta = 4$, $T = 1.5$ K.

Screening of magnetic flux by the Nb leads — Since the axial magnetic field $B_{||}$ is applied in the plane of the device substrate, the expected effect of the $50-80$ nm thick Nb leads is to screen (rather than focus) the magnetic flux by a small amount at the nanowire channel (see ref. [223] for a similar effect). We estimate[1] that the value of the field at the center of the nanowire channel is a factor of $\lesssim 20\%$ smaller than the applied field. Thus, the faster-than-expected decay of I_c versus $B_{||}$ is not due to field focusing.

Quantum dot regime — ABS have previously been studied in InAs nanowires contacted with Al [201, 202, 80, 203] and V [129] and in carbon nanotube devices [204, 205, 206, 207, 200, 208], as well as a range of other physical systems [235, 236, 237]. To our knowledge, this report is the first description of ABS in quantum dots in InAs nanowires connected to Nb leads. The larger transition temperature and superconducting gap of Nb compared to Al allows the experiment to be performed at 1.5 K, where the Kondo effect is not observed. A good agreement is reached between the Anderson-type model of ABS and the experimental data. This leads to exciting possibilities for further research on this system, including doublet-to-singlet transition of the ground state [129, 80] and search for Majorana fermions in phase-biased ABS [238].

4.5 Conclusions

We have studied quantum transport in diffusive, short-channel InAs nanowire/Nb Josephson junctions, and identified two distinct transport regimes. Relatively large supercurrents and Nb/InAs contact transparencies in the Josephson regime are encouraging results, indicating that junctions based on InAs nanowires with non-epitaxial Nb contacts are good candidates for exploring proximity effect and Majorana physics at relatively high magnetic fields. The behavior of the critical current versus the axial magnetic field, including modulation and persistence to high field, is not yet understood. We presented several hypotheses to explain this, but further study is needed. These effects need to be understood so that they can be distinguished from signatures of a topological phase transition [47, 85, 76]. In the quantum dot regime, subgap resonances can be well described as current-biased Andreev Bound States within an Anderson-type model. To explain the lack of an even-odd effect in the data, we hypothesize that the N-section provides spinful states that induce YSR-like bound states associated with the quantum dot. Numerical calculations using the NRG technique could be used to further test this idea. The reproducibility of our experimental observations across ~ 20 devices compels further research on InAs nanowire/Nb non-ballistic junctions, especially in light of recent proposals [238, 239] for detecting signatures of Majorana fermions using phase-biased ABS.

[1] Based on a magnetic penetration depth $\gtrsim 90$ nm for a $50-80$ nm thick Nb film [234], and assuming an exponential suppression of the parallel field inside the leads.

Chapter 5

High-transparency Nb/InAs Nanowire Josephson Junctions

5.1 Introduction

Motivated by Ref. [90], wherein an X-ray diffraction image of the cross section of a nanowire is seen to show presence of sulfur as a passivation agent, we set out to make a new generation of nanowire Josephson junction devices with high contact transparency with the sputter deposited Nb contacts. This chapter describes these "third generation" devices.

We succeed in creating high contact transparencies at the InAs and Nb interface, estimated to at least 95%, a considerable improvement. Supercurrents are observed at temperature $T = 1.5$ K, which is an achievement compared to the devices described in Ch. 4; signatures of ABS similar to those seen in Ch. 4 are also observed. A detailed description of the ABS behaviour proves to be difficult, and highlights the challenges which need to be overcome for future devices.

Section 5.2 describes devices fabrication and the technical improvements over devices in Ch. 4. Section 5.3 details the results of low-temperature transport experiments on devices in Josephson 5.3.1 and Quantum Dot 5.3.2 regimes.

5.2 Device Description

Our starting point for the third generation devices is the same as that of Ch. 4: a single batch of undoped InAs nanowires grown in a gas-source molecular beam epitaxy system, with diameters

in the range $40 - 65$ nm [210, 211]. Similar to before, an 8 nm thick Al_2O_3 shell was deposited via atomic layer deposition onto the nanowires on their growth substrate. Two types of Nb contacted Josephson junction devices, one short channel (175 nm) and one longer channel (300 nm) are made after the shelled nanowires are moved to n++ Si / 300 nm SiO_2 device substrates via dry deposition. The longer devices have a single top gate in the center of the channel, and are in a 25 nm trench dry etched into the 300 nm SiO_2 thermal oxide of the substrate. The idea was to form a quantum dot between the contacts snapping the entire channel, and tune the QD with the top gate as well as the n++ substrate used as a global back gate. The short devices have no top gate. A similar fabrication recipe as that of Ch. 4 was used, except for the following two crucial differences: firstly ZEP photoresist was used instead of PMMA for electron-beam lithography of the Nb contacts, followed by a metal lift-off step. This allowed the shorter $\sim 170 - 175$ nm channels for the shorter devices, due to the higher resolution achievable with ZEP. Secondly, significant surface preparations are made on the nanowire in order to improve the contact transparency, as we shall describe below.

We suspect that with the devices reported in Ch. 4, the surface tension of HF with the SiO2 termination layer of the substrate and/or the Al_2O_3 coating on the nanowire resulted in HF being "pulled" along the nanowire axis and/or trench and etching the Al_2O_3 inside the nanowire junction channel, in the area proximate to the PMMA window opened for Nb deposition. This is depicted schematically in figure 1. With the third generation devices, a thin (2 nm) layer of HMDS, a hydrophobic substance, is deposited before spin-coating with ZEP. This is expected to disrupt the mechanism described above, and result in the balling of HF droplet as the HF dip is made.

Furthermore, before the deposition of Nb contacts, a 5s HF dip is made to remove the Al_2O_3 shell, followed by a passivation step in a light-activated sulfur rich solution [233]. (See Appendix A for details.) The chip is then rapidly moved to the sputtering deposition chamber with exposure to air limited to about 30 seconds before a vacuum is pulled on the deposition chamber load-lock. The chip is put back into very-high-vacuum conditions within three minutes. Prior to Nb deposition, a finely calibrated Ar ion milling process (dc reverse sputtering) designed to gently remove 2 nm of InAs is carried out. The details of this ion-milling step are reported in Appendix A. This step is finely calibrated via performing AFM on a 2 dimensional InAs substrate to remove 2 nm of the surface / oxide layer, and is a crucial difference between the third and second generated devices.

After lift-off of Nb contacts, DC transport measurements are carried out at pumped He temperature $T = 1.5$ K and dilution refrigerator temperatures $10 - 25$ mK, revealing supercurrents as well as quantum dot behaviour.

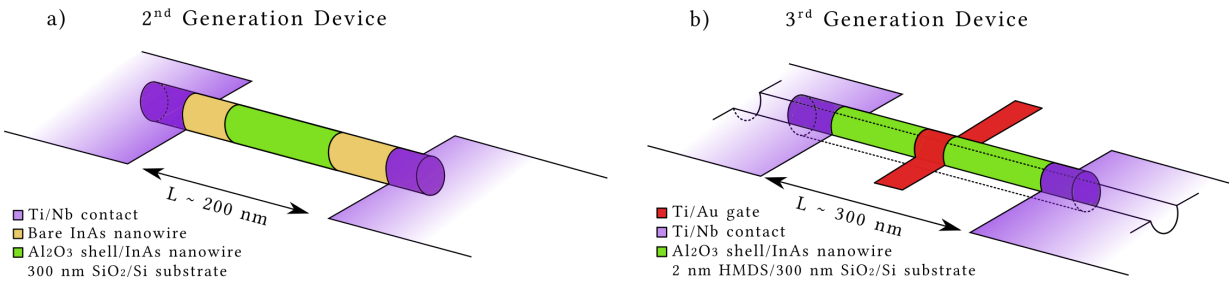

Figure 5.1: Schematic comparison of 2^{nd} generation nanowire devices discussed in Chapter 4 (panel a) vs 3^{rd} generation nanowire devices discussed in this chapter (panel b). (a) An InAs nanowire is contacted by Ti/Nb source/drain contacts after a 5 s HF dip to remove the Al_2O_3 shell. It is suspected the HF removes the Al_2O_3 shell inside the junction channel. A non-entrenched device is shown here; some devices are entrenched. See Chapter 4 for details. (b) A ~ 2 nm HMDS layer is deposited prior to lithography for the Ti/Nb (2 nm/80 nm) source/drain contacts. The 5 s HF dip to remove the Al_2O_3 shell is quickly succeeded by a 90 s immersion in a Sulfur passivation solution, and rapid transfer to the metal deposition chamber. The presence of the HMDS layer prevents the etching of the Al_2O_3 shell inside the channel junction. An entrenched device with a $\sim$ 50 nm wide top gate is shown here (as used in Section 5.3.2). Short-channel devices described in Section 5.3.1 are non-entrenched, lack the top gate, and have channel length $L \lesssim 175$ nm. To simplify the drawing, we have not shown the Ti/Nb contact thickness nor the top gate thickness.

5.3 Results

5.3.1 Short Devices

The recipe described above was successful for the short channel devices, and out of a batch of 14, 13 show a supercurrent at 1.5 K. Figure 5.2 shows the typical behaviour of the devices in the Josephson regime, as differential resistance versus the global back gate voltage. Supercurrents as large as 25 nA are routinely observed in these devices at 1.5 K. Pinching off the devices using the global back-gate was not possible with voltages down to ~ -20 V, at which point dielectric breakdown resulted. Therefore, transconductance measurement of the mobility is directly possible, unlike the devices in Ch. 2, 4. However, the pre pinch-off slope of the transconductance curves suggests a mobility greater than 20'000 cm^2/V.s for several devices, an $\sim 50\%$ improve-

ment over the previous generation devices. This is likely due to the HMDS step, which prevents the Al_2O_3 shell from being etched near the Nb contact, and creating scattering sites there. By applying a perpendicular or axial magnetic field, the supercurrent is suppressed at around 0.6 T (Fig.5.3). Signatures of the Orbital Josephson effect are small to non-existent, likely due to the higher temperature + shorter channel of these devices. However, clear signature of multiple Andreev reflections, which are suppressed with the magnetic field are observed in all devices showing a supercurrent (not shown). The Nb/InAs contact transparency is estimated, using a method similar to that described in Ch. 4, to be at or above 95%, which is also a considerable improvement over the previous devices at $\sim 75\%$. We attribute this to the effectiveness of the HMDS treatment + sulfur passivation + Ar Ion milling steps performed on these devices.

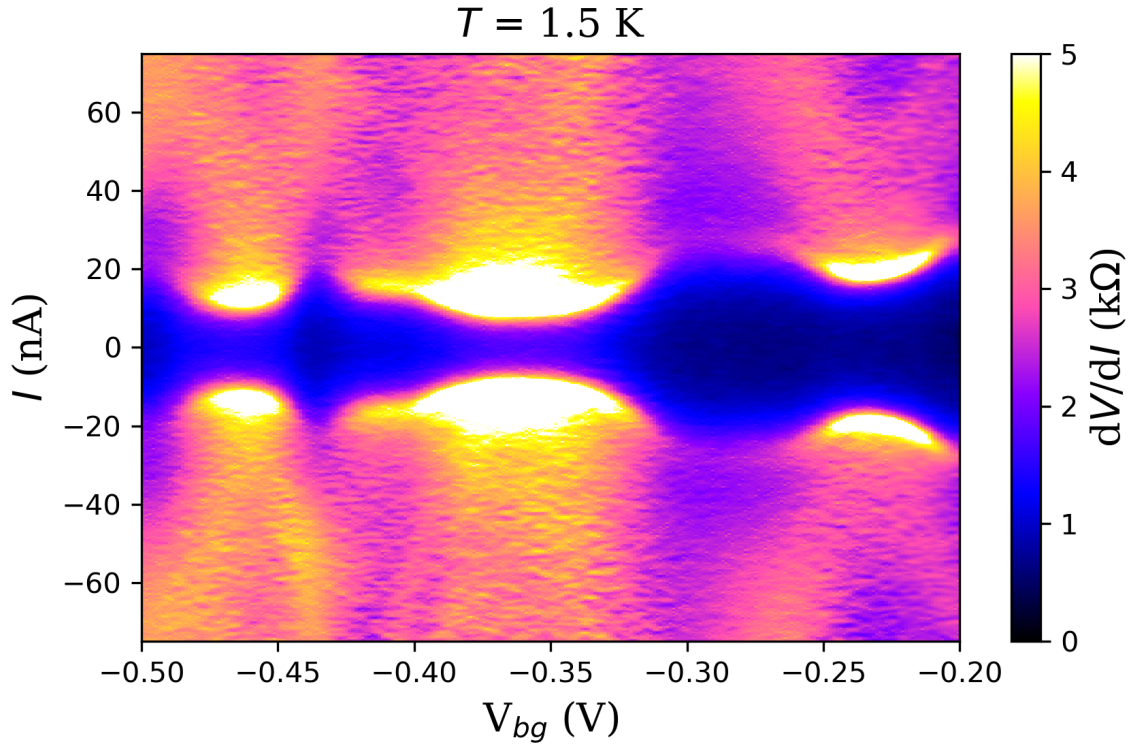

Figure 5.2: Differential resistance dV/dI of d2 vs backgate voltage, showing typical behaviour of the short-channel junctions in the Josephson regime. The dark blue region signifies a supercurrent observed at $T = 1.5K$, although the transitions are rounded due to the high temperature. Critical currents as large as $I_c = 25$ nA are observed in multiple devices.

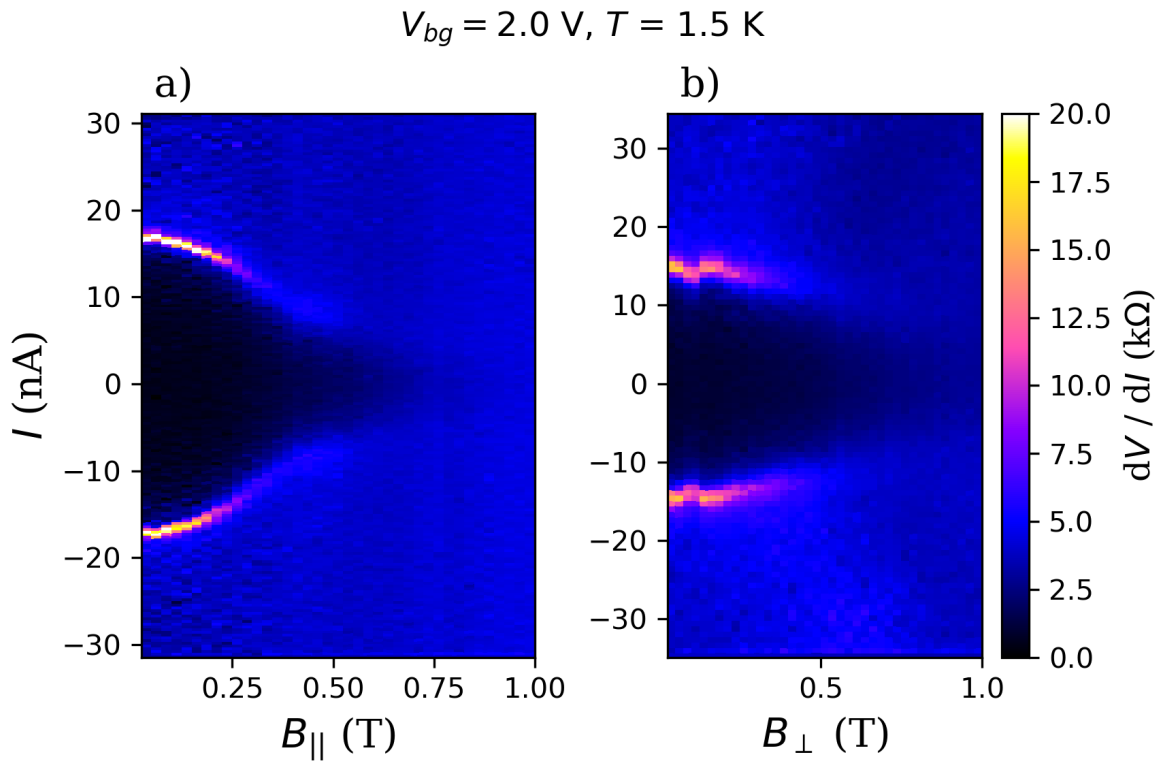

Figure 5.3: Differential resistance dV/dI of d2 vs an axial (a) and a perpendicular (out of plane) (b) magnetic fields. No oscillations of I_c vs $B_{||}$ is observed, as the supercurrent is suppressed at $B \sim 0.6T$ before oscillations could be observed. This is suspected to be due to the temperature $T = 1.5K$.

5.3.2 Long Devices

The expectation from the longer ~ 300 nm channel devices was that they would form quantum dots in the center of the channel, similar to the case of Ch. 4. Therefore, a 50 nm gate was put on top as a plunger gate to control the chemical potential of the QD (recall from Ch. 4 that the radius of the QD was estimated to be close to 50 nm. 5.1.) However, this assumption generally did not come true. The local top gate and back gate were generally incapable of tuning the device into the quantum dot regime, except for two devices out of 10. At 1.5 K, average conductance was high ($R \lesssim 2\text{k}\Omega$), but we don't see a supercurrent for any these devices at that temperature.

The general lack of QD behaviour in these devices further suggests that in the Ch. 4 devices,

the QD was formed as a result of the etching of the Al_2O_3 shell of the nanowire via HF, at which point the chemical potential inside the nanowire is expected to show a step-like behaviour. While successful at eliminating that unwanted effect, the HMDS + Sulfur passivation + Ar ion milling treatment received by these nanowires has increased conduction so much that effective gating of the nanowire junction has become difficult. This helps us identify the requirement for a potential device used for the observation of MZM: gatability as well as high conductance, which are competing effects. We further discuss this matter in Ch. 7.

One quantum dot device was identified, and measured at dilution refrigerator temperature 25 mK. Figure 5.4 (differential conductance vs the back gate voltage) shows the strong presence of Andreev Bound States (ABS) in the QD device, as rounded subgap states within the Coulomb diamonds, with the superconducting energy gap identified as 1.4 meV, appropriate for the Nb contacts. The ABS are not easy to understand as they don't follow a typical even-odd behaviour predicted by Ref. [209] and other Anderson-model based theories, including the current-biased YSR model presented in Chapter 4. Comparing the data to that shown in Ref. [205] suggests a strong asymmetry in the coupling strength Γ of the ABS towards one contact, again, in contrast with the date shown n in Chapter 4. However, the lack of significant slanting in the Coulomb blockade lines (which are proportional to capacitance) suggests that the electronic coupling strength is more or less symmetric, and the asymmetry is related to some aspect of the phase coherence of tunneling to one contact versus the other. This identifies an important "tuning parameter" in the study of YSR states: as well as the ratio of Γ/U, the asymmetry ration Γ_1/Γ_2 must also be taken into account.

Figure 5.5 shows the ABS states vs an axial magnetic field. We see a Zeeman-like splitting of the ABS, suggesting the states are spinful. Interestingly, this splitting persists across different Coulomb diamonds, further evidencing the lack of an even-odd effect in this device. At higher fields, around 1.8–2 T a zero-bias feature is created, which persists till around 3 T. This feature is well-resolved and shows an unambiguous pinning of the ABS at zero energy at the charge transition point. As of this writing we know of no simple explanation for this particular pinning behaviour of the ABS. While we refrain from presenting any detailed hypothesis, we note the following: firstly, that the behaviour appears to be more complex than a singlet-doublet transition of the ABS ground-state [209] in a current-biased configuration (unlike that seen in Ch. 4), and secondly, using the estimates in Ch. 1 as a guide, this is the field-range in which one spin channel would be expected to be pushed out of the energy window. The zero-energy pinning of this feature may be related to the YSR equivalent of a topological transition: i.e., as the system transitions from a dual-channel spin up or- down problem, to a single spin channel problem.

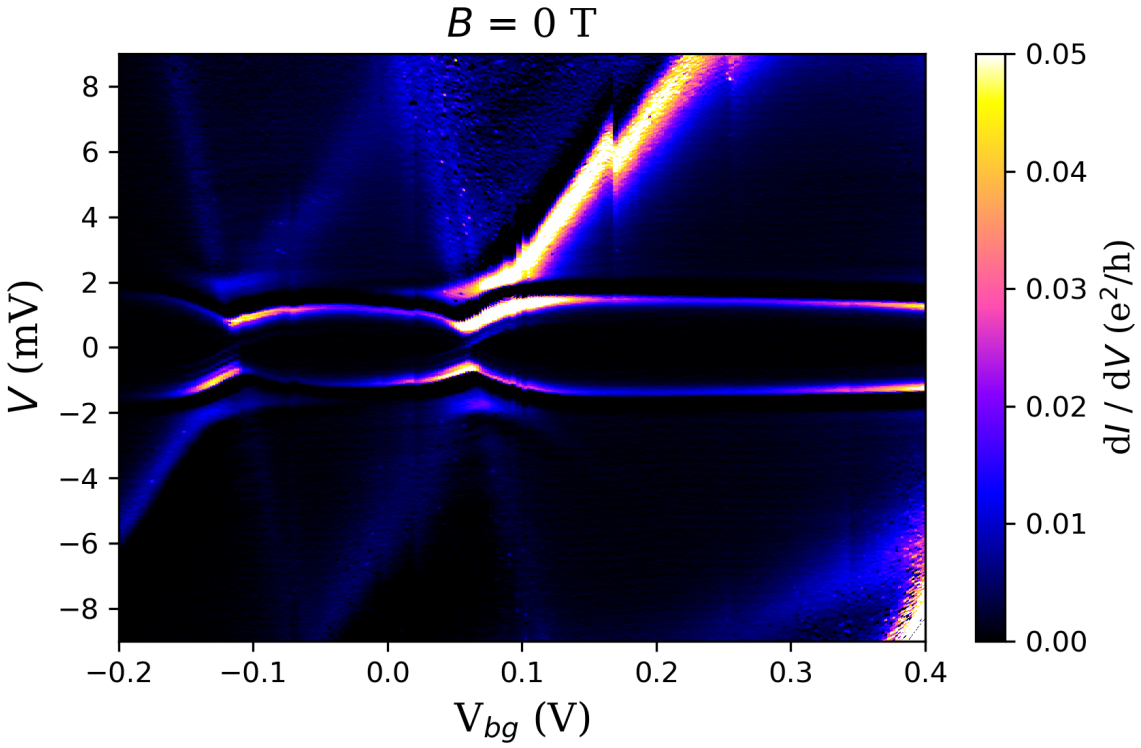

Figure 5.4: Differential conductance, dI/dV, of d1, one of only two devices that should Coulomb quantization, at $T = 25$ mK. From the charging energy $E_c \simeq 8$ meV, a dot radius of ~ 55 nm is estimated. Strong resonances observed at $\pm\Delta = 1.4$ meV, with weaker resonances inside the gap. As the resonant energies are modulated near the charge quantization lines, some form of localized Andreev Bound States (ABS) are suspected to be forming on the quantum dot. However, a straight-forward explanation using a Yu-Shiba-Rusinov (YSR) remains elusive.

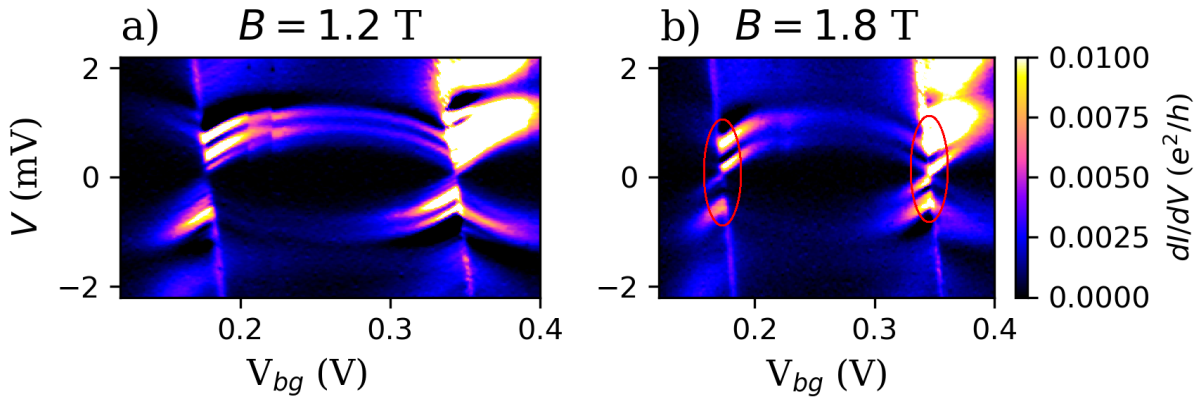

Figure 5.5: Differential resistance of d1 in the quantum dot regime for two values of axial magnetic field. The separation of the resonant states w/r/t magnetic field points at a spinful YSR state; however, no even-odd effect is observed (i.e., states on both sides of the charge transition move as function of the magnetic field), pointing at a complex and not fully-understood phenomenon behind the ABS resonance. The zero-crossing feature forming in panel (b), highlighted with red ovals, forms at around 1.6 T (shown here at 1.8 T) and persists up to $B \simeq 3$ T, close to the critical magnetic field of Nb thin films.

The complexity of the YSR / ABS behaviour in this device presents evidence of rich phenomenology that must be fully understood in candidate MZM devices. In these, our third generation devices, we were successful at significantly improving contact transports between InAs and Nb, and in developing the technical skill to do so we developed valuable expertise in the design of future devices. However, these device also reveal that as well as transparency, the gatability and symmetry of these devices are critical parameters for designing an ideal candidate device for the study of MZM. We expand on this point in Ch. 7.

Chapter 6

Readout of Majorana parity states using a quantum dot

6.1 Introduction

In the previous chapters we discussed three generations of nanowire-based proximity Josephson junctions, and described how the critical current I_c of the junction and the Andreev Bound states (ABS) can be used as tools look for signatures of Majorana Bound states (MBS) in the system, should the system go through a transition to the topological phase.

A salient question is, assuming that a topological phase can be reliably created in nanowire junctions or networks of nanowire junctions, what are the interesting experiments that can be carried out to pave the way towards the realization of a topological quantum computer? The "holy grail" experiment proving the topological nature of the system is the braiding (physically exchanging the positions of) two MBS. Because of the topological nature (i.e. the non-Abelian exchange statistics) of MBS, the joint quantum state shared by the MBS goes through a parity transformation after braiding. In this chapter we build towards the realization of a braiding experiment.

Here we propose an experiment that will allow the non-local nature of the MBS in the nanowire to be verified, and the joint parity of the MBS to be read out [68]. The system involves a quantum dot tunnel coupled to one MBS at the end of a topological wire. This is a natural extension of a nanowire junction hosting a pair of MBS.

We theoretically examine a scheme for projectively reading out the parity state of a pair of Majorana bound states (MBS) using a tunnel coupled quantum dot. The dot is coupled to

one end of the topological wire but isolated from any reservoir, and is capacitively coupled to a charge sensor for measurement. The combined parity of the MBS-dot system is conserved and charge transfer between the MBS and dot only occurs through resonant tunnelling. Resonance is controlled by the dot potential through a local gate and by the MBS energy splitting due to the overlap of the MBS pair wavefunctions. The latter splitting can be tuned from zero (topologically protected regime) to a finite value by gate-driven shortening of the topological wire. Simulations show that the oscillatory nature of the MBS splitting is not a fundamental obstacle to readout, but requires precise gate control of the MBS spatial position and dot potential. With experimentally realistic parameters, we find that high-fidelity parity readout is achievable given nanometer-scale spatial control of the MBS, and that there is a tradeoff between the precision requirements of temporal and spatial control. Use of the scheme to measure the MBS splitting versus separation would present a clear signature of topological order, and could be used to test the robustness of this order to spatial motion, a key requirement in certain schemes for scalable topological qubits. We show how the scheme can be extended to distinguish valid parity measurements from invalid ones due to gate calibration errors.

6.2 Motivation

The elementary quasi-particle excitations of one-dimensional topological superconductors are called Majorana Bound States (MBS), and are equal to their own anti-particles. This was first discovered by Kitaev [32], and has spurred enormous interest [240, 83, 241, 121, 242, 243, 244, 245, 50] from the condensed matter community in the fundamental properties of this novel phase of matter, as well as its potential applications in topological quantum computation (TQC) [4, 246, 31]. One recipe for MBS involves a semiconducting nanowire with a strong spin-orbit coupling, with induced superconductivity due to proximity with an s-wave superconductor. With the application of an external magnetic field of appropriate direction and magnitude, a pair of MBS appear at the ends of the nanowire as edge modes [6, 35, 116, 7]. As the MBS are zero energy modes, the ground-state is 2-fold degenerate. Several reports have been made on experimental evidence [76, 78, 81, 77, 79, 247] for the existence of this type of MBS, although a complete picture of the physics of systems hosting MBS, including conclusive evidence of the topological nature of the observed ground states, remains out of reach as of yet.

For the purposes of TQC, the degenerate MBS edge modes can be labelled $|0\rangle, |1\rangle$ in the computational basis, according to the *parity* of the many-body ground state, with $|0\rangle$ ($|1\rangle$) referring to an even (odd) number of electrons. A so-called topological gap protects these states from the environment, providing an intrinsic, hardware-level protection against decoherence [63]. A *logical* Majorana qubit is defined as the joint state of two MBS pairs within a particular parity

manifold [25]. We shall focus on a single MBS pair here, as readout of a logical qubit can be constructed from pair readouts. A bit-flip operation $|0\rangle \leftrightarrow |1\rangle$ can be performed by utilizing the unusual MBS property of non-Abelian anyonic statistics. This involves braiding (physically exchanging the positions of) the two particles. The details of braiding operations were explored in ref. [63], where it was also shown that these operations, as implemented in a network of quantum wires, benefit from topological error protection. However, in order to obtain a universal set of operations, one needs to supplement braiding with a set of quantum gates that are not topologically protected [25, 248, 21]. Several proposals exist for achieving universality, such as bringing the MBS close together to break topological protection and applying phase gates [63, 25], or coupling MBS with conventional qubits [117, 249, 250].

Additional challenges facing the realization of TQC are state initialization and readout of the MBS parity states. Following the methodology of the $\nu = 5/2$ fractional quantum Hall system[30, 24], a creation/annihilation approach was suggested by Alicea et al. [63], wherein a pair of MBS are created from the vacuum of the underlying quantum field, braided to perform computation, and then fused (annihilated) to create either vacuum or a finite energy quasiparticle (i.e. a Dirac fermion), depending on the parity state of the MBS. The extra quasiparticle can be detected by some form of charge measurement. There are also recent proposals for readout based on monitoring the current-phase relation of a Josephson junction hosting an MBS pair [6, 118], coupling MBS to flux [117] or transmon [251, 252, 50] qubits, and coupling to charge or spin states of quantum dots [249, 253, 250]. All of these methods rely on some form of parity-to-charge conversion, and also necessarily take the MBS out of the topologically protected regime by breaking the degeneracy of the parity states. This can be achieved by reducing the spatial separation of the two MBS so their wavefunctions overlap [63], or by using long-range Coulomb control interactions [251, 252] on a superconducting island hosting the MBS. Charge state coherence during the parity-to-charge conversion operation is generally required.

In this chapter, we propose and theoretically model a readout scheme that is relevant to the setup of MBS tunnel coupled to a quantum dot (QD). Previous theoretical work has demonstrated the power and versatility of the MBS-QD system for detecting the presence [119] and lifetime [254] of topological order, gate-driven manipulation of topological qubits [249, 250, 253] and coherent transfer to dot spin and dot charge states. In a realization based on a top-gated two-dimensional electron gas (2DEG), for example, the MBS-QD setup is natural and could lead to a scalable architecture for topological qubits. While parity measurement was mentioned in the MBS-QD context [249], to our knowledge, no detailed study has been conducted to validate the experimental feasibility of such a readout scheme. Our setup involves an MBS pair, a QD isolated from any reservoir, and a charge sensor to measure the QD charge state. As there are no reservoirs present, the joint parity state of the QD + MBS system is conserved. By reducing the spatial separation of the two MBS (e.g. with a set of keyboard gates), the overlap of the MBS

wavefunctions grow, resulting in an energy splitting between the $|0\rangle$ and $|1\rangle$ states. This splitting is oscillatory and has an exponential envelope versus the MBS separation [32, 82]. The QD level is tuned so that a charge transition is on resonance with a target MBS energy splitting, allowing MBS $\rightarrow$ QD charge transport to occur for one parity state but not the other. Similar to other schemes, we assume a coherent charge transfer process. Finally, the charge state of the QD is projectively measured with a charge sensor such as a single electron transistor (SET) [255].

Numerical simulations with realistic system parameters show that this setup can be used to map out the energy splitting between the $|0\rangle$ and $|1\rangle$ states versus the spatial separation of the MBS pair (or as a function of chemical potential or external magnetic field). Such a signature has been cited as "smoking gun" evidence for topological order, and could also open avenues for studying the robustness of the topological state to domain wall motion. The charge transfer in our scheme can be performed on a fast timescale of < 10 nanoseconds with a high theoretical fidelity of $> 99\%$. These attributes can be further improved, but at a cost in the precision of voltage and timing controls. The isolation of the QD from reservoirs leads to a resonance in the tunneling probability versus gate voltage that is typically very sharp, and controlled only by the tunneling rate. While this requires some fine tuning of control parameters, it is very effective at decoupling the MBS and QD when readout is not being performed.

This chapter is organized as follows: In Section 6.3, a model for the MBS pair coupled on one end to a QD is presented. In Section 6.4, we show how this setup can be used to experimentally determine the energy splitting between the MBS parity states as a function of their spatial separation. The MBS parity measurement is numerically studied and discussed in Section 6.5, and concluding remarks are presented in Section 6.8.

6.3 Model

Figure 6.1a schematically illustrates the proposed setup for the initialization/readout scheme of the MBS parity state. A semiconducting nanowire with a strong Rashba-type spin-orbit coupling [39, 38] is contacted by a bulk s-wave superconductor, resulting in proximity induced superconductivity in the nanowire. The application of an axial magnetic field $\vec{B} = B\hat{x}$ of appropriate magnitude results in a phase transition to the topological regime [6], with a pair of MBS emerging at the edges of the topological region. Using an array of keyboard gates located near one end of the nanowire, the chemical potential in the nanowire can be manipulated to move the edge of the topological region [5, 63], thus tuning the separation between the two MBS from an initial value L_i to a final value L_f. The MBS at the other end of the nanowire is tunnel coupled to an isolated quantum dot (QD) defined inside the nanowire. The energy level

of the QD is controlled by the plunger gate voltage V_g, and the strength of the tunnel coupling by V_t. In particular, V_g can be tuned such that the energy required to change the electron number on the dot matches the energy splitting of the MBS, i.e. the resonant tunneling condition. A nearby charge sensor, e.g. a single-electron transistor (SET) or quantum point contact, couples capacitively to the QD. A measurement of the sensor current results in a projective measurement of the QD charge state on a measurement timescale t_m, typically microseconds [256, 257], but as short as $\sim$ 400 ns [258]. Readout of the QD charge state is the last stage of the MBS parity readout procedure, and t_m is assumed to be much longer than the timescale for QD $\leftrightarrow$ MBS resonant tunneling, so the back-action from the charge sensor on the tunneling process is assumed to be negligible.

The two MBS are described by normalized second-quantized operators γ, which follow the Majorana fermion rules $\gamma_i = \gamma_i^\dagger$ and $\gamma_i^2 = 1$ for $i = 1, 2$. From these, we define a non-local Dirac fermion, with annihilation/creation operators $f = (\gamma_1 + i\gamma_2)/2$, $f^\dagger = (\gamma_1 - i\gamma_2)/2$. The MBS parity state is encoded as a single fermionic mode $|m\rangle$, where $m \in \{0, 1\}$ is the occupation number of the non-local Dirac fermion.

A charge state with N electrons on the QD, $|N\rangle$, is associated with electrostatic energy E_N. For even N, electrons are paired and form the spin singlet state $|S\rangle$; for odd N the excess electron gives an overall spin-up $|\uparrow\rangle$ or spin-down $|\downarrow\rangle$ state. A Zeeman splitting is induced for odd N by the applied magnetic field $\vec{B}$. Figure 6.1b shows the QD energy level diagram.

Without loss of generality, let the QD ground state consist of an even number of electrons n. The minimal model of the system consists of three fermionic modes: one each for spin-up and spin-down excitation on the QD and one for the MBS parity state. The charge on the QD is restricted to n, $n + 1$, or $n + 2$ electrons, which is made possible with a suitable choice for the gate voltage V_g. The $n \leftrightarrow n+1$ charge transition of the dot is later brought into resonance with the MBS, and used for parity readout. Charge transitions to the $n - 1, n + 2$ states, however, are not resonant because of energy separations on the order of the Coulomb charging energy, a few meV. This justifies excluding the $n - 1$ state from the model. The $n + 2$ state corresponds to both spin modes on the QD being occupied and is therefore included in the model, but its occupation probability remains negligibly small. This minimal model describes the system with an eight-dimensional Hilbert space, which is sufficient to capture the relevant dynamics while also being small enough for efficient numerical simulation.

The basis states are represented by $|N, \sigma, m\rangle$ where, $N \in \{n, n + 1, n + 2\}$, $\sigma \in \{S, \uparrow, \downarrow\}$, $m \in \{0, 1\}$. However, it must be kept in mind that only the spin singlet is allowed for $N = n, n + 2$, while for $n + 1$ the singlet is disallowed.

The Hamiltonian is composed of four terms: $\mathcal{H} = \mathcal{H}_q + \mathcal{H}_s + \mathcal{H}_m + \mathcal{H}_t$, where the first three terms are diagonal and represent the dot charge, dot spin, and MBS energies, and $\mathcal{H}_t$ represents

the tunnel coupling between the QD and MBS, which can depend on the spins of both systems. The dot charge term is

$$\mathcal{H}_q|N\rangle = E_N|N\rangle,$$

where the constant interaction [259] energy $E_N = -eV_gN + \frac{U}{2}N(N-1)$ is used. V_g is the voltage on the plunger gate and U is the Coulomb charging energy. The remaining terms are:

$$\begin{aligned}
\mathcal{H}_s &= \frac{\delta}{2}(|\uparrow\rangle\langle\uparrow| - |\downarrow\rangle\langle\downarrow|), \\
\mathcal{H}_m &= \frac{\epsilon}{2}(f^\dagger f - \frac{1}{2}), \\
\mathcal{H}_t &= [\lambda_\uparrow(d_\uparrow - d_\uparrow^\dagger) + \lambda_\downarrow(d_\downarrow + d_\downarrow^\dagger)](f^\dagger + f),
\end{aligned}$$

where $\delta = g\mu_B B$ is the Zeeman energy of the dot spin, ϵ is the MBS energy splitting (which depends on the MBS separation L), $d_\sigma(d_\sigma^\dagger)$ annihilates (creates) an electron with spin σ on the dot, λ_σ is the strength of the spin-dependent dot-MBS tunnel coupling, and $f, f^\dagger$ describe the non-local fermion defined previously. A matrix representation of the d_σ, f operators is given in Section 6.3.1.

The spin polarization direction of the MBS depends on the relative strengths of the spin-orbit field of the nanowire and the Zeeman energy due to the external magnetic field [7, 260]. If dominated by the Zeeman energy due to the axial magnetic field, the MBS spin will be polarized along the $\pm\hat{x}$ (axial) direction. By contrast, for the spin-orbit dominated case, it will be polarized along the $\pm\hat{y}$ direction (in-plane, perpendicular to the nanowire axis). The MBS readout procedure is equally applicable to both cases, as explained below.

The QD-MBS tunnelling constant λ_σ depends on the spins of both systems. An MBS spin along the $\pm\hat{x}$ direction is only coupled to one spin state on the dot. Specifically, $\lambda_\downarrow = \lambda, \lambda_\uparrow = 0$ for the $-\hat{x}$ direction, and $\lambda_\uparrow = \lambda, \lambda_\downarrow = 0$ for the $+\hat{x}$ direction. In contrast, an MBS spin along $\pm\hat{y}$ direction will couple to the two $\pm\hat{x}$ spins on the QD equally [250], e.g. $\lambda_\uparrow = \lambda/\sqrt{2}$ and $\lambda_\downarrow = -i\lambda/\sqrt{2}$ for the $-\hat{y}$ direction. For a generic MBS spin polarization (used below), λ_σ will be in between these two limiting cases. Spin rotations induced by the nanowire spin-orbit interaction during the tunneling process are neglected: their effect is to give the tunneling spin a component along $\pm\hat{z}$, which can be captured by assuming an arbitrary MBS spin polarization.

The MBS splitting ϵ is proportional to the overlap of the MBS wavefunctions [32, 82], which are localized at the edges of the topological region. The wavefunctions decay exponentially inside the topological region, with a characteristic length ξ on the order of the phase coherence length inside the nanowire. For $L \gg \xi$, the parity states are sufficiently degenerate for topological protection of the system. As L is shortened, the splitting oscillates within an exponentially

increasing envelope, as described in ref. [82]. This is illustrated qualitatively in Figure 6.1c. In the regime $L \gtrsim \xi$, ref. [82] gives the splitting as a function of L as:

$$\epsilon(L) \approx \hbar^2 \tilde{k}_F \frac{e^{-2L/\xi}}{m^* \xi} \cos \tilde{k}_F L, \tag{6.1}$$

where $\tilde{k}_F$ is the effective Fermi wavevector of the MBS wavefunctions inside the nanowire, and m^* is the effective electron mass. We show in the next section how a series of experiments can be used to map out $\epsilon(L)$. Precise knowledge of this function is required for the MBS parity readout scheme described in Section 6.5.

6.3.1 Matrix Representations

Recall that the system state is represented by $|N, \sigma, m\rangle$ where, $N \in \{n, n+1, n+2\}$, $\sigma \in \{S, \uparrow, \downarrow\}$, $m \in \{0, 1\}$. It must be kept in mind that some combinations of (N, σ, m) do not correspond to physically allowed states. It is therefore convenient to represent the state of the QD in terms of its fermionic modes as a Fock state: $|s_\uparrow, s_\downarrow\rangle$, where $s_\uparrow, s_\downarrow \in \{0, 1\}$. Connecting the two representations, we observe that $|n, S\rangle = |0, 0\rangle$, $|n+1, \uparrow\rangle = |1, 0\rangle$, $|n+1, \downarrow\rangle = |0, 1\rangle$, and $|n+2, S\rangle = |1, 1\rangle$. The total Fock state, including the mode corresponding to the MBS parity state, is given by including a third fermionic mode labelled by m. The matrix representation of operators on the combined MBS-dot system are then constructed via the standard formalism of second quantization.

In general, for *n* fermionic modes, the creation and annihilation operators of the *n*th mode, $a_n^\dagger$ and a_n, obey the anti-commutation relation $\{a_n, a_n^\dagger\} = \mathbb{I}$. For a single mode, we choose:

$$a = \begin{pmatrix} 0 & 0 \\ 1 & 0 \end{pmatrix}, \quad a^\dagger = \begin{pmatrix} 0 & 1 \\ 0 & 0 \end{pmatrix}, \tag{6.2}$$

and represent the associated Fock states as

$$|0\rangle = \begin{pmatrix} 0 \\ 1 \end{pmatrix}, \quad |1\rangle = \begin{pmatrix} 1 \\ 0 \end{pmatrix}. \tag{6.3}$$

The creation and annihilation operators for different modes anti-commute: $\{a_n, a_m^\dagger\} = \{a_n, a_m\} = \{a_n^\dagger, a_m^\dagger\} = 0$, for $n \neq m$. For our model consisting of three fermionic modes, the single mode operators are extended in the usual way to the full eight-dimensional Hilbert space

in keeping with these relations:

$$d_\uparrow = a \otimes \sigma_z \otimes \sigma_z, \tag{6.4}$$
$$d_\downarrow = \mathbb{I} \otimes a \otimes \sigma_z, \tag{6.5}$$
$$f = \mathbb{I} \otimes \mathbb{I} \otimes a, \tag{6.6}$$

where σ_z is the Pauli z-matrix, and similarly for the creation operators. The Fock states on the full Hilbert space are likewise constructed as tensor products of $|0\rangle$ and $|1\rangle$.

We shift $\mathcal{H}_q$ by $-E_n\mathbb{I}$ so that its ground state has zero energy. Thus, letting $E'_n = 0$, $E'_{n+1} = -eV_g + UN$, and $E'_{n+2} = -2eV_g + U(2N+1)$, we have the following expressions for the terms in the Hamiltonian:

$$\begin{aligned}\mathcal{H}_q = \text{diag}(&E'_{n+2}, E'_{n+2}, E'_{n+1}, E'_{n+1},\\ &E'_{n+1}, E'_{n+1}, E'_n, E'_n),\end{aligned} \tag{6.7}$$

$$\begin{aligned}\mathcal{H}_s = \text{diag}(&0, 0, \delta/2, \delta/2,\\ &-\delta/2, -\delta/2, 0, 0),\end{aligned} \tag{6.8}$$

$$\begin{aligned}\mathcal{H}_m = \text{diag}(&\epsilon/2, -\epsilon/2, \epsilon/2, -\epsilon/2,\\ &\epsilon/2, -\epsilon/2, \epsilon/2, -\epsilon/2),\end{aligned} \tag{6.9}$$

$$\mathcal{H}_t = \lambda/\sqrt{2} \begin{pmatrix} 0 & 0 & 0 & -i & 0 & -1 & 0 & 0 \\ 0 & 0 & i & 0 & 1 & 0 & 0 & 0 \\ 0 & -i & 0 & 0 & 0 & 0 & 0 & 1 \\ i & 0 & 0 & 0 & 0 & 0 & -1 & 0 \\ 0 & 1 & 0 & 0 & 0 & 0 & 0 & -i \\ -1 & 0 & 0 & 0 & 0 & 0 & i & 0 \\ 0 & 0 & 0 & -1 & 0 & -i & 0 & 0 \\ 0 & 0 & 1 & 0 & i & 0 & 0 & 0 \end{pmatrix}. \tag{6.10}$$

Here, H_t has been written for MBS polarization along the $-\hat{y}$ direction, i.e. for tunneling constants $\lambda_\uparrow = \lambda/\sqrt{2}$, $\lambda_\downarrow = -i\lambda/\sqrt{2}$. Using these matrix representations of the states and

operators, the time dependent Schrödinger equation was solved numerically using the QuTiP module for Python 2.7 [261].

As described in the main text, the resonant tunnelling process used here only involves the spin-down state of the QD, and transitions to the spin-up state do not occur through our choice of the dot gate voltage V_g.

6.4 MBS Energy Splitting

In Section 6.4.1, we describe how to measure the MBS splitting ϵ at fixed L using resonant tunneling with the QD. In Section 6.4.2, L is varied to show how the function $\epsilon(L)$ is mapped out. Parameters relevant to InSb nanowires are used throughout this chapter, as listed in table 6.1. The results of this chapter do not depend strongly on the values of these parameters; rather they are chosen for their experimental relevance. We assume the quantum dot charging energy is $U = 5$ meV, and an effective superconducting gap of $\Delta = 0.5$ meV opens in the regions of the nanowire proximate to the superconductor. This value of Δ is chosen conservatively to pertain to experiments involving Nb, which has a superconducting gap of 1.4 meV. No sub-gap states (other than the two-fold degenerate MBS) are assumed to exist at energies below Δ. An external axial magnetic field $\vec{B} = B\hat{x}$ of magnitude $B = 0.75$ T induces topological order in the superconducting section of the nanowire, where a chemical potential $\mu = 2$ meV is assumed. The spin-orbit energy in InSb nanowires is expected [39] to be in the range $0.25 - 1$ meV, smaller than the Zeeman splitting $\delta = 2.0$ meV at $B = 0.75$ T. A temperature $T = 50$ mK is used. Thus, the thermal energy k_BT is much smaller than the superconducting gap, $k_BT \ll \Delta$, and also the topological gap $k_BT \ll |\delta - \sqrt{\mu^2 + \Delta^2}|$. Under these conditions, the low energy states of the topological superconductor (i.e. the MBS) are well separated from all higher energy states, including the bulk superconducting states. The MBS are therefore isolated from the superconducting 'lead'. As the quantum dot in our scheme is also isolated from metallic leads, we assume that temperature plays no role in the tunneling, which occurs between two isolated two-level systems.

6.4.1 Fixed MBS Separation

We fix the MBS pair separation so that the energy splitting ϵ at a value ϵ^* smaller than the (proximity) superconducting gap Δ, hence the MBS do not couple to the continuum of quasiparticle states. The $|1\rangle, |0\rangle$ MBS parity states are then at energies $+\epsilon^*/2, -\epsilon^*/2$ respectively. The gate voltage V_g is tuned so that the number of electrons on the QD is n, as measured by the charge sensor.

T (mK)	B (T)	m^* (m_e)	g	k_BT (μeV)	ϵ^*	Δ (meV)	δ	μ	U
50	0.75	0.014	50	4.3	$20-50$	0.5	2.0	2.0	5.0

Table 6.1: Fixed parameters used throughout this chapter, chosen based on their relevance to experiments on proximitized InSb nanowires. T is the temperature (k_B is Boltzmann's constant), B the external axial magnetic field, m^* the effective electron mass (in units of free electron mass m_e), and g the Landé factor on the QD. Columns 5–10 show energies in ascending order: the thermal energy k_BT is the lowest, followed by maximum MBS splitting ϵ^*, proximity superconducting gap Δ, Zeeman splitting δ, chemical potential inside the InSb nanowire μ, and QD charging energy U. The MBS parity readout procedure does not depend critically on these values, and is feasible over a large range of energy scales as long as the conditions $k_BT \ll \Delta$ and $k_BT \ll |\delta - \sqrt{\mu^2+\Delta^2}|$ hold.

Consider an initial MBS parity state $|1\rangle$, so the initial state of the system is $|\psi_i\rangle = |n, S, 1\rangle$. The process $|n, S, 1\rangle \leftrightarrow |n+1, \sigma, 0\rangle$ is resonant when ϵ^* equals the energy cost $\Delta E_{n,\sigma}$ of the $|n, S\rangle \rightarrow |n+1, \sigma\rangle$ transition of the dot, with $\sigma = \uparrow$ or $\downarrow$. From the constant interaction model, we have $\Delta E_{n,\sigma} = -eV_g + nU \pm \delta/2$, where the Zeeman energy $\delta = g\mu_B B$ enters with a plus (minus) sign for $\sigma = \uparrow$ ($\downarrow$). Determining ϵ^* is based on finding the resonant gate voltage V^*. The value for the resonant gate voltage depends on the initial MBS parity state: had we started with the other parity state $|0\rangle$, both processes $|n, S, 0\rangle \leftrightarrow |n+1, \sigma, 1\rangle$ and $|n, S, 0\rangle \leftrightarrow |n-1, \sigma, 1\rangle$ would have been *off-resonance* at the V^* mentioned above. The first of the two processes is resonant at $V_g = V^* + 2\epsilon^*/e$ and the latter at $V_g = V^* + \delta/e - U/e$. This allows the MBS-dot setup to distinguish between the two MBS parity states.

Note that, due to Zeeman splitting of the spin levels of the QD, there are generally two possible values for V^*, labelled V^*_σ for $\sigma = \uparrow, \downarrow$. Without loss of generality, we focus on the lower resonance voltage $V^*_\downarrow$ from this point onwards. Hence, we use the shorthand notation λ to refer to $\lambda_\downarrow$, the tunnel coupling strength to the spin down state of the QD. For a generic MBS spin polarization direction, a second resonance voltage $V^*_\uparrow$ is present at $V^*_\uparrow = V^*_\downarrow + \delta/e$, but not used. The procedure can be readily extended to the special case of spin polarization along the $\pm\hat{x}$ axis, where only one resonant voltage is present: $V^*_\downarrow$ for the $-\hat{x}$ and $V^*_\uparrow$ for the $+\hat{x}$ directions, respectively. We now turn our attention to finding ϵ^*.

A procedure for determining ϵ^* is depicted in Figure 6.2, and is comprised of three steps: (i) The system starts in the state $|\psi_i\rangle$ with V_g tuned to an initial value V_0, and V_t at a large negative value so that tunneling between the MBS and QD is suppressed. At $t = 0$, the tunnel coupling is turned on to a value $\lambda = h \times 100$ MHz by tuning V_t. Then, at $t = 2$ ns, V_g is rapidly ramped up to a trial value V^{trial}, such that $\lambda^2 \ll \hbar e|d(V_g)/dt|$ at all times t, i.e. the state

	λ/h (MHz)	$d(eV_g)/dt$ (meV/ns)	$d(\epsilon)/dt$ (meV/ns)	$\frac{(\Delta-\epsilon)^2}{\hbar d(eV_g)/dt}$	$\frac{(\Delta-\epsilon)^2}{\hbar d(\epsilon)/dt}$	$\frac{\lambda^2}{\hbar d(eV_g)/dt}$
Calibration	100	0.2	–	1.5×10^3	–	1.3×10^{-3}
Readout – 1	100	1.3	0.8	2.3×10^2	3.8×10^2	2.0×10^{-4}
Readout – 2	1000	1.3	0.8	2.3×10^2	3.8×10^2	2.0×10^{-2}

Table 6.2: Tunneling rate λ/h, maximum sweep rates of gate voltage energy $d(eV_g)/dt$ and MBS splitting energy $d(\epsilon)/dt$, and adiabaticity condition estimates, for three procedures discussed in the main text. "Calibration" refers to procedure for finding $\epsilon^*(L)$ in Section 6.4.1; "Readout – 1" refers to the MBS parity readout procedure discussed in detail in Section 6.5, and "Readout – 2" to the procedure at the end of Section 6.5 with $\lambda/h = 1$ GHz. The probabilities of transitions between energy levels due to V_g, ϵ sweeps are calculated accurately in the numerical TDSE simulations. The Landau-Zener formula $\exp(-2\pi\Gamma)$ is used here to illustrate rough (order-of-magnitude) estimates of the adiabaticity conditions. The dimensionless quantity Γ compares the level repulsion of the anti-crossing energy levels with the rate of sweep of the energy level. It is explicitly given in the column headers pertaining to transitions to higher energy states due to V_g sweep (Column 4), ϵ sweep (Column 5), and resonant dot-MBS state transfer (Column 6). A large number indicates a low probability of transition across the energy gap, whereas a small number indicates a high transition probability. Columns 4, 5: The probability of excitation of the MBS to a state within the continuum of states above and below $\pm|\Delta|$ is expected to be negligibly small, i.e. the sweeps rates given for V_g and ϵ are well within the adiabatic regime. This is confirmed in our numerical TDSE simulations. Column 6: The sweep rate of V_g is fast compared to the tunnel repulsion λ of the anti-crossing resonant states $|n, S, 1\rangle, |n+1, \downarrow, 0\rangle$, allowing an equal superposition to form with high probability. Thus, Rabi oscillations can occur as described in Section 6.4.1.

evolution is fast and non-adiabatic. This point is further discussed below. (ii) V_g is held constant for the duration T^{trial}, then (iii) rapidly ramped down to its initial value. The tunnel coupling is then turned off at $t = 7$ ns. Figure 6.2a shows V_g versus time, with $(V^{\text{trial}}, T^{\text{trial}}) = (V^*, T^*)$, the values which produce resonant MBS-dot charge transfer for the chosen system parameters. The corresponding probability for charge transfer is shown in Figure 6.2b.

Rapid sweep of V_g and Rabi oscillations – Let us explore the resonant state transfer process (Figure 6.2a) in more detail. Starting at V_0, V_g is swept to $V_\downarrow^*$. At this gate voltage, the states $|n, S, 1\rangle$ and $|n+1, \downarrow, 0\rangle$ anti-cross due to the tunnel coupling λ. Note that V_g is swept rapidly compared to the level repulsion λ, i.e. $\lambda^2 \ll \hbar e|d(V_g)/dt|$; however, it is swept *adiabatically* slowly with respect to the continuum of states above the proximity gap:

$|\Delta - \epsilon|^2 \gg \hbar e|d(V_g)/dt|$. Therefore, the probability of exciting to higher energy states is negligibly small. This is shown quantitatively in table 6.2.

At the anti-crossing point, the eigenstates of the system are $|\pm\rangle = (\sqrt{2})^{-1}(|n, S, 1\rangle \pm |n+1, \downarrow, 0\rangle)$. However, since V_g was swept rapidly, the system stays in its initial state $|\psi_i\rangle = |n, S, 1\rangle = (\sqrt{2})^{-1}(|+\rangle + |-\rangle)$. A Rabi oscillation occurs in the $\{|+\rangle, |-\rangle\}$ subspace, and after time T^* the state of the system is $(\sqrt{2})^{-1}(|+\rangle - |-\rangle) = |n+1, \downarrow, 0\rangle$, up to an unimportant global phase. The system stays in this state after a rapid sweep of V_g away from the anti-crossing point. Figure 6.2b shows the simulated outcome of this process, obtained by numerically solving the time-dependent Schrödinger equation (TDSE) to find $|\psi(t)\rangle$, the system state at time t. The quantity of interest is the probability of finding the dot in the $n+1$ charge state (with either spin), $\Pi_{n+1}(t) = \sum_{\sigma=\uparrow,\downarrow} |\langle n+1, \sigma, 0|\psi(t)\rangle|^2$. It can be seen that Π_{n+1} goes from zero to $> 99\%$.

By comparison, panels c,d of Figure 6.2 pertain to the case of off-resonance charge transfer. For the same value of the initial gate voltage V_0 as in panel a, panel c shows V_g versus time when $V^{\text{trial}} = V_\downarrow^* + 2$ μV and $T = T^* - 1$ ns (curve '***a***'), $T^{\text{trial}} = T^*$ and $V^{\text{trial}} = V_\downarrow^* - 1$ μV (curve '***b***'), $V^{\text{trial}} = V_\downarrow^*$ and $T^{\text{trial}} = T^* + 1$ ns (curve '***c***'). The corresponding Π_{n+1} values are shown in Figure 6.2d, and indicate significant decreases compared to Figure 6.2b. The results indicate that the precision required for external control of voltage and time should be at the 100 nV and 100 ps levels, respectively, for a transfer probability close to 1. Both requirements can be satisfied with current technologies.

A small ripple oscillation can be seen in figures 6.2b and 6.2d. This is due to a finite off-resonant dot-MBS coupling when the initial voltage V_0 is not very far from the resonant voltage $V_\downarrow^*$. In figures 6.2b and 6.2d, the $V_\downarrow^* - V_0$ is only 20 μV. In Section 6.5, we use a much larger value ~ 1.3 mV for this difference and find that the ripple is no longer observed.

Measurement of ϵ^* — To determine $V_\downarrow^*$ and T^*, one would repeat the sequence (i-iii) many times for each set of trial input parameters, each time measuring the charge state of the dot using the SET after step (iii). The frequency of the $|n+1\rangle$ outcomes yields an estimate of Π_{n+1}. The parameter space (V, T) is then surveyed to find the resonant tunneling time $T^* = h/\lambda$ and resonant gate voltage $V_\downarrow^*$. The MBS splitting is given by

$$\epsilon^* = -eV_\downarrow^* + nU - \delta/2.$$

Mixture of parity states — The calibration procedure as described here assumes the ability to reliably prepare the MBS in a particular parity state. Suppose, instead, that one can only prepare the MBS in a statistical mixture $\rho = p|0\rangle\langle 0| + (1-p)|1\rangle\langle 1|$. Then, due to the sharp dependence of transition probability on V_g, the procedure is still effective at measuring ϵ^*. We note that if $V_\downarrow^*$ is the resonant gate voltage for the $|1\rangle \to |0\rangle$ parity transition process, then the

$|0\rangle \to |1\rangle$ process will be resonant at $V_g = V_\downarrow^* + 2\epsilon^*/e$. Thus, one would observe two peaks in $\Pi_{n+1}(t)$ of height p and $1-p$, separated by $2\epsilon^*$ along the V_g-axis. Peaks corresponding to the spin-up state of the QD will generally be visible as well (for MBS spin polarization not along $\hat{x}$), at $V_\uparrow^* = V_\downarrow^* + \delta/e$.

6.4.2 Energy Splitting versus MBS Separation

The procedure outlined in the previous section may be repeated for a variety of L values using the keyboard gates, thereby allowing the experimenter to map out the oscillatory function $\epsilon(L)$. In Section 6.6.1, we estimate a typical spatial period of the oscillations of ϵ to be ~ 30 nm. Therefore, reliably varying ϵ with a precision ~ 100 neV requires tuning L (e.g. using keyboard gates) with a precision at the ~ 1 nm level.

Empirical measurement of the function $\epsilon(L)$ is itself desirable, as it is a direct test of the validity of Eq. 6.1. Indeed, in ref. [47], ϵ is measured for several devices of different lengths, where an exponential envelope in $\epsilon(L)$ is observed. Performing a similar experiment in a single device with varying L would provide stronger evidence for the non-local nature of the MBS wavefunctions and the presence of topological order. The search over the (V, T) parameter space at each L point can be speeded up by noting that T^* depends only on the tunnel coupling strength λ (Section 6.6.1), which can be assumed constant, reducing the optimization to a one dimensional search for $V_\downarrow^*$ once T^* is known.

Along with the dependence of ϵ on MBS separation, the dependence of ϵ on other physical parameters such as the strength of the Zeeman field and the chemical potential may be mapped out. Although only the L-dependence is required for our proposed read out scheme, the model for the MBS system described in ref. [82] may be empirically tested with respect to several independent variables. Below, we describe how knowledge of the function $\epsilon(L)$ may be used for readout of the MBS parity state.

6.5 Parity Readout

Initial state — The keyboard gates separate the two MBS by $L_i = 5\,\mu$m where the two parity states are degenerate to within $0.5\ \mu\text{eV} \ll k_B T \simeq 4.3\ \mu\text{eV}$, given the parameters we have chosen. From data collected by the calibration procedure in Section 6.4.2, a target readout length L_f for the topological wire is chosen. At L_f, the MBS splitting $\epsilon(L_f)$ is such that $\epsilon(L_f) > \epsilon(L)$ for all $L > L_f$, so L_f corresponds to a local peak of the function $\epsilon(L)$. For the numerical calculation of the TDSE, we choose $L_f = 0.775\,\mu$m, resulting in $\epsilon(L_f) = 49\,\mu$eV. The optimal

gate voltage $V_{\downarrow}^{*}$ at L_f for resonance with the spin-down dot state is assumed to be known, based on the calibration procedure above. Since L_f corresponds to a peak in $\epsilon(L)$, resonance with the dot does not occur for $L > L_f$. The dot is initially in the $|n, S\rangle$ state, where we have arbitrarily chosen $n = 20$. The gate voltage V_g is initially held at a value $V_0 = (1/e)U(n-1/2)$, halfway between the $(n+1) \leftrightarrow n$ and $n \leftrightarrow (n-1)$ charge degeneracy points of the QD, so $V_{\downarrow}^{*} - V_0 = (1/e)(U/2 - \delta/2 - \epsilon) \simeq 1.3$ mV. To restrict the dot to the $\{|n\rangle, |n+1\rangle\}$ charge states, it is necessary that V_g is kept within the range $(n-1)U + \epsilon + \delta/2 < eV_g \leq eV_{\downarrow}^{*} = nU - \epsilon - \delta/2$ at all times.

MBS Parity readout procedure — With the system in its initial configuration, there are three stages of the read out, labelled (i), (ii), and (iii) in Fig. 6.3. In Fig. 6.3a, the MBS separation L, and the energy splitting $\epsilon(L)$ are shown as a function of time. Fig. 6.3b shows the gate voltage V_g, and the simulated probability $\Pi_{n+1}(t) = \sum_{\sigma=\uparrow,\downarrow} |\langle n+1, \sigma, 0|\psi(t)\rangle|^2$, with the MBS initially in the $|1\rangle$ parity state. Considering each stage in turn:

Stage (i): The keyboard gates move the left MBS towards the tunnel coupled end so that the MBS separation is reduced from $L_i = 5\,\mu$m to $L_f = 0.775\,\mu$m. This is performed uniformly over a duration of 10 ns in our calculation. Table 6.2 shows that the adiabaticity condition $|\Delta - \epsilon|^2 \gg \hbar|d\epsilon/dt|$ is satisfied at all times, so the probability of coupling to the continuum of quasi-particle states above and below Δ is negligible. Note that this step could be carried out as much as ~ 100 times more slowly without affecting the results. The process of moving the left MBS can possibly incur dephasing errors within the $|0\rangle, |1\rangle$ parity basis. However, this does not adversely affect the readout procedure in any regard, as the readout is performed in the same parity basis. The parity eigenstates are *preserved* under this transformation, as their levels cross but do not couple. At the end of this stage, V_g controlling the dot potential is rapidly switched from V_0 to $V_{\downarrow}^{*}$. As discussed in table 6.2, this transition is rapid with respect to λ (so Rabi oscillation occur as explained in Section 6.4.1), but adiabatic with respect to $|\Delta - \epsilon|$, so there is negligible chance of excitation to higher energy states. In our calculation the voltage ramping time is 1 ns.

Stage (ii): The control parameters are held fixed for the optimal tunneling time T^{*}, which is 2.5 ns in the case simulated here. With the MBS initially in the $|1\rangle$ state, the $|n, S, 1\rangle \leftrightarrow |n+1, \downarrow, 0\rangle$ transition is on resonance, and an electron will tunnel from the topological wire to the dot with transition probability very close to one (Fig. 6.3b).

If, however, the MBS was initially in the $|0\rangle$ state, changing the parity state will *cost* (rather than supply) an energy $\epsilon(L_f)$. The corresponding process, $|n, S, 0\rangle \leftrightarrow |n+1, \downarrow, 1\rangle$, is off resonance — its resonant gate voltage is $V_g = V_{\downarrow}^{*} + 2\epsilon/e$. For the $|0\rangle$ parity state then, the procedure illustrated in Fig. 6.3 would result in an electron transfer probability very close to zero.

Stage (iii): The reverse of stage (i), the gate voltage is rapidly ramped back to V_0 and the

keyboard gates are used to move the left MBS back to its initial position. Note that, whereas sweeping V_g away from the resonance point is necessary in order to prevent the electron from tunneling back to the MBS, moving the left MBS with the keyboard gates is not always required. It is included here to allow the system to recover its initial configuration, in case the cycle is repeated. At this point, a charge measurement of the dot is performed via the charge sensor, e.g. SET. A measurement outcome of $n+1$ indicates with high probability that the initial MBS state was $|1\rangle$ while a measurement of n indicates with high probability that the initial MBS state was $|0\rangle$. Hence, the dot charge measurement amounts to a projective measurement in the MBS parity basis.

6.6 Splitting of MBS Parity States

For our numerical analysis, a theoretical expression for the MBS splitting ϵ as a function of the nanowire length L is taken from ref. [82]:

$$\epsilon(L) \approx \hbar^2 \tilde{k}_F \frac{e^{-2L/\xi}}{m^* \xi} \cos\left(\tilde{k}_F L\right). \tag{6.11}$$

For InSb, we have $g \approx 50$, (Landé g-factor), $m^* = 0.014 m_e$ (effective electron mass) and a spin-orbit length $L_{SO} = 200$ nm. Additionally, the Zeeman field for inducing the topological regime is $B = 0.75$ T with a superconducting gap of $\Delta = 0.5$ meV and a chemical potential of $\mu = 2$ meV. With these parameters, we have an effective coherence length $\xi = 1.71\mu$m and an effective Fermi wavevector $\tilde{k}_F = 4.05 \times 10^7$ m^{-1}. The energy splitting according to Eq. 6.11 is shown in Figure 6.4.

We observe that the spatial period of the oscillations is roughly 30 nm and that for a final nanowire length of $L_f = 0.775$ μ m, the splitting reaches a local maximum of about 50 μ eV.

6.6.1 Period of Resonant Tunnelling Oscillations

As part of the calibration procedure described above, we state that the optimal resonant tunnelling time T^* depends only on the tunnel coupling strength λ. To prove this, we observe that in the range of V_g considered, the MBS-dot system is effectively restricted to the 2D subspace of the full Hilbert space spanned by $\{|n, S, 1\rangle, |n+1, \downarrow, 0\rangle\}$. This effective Hamiltonian restricted to this subspace (and, as above, shifted so $\mathcal{H}_q|n\rangle = 0$) is:

$$\mathcal{H}_{eff} = \begin{pmatrix} \epsilon/2 & -i\lambda/\sqrt{2} \\ i\lambda/\sqrt{2} & -eV_g + UN - \frac{\delta}{2} - \frac{\epsilon}{2} \end{pmatrix}. \tag{6.12}$$

The eigenvalues of this matrix are:

$$E_{\pm} = \frac{E_0}{2} \pm \frac{1}{2}\sqrt{(E_0 - \epsilon)^2 + 2\lambda^2}\,; \tag{6.13}$$

$$\text{where} \quad E_0 = -eV_g + UN - \frac{\delta}{2}. \tag{6.14}$$

The angular frequency for relative phase rotations of the stationary states is therefore

$$\omega = \frac{E_+ - E_-}{\hbar} = \frac{\sqrt{(E_0 - \epsilon)^2 + 2\lambda^2}}{\hbar}, \tag{6.15}$$

which, on resonance between the dot and MBS, reduces to $\omega = \sqrt{2}\lambda/\hbar$. With respect to this subspace, switching V_g between its initial and final values is a diabatic process: as V_g is swept from V_0 to V^*, the system remains in $|n, S, 1\rangle$. On resonance, ω is the frequency of Rabi oscillations between $|n, S, 1\rangle$ and $|n+1, \downarrow, 0\rangle$. The optimal transition time, $T^* = \frac{1}{4\pi\omega}$, depends only on λ.

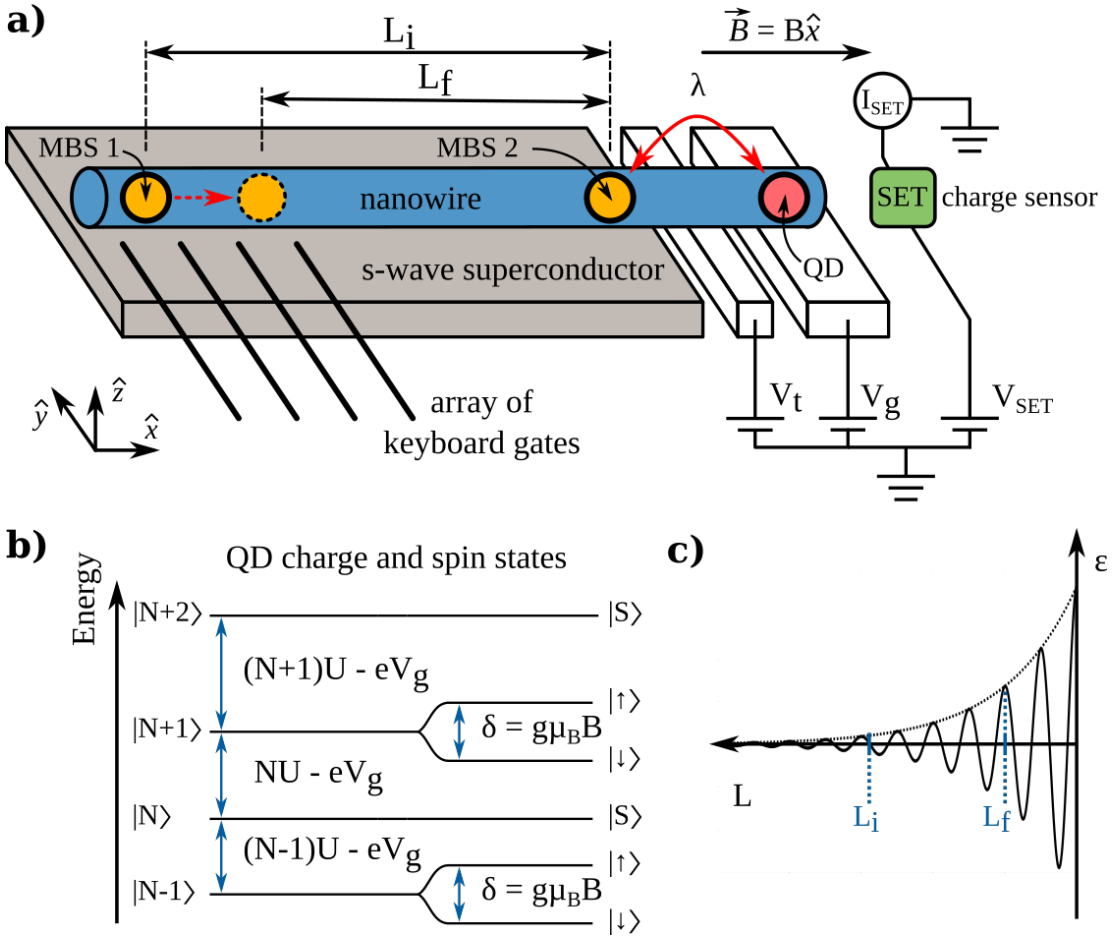

Figure 6.1: (a) Schematic of the proposed device. A bulk s-wave superconductor is in close proximity to a semiconducting nanowire, inducing superconductivity in the nanowire. With the application of an axial (along $\hat{x}$) magnetic field, a pair of MBS appear at the ends of the topological region. An array of keyboard gates can be used to move MBS 1, tuning the MBS spatial separation from L_i to L_f. MBS 2 is tunnel coupled to an isolated quantum dot (QD), with a tunneling strength λ controlled by the gate voltage V_t. The chemical potential of the QD can be tuned using the plunger gate voltage V_g. A charge sensor reads out the charge state of the QD, shown here as a SET with current I_{SET}. (b) Schematic of the energy levels of the QD. U is the charging energy, and the charge state is indicated on the left by number of electrons on the QD. Integer N is arbitrarily chosen to be even. Spin states are indicated on the right, with spin singlets (doublets) occurring for even (odd) charge states. A Zeeman splitting δ is induced between the spin-1/2 states by the external magnetic field. (c) The qualitative behaviour of MBS energy splitting ϵ versus the separation L is oscillatory with an exponential envelope.

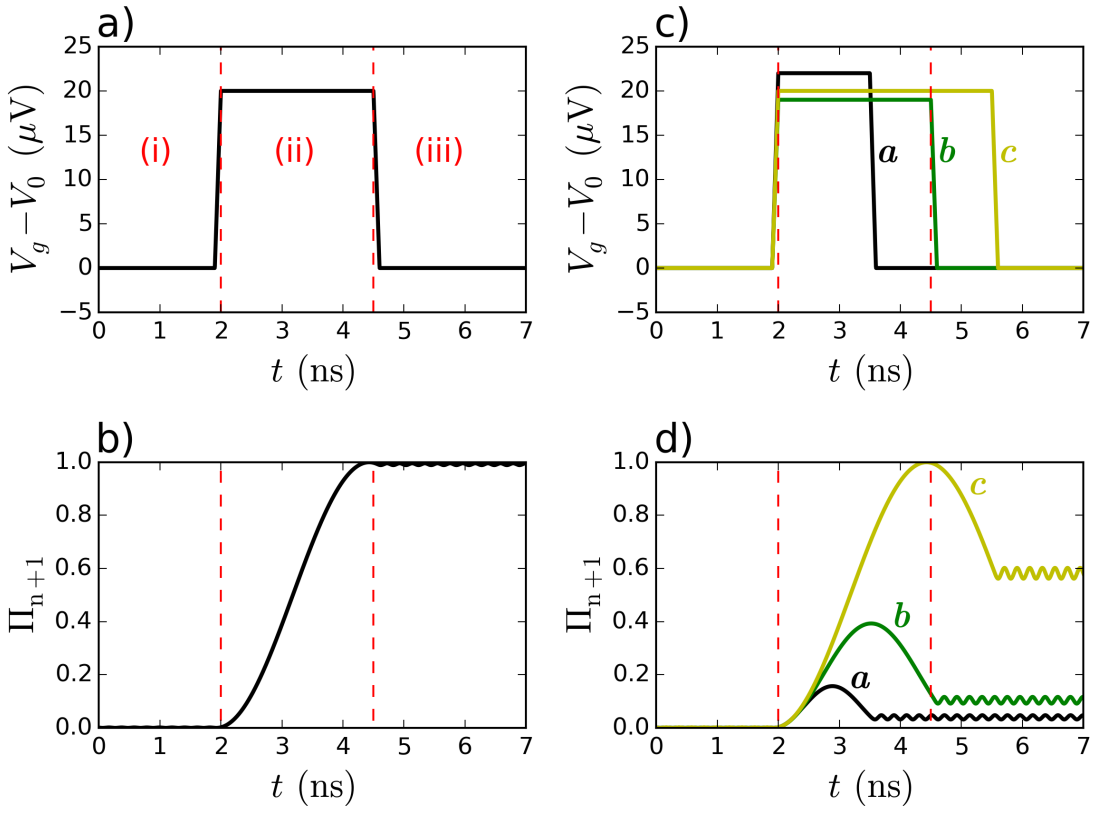

Figure 6.2: Procedure for determining ϵ for a fixed L: gate voltage V_g, and calculated probability of having $n+1$ electrons on the quantum dot, Π_{n+1}, versus time. Panels (a, b) show the case in which the MBS and dot are brought into perfect resonance for the optimal charge transfer time. (a) V_g is raised from the initial value V_0 to the resonance value $V_\downarrow^* = 20\,\mu$V, and held there for the optimal duration $T^* = 2.5$ ns, before being returned to V_0. The sequence is broken into three steps (i-iii). (b) The corresponding probability Π_{n+1} goes from zero to $> 99\%$. Panels (c, d) show three cases involving miscalibration of $V_\downarrow^*$ and T^*. (c) Voltage sequences with $V^{\text{trial}} = V_\downarrow^* + 2\,\mu$V and $T = T^* - 1$ ns (curve '***a***'), $T^{\text{trial}} = T^*$ and $V^{\text{trial}} = V_\downarrow^* - 1\,\mu$V (curve '***b***'), $V^{\text{trial}} = V_\downarrow^*$ and $T^{\text{trial}} = T^* + 1$ ns (curve '***c***'). (d) Probabilities Π_{n+1} corresponding to the sequences in panel (c). In all panels, the vertical dashed lines show the optimal duration T^* for resonant charge transfer. The following parameters are used: $\lambda/h = 100$ MHz, $L = 1.12\,\mu$m, $\mu = 2$ meV, $B = 0.75$ T. These correspond to $\epsilon^* = 20\mu$eV.

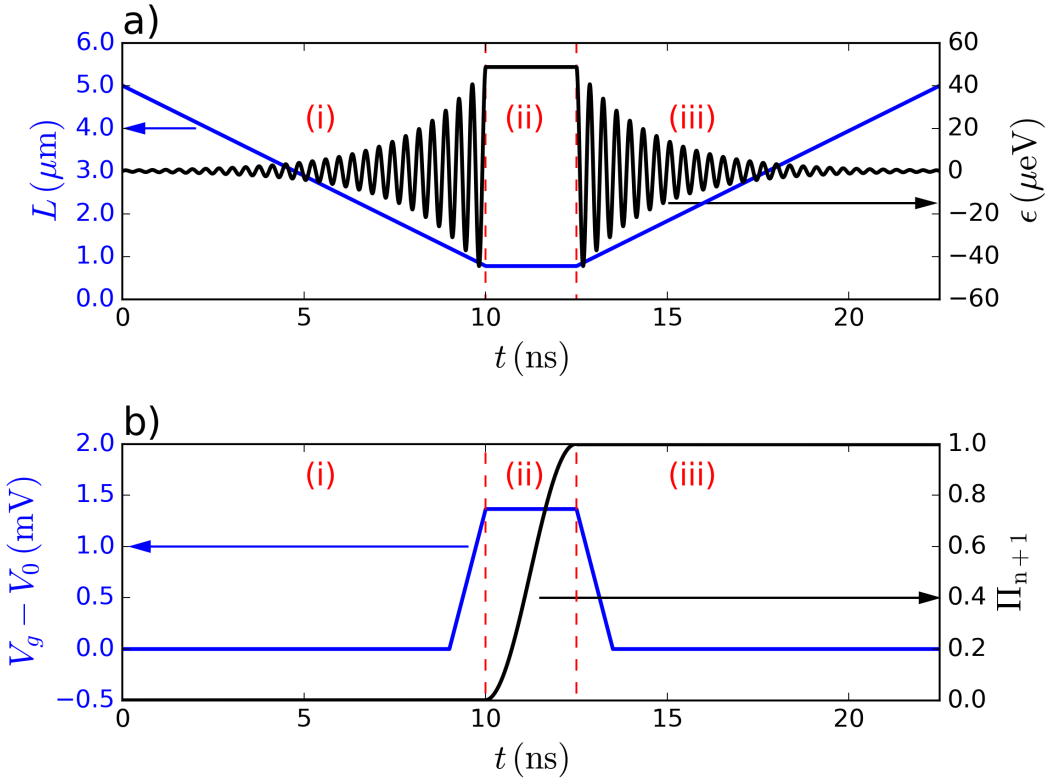

Figure 6.3: Readout procedure (stages i-iii) of the MBS parity state as described in the text. The MBS is initially in the $|1\rangle$ parity state. (a) The MBS separation L (blue/dark grey) and the corresponding MBS splitting $\epsilon(L)$ (black) as predicted from Eq. 6.1. (b) The gate voltage V_g (blue/dark grey) and the calculated probability of adding a charge to the dot, Π_{n+1}, versus time (black). The resonant gate voltage $V_{\downarrow}^{*}$ is known, obtained using the calibration procedure given in Section 6.4.1. As V_g is tuned to $V_{\downarrow}^{*}$, the probability of finding $n+1$ electrons on the dot rises from zero to a value greater than 0.9999. Conversely, if MBS initial state is $|0\rangle$, the maximum Π_{n+1} obtained is 0.004 (not shown). A charge readout of the dot then constitutes a readout of the MBS parity state. A tunneling strength $\lambda/h = 100$ MHz is used in the numerical calculations.

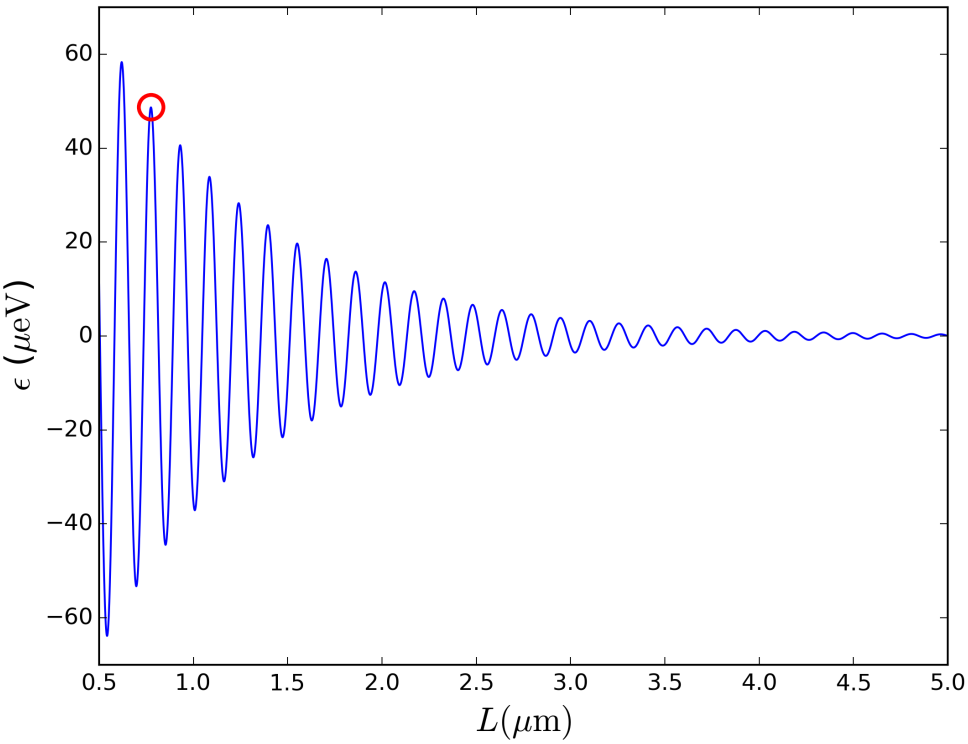

Figure 6.4: Energy splitting of the MBS parity states as a function of the topological wire length L for the parameters given in section B. The parity readout simulated in section IV of the main text used the value indicated by a circle, with $L_f = 0.775\,\mu$m, corresponding to a splitting $\epsilon = 49\,\mu$eV.

6.7 Discussion

Fidelity of readout — Using the parameters given previously and with $\epsilon(L_f) = 49$ μeV, the numerically obtained probability of finding $n+1$ electrons on the dot after stage (iii) is greater than 0.9996 with the MBS initially in $|1\rangle$. The probability of finding n electrons is greater than 0.9999 with the MBS initially in $|0\rangle$. The readout scheme therefore allows the two MBS states to be distinguished with a visibility up to 0.9996, defined simply as the smaller of the two probabilities above. The term 'readout fidelity' is used interchangeably with this measure of visibility. The residual error is dominated by the finite voltage ramping time: a faster ramp would increase the visibility. However, so far we haven't considered limitations on control precision (discussed below), which in practice lead to lower fidelities.

Diabatic errors and readout timescale — The motion of the topological domain wall and its interaction with the disorder potential in a finite-sized system can potentially cause diabatic transitions to high-energy states that will spoil the parity readout. Throughout this chapter we have assumed that diabatic errors do not occur. The dynamics of MBS in the presence of a moving domain wall and disorder potential have been theoretically studied [262, 263, 264, 265], indicating that diabatic errors can be avoided as long as the velocity v of the moving domain wall is below some critical value v_c. Ref. [262] calculates the condition for adiabatic and phase-coherent manipulation of an MBS qubit (i.e., a stronger criterion than strictly required for parity readout) as $v \ll v_c = 2E_{\text{min}}/(\hbar k_F) \simeq 2\alpha\Delta/(\hbar\delta)$, where k_F is the Fermi wave-vector and E_{min} is the value of the system gap at $k = k_F$ (i.e., the minimal eigenenergy of the appropriate Bogoliubov-de Gennes Hamiltonian), α the Rashba spin-orbit strength, Δ the superconducting gap, and δ the Zeeman energy. Using the parameters in Table 6.1, we calculate $v_c = 0.2 - 1.0 \times 10^6$ m.s^{-1}. In comparison, the motion of the domain wall in the parity readout process (fig. 6.3a) occurs at a velocity $v = 4.2 \times 10^2$ m.s^{-1}, so the above condition is satisfied. Based on this, we conclude that the 25 ns sequence shown in fig. 6.3 for the parity-dependent MBS $\rightarrow$ QD tunneling incurs no diabatic errors. On the other hand, single-charge readout of the QD state requires integration times in the range of 0.4 μs [258] to 10 μs [257] or longer and bottlenecks the timescale of the parity readout process.

In the above analysis we have ignored the interaction of the domain wall motion with the disorder potential, which may itself cause diabatic transitions to high-energy states [265]. Such undesirable effects need to be mitigated by using a slower motion of the left MBS. As mentioned above, this can be done up to ~ 100 times slower without seriously affecting our numerical results. In doing so one must also keep in mind the upper limit for the timescale of MBS manipulation due to quasiparticle poisoning [266, 267] (i.e. the lifetime of the parity states). A tight upper bound $\lesssim 100$ ns would pose very serious challenges for MBS parity readout. However, experimental evidence on this front is encouraging, as measurements have indicated (non-topological)

bound-state parity lifetimes exceeding 10 ms in proximitized Al-InAs nanowire devices [268], and ~ 1 minute in NiTiN Cooper-pair boxes [269].

Bias in parity readout due to miscalibration — Throughout the readout operation (stages i-iii), it was assumed that the calibration of $\epsilon(L)$ performed in Section 6.4.2 is valid. Drift or noise in the applied voltage or pulse timing will cause miscalibration errors and bias the charge measurement outcome in favour of n over $n+1$ (see Figure 6.2), i.e. a bias towards detecting $|0\rangle$ over $|1\rangle$ for the MBS parity. However, a straightforward modification of our scheme allows for distinguishing a calibration error from a genuine $|0\rangle$ outcome. This is done by appending a second readout operation involving the $n-1$ charge state of the QD.

Starting with V_g at $V_0 = (1/e)U(n-1/2)$, i.e. halfway between the $(n+1) \leftrightarrow n$ and $n \leftrightarrow (n-1)$ charge degeneracy points of the QD, two parity-to-charge conversions are attempted: First, $|n, S, 1\rangle \rightarrow |n+1, \downarrow, 0\rangle$, by using the resonance at gate voltage $V_{\downarrow}^{*} = V_0 + (1/e)(U/2 - \delta/2 - \epsilon)$ as described previously. Subsequently, the $|n, S, 0\rangle \rightarrow |n-1, \downarrow, 1\rangle$ transition is made resonant at $V_g = V_0 + (1/e)(-U/2 + \delta/2 + \epsilon)$. Then, the charge sensor is used to perform a charge readout of the QD. The following outcomes can be distinguished: $n+1$ electrons indicates with high probability that the initial MBS state was $|1\rangle$, while $n-1$ indicates $|0\rangle$. The outcome n indicates that neither transition took place (i.e. a calibration error), thus providing an *in situ* test for the validity of the readout procedure.

Sensitivity to precision of control — For the system parameters chosen in our simulations, the MBS separation L must be controlled within approximately 1 nm in order to maintain an accuracy $> 99\%$ in distinguishing the parity outcomes. The tolerance can be improved by about a factor of three by choosing parameters at the edge of the topological phase region, which corresponds to a period for the MBS energy oscillations about three times longer — however such a case may be less experimentally feasible. Alternatively, the effect of tunnel broadening may be exploited to reduce the sharpness of the resonance condition and increase robustness. For example, we solved the TDSE again with a tunnel coupling strength of 1 GHz, corresponding to "Readout − 2" in Table 6.2. This shows that the stronger tunnel coupling allows a tolerance of ± 4 nm in precision of the MBS location while still maintaining a readout fidelity of $\sim 97\%$, at the cost of reducing T^{*} by a factor of 10. However, a 4 nm error in the case of the 100 MHz tunnel coupling yields a dramatically lower visibility of $\sim 3\%$. Hence, there is a tradeoff between the required precision of spatial control of the MBS separation versus the timing precision of gate voltage control.

6.8 Conclusions

We examined theoretically a protocol to read out the parity of an MBS pair in a topological superconductor using an isolated quantum dot. The MBS pair is brought from a well-separated (topologically protected) state to a spatially overlapping (unprotected) state in which there is a finite energy splitting; one MBS is then resonantly tunnel coupled with the quantum dot. The MBS parity state is projectively measured by a charge measurement of the quantum dot, and we showed that this can be accomplished, in principle, with high fidelity. It is straightforward to extend this to the readout of a logical qubit based on two MBS pairs. This protocol fits naturally into the MBS-dot system, which could be a powerful and versatile setting for achieving scalable control of topological qubits.

As an intermediate step, we discussed a calibration procedure for mapping out the MBS energy splitting versus separation, $\epsilon(L)$. A similar experiment is performed in ref. [47] where an exponential envelope is observed, strongly indicating the presence of topological order. Our setup allows for this experiment to be performed in a parity-protected manner, so that one can test the robustness of the MBS parity state against gate-driven motion of the topological domain wall. As with any projective measurement, the readout protocol can also be used to prepare the MBS into a desired parity eigenstate. The key for both readout and state preparation is that parity eigenstates should be preserved under adiabatic motion of the topological wire.

Chapter 7

Conclusions and Outlook

Our experiments on proximity superconductivity nanowire junction devices have revealed a rich and complex phenomenology of interplaying effects. Exploring and understanding these phenomena are interesting avenues of physics unto themselves, as well as being necessary for any future devices aimed at displaying unambiguous signatures of MZM. Specifically, mastery of the interplay of proximity superconductivity with the Zeeman and SOI effects, which results in effective p-wave pairing [44]; the presence of a non-zero charging energy in spinful Yu-Shiba-Rusinov states; the non-homogeneity of contact couplings in complex YSR behaviour, which doesn't necessarily follow the even-odd effect predicted by simple theoretical models; and the electrostatic landscape of the nanowire are crucial for future MZM research. Specifically, the potential landscape of the device will result in complex subgap state behaviour, as predicted by multiple theory papers, to the extent that a quantized zero-bias conduction peak may no longer be considered an unequivocal signature of the MZM.

In this thesis we explored the experimental signatures of proximity superconductivity in Chapter 2, reporting on the hitherto little-known effect of orbital Josephson effect, which arises from the interplay of proximity superconductivity and the electrostatic landscape of the nanowire. In Chapter 4, further interplay of these effects with Coulomb blockade is explored in devices with charging energies $\sim 10 - -20$ meV, resulting in current-biased YSR states. In Chapter 5, technical improvements including better mobility and contact transparency were achieved, with supercurrent observed at $T = 1.5$ K. Signatures of complex and robust YSR states were observed up to high magnetic fields ~ 3 T. A straightforward description of the YSR states using simple theoretical models was not possible, likely due to the effects of asymmetric superconductive coupling to one of the leads.

While there are ongoing efforts to improve and realize nanowire-based MZM devices, our

future efforts will likely focus on 2 dimensional heterostructures as the platform for MZM [270]. An InAs or InSb 2 dimensional electron gas (2DEG) created in an epitaxially grown heterostructure benefit from higher mobility, better gatability due to larger gate areas, and larger contact areas ideally resulting in less "contact-inhomogeneity" effect. Furthermore, the possibility of epitaxially grown Al in transparent contact with the 2DEG exists [88, 89], and the quality of an ex-situ deposited dielectric may be greatly improved over the nanowire case due to the flatness and cleanness of the surface unto which it is deposited. Unlike nanowires which need to be mechanically deposited in another substrate with a thermally grown oxide, no such "external" factors affect the quality of the electrostatic landscape in 2DEG devices. These advantages come at the trade-off cost of a more complex device fabrication process, with more possibility of error or non-reproducibility in the fabrication stage. Valuable lessons in improving ex-situ deposited contact transparency with the semiconductor carry over from the nanowire case.

A ZBP measurement requires the local tuning of the device so that it is highly conducting in the topological region, but tunnel-coupled to some normal contact for tunneling spectroscopy measurement. This provides a significant challenge in gating — as observed in Chapter 5, highly conductive nanowires are difficult to gate using small local top gates and $\sim$ 50 nm dielectric separation + a global back gate with a $\sim$ 200 nm dielectric separation. This is further complicated in nanowire devices in Refs. [92, 84, 93] with epitaxially contacted superconductors: the presence of the superconductor shields the nanowire from Coulomb effect of the gate. Therefore, some groups have developed an epitaxial contact with covers only 2 or 3 facets of the nanowire [271] — a highly advanced technique which, nevertheless, could negate one of the advantages of epitaxial contacts: uniformity. In such devices, it can be expected that the proximity effect is stronger near the contacted facets of the nanowire compared to the others, similar to the case of ex-situ deposited contacts.

Assuming gating challenges can be effectively overcome in devices based on InAs or InSb 2DEG, we propose the following platform be developed in order to perform several interesting experiments. Assume a double quantum dot device created on the 2DEG, e.g. via top-deposited finger gates [272, 273]. The flexibility in the fabrication of the device allows the quantum dots to be created in an elongated geometry, with the distance between the reservoir leads $\sim 1\mu$m, but the "width" smaller by a factor of 10 or so, resulting in a nanowire-like geometry. The leads can be epitaxial or ex-situ deposited superconductors. Quantum point contacts tune the coupling strengths of the reservoirs to the quantum dots, while plunger gates tune the chemical potential on the quantum dots, and separation gates can tune the double dot system from the regime of a single large dot to that of two separated dots. The effective size of the quantum dots can therefore also be tunable to some extent. A further iteration could be a 3-contact device, with one of the quantum dots contacted to a normal reservoir, and the other one a proximity superconducting quantum dot.

This is a platform on which the complex phenomenology seen in our nanowire devices can be extensively tested and explored. With the system tuned to a large quantum dot regime, Andreev bound states are expected to be observed in a current-biased mode. By tuning the effective size of the quantum dot (therefore the charging energy U) as well as coupling strengths Γ, the device can be tuned from a strong coupling regime showing a supercurrent to a YSR regime. This can be compared to the ABS states in the double quantum dot regime. If the principle of spin-blockade is used to load a known spin state into one quantum dot, the spinful nature of the YSR states can be explored, and compared with the case of a double-occupation dot expected to show a spin singlet. If the effective size of one dot can be made very large so as to resemble a nanowire, it can be expected to show MZM in an axial magnetic field. The second dot and/or the third normal contact can then be used for tunneling spectroscopy. In such a system, the readout scheme detailed in Chapter 6 can also be implemented. If MBS/coherent ABS are observed over a large distance in a large quantum dot resembling a nanowire, a Crossed Andreev reflection experiment can be performed. Finally, if the ABS is created in a large strongly coupled quantum dot in which more than one orbital level is occupied, the Orbital Josephson effect can also be measured.

In Chapter 3 we provided a simple and idealized theory of the Orbital Josephson effect. With the help of our colleagues at the University of Mumbai, this model has been expanded, and the supercurrent of a much more realistic nanowire is calculated using the non-equilibrium Green's functions formalism [169, 274, 275]. Ref. [274] elevates the shortcomings of the shell model used in Chapter 3, and considers a full (non-shell) IsAs nanowire, contacted with Nb, including a fermi wave-vector mismatch at the interfaces, normal reflections at the interfaces, and not relying on an Andreev approximation ($\Delta \ll \mu$). It shows robust Orbital Josephson effect for realistic InAs parameters, and confirms the general findings of Chapter 3. While the exact frequencies of the supercurrent oscillations aren't correctly predicted by the model in Chapter 3, they give the correct order of magnitude, within a factor of ~ 2. Qualitatively, the predicted results are quite similar.

Ref, [275] focuses on the effects of disorder and dephasing, and quantifies the robustness of the device to these effects. The Orbital Josephson effect appears to be robust, with coherence lengths needing to be made smaller than the channel length before it is badly affected — at which point the proximity superconductivity appears to be generally suppressed. The effect appears generally robust against elastic scattering in the nanowire channel as well.

Therefore, Orbital Josephson effect is an important aspect of the complex and rich physics occurring in devices designed to explore MBS. It, as well as other phenomenology mentioned above, need to be further explored before such devices and their physics can be fully understood.

References

[1] E. Majorana, "A symmetric theory of electrons and positrons," *Soryushiron Kenkyu* **63** (1981) 149. Translation from Nuovo Cimento 14:171, 1937.

[2] F. T. Avignone, S. R. Elliott, and J. Engel, "Double beta decay, majorana neutrinos, and neutrino mass," *Rev. Mod. Phys.* **80** (Apr, 2008) 481–516. https://link.aps.org/doi/10.1103/RevModPhys.80.481.

[3] L. Fu and C. L. Kane, "Superconducting proximity effect and majorana fermions at the surface of a topological insulator," *Phys. Rev. Lett.* **100** (Mar, 2008) 096407. https://link.aps.org/doi/10.1103/PhysRevLett.100.096407.

[4] C. Nayak, S. H. Simon, A. Stern, M. Freedman, and S. Das Sarma, "Non-abelian anyons and topological quantum computation," *Rev. Mod. Phys.* **80** (Sep, 2008) 1083–1159. http://link.aps.org/doi/10.1103/RevModPhys.80.1083.

[5] J. Alicea, "Majorana fermions in a tunable semiconductor device," *Phys. Rev. B* **81** (Mar, 2010) 125318. http://link.aps.org/doi/10.1103/PhysRevB.81.125318.

[6] R. M. Lutchyn, J. D. Sau, and S. Das Sarma, "Majorana fermions and a topological phase transition in semiconductor-superconductor heterostructures," *Phys. Rev. Lett.* **105** (Aug, 2010) 077001. http://link.aps.org/doi/10.1103/PhysRevLett.105.077001.

[7] Y. Oreg, G. Refael, and F. von Oppen, "Helical liquids and majorana bound states in quantum wires," *Phys. Rev. Lett.* **105** (Oct, 2010) 177002. http://link.aps.org/doi/10.1103/PhysRevLett.105.177002.

[8] T. D. Stanescu, R. M. Lutchyn, and S. Das Sarma, "Majorana fermions in semiconductor nanowires," *Phys. Rev. B* **84** (Oct, 2011) 144522. http://link.aps.org/doi/10.1103/PhysRevB.84.144522.

[9] M. Kardar, *Statistical Physics of Fields*. Cambridge University Press, 2007. https://books.google.ca/books?id=_XQgAwAAQBAJ.

[10] M. Peskin, *An Introduction To Quantum Field Theory*. CRC Press, 2018. https://books.google.ca/books?id=9EpnDwAAQBAJ.

[11] M. Schwartz, *Quantum Field Theory and the Standard Model*. Quantum Field Theory and the Standard Model. Cambridge University Press, 2014. https://books.google.ca/books?id=HbdEAgAAQBAJ.

[12] S. Weinberg, *The Quantum Theory of Fields: Volume 1, Foundations*. Cambridge University Press, 2005. https://books.google.ca/books?id=MSdywQEACAAJ.

[13] J. M. Leinaas and J. Myrheim, "On the theory of identical particles," *Nuovo Cimento Soc. Ital. Fis.* **B** (1977) 37B.

[14] F. Wilczek, "Magnetic flux, angular momentum, and statistics," *Phys. Rev. Lett.* **48** (Apr, 1982) 1144–1146. https://link.aps.org/doi/10.1103/PhysRevLett.48.1144.

[15] Y.-S. Wu, "General theory for quantum statistics in two dimensions," *Phys. Rev. Lett.* **52** (Jun, 1984) 2103–2106. https://link.aps.org/doi/10.1103/PhysRevLett.52.2103.

[16] F. Wilczek, *Fractional statistics and anyon superconductivity*, vol. 5. World scientific, 1990.

[17] M. V. Berry, "Quantal phase factors accompanying adiabatic changes," *Proc. R. Soc. Lond. A* **A** no. 392, (1984) 45–57.

[18] D. J. Thouless and Y. Gefen, "Fractional quantum hall effect and multiple aharonov-bohm periods," *Phys. Rev. Lett.* **66** (Feb, 1991) 806–809. https://link.aps.org/doi/10.1103/PhysRevLett.66.806.

[19] E. Witten, "Quantum field theory and the jones polynomial," *Communications in Mathematical Physics* **121** no. 3, (Sep, 1989) 351–399. https://doi.org/10.1007/BF01217730.

[20] D. Arovas, J. R. Schrieffer, and F. Wilczek, "Fractional statistics and the quantum hall effect," *Phys. Rev. Lett.* **53** (Aug, 1984) 722–723. https://link.aps.org/doi/10.1103/PhysRevLett.53.722.

[21] P. Bonderson, D. J. Clarke, C. Nayak, and K. Shtengel, "Implementing arbitrary phase gates with ising anyons," *Phys. Rev. Lett.* **104** (May, 2010) 180505. http://link.aps.org/doi/10.1103/PhysRevLett.104.180505.

[22] M. Sato and Y. Ando, "Topological superconductors: a review," *Reports on Progress in Physics* **80** no. 7, (May, 2017) 076501. https://doi.org/10.1088/1361-6633/aa6ac7.

[23] M. Z. Hasan and C. L. Kane, "Colloquium: Topological insulators," *Rev. Mod. Phys.* **82** (Nov, 2010) 3045–3067. https://link.aps.org/doi/10.1103/RevModPhys.82.3045.

[24] M. Freedman, C. Nayak, and K. Walker, "Towards universal topological quantum computation in the $\nu = \frac{5}{2}$ fractional quantum hall state," *Phys. Rev. B* **73** (Jun, 2006) 245307. http://link.aps.org/doi/10.1103/PhysRevB.73.245307.

[25] S. Bravyi, "Universal quantum computation with the $\nu = \frac{5}{2}$ fractional quantum Hall state," *Phys. Rev. A* **73** (Apr, 2006) 042313. http://link.aps.org/doi/10.1103/PhysRevA.73.042313.

[26] P. Bonderson, A. Kitaev, and K. Shtengel, "Detecting non-abelian statistics in the $\nu = 5/2$ fractional quantum hall state," *Phys. Rev. Lett.* **96** (Jan, 2006) 016803. https://link.aps.org/doi/10.1103/PhysRevLett.96.016803.

[27] T. Karzig, C. Knapp, R. M. Lutchyn, P. Bonderson, M. B. Hastings, C. Nayak, J. Alicea, K. Flensberg, S. Plugge, Y. Oreg, C. M. Marcus, and M. H. Freedman, "Scalable designs for quasiparticle-poisoning-protected topological quantum computation with majorana zero modes," *Phys. Rev. B* **95** (Jun, 2017) 235305. https://link.aps.org/doi/10.1103/PhysRevB.95.235305.

[28] M. A. Levin and X.-G. Wen, "String-net condensation: A physical mechanism for topological phases," *Phys. Rev. B* **71** (Jan, 2005) 045110. https://link.aps.org/doi/10.1103/PhysRevB.71.045110.

[29] A. Mackenzie and Y. Maeno, "p-wave superconductivity," *Physica B: Condensed Matter* **280** no. 1, (2000) 148–153. https://www.sciencedirect.com/science/article/pii/S092145269901546X.

[30] N. Read and D. Green, "Paired states of fermions in two dimensions with breaking of parity and time-reversal symmetries and the fractional quantum hall effect," *Phys. Rev. B* **61** (Apr, 2000) 10267–10297. http://link.aps.org/doi/10.1103/PhysRevB.61.10267.

[31] D. A. Ivanov, "Non-Abelian Statistics of Half-Quantum Vortices in p-Wave Superconductors," *Phys. Rev. Lett.* **86** (Jan, 2001) 268–271. http://link.aps.org/doi/10.1103/PhysRevLett.86.268.

[32] A. Y. Kitaev, "Unpaired Majorana fermions in quantum wires," *Physics-Uspekhi* **44** no. 10S, (2001) 131. http://stacks.iop.org/1063-7869/44/i=10S/a=S29.

[33] R. W. Cherng and C. A. R. Sá de Melo, "f-wave versus p-wave superconductivity in organic conductors," *Phys. Rev. B* **67** (Jun, 2003) 212505. https://link.aps.org/doi/10.1103/PhysRevB.67.212505.

[34] M. Sato, Y. Takahashi, and S. Fujimoto, "Non-Abelian Topological Order in s-Wave Superfluids of Ultracold Fermionic Atoms," *Phys. Rev. Lett.* **103** (Jul, 2009) 020401. http://link.aps.org/doi/10.1103/PhysRevLett.103.020401.

[35] J. D. Sau, R. M. Lutchyn, S. Tewari, and S. Das Sarma, "Generic New Platform for Topological Quantum Computation Using Semiconductor Heterostructures," *Phys. Rev. Lett.* **104** (Jan, 2010) 040502. http://link.aps.org/doi/10.1103/PhysRevLett.104.040502.

[36] S. Estévez Hernández, M. Akabori, K. Sladek, C. Volk, S. Alagha, H. Hardtdegen, M. G. Pala, N. Demarina, D. Grützmacher, and T. Schäpers, "Spin-orbit coupling and phase coherence in InAs nanowires," *Phys. Rev. B* **82** (Dec, 2010) 235303. http://link.aps.org/doi/10.1103/PhysRevB.82.235303.

[37] S. Chuang, Q. Gao, R. Kapadia, A. C. Ford, J. Guo, and A. Javey, "Ballistic InAs Nanowire Transistors," *Nano Letters* **13** no. 2, (2013) 555–558.

[38] S. Nadj-Perge, V. S. Pribiag, J. W. G. van den Berg, K. Zuo, S. R. Plissard, E. P. A. M. Bakkers, S. M. Frolov, and L. P. Kouwenhoven, "Spectroscopy of Spin-Orbit Quantum Bits in Indium Antimonide Nanowires," *Phys. Rev. Lett.* **108** (Apr, 2012) 166801. http://link.aps.org/doi/10.1103/PhysRevLett.108.166801.

[39] I. van Weperen, B. Tarasinski, D. Eeltink, V. S. Pribiag, S. R. Plissard, E. P. A. M. Bakkers, L. P. Kouwenhoven, and M. Wimmer, "Spin-orbit interaction in insb nanowires," *Phys. Rev. B* **91** (May, 2015) 201413. http://link.aps.org/doi/10.1103/PhysRevB.91.201413.

[40] T. Schäpers, *Superconductor/Semiconductor Junctions.* No. 174 in Springer Tracts in Modern Physics. Springer, 2001. p.8.

[41] P. G. de Gennes, *Superconductivity of Metals and Alloys*. Benjamin, New York, 1966. p. 141.

[42] M. Tinkham, *Introduction to Superconductivity*. McGraw-Hill, 2nd ed., 1996. p. 63.

[43] C. W. Groth, M. Wimmer, A. R. Akhmerov, and X. Waintal, "Kwant: a software package for quantum transport," *New Journal of Physics* **16** no. 6, (Jun, 2014) 063065. https://doi.org/10.1088/1367-2630/16/6/063065.

[44] R. Aguado, "Majorana quasiparticles in condensed matter," *La Rivista del Nuovo Cimento* **40** no. 11, (Nov, 2017) 523–593. https://doi.org/10.1393/ncr/i2017-10141-9.

[45] J. Klinovaja and D. Loss, "Composite majorana fermion wave functions in nanowires," *Phys. Rev. B* **86** (Aug, 2012) 085408. https://link.aps.org/doi/10.1103/PhysRevB.86.085408.

[46] E. Prada, P. San-Jose, M. W. A. de Moor, A. Geresdi, E. J. H. Lee, J. Klinovaja, D. Loss, J. Nygård, R. Aguado, and L. P. Kouwenhoven, "From andreev to majorana bound states in hybrid superconductor–semiconductor nanowires," *Nature Reviews Physics* **2** no. 10, (Oct, 2020) 575–594. https://doi.org/10.1038/s42254-020-0228-y.

[47] S. M. Albrecht, A. P. Higginbotham, M. Madsen, F. Kuemmeth, T. S. Jespersen, J. Nygård, P. Krogstrup, and C. M. Marcus, "Exponential protection of zero modes in majorana islands," *Nature* **531** no. 7593, (Mar, 2016) 206–209. http://dx.doi.org/10.1038/nature17162. Letter.

[48] M.-T. Deng, S. Vaitiekėnas, E. Prada, P. San-Jose, J. Nygård, P. Krogstrup, R. Aguado, and C. M. Marcus, "Nonlocality of majorana modes in hybrid nanowires," *Phys. Rev. B* **98** (Aug, 2018) 085125. https://link.aps.org/doi/10.1103/PhysRevB.98.085125.

[49] O. Zilberberg, B. Braunecker, and D. Loss, "Controlled-not gate for multiparticle qubits and topological quantum computation based on parity measurements," *Phys. Rev. A* **77** (Jan, 2008) 012327. https://link.aps.org/doi/10.1103/PhysRevA.77.012327.

[50] D. Aasen, M. Hell, R. V. Mishmash, A. Higginbotham, J. Danon, M. Leijnse, T. S. Jespersen, J. A. Folk, C. M. Marcus, K. Flensberg, and J. Alicea, "Milestones toward majorana-based quantum computing," *Phys. Rev. X* **6** (Aug, 2016) 031016, arXiv:1511.05153. https://link.aps.org/doi/10.1103/PhysRevX.6.031016.

[51] T. Karzig, W. S. Cole, and D. I. Pikulin, "Quasiparticle poisoning of majorana qubits," *Phys. Rev. Lett.* **126** (Feb, 2021) 057702. https://link.aps.org/doi/10.1103/PhysRevLett.126.057702.

[52] M. Tinkham, *Introduction to Superconductivity*. McGraw-Hill, 2nd ed., 1996. p. 52.

[53] A. Mishra, P. Simon, T. Hyart, and M. Trif, "Yu-shiba-rusinov qubit," *PRX Quantum* **2** (Dec, 2021) 040347. https://link.aps.org/doi/10.1103/PRXQuantum.2.040347.

[54] Y.-H. Lai, S. Das Sarma, and J. D. Sau, "Theory of coulomb blockaded transport in realistic majorana nanowires," *Phys. Rev. B* **104** (Aug, 2021) 085403. https://link.aps.org/doi/10.1103/PhysRevB.104.085403.

[55] S. Plugge, A. Rasmussen, R. Egger, and K. Flensberg, "Majorana box qubits," *New Journal of Physics* **19** no. 1, (Jan, 2017) 012001. https://doi.org/10.1088/1367-2630/aa54e1.

[56] S. Vijay and L. Fu, "Teleportation-based quantum information processing with majorana zero modes," *Phys. Rev. B* **94** (Dec, 2016) 235446. https://link.aps.org/doi/10.1103/PhysRevB.94.235446.

[57] V. Kornich, X. Huang, E. Repin, and Y. V. Nazarov, "Braiding and all quantum operations with majorana modes in 1d," *Phys. Rev. Lett.* **126** (Mar, 2021) 117701. https://link.aps.org/doi/10.1103/PhysRevLett.126.117701.

[58] J. Liu, W. Chen, M. Gong, Y. Wu, and X. Xie, "Minimal setup for non-abelian braiding of majorana zero modes," *Science China Physics, Mechanics & Astronomy* **64** no. 11, (Sep, 2021) 117811. https://doi.org/10.1007/s11433-021-1773-3.

[59] C. Tutschku, R. W. Reinthaler, C. Lei, A. H. MacDonald, and E. M. Hankiewicz, "Majorana-based quantum computing in nanowire devices," *Phys. Rev. B* **102** (Sep, 2020) 125407. https://link.aps.org/doi/10.1103/PhysRevB.102.125407.

[60] F. Harper, A. Pushp, and R. Roy, "Majorana braiding in realistic nanowire y-junctions and tuning forks," *Phys. Rev. Research* **1** (Dec, 2019) 033207. https://link.aps.org/doi/10.1103/PhysRevResearch.1.033207.

[61] Z.-C. Yang, T. Iadecola, C. Chamon, and C. Mudry, "Hierarchical majoranas in a programmable nanowire network," *Phys. Rev. B* **99** (Apr, 2019) 155138. https://link.aps.org/doi/10.1103/PhysRevB.99.155138.

[62] D. J. Clarke, J. D. Sau, and S. Das Sarma, "Probability and braiding statistics in majorana nanowires," *Phys. Rev. B* **95** (Apr, 2017) 155451. https://link.aps.org/doi/10.1103/PhysRevB.95.155451.

[63] J. Alicea, Y. Oreg, G. Refael, F. von Oppen, and M. P. A. Fisher, "Non-Abelian statistics and topological quantum information processing in 1D wire networks," *Nat Phys* **7** no. 5, (May, 2011) 412–417. http://dx.doi.org/10.1038/nphys1915.

[64] M. C. Dartiailh, W. Mayer, J. Yuan, K. S. Wickramasinghe, A. Matos-Abiague, I. Žutić, and J. Shabani, "Phase signature of topological transition in josephson junctions," *Phys. Rev. Lett.* **126** (Jan, 2021) 036802. https://link.aps.org/doi/10.1103/PhysRevLett.126.036802.

[65] T. Zhou, M. C. Dartiailh, W. Mayer, J. E. Han, A. Matos-Abiague, J. Shabani, and I. Žutić, "Phase control of majorana bound states in a topological X junction," *Phys. Rev. Lett.* **124** (Apr, 2020) 137001. https://link.aps.org/doi/10.1103/PhysRevLett.124.137001.

[66] H. Ren, F. Pientka, S. Hart, A. T. Pierce, M. Kosowsky, L. Lunczer, R. Schlereth, B. Scharf, E. M. Hankiewicz, L. W. Molenkamp, B. I. Halperin, and A. Yacoby, "Topological superconductivity in a phase-controlled josephson junction," *Nature* **569** no. 7754, (May, 2019) 93–98. https://doi.org/10.1038/s41586-019-1148-9.

[67] S. Hoffman, C. Schrade, J. Klinovaja, and D. Loss, "Universal quantum computation with hybrid spin-majorana qubits," *Phys. Rev. B* **94** (Jul, 2016) 045316. https://link.aps.org/doi/10.1103/PhysRevB.94.045316.

[68] K. Gharavi, D. Hoving, and J. Baugh, "Readout of majorana parity states using a quantum dot," *Phys. Rev. B* **94** (Oct, 2016) 155417. https://link.aps.org/doi/10.1103/PhysRevB.94.155417.

[69] J. F. Steiner and F. von Oppen, "Readout of majorana qubits," *Phys. Rev. Research* **2** (Aug, 2020) 033255. https://link.aps.org/doi/10.1103/PhysRevResearch.2.033255.

[70] T. Zhou, M. C. Dartiailh, K. Sardashti, J. E. Han, A. Matos-Abiague, J. Shabani, and I. Žutić, "Fusion of majorana bound states with mini-gate control in two-dimensional systems," *Nature Communications* **13** no. 1, (Apr, 2022) 1738. https://doi.org/10.1038/s41467-022-29463-6.

[71] D. Litinski and F. von Oppen, "Quantum computing with majorana fermion codes," *Phys. Rev. B* **97** (May, 2018) 205404. https://link.aps.org/doi/10.1103/PhysRevB.97.205404.

[72] K. Flensberg, F. von Oppen, and A. Stern, "Engineered platforms for topological superconductivity and majorana zero modes," *Nature Reviews Materials* **6** no. 10, (Oct, 2021) 944–958. https://doi.org/10.1038/s41578-021-00336-6.

[73] J.-B. Fu, B. Li, X.-F. Zhang, G.-Z. Yu, G.-Y. Huang, and M.-T. Deng, "Experimental review on majorana zero-modes in hybrid nanowires," *Science China Physics, Mechanics & Astronomy* **64** no. 10, (Sep, 2021) 107001. https://doi.org/10.1007/s11433-021-1737-4.

[74] S. M. Frolov, M. J. Manfra, and J. D. Sau, "Topological superconductivity in hybrid devices," *Nature Physics* **16** no. 7, (Jul, 2020) 718–724. https://doi.org/10.1038/s41567-020-0925-6.

[75] H. Zhang, D. E. Liu, M. Wimmer, and L. P. Kouwenhoven, "Next steps of quantum transport in majorana nanowire devices," *Nature Communications* **10** no. 1, (Nov, 2019) 5128. https://doi.org/10.1038/s41467-019-13133-1.

[76] V. Mourik, K. Zuo, S. M. Frolov, S. R. Plissard, E. P. A. M. Bakkers, and L. P. Kouwenhoven, "Signatures of Majorana Fermions in Hybrid Superconductor-Semiconductor Nanowire Devices," *Science* **336** no. 6084, (2012) 1003–1007. http://dx.doi.org/10.1126/science.1222360.

[77] M. T. Deng, C. L. Yu, G. Y. Huang, M. Larsson, P. Caroff, and H. Q. Xu, "Anomalous Zero-Bias Conductance Peak in a Nb-InSb Nanowire-Nb Hybrid Device," *Nano Letters* **12** (2012) 6414. http://dx.doi.org/10.1021/nl303758w.

[78] A. Das, Y. Ronen, Y. Most, Y. Oreg, M. Heiblum, and H. Shtrikman, "Zero-bias peaks and splitting in an Al-InAs nanowire topological superconductor as a signature of Majorana fermions," *Nat Phys* **8** no. 12, (Dec, 2012) 887–895. http://dx.doi.org/10.1038/nphys2479.

[79] A. D. K. Finck, D. J. Van Harlingen, P. K. Mohseni, K. Jung, and X. Li, "Anomalous Modulation of a Zero-Bias Peak in a Hybrid Nanowire-Superconductor Device," *Phys. Rev. Lett.* **110** (Mar, 2013) 126406. http://link.aps.org/doi/10.1103/PhysRevLett.110.126406.

[80] W. Chang, V. E. Manucharyan, T. S. Jespersen, J. Nygård, and C. M. Marcus, "Tunneling spectroscopy of quasiparticle bound states in a spinful josephson junction," *Phys. Rev. Lett.* **110** (May, 2013) 217005. http://link.aps.org/doi/10.1103/PhysRevLett.110.217005.

[81] L. P. Rokhinson, X. Liu, and J. K. Furdyna, "The fractional a.c. Josephson effect in a semiconductor-superconductor nanowire as a signature of Majorana particles," *Nat Phys* **8** no. 11, (Nov, 2012) 795–799. http://dx.doi.org/10.1038/nphys2429.

[82] S. Das Sarma, J. D. Sau, and T. D. Stanescu, "Splitting of the zero-bias conductance peak as smoking gun evidence for the existence of the Majorana mode in a superconductor-semiconductor nanowire," *Phys. Rev. B* **86** (Dec, 2012) 220506. http://link.aps.org/doi/10.1103/PhysRevB.86.220506.

[83] J. Alicea, "New directions in the pursuit of Majorana fermions in solid state systems," *Reports on Progress in Physics* **75** no. 7, (2012) 076501. http://stacks.iop.org/0034-4885/75/i=7/a=076501.

[84] S. Vaitiekėnas, G. W. Winkler, B. van Heck, T. Karzig, M.-T. Deng, K. Flensberg, L. I. Glazman, C. Nayak, P. Krogstrup, R. M. Lutchyn, and C. M. Marcus, "Flux-induced topological superconductivity in full-shell nanowires," *Science* **367** no. 6485, (2020) eaav3392, https://www.science.org/doi/pdf/10.1126/science.aav3392. https://www.science.org/doi/abs/10.1126/science.aav3392.

[85] Ö. Gül, H. Zhang, J. D. S. Bommer, M. W. A. de Moor, D. Car, S. R. Plissard, E. P. A. M. Bakkers, A. Geresdi, K. Watanabe, T. Taniguchi, and L. P. Kouwenhoven, "Ballistic majorana nanowire devices," *Nature Nanotechnology* **13** no. 3, (Mar, 2018) 192–197. https://doi.org/10.1038/s41565-017-0032-8.

[86] Ö. Gül, H. Zhang, F. K. de Vries, J. van Veen, K. Zuo, V. Mourik, S. Conesa-Boj, M. P. Nowak, D. J. van Woerkom, M. Quintero-Pérez, M. C. Cassidy, A. Geresdi, S. Koelling, D. Car, S. R. Plissard, E. P. A. M. Bakkers, and L. P. Kouwenhoven, "Hard superconducting gap in insb nanowires," *Nano Letters* **17** no. 4, (Apr, 2017) 2690–2696. https://doi.org/10.1021/acs.nanolett.7b00540.

[87] X. Yuan, D. Pan, Y. Zhou, X. Zhang, K. Peng, B. Zhao, M. Deng, J. He, H. H. Tan, and C. Jagadish, "Selective area epitaxy of iii–v nanostructure arrays and networks: Growth, applications, and future directions," *Applied Physics Reviews* **8** no. 2, (2021) 021302, https://doi.org/10.1063/5.0044706. https://doi.org/10.1063/5.0044706.

[88] W. Mayer, W. F. Schiela, J. Yuan, M. Hatefipour, W. L. Sarney, S. P. Svensson, A. C. Leff, T. Campos, K. S. Wickramasinghe, M. C. Dartiailh, I. Žutić, and J. Shabani, "Superconducting proximity effect in inassb surface quantum wells with in situ al contacts," *ACS Applied Electronic Materials* **2** no. 8, (Aug, 2020) 2351–2356. https://doi.org/10.1021/acsaelm.0c00269.

[89] J. O'Connell Yuan, K. S. Wickramasinghe, W. M. Strickland, M. C. Dartiailh, K. Sardashti, M. Hatefipour, and J. Shabani, "Epitaxial superconductor-semiconductor two-dimensional systems for superconducting quantum circuits," *Journal of Vacuum Science & Technology A* **39** no. 3, (2021) 033407, https://doi.org/10.1116/6.0000918. https://doi.org/10.1116/6.0000918.

[90] M. T. Deng, S. Vaitiekėnas, E. B. Hansen, J. Danon, M. Leijnse, K. Flensberg, J. Nygård, P. Krogstrup, and C. M. Marcus, "Majorana bound state in a coupled quantum-dot hybrid-nanowire system," *Science* **354** no. 6319, (2016) 1557–1562, https://www.science.org/doi/pdf/10.1126/science.aaf3961. https://www.science.org/doi/abs/10.1126/science.aaf3961.

[91] F. Nichele, A. C. C. Drachmann, A. M. Whiticar, E. C. T. O'Farrell, H. J. Suominen, A. Fornieri, T. Wang, G. C. Gardner, C. Thomas, A. T. Hatke, P. Krogstrup, M. J. Manfra, K. Flensberg, and C. M. Marcus, "Scaling of majorana zero-bias conductance peaks," *Phys. Rev. Lett.* **119** (Sep, 2017) 136803. https://link.aps.org/doi/10.1103/PhysRevLett.119.136803.

[92] P. Krogstrup, N. L. B. Ziino, W. Chang, S. M. Albrecht, M. H. Madsen, E. Johnson, J. Nygård, C. M. Marcus, and T. S. Jespersen, "Epitaxy of semiconductor–superconductor nanowires," *Nature Materials* **14** no. 4, (Apr, 2015) 400–406. https://doi.org/10.1038/nmat4176.

[93] R. L. M. Op het Veld, D. Xu, V. Schaller, M. A. Verheijen, S. M. E. Peters, J. Jung, C. Tong, Q. Wang, M. W. A. de Moor, B. Hesselmann, K. Vermeulen, J. D. S. Bommer, J. Sue Lee, A. Sarikov, M. Pendharkar, A. Marzegalli, S. Koelling, L. P. Kouwenhoven, L. Miglio, C. J. Palmstrøm, H. Zhang, and E. P. A. M. Bakkers, "In-plane selective area insb–al nanowire quantum networks," *Communications Physics* **3** no. 1, (Mar, 2020) 59. https://doi.org/10.1038/s42005-020-0324-4.

[94] C. Moore, C. Zeng, T. D. Stanescu, and S. Tewari, "Quantized zero-bias conductance plateau in semiconductor-superconductor heterostructures without topological majorana zero modes," *Phys. Rev. B* **98** (Oct, 2018) 155314. https://link.aps.org/doi/10.1103/PhysRevB.98.155314.

[95] Z.-G. Liu, Y.-X. Huang, G.-C. Guo, and M. Gong, "Majorana and non-majorana modes in a nanowire in partially proximity to a superconductor," *Journal of Applied Physics* **129** no. 9, (2021) 094301, https://doi.org/10.1063/5.0038612. https://doi.org/10.1063/5.0038612.

[96] D. Liu, Z. Cao, X. Liu, H. Zhang, and D. E. Liu, "Topological kondo device for distinguishing quasi-majorana and majorana signatures," *Phys. Rev. B* **104** (Nov, 2021) 205125. https://link.aps.org/doi/10.1103/PhysRevB.104.205125.

[97] P. Bonderson and C. Nayak, "Quasi-topological phases of matter and topological protection," *Phys. Rev. B* **87** (May, 2013) 195451. https://link.aps.org/doi/10.1103/PhysRevB.87.195451.

[98] B. D. Woods, J. Chen, S. M. Frolov, and T. D. Stanescu, "Zero-energy pinning of topologically trivial bound states in multiband semiconductor-superconductor nanowires," *Phys. Rev. B* **100** (Sep, 2019) 125407. https://link.aps.org/doi/10.1103/PhysRevB.100.125407.

[99] P. Yu, J. Chen, M. Gomanko, G. Badawy, E. P. A. M. Bakkers, K. Zuo, V. Mourik, and S. M. Frolov, "Non-majorana states yield nearly quantized conductance in proximatized nanowires," *Nature Physics* **17** no. 4, (Apr, 2021) 482–488. https://doi.org/10.1038/s41567-020-01107-w.

[100] H. Zhang, C.-X. Liu, S. Gazibegovic, D. Xu, J. A. Logan, G. Wang, N. van Loo, J. D. S. Bommer, M. W. A. de Moor, D. Car, R. L. M. Op het Veld, P. J. van Veldhoven, S. Koelling, M. A. Verheijen, M. Pendharkar, D. J. Pennachio, B. Shojaei, J. S. Lee, C. J. Palmstrøm, E. P. A. M. Bakkers, S. D. Sarma, and L. P. Kouwenhoven, "Retracted article: Quantized majorana conductance," *Nature* **556** no. 7699, (Apr, 2018) 74–79. https://doi.org/10.1038/nature26142.

[101] H. Zhang, C.-X. Liu, S. Gazibegovic, D. Xu, J. A. Logan, G. Wang, N. van Loo, J. D. S. Bommer, M. W. A. de Moor, D. Car, R. L. M. Op het Veld, P. J. van Veldhoven, S. Koelling, M. A. Verheijen, M. Pendharkar, D. J. Pennachio, B. Shojaei, J. S. Lee, C. J. Palmstrøm, E. P. A. M. Bakkers, S. D. Sarma, and L. P. Kouwenhoven, "Editorial expression of concern: Quantized majorana conductance," *Nature* **581** no. 7807, (May, 2020) E4–E4. https://doi.org/10.1038/s41586-020-2252-6.

[102] D. Rosenbach, T. W. Schmitt, P. Schüffelgen, M. P. Stehno, C. Li, M. Schleenvoigt, A. R. Jalil, G. Mussler, E. Neumann, S. Trellenkamp, A. A. Golubov, A. Brinkman, D. Grützmacher, and T. Schäpers, "Reappearance of first shapiro step in narrow topological josephson junctions," *Science Advances* **7** no. 26, (2021) eabf1854, https://www.science.org/doi/pdf/10.1126/sciadv.abf1854. https://www.science.org/doi/abs/10.1126/sciadv.abf1854.

[103] C.-K. Chiu and S. Das Sarma, "Fractional josephson effect with and without majorana zero modes," *Phys. Rev. B* **99** (Jan, 2019) 035312. https://link.aps.org/doi/10.1103/PhysRevB.99.035312.

[104] F. K. de Vries, M. L. Sol, S. Gazibegovic, R. L. M. o. h. Veld, S. C. Balk, D. Car, E. P. A. M. Bakkers, L. P. Kouwenhoven, and J. Shen, "Crossed andreev reflection in insb flake josephson junctions," *Phys. Rev. Research* **1** (Dec, 2019) 032031. https://link.aps.org/doi/10.1103/PhysRevResearch.1.032031.

[105] E. Prada, R. Aguado, and P. San-Jose, "Measuring majorana nonlocality and spin structure with a quantum dot," *Phys. Rev. B* **96** (Aug, 2017) 085418. https://link.aps.org/doi/10.1103/PhysRevB.96.085418.

[106] S. Nadj-Perge, I. K. Drozdov, J. Li, H. Chen, S. Jeon, J. Seo, A. H. MacDonald, B. A. Bernevig, and A. Yazdani, "Observation of majorana fermions in ferromagnetic atomic chains on a superconductor," *Science* **346** (2014) 602–607. https://www.science.org/doi/abs/10.1126/science.1259327.

[107] S. Nadj-Perge, I. K. Drozdov, B. A. Bernevig, and A. Yazdani, "Proposal for realizing majorana fermions in chains of magnetic atoms on a superconductor," *Phys. Rev. B* **88** (Jul, 2013) 020407. https://link.aps.org/doi/10.1103/PhysRevB.88.020407.

[108] A. Palacio-Morales, E. Mascot, S. Cocklin, H. Kim, S. Rachel, D. K. Morr, and R. Wiesendanger, "Atomic-scale interface engineering of majorana edge modes in a 2d magnet-superconductor hybrid system," *Science Advances* **5** (2019) eaav6600. https://www.science.org/doi/abs/10.1126/sciadv.aav6600.

[109] G. C. Ménard, A. Mesaros, C. Brun, F. Debontridder, D. Roditchev, P. Simon, and T. Cren, "Isolated pairs of majorana zero modes in a disordered superconducting lead monolayer," *Nature communications* **10** (June, 2019) 2587. https://europepmc.org/articles/PMC6565688.

[110] G. C. Ménard, S. Guissart, C. Brun, R. T. Leriche, M. Trif, F. Debontridder, D. Demaille, D. Roditchev, P. Simon, and T. Cren, "Two-dimensional topological superconductivity in pb/co/si(111)," *Nature communications* **8** (December, 2017) 2040. https://europepmc.org/articles/PMC5725560.

[111] J. Wiedenmann, E. Bocquillon, R. S. Deacon, S. Hartinger, O. Hermann, T. M. Klapwijk, L. Maier, C. Ames, C. Brüne, C. Gould, A. Oiwa, K. Ishibashi, S. Tarucha, H. Buhmann, and L. W. Molenkamp, "4 pi-periodic josephson supercurrent in hgte-based topological josephson junctions," *Nature Communications* **7** (Jan, 2016) .

[112] L. Fu and C. L. Kane, "Josephson current and noise at a superconductor/quantum-spin-hall-insulator/superconductor junction," *Phys. Rev. B* **79** (Apr, 2009) 161408. https://link.aps.org/doi/10.1103/PhysRevB.79.161408.

[113] K. Gharavi, G. W. Holloway, C. M. Haapamaki, M. H. Ansari, M. Muhammad, R. R. LaPierre, and J. Baugh, "Josephson Interference due to Orbital States in a Nanowire Proximity Effect Junction," *arXiv e-prints* (May, 2014) arXiv:1405.7455, arXiv:1405.7455 [cond-mat.mes-hall].

[114] K. T. Law, P. A. Lee, and T. K. Ng, "Majorana Fermion Induced Resonant Andreev Reflection," *Phys. Rev. Lett.* **103** (Dec, 2009) 237001. http://link.aps.org/doi/10.1103/PhysRevLett.103.237001.

[115] K. Flensberg, "Tunneling characteristics of a chain of Majorana bound states," *Phys. Rev. B* **82** (Nov, 2010) 180516. http://link.aps.org/doi/10.1103/PhysRevB.82.180516.

[116] J. D. Sau, S. Tewari, R. M. Lutchyn, T. D. Stanescu, and S. Das Sarma, "Non-Abelian quantum order in spin-orbit-coupled semiconductors: Search for topological Majorana particles in solid-state systems," *Phys. Rev. B* **82** (Dec, 2010) 214509. http://link.aps.org/doi/10.1103/PhysRevB.82.214509.

[117] F. Hassler, A. R. Akhmerov, C.-Y. Hou, and C. W. J. Beenakker, "Anyonic interferometry without anyons: how a flux qubit can read out a topological qubit," *New Journal of Physics* **12** no. 12, (2010) 125002. http://stacks.iop.org/1367-2630/12/i=12/a=125002.

[118] B. van Heck, F. Hassler, A. R. Akhmerov, and C. W. J. Beenakker, "Coulomb stability of the 4π-periodic Josephson effect of Majorana fermions," *Phys. Rev. B* **84** (Nov, 2011) 180502. http://link.aps.org/doi/10.1103/PhysRevB.84.180502.

[119] D. E. Liu and H. U. Baranger, "Detecting a Majorana-fermion zero mode using a quantum dot," *Phys. Rev. B* **84** (Nov, 2011) 201308. http://link.aps.org/doi/10.1103/PhysRevB.84.201308.

[120] E. Prada, P. San-Jose, and R. Aguado, "Transport spectroscopy of NS nanowire junctions with Majorana fermions," *Phys. Rev. B* **86** (Nov, 2012) 180503. http://link.aps.org/doi/10.1103/PhysRevB.86.180503.

[121] T. D. Stanescu and S. Tewari, "Majorana fermions in semiconductor nanowires: fundamentals, modeling, and experiment," *Journal of Physics: Condensed Matter* **25** no. 23, (2013) 233201. http://stacks.iop.org/0953-8984/25/i=23/a=233201.

[122] D. Bagrets and A. Altland, "Class D Spectral Peak in Majorana Quantum Wires," *Physical Review Letters* **109** no. 22, (Nov., 2012) 227005, arXiv:1206.0434 [cond-mat.mes-hall].

[123] F. Pientka, G. Kells, A. Romito, P. W. Brouwer, and F. von Oppen, "Enhanced Zero-Bias Majorana Peak in the Differential Tunneling Conductance of Disordered Multisubband Quantum-Wire/Superconductor Junctions," *Physical Review Letters* **109** no. 22, (Nov., 2012) 227006, arXiv:1206.0723 [cond-mat.mes-hall].

[124] J. Liu, A. C. Potter, K. T. Law, and P. A. Lee, "Zero-Bias Peaks in the Tunneling Conductance of Spin-Orbit-Coupled Superconducting Wires with and without Majorana End-States," *Physical Review Letters* **109** no. 26, (Dec., 2012) 267002, arXiv:1206.1276 [cond-mat.mes-hall].

[125] E. J. H. Lee, X. Jiang, R. Aguado, G. Katsaros, C. M. Lieber, and S. De Franceschi, "Zero-Bias Anomaly in a Nanowire Quantum Dot Coupled to Superconductors," *Physical Review Letters* **109** no. 18, (Nov., 2012) 186802, arXiv:1207.1259 [cond-mat.mes-hall].

[126] G. Kells, D. Meidan, and P. W. Brouwer, "Near-zero-energy end states in topologically trivial spin-orbit coupled superconducting nanowires with a smooth confinement," *Phys. Rev. B* **86** no. 10, (Sept., 2012) 100503, arXiv:1207.3067 [cond-mat.mes-hall].

[127] D. Rainis, L. Trifunovic, J. Klinovaja, and D. Loss, "Towards a realistic transport modeling in a superconducting nanowire with Majorana fermions," *Phys. Rev. B* **87** no. 2, (Jan., 2013) 024515, arXiv:1207.5907 [cond-mat.mes-hall].

[128] T. D. Stanescu and S. Tewari, "Disentangling Majorana fermions from topologically trivial low-energy states in semiconductor Majorana wires," *Phys. Rev. B* **87** no. 14, (Apr., 2013) 140504, arXiv:1208.6298 [cond-mat.mes-hall].

[129] E. J. H. Lee, X. Jiang, M. Houzet, R. Aguado, C. M. Lieber, and S. De Franceschi, "Spin-resolved Andreev levels and parity crossings in hybrid superconductor-semiconductor nanostructures," *Nat Nano* **9** no. 1, (Jan, 2014) 79–84. http://dx.doi.org/10.1038/nnano.2013.267. Article.

[130] R. M. Lutchyn, T. D. Stanescu, and S. Das Sarma, "Search for Majorana Fermions in Multiband Semiconducting Nanowires," *Phys. Rev. Lett.* **106** (Mar, 2011) 127001. http://link.aps.org/doi/10.1103/PhysRevLett.106.127001.

[131] C. Blömers, T. Rieger, P. Zellekens, F. Haas, M. I. Lepsa, H. Hardtdegen, O. Gül, N. Demarina, D. Grützmacher, H. Lüth, and T. Schäpers, "Realization of nanoscaled tubular conductors by means of gaas/inas core/shell nanowires," *Nanotechnology* **24** no. 3, (2013) 035203. http://stacks.iop.org/0957-4484/24/i=3/a=035203.

[132] T. Klapwijk, "Proximity Effect From an Andreev Perspective," *Journal of Superconductivity* **17** no. 5, (2004) 593–611. http://dx.doi.org/10.1007/s10948-004-0773-0.

[133] P. San-Jose, E. Prada, and R. Aguado, "Mapping the Topological Phase Diagram of Multiband Semiconductors with Supercurrents," *Phys. Rev. Lett.* **112** (Apr, 2014) 137001. https://doi.org/10.1103/PhysRevLett.112.137001.

[134] K. Flensberg, J. B. Hansen, and M. Octavio, "Subharmonic energy-gap structure in superconducting weak links," *Phys. Rev. B* **38** (Nov, 1988) 8707–8711. http://link.aps.org/doi/10.1103/PhysRevB.38.8707.

[135] Y.-J. Doh, J. A. van Dam, A. L. Roest, E. P. A. M. Bakkers, L. P. Kouwenhoven, and S. De Franceschi, "Tunable Supercurrent Through Semiconductor Nanowires," *Science* **309** no. 5732, (2005) 272–275, https://www.science.org/doi/pdf/10.1126/science.1113523. https://www.science.org/doi/abs/10.1126/science.1113523.

[136] H. Courtois, P. Gandit, D. Mailly, and B. Pannetier, "Long-Range Coherence in a Mesoscopic Metal near a Superconducting Interface," *Phys. Rev. Lett.* **76** (Jan, 1996) 130–133. http://link.aps.org/doi/10.1103/PhysRevLett.76.130.

[137] B. Pannetier and H. Courtois, "Andreev Reflection and Proximity effect," *Journal of Low Temperature Physics* **118** no. 5-6, (2000) 599–615. http://dx.doi.org/10.1023/A%3A1004635226825.

[138] C. Blömers, M. I. Lepsa, M. Luysberg, D. Grützmacher, H. Lüth, and T. Schäpers, "Electronic phase coherence in inas nanowires," *Nano Letters* **11** no. 9, (Sep, 2011) 3550–3556. https://doi.org/10.1021/nl201102a.

[139] H. Y. Günel, I. E. Batov, H. Hardtdegen, K. Sladek, A. Winden, K. Weis, G. Panaitov, D. Grützmacher, and T. Schäpers, "Supercurrent in Nb/InAs-nanowire/Nb Josephson

junctions," *Journal of Applied Physics* **112** no. 3, (2012) 034316. http://link.aip.org/link/?JAP/112/034316/1.

[140] R. Frielinghaus, I. E. Batov, M. Weides, H. Kohlstedt, R. Calarco, and T. Schäpers, "Josephson supercurrent in Nb/InN-nanowire/Nb junctions," *Applied Physics Letters* **96** no. 13, (2010) . http://scitation.aip.org/content/aip/journal/apl/96/13/10.1063/1.3377897.

[141] F. Bergeret and J. Cuevas, "The Vortex State and Josephson Critical Current of a Diffusive SNS Junction," *Journal of Low Temperature Physics* **153** no. 5-6, (2008) 304–324. http://dx.doi.org/10.1007/s10909-008-9826-2.

[142] J. C. Cuevas and F. S. Bergeret, "Magnetic Interference Patterns and Vortices in Diffusive SNS Junctions," *Phys. Rev. Lett.* **99** (Nov, 2007) 217002. http://link.aps.org/doi/10.1103/PhysRevLett.99.217002.

[143] J. C. Hammer, J. C. Cuevas, F. S. Bergeret, and W. Belzig, "Density of states and supercurrent in diffusive SNS junctions: Roles of nonideal interfaces and spin-flip scattering," *Phys. Rev. B* **76** (Aug, 2007) 064514. http://link.aps.org/doi/10.1103/PhysRevB.76.064514.

[144] T. Yokoyama, M. Eto, and Y. V. Nazarov, "Anomalous Josephson effect induced by spin-orbit interaction and Zeeman effect in semiconductor nanowires," *Phys. Rev. B* **89** (May, 2014) 195407. http://dx.doi.org/10.1103/PhysRevB.89.195407.

[145] E. Halpern, G. Cohen, S. Gross, A. Henning, M. Matok, A. V. Kretinin, H. Shtrikman, and Y. Rosenwaks, "Measuring surface state density and energy distribution in InAs nanowires," *Physica Status Solidi (a)* **211** no. 2, (2014) 473–482. http://dx.doi.org/10.1002/pssa.201300302.

[146] S. A. Dayeh, E. T. Yu, and D. Wang, "Transport Coefficients of InAs Nanowires as a Function of Diameter," *Small* **5** no. 1, (2009) 77–81. http://dx.doi.org/10.1002/smll.200800969.

[147] M. Noguchi, K. Hirakawa, and T. Ikoma, "Intrinsic electron accumulation layers on reconstructed clean InAs(100) surfaces," *Phys. Rev. Lett.* **66** (Apr, 1991) 2243–2246. http://link.aps.org/doi/10.1103/PhysRevLett.66.2243.

[148] L. Ö. Olsson, C. B. M. Andersson, M. C. Håkansson, J. Kanski, L. Ilver, and U. O. Karlsson, "Charge Accumulation at InAs Surfaces," *Phys. Rev. Lett.* **76** (May, 1996) 3626–3629. http://link.aps.org/doi/10.1103/PhysRevLett.76.3626.

[149] J. Eroms and D. Weiss, "Andreev reflection in nb-inas structures: Phase coherence, ballistic transport and edge channels," in *Advances in Solid State Physics*, vol. 46 of *Advances in Solid State Physics*, pp. 141–153. Springer Berlin Heidelberg, 2008. http://dx.doi.org/10.1007/978-3-540-38235-5_11.

[150] W. Belzig, F. K. Wilhelm, C. Bruder, G. Schön, and A. D. Zaikin, "Quasiclassical green's function approach to mesoscopic superconductivity," *Superlattices and Microstructures* **25** no. 5, (1999) 1251–1288. https://www.sciencedirect.com/science/article/pii/S0749603699907103.

[151] T. M. Eiles, J. M. Martinis, and M. H. Devoret, "Even-odd symmetry breaking in the NSN Coulomb blockade electrometer," *Physica B: Condensed Matter* **189** no. 1–4, (1993) 210–217. http://www.sciencedirect.com/science/article/pii/092145269390162Y.

[152] M. Tinkham, *Introduction to Superconductivity*. McGraw-Hill, 2nd ed., 1996.

[153] A. Barone and G. Paterno, *Physics and Applications of the Josephson Effect*. Wiley, New York, 1982.

[154] P. N. Racec, E. R. Racec, and H. Neidhardt, "Evanescent channels and scattering in cylindrical nanowire heterostructures," *Phys. Rev. B* **79** (Apr, 2009) 155305. http://link.aps.org/doi/10.1103/PhysRevB.79.155305.

[155] S. Datta, *Electronic Transport in Mesoscopic Systems*. Cambridge University Press, 1997.

[156] G. W. Holloway, D. Shiri, C. M. Haapamaki, K. Willick, G. Watson, R. R. LaPierre, and J. Baugh, "Magnetoconductance signatures of subband structure in semiconductor nanowires," *Phys. Rev. B* **91** (Jan, 2015) 045422. https://link.aps.org/doi/10.1103/PhysRevB.91.045422.

[157] M. C. Plante and R. R. LaPierre, "Analytical description of the metal-assisted growth of iii–v nanowires: Axial and radial growths," *Journal of Applied Physics* **105** no. 11, (2009) 114304, https://doi.org/10.1063/1.3131676. https://doi.org/10.1063/1.3131676.

[158] M. Sahu, M.-H. Bae, A. Rogachev, D. Pekker, T.-C. Wei, N. Shah, P. M. Goldbart, and A. Bezryadin, "Individual topological tunnelling events of a quantum field probed through their macroscopic consequences," *Nat Phys* **5** no. 7, (Jul, 2009) 503–508. http://dx.doi.org/10.1038/nphys1276.

[159] M. J. L. Sourribes, I. Isakov, M. Panfilova, and P. A. Warburton, "Minimization of the contact resistance between inas nanowires and metallic contacts," *Nanotechnology* **24** no. 4, (2013) 045703. https://dx.doi.org/10.1088/0957-4484/24/4/045703.

[160] T. S. Jespersen, M. L. Polianski, C. B. Sørensen, K. Flensberg, and J. Nygård, "Mesoscopic conductance fluctuations in inas nanowire-based sns junctions," *New Journal of Physics* **11** no. 11, (2009) 113025. http://stacks.iop.org/1367-2630/11/i=11/a=113025.

[161] S. Abay, D. Persson, H. Nilsson, H. Q. Xu, M. Fogelström, V. Shumeiko, and P. Delsing, "Quantized conductance and its correlation to the supercurrent in a nanowire connected to superconductors," *Nano Letters* **13** no. 8, (2013) 3614–3617.

[162] A. F. Andreev *Zh. Eksp. Teor. Fiz.* **46** (1964) 1823.

[163] P. Dubos, H. Courtois, B. Pannetier, F. K. Wilhelm, A. D. Zaikin, and G. Schön, "Josephson critical current in a long mesoscopic s-n-s junction," *Phys. Rev. B* **63** (Jan, 2001) 064502. http://link.aps.org/doi/10.1103/PhysRevB.63.064502.

[164] F. Chiodi, M. Ferrier, S. Guéron, J. C. Cuevas, G. Montambaux, F. Fortuna, A. Kasumov, and H. Bouchiat, "Geometry-related magnetic interference patterns in long SNS Josephson junctions," *Phys. Rev. B* **86** (Aug, 2012) 064510. http://link.aps.org/doi/10.1103/PhysRevB.86.064510.

[165] G. Montambaux, "Interference pattern of a long diffusive Josephson junction," *ArXiv e-prints* (July, 2007) , arXiv:0707.0411.

[166] S. Guéron, *Quasiparticles in a Diffusive Conductor: Interaction and Pairing*. PhD thesis, CEA-Saclay, 1997.

[167] A. Anthore, *Decoherence Mechanisms in Mesoscopic Conductors*. PhD thesis, CEA-Saclay, 2003.

[168] A. A. Golubov, "Proximity effect in dirty n/s multilayers," *in Superconducting Superlattices and Multilayers, Proc. SPIE* **2157** (1994) 353–362. http://dx.doi.org/10.1117/12.179172.

[169] A. Lahiri, K. Gharavi, J. Baugh, and B. Muralidharan, "Nonequilibrium green's function study of magnetoconductance features and oscillations in clean and disordered nanowires," *Phys. Rev. B* **98** (Sep, 2018) 125417. https://link.aps.org/doi/10.1103/PhysRevB.98.125417.

[170] K. Gharavi and J. Baugh, "Orbital josephson interference in a nanowire proximity-effect junction," *Phys. Rev. B* **91** (Jun, 2015) 245436. http://link.aps.org/doi/10.1103/PhysRevB.91.245436.

[171] B. Josephson, "Possible new effects in superconductive tunnelling," *Physics Letters* **1** no. 7, (1962) 251–253. http://www.sciencedirect.com/science/article/pii/0031916362913690.

[172] A. Andreev *Sov. Phys. JETP* **19** (1964) 1228.

[173] A. Andreev *Sov. Phys. JETP* **24** (1967) 1019.

[174] S. Nagata, H. C. Yang, and D. K. Finnemore, "Oscillations in the temperature dependence of Josephson supercurrents in SNS junctions," *Phys. Rev. B* **25** (May, 1982) 6012–6014. http://link.aps.org/doi/10.1103/PhysRevB.25.6012.

[175] H. C. Yang and D. K. Finnemore, "Pair-breaking mechanisms in superconductor-normal-metal-superconductor junctions," *Phys. Rev. B* **30** (Aug, 1984) 1260–1265. http://link.aps.org/doi/10.1103/PhysRevB.30.1260.

[176] B. Crouzy and D. A. Ivanov, "Magnetic interference patterns in long disordered Josephson junctions," *Phys. Rev. B* **87** (Jan, 2013) 024514. http://link.aps.org/doi/10.1103/PhysRevB.87.024514.

[177] H. A. Nilsson, P. Samuelsson, P. Caroff, and H. Q. Xu, "Supercurrent and Multiple Andreev Reflections in an InSb Nanowire Josephson Junction," *Nano Letters* **12** (2012) 228–233. http://dx.doi.org/10.1021/nl203380w.

[178] Ö. Gül, H. Y. Günel, H. Lüth, T. Rieger, T. Wenz, F. Haas, M. Lepsa, G. Panaitov, D. Grützmacher, and T. Schäpers, "Giant Magnetoconductance Oscillations in Hybrid Superconductor-Semiconductor Core/Shell Nanowire Devices," *Nano Letters* **14** (2014) 6269?6274.

[179] N. Byers and C. N. Yang, "Theoretical Considerations Concerning Quantized Magnetic Flux in Superconducting Cylinders," *Phys. Rev. Lett.* **7** (Jul, 1961) 46–49. http://link.aps.org/doi/10.1103/PhysRevLett.7.46.

[180] I. Kulik, "Macroscopic quantization and the proximity effect in s-n-s junctions," *Zh. Eksp. Teor. Fiz.* **57** (1969) 1745–1759. http://jetp.ac.ru/cgi-bin/e/index/e/30/5/p944?a=list. [JETP 30, No. 5, p. 944 (1970)].

[181] K. Jeganathan, V. Purushothaman, R. K. Debnath, R. Calarco, and H. Luth, "Raman scattering on intrinsic surface electron accumulation of InN nanowires," *Applied Physics Letters* **97** no. 9, (2010) . http://scitation.aip.org/content/aip/journal/apl/97/9/10.1063/1.3483758.

[182] R. A. Riedel, L.-F. Chang, and P. F. Bagwell, "Critical current and self-consistent order parameter of a superconductor-normal-metal-superconductor junction," *Phys. Rev. B* **54** (Dec, 1996) 16082–16095. http://link.aps.org/doi/10.1103/PhysRevB.54.16082.

[183] J. E. Han and V. H. Crespi, "Discrete transverse superconducting modes in nanocylinders," *Phys. Rev. B* **69** (Jun, 2004) 214526. http://link.aps.org/doi/10.1103/PhysRevB.69.214526.

[184] Y. Chen, A. A. Shanenko, and F. M. Peeters, "Hollow nanocylinder: Multisubband superconductivity induced by quantum confinement," *Phys. Rev. B* **81** (Apr, 2010) 134523. http://link.aps.org/doi/10.1103/PhysRevB.81.134523.

[185] M. Ashida, S. Aoyama, J. Hara, and K. Nagai, "Green's function in proximity-contact superconducting-normal double layers," *Phys. Rev. B* **40** (Nov, 1989) 8673–8686. http://link.aps.org/doi/10.1103/PhysRevB.40.8673.

[186] P. F. Bagwell, "Suppression of the Josephson current through a narrow, mesoscopic, semiconductor channel by a single impurity," *Phys. Rev. B* **46** (Nov, 1992) 12573–12586. http://link.aps.org/doi/10.1103/PhysRevB.46.12573.

[187] V. C. Y. Chang and C. S. Chu, "Andreev-level tunneling in a ballistic double superconductor-normal-metal-superconductor junction," *Phys. Rev. B* **55** (Mar, 1997) 6004–6014. http://link.aps.org/doi/10.1103/PhysRevB.55.6004.

[188] J. Bardeen and J. L. Johnson, "Josephson Current Flow in Pure Superconducting-Normal-Superconducting Junctions," *Phys. Rev. B* **5** (Jan, 1972) 72–78. http://link.aps.org/doi/10.1103/PhysRevB.5.72.

[189] A. Chrestin, T. Matsuyama, and U. Merkt, "Critical currents and supercurrent oscillations in Josephson field-effect transistors," *Phys. Rev. B* **49** (Jan, 1994) 498–504. http://link.aps.org/doi/10.1103/PhysRevB.49.498.

[190] T. Schäpers, *Superconductor/Semiconductor Junctions.* No. 174 in Springer Tracts in Modern Physics. Springer, 2001. p.68.

[191] B. J. van Wees, K.-M. H. Lenssen, and C. J. P. M. Harmans, "Transmission formalism for supercurrent flow in multiprobe superconductor-semiconductor-superconductor devices," *Phys. Rev. B* **44** (Jul, 1991) 470–473. http://link.aps.org/doi/10.1103/PhysRevB.44.470.

[192] C. W. J. Beenakker, "Universal limit of critical-current fluctuations in mesoscopic Josephson junctions," *Phys. Rev. Lett.* **67** (Dec, 1991) 3836–3839. http://link.aps.org/doi/10.1103/PhysRevLett.67.3836.

[193] T. Schäpers, *Superconductor/Semiconductor Junctions*. No. 174 in Springer Tracts in Modern Physics. Springer, 2001. p.108.

[194] A. Furusaki, H. Takayanagi, and M. Tsukada, "Josephson effect of the superconducting quantum point contact," *Phys. Rev. B* **45** (May, 1992) 10563–10575. http://link.aps.org/doi/10.1103/PhysRevB.45.10563.

[195] H. Tang, Z. Wang, and Y. Zhang, "Normal reflection effect on the critical current in a clean-limit superconductor-normal-metal-superconductor junction," *Zeitschrift für Physik B Condensed Matter* **101** no. 3, (1997) 359–366. http://dx.doi.org/10.1007/s002570050220.

[196] A. Furusaki, H. Takayanagi, and M. Tsukada, "Theory of quantum conduction of supercurrent through a constriction," *Phys. Rev. Lett.* **67** (Jul, 1991) 132–135. http://link.aps.org/doi/10.1103/PhysRevLett.67.132.

[197] C. Beenakker and H. van Houten, "The Superconducting Quantum Point Contact," in *Nanostructures and Mesoscopic Systems*, W. P. K. A. Reed, ed., pp. 481–497. Academic Press, 1992. http://www.sciencedirect.com/science/article/pii/B9780124096608500511.

[198] A. Furusaki, "Josephson current carried by Andreev levels in superconducting quantum point contacts," *Superlattices and Microstructures* **25** no. 5-6, (1999) 809–818. http://www.sciencedirect.com/science/article/pii/S0749603699907309.

[199] J. P. Heida, *Josephson currents in two dimensional mesoscopic ballistic conductors*. PhD thesis, University of Groningen, 1998. http://irs.ub.rug.nl/ppn/16623950X.

[200] J.-D. Pillet, C. H. L. Quay, P. Morfin, C. Bena, A. L. Yeyati, and P. Joyez, "Andreev bound states in supercurrent-carrying carbon nanotubes revealed," *Nat Phys* **6** no. 12, (Dec, 2010) 965–969. http://dx.doi.org/10.1038/nphys1811.

[201] A. Jellinggaard, K. Grove-Rasmussen, M. H. Madsen, and J. Nygård, "Tuning yu-shiba-rusinov states in a quantum dot," *Phys. Rev. B* **94** (Aug, 2016) 064520. http://link.aps.org/doi/10.1103/PhysRevB.94.064520.

[202] W. Chang, S. M. Albrecht, T. S. Jespersen, F. Kuemmeth, P. Krogstrup, J. Nygård, and C. M. Marcus, "Hard gap in epitaxial semiconductor–superconductor nanowires," *Nature Nanotechnology* **10** no. 3, (Mar, 2015) 232–236. https://doi.org/10.1038/nnano.2014.306.

[203] T. Sand-Jespersen, J. Paaske, B. M. Andersen, K. Grove-Rasmussen, H. I. Jørgensen, M. Aagesen, C. B. Sørensen, P. E. Lindelof, K. Flensberg, and J. Nygård, "Kondo-enhanced andreev tunneling in inas nanowire quantum dots," *Phys. Rev. Lett.* **99** (Sep, 2007) 126603. http://link.aps.org/doi/10.1103/PhysRevLett.99.126603.

[204] A. Kumar, M. Gaim, D. Steininger, A. L. Yeyati, A. Martín-Rodero, A. K. Hüttel, and C. Strunk, "Temperature dependence of andreev spectra in a superconducting carbon nanotube quantum dot," *Phys. Rev. B* **89** (Feb, 2014) 075428. http://link.aps.org/doi/10.1103/PhysRevB.89.075428.

[205] M. Gaass, S. Pfaller, T. Geiger, A. Donarini, M. Grifoni, A. K. Hüttel, and C. Strunk, "Subgap spectroscopy of thermally excited quasiparticles in a nb-contacted carbon nanotube quantum dot," *Phys. Rev. B* **89** (Jun, 2014) 241405. http://link.aps.org/doi/10.1103/PhysRevB.89.241405.

[206] J.-D. Pillet, P. Joyez, R. Žitko, and M. F. Goffman, "Tunneling spectroscopy of a single quantum dot coupled to a superconductor: From kondo ridge to andreev bound states," *Phys. Rev. B* **88** (Jul, 2013) 045101. http://link.aps.org/doi/10.1103/PhysRevB.88.045101.

[207] B.-K. Kim, Y.-H. Ahn, J.-J. Kim, M.-S. Choi, M.-H. Bae, K. Kang, J. S. Lim, R. López, and N. Kim, "Transport measurement of andreev bound states in a kondo-correlated quantum dot," *Phys. Rev. Lett.* **110** (Feb, 2013) 076803. http://link.aps.org/doi/10.1103/PhysRevLett.110.076803.

[208] A. Eichler, M. Weiss, S. Oberholzer, C. Schönenberger, A. Levy Yeyati, J. C. Cuevas, and A. Martín-Rodero, "Even-odd effect in andreev transport through a carbon nanotube quantum dot," *Phys. Rev. Lett.* **99** (Sep, 2007) 126602. http://link.aps.org/doi/10.1103/PhysRevLett.99.126602.

[209] G. Kiršanskas, M. Goldstein, K. Flensberg, L. I. Glazman, and J. Paaske, "Yu-shiba-rusinov states in phase-biased superconductor–quantum

dot–superconductor junctions," *Phys. Rev. B* **92** (Dec, 2015) 235422. http://link.aps.org/doi/10.1103/PhysRevB.92.235422.

[210] N. Gupta, Y. Song, G. W. Holloway, U. Sinha, C. M. Haapamaki, R. R. LaPierre, and J. Baugh, "Temperature-dependent electron mobility in inas nanowires," *Nanotechnology* **24** no. 22, (2013) 225202. http://stacks.iop.org/0957-4484/24/i=22/a=225202.

[211] G. W. Holloway, Y. Song, C. M. Haapamaki, R. R. LaPierre, and J. Baugh, "Electron transport in inas-inalas core-shell nanowires," *Applied Physics Letters* **102** no. 4, (2013) 043115. http://scitation.aip.org/content/aip/journal/apl/102/4/10.1063/1.4788742.

[212] G. W. Holloway, C. M. Haapamaki, P. Kuyanov, R. R. LaPierre, and J. Baugh, "Electrical characterization of chemical and dielectric passivation of inas nanowires," *Semiconductor Science and Technology* **31** no. 11, (Oct, 2016) 114004, arXiv:1606.01405. https://dx.doi.org/10.1088/0268-1242/31/11/114004.

[213] M. H. Sun, H. J. Joyce, Q. Gao, H. H. Tan, C. Jagadish, and C. Z. Ning, "Removal of surface states and recovery of band-edge emission in inas nanowires through surface passivation," *Nano Letters* **12** no. 7, (2012) 3378–3384, http://dx.doi.org/10.1021/nl300015w. http://dx.doi.org/10.1021/nl300015w. PMID: 22663381.

[214] Q. Hang, F. Wang, P. D. Carpenter, D. Zemlyanov, D. Zakharov, E. A. Stach, W. E. Buhro, and D. B. Janes, "Role of molecular surface passivation in electrical transport properties of inas nanowires," *Nano Letters* **8** no. 1, (2008) 49–55, http://dx.doi.org/10.1021/nl071888t. http://dx.doi.org/10.1021/nl071888t. PMID: 18052229.

[215] D. Y. Petrovykh, J. C. Smith, T. D. Clark, R. Stine, L. A. Baker, and L. J. Whitman, "Self-assembled monolayers of alkanethiols on inas," *Langmuir* **25** no. 20, (2009) 12185–12194, http://dx.doi.org/10.1021/la804314j. http://dx.doi.org/10.1021/la804314j. PMID: 19778053.

[216] H. Courtois, M. Meschke, J. T. Peltonen, and J. P. Pekola, "Origin of hysteresis in a proximity josephson junction," *Phys. Rev. Lett.* **101** (Aug, 2008) 067002. http://link.aps.org/doi/10.1103/PhysRevLett.101.067002.

[217] H. Takayanagi, J. B. Hansen, and J. Nitta, "Mesoscopic fluctuations of the critical current in a superconductor–normal-conductor–superconductor," *Phys. Rev. Lett.* **74** (Jan, 1995) 166–169. http://link.aps.org/doi/10.1103/PhysRevLett.74.166.

[218] M. Tinkham, *Introduction to Superconductivity*. McGraw-Hill, New York, 2nd ed., 1996. p. 202.

[219] M. L. Della Rocca, M. Chauvin, B. Huard, H. Pothier, D. Esteve, and C. Urbina, "Measurement of the current-phase relation of superconducting atomic contacts," *Phys. Rev. Lett.* **99** (Sep, 2007) 127005. http://link.aps.org/doi/10.1103/PhysRevLett.99.127005.

[220] S. Abay, D. Persson, H. Nilsson, F. Wu, H. Q. Xu, M. Fogelström, V. Shumeiko, and P. Delsing, "Charge transport in inas nanowire josephson junctions," *Phys. Rev. B* **89** (Jun, 2014) 214508. http://link.aps.org/doi/10.1103/PhysRevB.89.214508.

[221] P. A. Lee and A. D. Stone, "Universal conductance fluctuations in metals," *Phys. Rev. Lett.* **55** (Oct, 1985) 1622–1625. http://link.aps.org/doi/10.1103/PhysRevLett.55.1622.

[222] S. Datta, *Electronic Transport in Mesoscopic Systems*. Cambridge University Press, Cambridge, 1997. p. 212.

[223] J. Tiira, E. Strambini, M. Amado, S. Roddaro, P. San-Jose, R. Aguado, F. S. Bergeret, D. Ercolani, L. Sorba, and F. Giazotto, "Magnetically-driven colossal supercurrent enhancement in inas nanowire josephson junctions," *Nature Communications* **8** no. 1, (Apr, 2017) 14984, arXiv:1601.02955. https://doi.org/10.1038/ncomms14984.

[224] K. D. Usadel, "Generalized diffusion equation for superconducting alloys," *Phys. Rev. Lett.* **25** (Aug, 1970) 507–509. http://link.aps.org/doi/10.1103/PhysRevLett.25.507.

[225] Holloway, Gregory, *Electron transport in semiconducting nanowires and quantum dots*. PhD thesis, 2017. http://hdl.handle.net/10012/11155.

[226] W. G. van der Wiel, S. De Franceschi, J. M. Elzerman, T. Fujisawa, S. Tarucha, and L. P. Kouwenhoven, "Electron transport through double quantum dots," *Rev. Mod. Phys.* **75** (Dec, 2002) 1–22. https://link.aps.org/doi/10.1103/RevModPhys.75.1.

[227] R. Hanson, L. P. Kouwenhoven, J. R. Petta, S. Tarucha, and L. M. K. Vandersypen, "Spins in few-electron quantum dots," *Rev. Mod. Phys.* **79** (Oct, 2007) 1217–1265. https://link.aps.org/doi/10.1103/RevModPhys.79.1217.

[228] F. D. M. Haldane, "Scaling theory of the asymmetric anderson model," *Phys. Rev. Lett.* **40** (Feb, 1978) 416–419. http://link.aps.org/doi/10.1103/PhysRevLett.40.416.

[229] A. V. Kretinin, H. Shtrikman, D. Goldhaber-Gordon, M. Hanl, A. Weichselbaum, J. von Delft, T. Costi, and D. Mahalu, "Spin-$\frac{1}{2}$ kondo effect in an inas nanowire quantum dot: Unitary limit, conductance scaling, and zeeman splitting," *Phys. Rev. B* **84** (Dec, 2011) 245316. http://link.aps.org/doi/10.1103/PhysRevB.84.245316.

[230] P. W. Anderson, "Localized magnetic states in metals," *Phys. Rev.* **124** (Oct, 1961) 41–53. http://link.aps.org/doi/10.1103/PhysRev.124.41.

[231] A. V. Balatsky, I. Vekhter, and J.-X. Zhu, "Impurity-induced states in conventional and unconventional superconductors," *Rev. Mod. Phys.* **78** (May, 2006) 373–433. http://link.aps.org/doi/10.1103/RevModPhys.78.373.

[232] T. Schäpers, *Superconductor/Semiconductor Junctions*. No. 174 in Springer Tracts in Modern Physics. Springer, Berlin, 2001. p. 72.

[233] D. B. Suyatin, C. Thelander, M. T. Björk, I. Maximov, and L. Samuelson, "Sulfur passivation for ohmic contact formation to InAs nanowires," *Nanotechnology* **18** no. 10, (Feb, 2007) 105307. https://doi.org/10.1088/0957-4484/18/10/105307.

[234] A. I. Gubin, K. S. Il'in, S. A. Vitusevich, M. Siegel, and N. Klein, "Dependence of magnetic penetration depth on the thickness of superconducting nb thin films," *Phys. Rev. B* **72** (Aug, 2005) 064503. http://link.aps.org/doi/10.1103/PhysRevB.72.064503.

[235] C. Janvier, L. Tosi, L. Bretheau, Ç. Ö. Girit, M. Stern, P. Bertet, P. Joyez, D. Vion, D. Esteve, M. F. Goffman, H. Pothier, and C. Urbina, "Coherent manipulation of andreev states in superconducting atomic contacts," *Science* **349** no. 6253, (2015) 1199–1202, http://science.sciencemag.org/content/349/6253/1199.full.pdf. http://science.sciencemag.org/content/349/6253/1199.

[236] F. Deon, V. Pellegrini, F. Giazotto, G. Biasiol, L. Sorba, and F. Beltram, "Quantum dot spectroscopy of proximity-induced superconductivity in a two-dimensional electron gas," *Applied Physics Letters* **98** no. 13, (2011) 132101. http://scitation.aip.org/content/aip/journal/apl/98/13/10.1063/1.3570660.

[237] C. Buizert, A. Oiwa, K. Shibata, K. Hirakawa, and S. Tarucha, "Kondo universal scaling for a quantum dot coupled to superconducting leads," *Phys. Rev. Lett.* **99** (Sep, 2007) 136806. http://link.aps.org/doi/10.1103/PhysRevLett.99.136806.

[238] E. B. Hansen, J. Danon, and K. Flensberg, "Phase-tunable majorana bound states in a topological n-sns junction," *Phys. Rev. B* **93** (Mar, 2016) 094501. http://link.aps.org/doi/10.1103/PhysRevB.93.094501.

[239] G.-Y. Huang, M. Leijnse, K. Flensberg, and H. Q. Xu, "Tunnel spectroscopy of majorana bound states in topological superconductor/quantum dot josephson junctions," *Phys. Rev. B* **90** (Dec, 2014) 214507. http://link.aps.org/doi/10.1103/PhysRevB.90.214507.

[240] C. Beenakker, "Search for Majorana Fermions in Superconductors," *Annual Review of Condensed Matter Physics* **4** no. 1, (2013) 113–136. http://dx.doi.org/10.1146/annurev-conmatphys-030212-184337.

[241] M. Leijnse and K. Flensberg, "Introduction to topological superconductivity and Majorana fermions," *Semiconductor Science and Technology* **27** no. 12, (2012) 124003. http://stacks.iop.org/0268-1242/27/i=12/a=124003.

[242] S. Das Sarma, M. Freedman, and C. Nayak, "Majorana zero modes and topological quantum computation," *Npj Quantum Information* **1** (Oct, 2015) 15001 EP–. http://dx.doi.org/10.1038/npjqi.2015.1.

[243] J. Li, H. Chen, I. K. Drozdov, A. Yazdani, B. A. Bernevig, and A. H. MacDonald, "Topological superconductivity induced by ferromagnetic metal chains," *Phys. Rev. B* **90** (Dec, 2014) 235433. http://link.aps.org/doi/10.1103/PhysRevB.90.235433.

[244] H.-Y. Hui, P. M. R. Brydon, J. D. Sau, S. Tewari, and S. D. Sarma, "Majorana fermions in ferromagnetic chains on the surface of bulk spin-orbit coupled s-wave superconductors," *Scientific Reports* **5** (Mar, 2015) 8880 EP–. http://dx.doi.org/10.1038/srep08880.

[245] T. Kawakami and X. Hu, "Evolution of Density of States and a Spin-Resolved Checkerboard-Type Pattern Associated with the Majorana Bound State," *Phys. Rev. Lett.* **115** (Oct, 2015) 177001. http://link.aps.org/doi/10.1103/PhysRevLett.115.177001.

[246] L.-H. Wu, Q.-F. Liang, and X. Hu, "New scheme for braiding Majorana fermions," *Science and Technology of Advanced Materials* **15** no. 6, (2014) 064402. http://stacks.iop.org/1468-6996/15/i=6/a=064402.

[247] H. O. H. Churchill, V. Fatemi, K. Grove-Rasmussen, M. T. Deng, P. Caroff, H. Q. Xu, and C. M. Marcus, "Superconductor-nanowire devices from tunneling to the multichannel

regime: Zero-bias oscillations and magnetoconductance crossover," *Phys. Rev. B* **87** (Jun, 2013) 241401. http://link.aps.org/doi/10.1103/PhysRevB.87.241401.

[248] S. Bravyi and A. Kitaev, "Universal quantum computation with ideal clifford gates and noisy ancillas," *Phys. Rev. A* **71** (Feb, 2005) 022316. http://link.aps.org/doi/10.1103/PhysRevA.71.022316.

[249] K. Flensberg, "Non-Abelian Operations on Majorana Fermions via Single-Charge Control," *Phys. Rev. Lett.* **106** (Mar, 2011) 090503. http://link.aps.org/doi/10.1103/PhysRevLett.106.090503.

[250] M. Leijnse and K. Flensberg, "Quantum Information Transfer between Topological and Spin Qubit Systems," *Phys. Rev. Lett.* **107** (Nov, 2011) 210502. http://link.aps.org/doi/10.1103/PhysRevLett.107.210502.

[251] F. Hassler, A. R. Akhmerov, and C. W. J. Beenakker, "The top-transmon: a hybrid superconducting qubit for parity-protected quantum computation," *New Journal of Physics* **13** no. 9, (2011) 095004. http://stacks.iop.org/1367-2630/13/i=9/a=095004.

[252] T. Hyart, B. van Heck, I. C. Fulga, M. Burrello, A. R. Akhmerov, and C. W. J. Beenakker, "Flux-controlled quantum computation with majorana fermions," *Phys. Rev. B* **88** (Jul, 2013) 035121. http://link.aps.org/doi/10.1103/PhysRevB.88.035121.

[253] P. Bonderson and R. M. Lutchyn, "Topological Quantum Buses: Coherent Quantum Information Transfer between Topological and Conventional Qubits," *Phys. Rev. Lett.* **106** (Mar, 2011) 130505. http://link.aps.org/doi/10.1103/PhysRevLett.106.130505.

[254] M. Leijnse and K. Flensberg, "Scheme to measure Majorana fermion lifetimes using a quantum dot," *Phys. Rev. B* **84** (Oct, 2011) 140501. http://link.aps.org/doi/10.1103/PhysRevB.84.140501.

[255] H. A. Nilsson, T. Duty, S. Abay, C. Wilson, J. B. Wagner, C. Thelander, P. Delsing, and L. Samuelson, "A radio frequency single-electron transistor based on an inas/inp heterostructure nanowire," *Nano Letters* **8** no. 3, (Mar, 2008) 872–875. https://doi.org/10.1021/nl0731062.

[256] M. Veldhorst, J. Hwang, C. Yang, W. Leenstra, B. de Ronde, J. Dehollain, J. Muhonen, F. Hudson, K. Itoh, A. Morello, and A. Dzurak, "An addressable quantum dot qubit with

fault-tolerant control-fidelity," *Nat Nano* **9** no. 12, (Dec, 2014) 981–985. http://dx.doi.org/10.1038/nnano.2014.216.

[257] D. J. Reilly, C. M. Marcus, M. P. Hanson, and A. C. Gossard, "Fast single-charge sensing with a rf quantum point contact," *Applied Physics Letters* **91** no. 16, (2007) . http://scitation.aip.org/content/aip/journal/apl/91/16/10.1063/1.2794995.

[258] J. Stehlik, Y.-Y. Liu, C. M. Quintana, C. Eichler, T. R. Hartke, and J. R. Petta, "Fast charge sensing of a cavity-coupled double quantum dot using a josephson parametric amplifier," *Phys. Rev. Applied* 4 (Jul, 2015) 014018. http://link.aps.org/doi/10.1103/PhysRevApplied.4.014018.

[259] C. W. J. Beenakker, "Theory of Coulomb-blockade oscillations in the conductance of a quantum dot," *Phys. Rev. B* **44** (Jul, 1991) 1646–1656. http://link.aps.org/doi/10.1103/PhysRevB.44.1646.

[260] D. Sticlet, C. Bena, and P. Simon, "Spin and majorana polarization in topological superconducting wires," *Phys. Rev. Lett.* **108** (Mar, 2012) 096802. http://link.aps.org/doi/10.1103/PhysRevLett.108.096802.

[261] J. Johansson, P. Nation, and F. Nori, "QuTiP 2: A Python framework for the dynamics of open quantum systems," *Computer Physics Communications* **184** no. 4, (2013) 1234–1240. http://www.sciencedirect.com/science/article/pii/S0010465512003955.

[262] M. S. Scheurer and A. Shnirman, "Nonadiabatic processes in majorana qubit systems," *Phys. Rev. B* **88** (Aug, 2013) 064515. http://link.aps.org/doi/10.1103/PhysRevB.88.064515.

[263] C. S. Amorim, K. Ebihara, A. Yamakage, Y. Tanaka, and M. Sato, "Majorana braiding dynamics in nanowires," *Phys. Rev. B* **91** (May, 2015) 174305. http://link.aps.org/doi/10.1103/PhysRevB.91.174305.

[264] T. Karzig, A. Rahmani, F. von Oppen, and G. Refael, "Optimal control of majorana zero modes," *Phys. Rev. B* **91** (May, 2015) 201404. http://link.aps.org/doi/10.1103/PhysRevB.91.201404.

[265] T. Karzig, G. Refael, and F. von Oppen, "Boosting majorana zero modes," *Phys. Rev. X* **3** (Nov, 2013) 041017. http://link.aps.org/doi/10.1103/PhysRevX.3.041017.

[266] M. Hell, J. Danon, K. Flensberg, and M. Leijnse, "Time scales for majorana manipulation using coulomb blockade in gate-controlled superconducting nanowires," *Phys. Rev. B* **94** (Jul, 2016) 035424. http://link.aps.org/doi/10.1103/PhysRevB.94.035424.

[267] D. Rainis and D. Loss, "Majorana qubit decoherence by quasiparticle poisoning," *Phys. Rev. B* **85** (May, 2012) 174533. http://link.aps.org/doi/10.1103/PhysRevB.85.174533.

[268] A. P. Higginbotham, S. M. Albrecht, G. Kirsanskas, W. Chang, F. Kuemmeth, P. Krogstrup, T. S. Jespersen, J. Nygard, K. Flensberg, and C. M. Marcus, "Parity lifetime of bound states in a proximitized semiconductor nanowire," *Nat Phys* **11** no. 12, (Dec, 2015) 1017–1021. http://dx.doi.org/10.1038/nphys3461. Letter.

[269] D. J. van Woerkom, A. Geresdi, and L. P. Kouwenhoven, "One minute parity lifetime of a nbtin cooper-pair transistor," *Nat Phys* **11** no. 7, (Jul, 2015) 547–550. http://dx.doi.org/10.1038/nphys3342. Letter.

[270] T. Schäpers, *Superconductor/Semiconductor Junctions.* No. 174 in Springer Tracts in Modern Physics. Springer, 2001.

[271] M. W. A. de Moor, J. D. S. Bommer, D. Xu, G. W. Winkler, A. E. Antipov, A. Bargerbos, G. Wang, N. van Loo, R. L. M. O. het Veld, S. Gazibegovic, D. Car, J. A. Logan, M. Pendharkar, J. S. Lee, E. P. A. M. Bakkers, C. J. Palmstrøm, R. M. Lutchyn, L. P. Kouwenhoven, and H. Zhang, "Electric field tunable superconductor-semiconductor coupling in majorana nanowires," *New Journal of Physics* **20** no. 10, (Oct, 2018) 103049. https://doi.org/10.1088/1367-2630/aae61d.

[272] Y. Li, G. W. Holloway, S. C. Benjamin, G. A. D. Briggs, J. Baugh, and J. A. Mol, "Double quantum dot memristor," *Phys. Rev. B* **96** (Aug, 2017) 075446. https://link.aps.org/doi/10.1103/PhysRevB.96.075446.

[273] M. Fogarty, K. Chan, B. Hensen, W. Huang, T. Tanttu, H. Yang, A. Laucht, M. Veldhorst, F. Hudson, K. Itoh, D. Culcer, A. Morello, and A. Dzurak, "Integrated silicon qubit platform with single-spin addressability, exchange control and robust single-shot singlet-triplet readout," *Nature Communications* **9** (10, 2018) .

[274] P. Sriram, S. S. Kalantre, K. Gharavi, J. Baugh, and B. Muralidharan, "Supercurrent interference in semiconductor nanowire josephson junctions," *Phys. Rev. B* **100** (Oct, 2019) 155431. https://link.aps.org/doi/10.1103/PhysRevB.100.155431.

[275] C. Duse, P. Sriram, K. Gharavi, J. Baugh, and B. Muralidharan, "Role of dephasing on the conductance signatures of majorana zero modes," *Journal of Physics: Condensed Matter* **33** no. 36, (Jul, 2021) 365301. https://doi.org/10.1088/1361-648x/ac0d16.

[276] C. R. Harris, K. J. Millman, S. J. van der Walt, R. Gommers, P. Virtanen, D. Cournapeau, E. Wieser, J. Taylor, S. Berg, N. J. Smith, R. Kern, M. Picus, S. Hoyer, M. H. van Kerkwijk, M. Brett, A. Haldane, J. F. del Río, M. Wiebe, P. Peterson, P. Gérard-Marchant, K. Sheppard, T. Reddy, W. Weckesser, H. Abbasi, C. Gohlke, and T. E. Oliphant, "Array programming with numpy," *Nature* **585** no. 7825, (Sep, 2020) 357–362. https://doi.org/10.1038/s41586-020-2649-2.

Appendix A

Device Fabrication

The devices discussed in this thesis were fabricated at the Mike and Ophelia Lazaridis Quantum NanoFab facility at the University of Waterloo. I am very grateful to the staff at the NanoFab facility who over the course of many years taught me the ins and outs of working in a cleanroom in a manner that resulted in reproducible and useful devices.

Device fabrication is an art and a craft more than a science, and one that can only be perfected with practice. However, a necessary component is a deep and complete understanding of the physics and chemistry of the steps involved in the fabrication of the device. Detailed and strict attention to every aspect of the process is an absolute must; for reproducibility of the results, the recipe needs to be followed exactly, down to such details as using the same glassware and pouring liquids to the same level each and every time.

Below I provide recipes for the fabrication of the second and third generation of proximitized nanowire Josephson devices. First comes an outline, and then details and notes about the crucial steps of the fabrication. I'm grateful to my fellow PhD student Greg Holloway who helped develop many of the steps involved in this recipe. Appendix A in Ref. [225] provides a thorough breakdown of and more information about the fabrication steps not discussed in detail here, including preparatory steps performed on the nanowires.

Outline of recipe for Nanowire-based Josephson junctions

1. **Preparation**
    - Prepare desired nanowires (w/ or w/o Al_2O_3 shells)

- Cleave 4” Si wafer with 300 nm thermal oxide into 1cm x 1cm chips.

2. **Bonding pads**
    - Photolithography (bi-layer) nanowire wirebonding pads
    - E-beam evaporation: Metal deposition (Ti/Au 30/50 nm)
    - Liftoff metal in heated Remover PG solution
3. **Fine Alignment Marks**
    - EBL (PMMA A4 950K) for alignment marks
    - E-beam evaporation: Metal deposition of alignment marks Ti/Au 30/50 nm
    - Liftoff metal in heated Remover PG solution
4. **Optional: for devices with trenches**
    - EBL (PMMA A3 950K) for trenches
    - Etch 60 nm oxide in dry etcher
    - Etch in HF to remove 3 nm
    - Liftoff resist in heated PG
5. **Nanowire deposition and location**
    - Deposit nanowires onto chip/into trenches
    - Use SEM to locate nanowires
6. **Optional: for devices with top-gates**
    - (Use nanowires with Al_2O_3 shells, and in trenches to ensure continuity of top-gate.)
    - EBL (PMMA A3 950K) top gates
    - E-beam evaporation: Metal deposition Ti/Au 10/30 nm
    - Liftoff metal in heated PG
7. **Source/Drain contacts**
    - **3rd generation only**: Apply HMDS layer
    - EBL (ZEP 520A) for source/drain contacts

- HF etch nanowire shell material and/or native oxide
- **3rd generation only**: Surface passivation in a sulfur-rich solution
- Quickly move to AJA sputtering system
- In-situ ion milling + sputtering of source/drain contacts (Ti/Nb 2/80 nm)
- Liftoff metal in heated Remover PG solution

Deposition of Source/Drain contacts

This is the last and the most crucial step of the device fabrication. Achieving high superconductor/semiconductor interface transparency t critically depends on this step. Application of an HMDS layer helps with devices that have an $Al_2 O_3$ shell, as the subsequent HF etch can remove the alumina shell *inside* the junction channel. The HMDS layer helps with the adhesion of the ZEP resist to the surface and ensures that the alumina shell is only removed in the source/drain contact region. The sulfur passivation step was found to make a noticeable difference in improving the Nb/InAs interface quality, and the 3rd generation devices have a greatly increased contact transparency t compared to the 2nd generation devices.

It is important that after the HF etch which removes the native oxide and sulfur passivation, the chips be moved to a loadlock quickly so that the vacuum can be pulled, preventing the native InAs oxide to regrow. With practice I could have the loadlock on the AJA sputterer pumped to very high vacuum within three minutes of taking the chip out the sulfur solution. This required walking at a very brisk pace from one chamber of the cleanroom to the other where the AJA was located (running is not allowed in the cleanroom).

After the chip was inserted in the chamber of the sputter system the following recipe was used for Ti/Nb deposition:

- (Chips mounted at the center of the chuck. Using a 60 rpm rotation of the chuck. All the steps are performed at room temperature.)
- Reverse RF-sputtering (ion milling) in an Ar environment, 50 W power, 1.5 mTorr Ar pressure, for 6.5 minutes.
- Deposit 2 nm Ti with DC sputtering. Ar environment, 200 W power, 3 mTorr Ar pressure, 17 seconds.
- Deposit 80 nm Nb with DC sputtering. Ar environment, 200 W power, 3 mTorr Ar pressure, 641 seconds.

The Ar ion milling pressure and time used was calibrated to remove ~ 2.5 nm of material (native oxide) from a planar InAs substrate, as measured with atomic force microscopy (AFM).

Appendix B

Code Used in this Thesis

Almost every stage of the work that went into this thesis involved some form of data analysis or modeling. We posit that NumPy [276], the numerical analysis library for the Python programming language is generally the best tool available for Scientific Computing. This assessment is based on several points: Firstly, that Python is a sophisticated, general purpose programming language, and students can learn good coding practices and high level coding concepts by using it over, e.g., Matlab. Secondly, prototype code can be developed and debugged fast and relatively painlessly — especially when using Jupyter Notebook, which provides a web-server in which code can be executed in cells, similar to how the Mathematica interface works. Thirdly, and even though this never really was a bottleneck for the code written for this thesis, well written Python code can be very fast, especially if tools like Just-in-Time compilation are used. If one can develop code 1'000 times faster than C code which executes in a time that differs from the C code by a factor ~ 1, and that code is a lot more human-readable and less prone to design errors, I think that is a very good compromise. I would therefore recommend to all scientists to consider using Anaconda form Continuum Analytics which provides an easily deployable, well-contained Python environment with its own package management tools for all of their scientific computing needs. Lastly, but not least, the Python / NumPy / Matplotlib stack is free and open-source software, the use of which is one of the principals of Open Science, a practice in science behind which I stand.

Below is provided a short description of the code used in this thesis. The source for this code can be found at `https://github.com/kayghar/` under a GNU LGPLv3 license. If there are any shortcomings in the quality of the code, I preemptively apologize; however, I must argue that to a certain degree such is the nature of academic code where the standard for success is such that the code needs to run correctly only once (e.g. to produce a figure), and in a trusted

environment. If there are any questions or comments please do not hesitate to contact me via github.

Data Analysis and Plotter Tool

https://github.com/kayghar/plottertool/

A simple tool to format csv data outputted by the data acquisition program Spanish Acquisition into a database, and to perform analyses such as differentiation and smoothing, and to the plot the experimental data. Used in chapters 2, 3, 4, and 5.

Orbital Josephson Interference Model

https://github.com/kayghar/orbitalinterference/

The code used in Chapter 3 to simulate the critical current of a nanowire Josephson junction in the presence of an external axial magnetic field. It can be used to observe the orbital Josephson interference effect and its dependence on the subband structure of the nanowire.

Model for Current-biased Andreev Bound-state Energies

https://github.com/kayghar/currentABS/

Used in Chapter 4 to calculate the energy levels of current biased Andreev Bound states (ABS) and fit to the experimental data. Based on the theoretical work presented in ref. [209], which calculates phase-biased ABS energy levels.

Fermionic Space

https://github.com/kayghar/FermionicSpace/

A tool to provide a matrix representation of the Hilbert space of fermions, in a manner that respects their anti-symmetric exchange statistics. Also provides matrix representations for the second-quantized fermionic operators. Useful for simulations of fermionic Hamiltonians.

Majorana Parity Readout

https://github.com/kayghar/parityReadout/

The code used in Chapter 6 to simulate the calibration and parity-readout procedure of MBS using a tunnel coupled quantum dot. Numerically integrates Time-dependent Schrödinger equations. Depends on FermionicSpace.